-

SAPIENZA
UNIVERSITÀ DI ROMA

Department of Basic and Applied Sciences for Engineering

DOCTORATE IN
MATHEMATICAL MODELS FOR ENGINEERING, ELECTROMAGNETICS AND NANOSCIENCES - CURRICULUM IN MATERIALS SCIENCE

Studies of molecular photoionization of simple systems by advanced photon sources

Candidate:
Luca Schio

Coordinators:
Prof. Paola Loreti
Prof. Carlo Mariani

Advisor:
Prof. Stefano Stranges

Co-Advisor:
Assoc. Prof. Vitali Zhaunerchyk

Reviewers:
Prof. Giovanna Fronzoni
Prof. Robert Donovan

CYCLE XXXII

A Mio Padre

Contents

List of Abbreviations

ADF	Amsterdam Density Functional
ARPES	Angle Resolved Photoelectron Spectroscopy
CASSCF	Complete Active Space Self Consistent Field
CD	Circular Dichroism
CI	Configuration Interaction
CM	Cooper Minimum
DFT	Density Functional Theory
ESCA	Electron Spectroscopy for Chemical Analysis
EUV	Extreme Ultraviolet
FEL	Free Electron Laser
HF	Hartree-Fock
HDA	Hemispherical Deflector Analyzer
IRMPD	Infra-Red Multi-Photon Dissociation
IVR	Intramolecular Vibrational Redistribution
KT	Koopmans' Theorem
LCAO	Linear Combination of Atomic Orbitals
MCP	Micro Channel Plate
PAD	Photoelectron Angular Distribution
PECD	Photoelectron Circular Dichroism
PEPIPICO	Photoelectron-Photoion-Photoion Coincidence
PES	Photoelectron Spectroscopy
PSD	Position Sensitive Detector
SCF	Self Consistent Field
SR	Synchrotron Radiation
SRPES	Synchrotron Radiation Photoelectron Spectroscopy
TDDFT	Time Dependent Density Functional Theory

TOF	Time of flight
UPS	Ultra-violet Photoelectron Spectroscopy
VMI	Velocity Map Imaging
VUV	Vacuum Ultraviolet
XPS	X-ray Photoelectron Spectroscopy

List of papers

The results presented in this Thesis are based on the following papers:

I **Double photoionization of propylene oxide: A coincidence study of the ejection of a pair of valence-shell electrons**, S. Falcinelli, F. Vecchiocattivi, M. Alagia, L. Schio, R. Richter, S. Stranges, D. Catone, M. S. Arruda, L. A. V. Mendes, F. Palazzetti, V. Aquilanti, F. Pirani, *J. Chem. Phys.* **148**, 114302 (2018), DOI: 10.1063/1.5024408.

II **Angular Distribution of Ion Products in the Double Photoionization of Propylene Oxide**, S. Falcinelli, M. Rosi, F. Pirani, D. Bassi, M. Alagia, L. Schio, R. Richter, S. Stranges, N. Balucani, V. Lorent, F. Vecchiocattivi, *Front. Chem.* **7**, 621 (2019), DOI: 10.3389/fchem.2019.00621.

III **Cooper minimum photoelectron dynamics beyond the one-particle picture in chiral molecules**, L. Schio, M. Alagia, D. Toffoli, P. Decleva, M. Stener, A. Ponzi, O. Rebrov, V. Zhaunerchyk, M. Larsson, S. Falcinelli, D. Catone, S. Turchini, N. Zema, F. Salvador, P. Bertoch, D. Benedetti, D. Vivoda, S. Stranges, 2019, *Manuscript.*

IV **Photoionization dynamics of the tetraoxo complexes OsO_4 and RuO_4**, L. Schio, M. Alagia, D. Toffoli, P. Decleva, R. Richter, O. Schalk, R. Thomas, M. Mucke, F. Salvador, P. Bertoch, D. Benedetti, C. Dri, G. Cautero, R. Sergo, L. Stebel, D. Vivoda, S. Stranges, 2019, *Manuscript.*

Comments on my own partecipation

The presented Doctorate Thesis is the result of the collective work of a wide research group, involving a huge number of people, which is common when dealing with large scale light source facilities as Elettra. My personal contribution to the papers, experiments and data analysis varied, as reported in greater detail below, but was focused for the most on the preparation and execution of the experiments on the GasPhase and CiPo beamlines, and on the on-line and post-data acquisition analysis. Regarding papers I and II, my work was focused on the preparation of the experimental apparatus and was focused in performing the experimental measurements during the assigned beamtimes. I have also actively contributed to the data analysis, as well as to the writing of the papers. In the case of paper III, I worked on the preparation and execution of the several beamtimes required to obtain a large set of data on the photoionization dynamics of the epichlorohydrin molecule, as well as on the data analysis and in the writing of the manuscript. In case of paper IV, I worked extensively on the development of the position sensitive cross delay line anode detector, and I was in charge of the software development for the data acquisition and analysis. I was involved in the preparation and attendance of the experiments on the osmium tetroxide molecule, as in the data analysis and in manuscript writing. The data reported in this thesis on the 1-methoxy-2-propanol molecule has been the subject of my period spent abroad, at the department of Physics of the Gothenburg University, in the group lead by Assoc. Prof. V. Zhaunerchyk, and are part of a set of experimental data obtained at the FELIX Laboratory (Nijmegen, The Netherlands). I was involved in the preparation and running of the experimental campaigns, and I was in charge of the IRMPD-VUV data analysis, while the theoretical calculations were performed by Dr. V. Yatsina of the University of Gothenburg.

All the theoretical calculations in Papers III and IV were performed by Prof. P. Decleva and his research group of the university of Trieste. The SIMION particle trajectory simulations were mainly performed by Dr. Michele Alagia from the CNR-IOM institute.

The publications and the data presented in this thesis reflect only a fraction of the work done during the doctoral project. This work also includes several unsuccessful beamtimes, or successful ones but still under data analysis, offline work for the preparation of the various experimental setups, as well as in the detector and software development. Of great importance was the time spent in the study of the subjects and techniques presented here that also contributed to my development as independent researcher.

Other papers

The following papers are my publications produced during the doctorate program but are not part of the thesis project.

i **The escape of O^+ ions from the atmosphere: An explanation of the observed ion density profiles on Mars**, S. Falcinelli, F. Pirani, M. Alagia, L. Schio, R. Richter, S. Stranges, F. Vecchiocattivi, *Chem. Phys. Lett.* **666**, 1 (2016), DOI: 10.1016/j.cplett.2016.09.003.

ii **Single Thermal Photoionization of C_{60} molecule**, K. Hansen, R. Richter, M. Alagia, S. Stranges, L. Schio, P. Salen, V. Yatsyna, R. Feifel, V. Zhaunerchyk, *Phys. Rev. Lett.* **118**, 103001 (2017), DOI: 10.1103/PhysRevLett.118.103001.

iii **Double photoionization of simple molecules of astrochemical interest**, F. Falcinelli, M. Rosi, F. Vecchiocattivi, F. Pirani, M. Alagia, L. Schio, R. Richter, S. Stranges, *In: Gervasi O. et al. (eds) Computational Science and Its Applications-ICCSA 2018. Lecture Notes in Computer Science* **10961** (2018), DOI: 10.1007/978-3-319-95165-2$_5$2.

iv **Investigating core-excited states of nitrosyl chloride (ClNO) and their break-up dynamics following Auger decay**, P. Salen, L. Schio, R. Richter, M. Alagia, S. Stranges, V. Zhaunerchyk, *J. Chem. Phys.* **149**, 164305 (2018), DOI: 10.1063/1.5047262.

v **The Fragmentation Dynamics of Simple Organic Molecules of Astrochemical Interest Interacting with VUV Photons**, S. Falcinelli, F. Vecchiocattivi, F. Pirani, M. Alagia, L. Schio, R. Richter, S. Stranges, V. Zhaunerchyk, N. Balucani, M. Rosi, *ACS Earth Space Chem.* **3**, 1862 (2019), DOI: 10.1021/acsearthspacechem.9b00115.

Abstract

The research activity of my doctoral project was mainly carried out at Elettra, Trieste, the Italian national synchrotron radiation (SR) laboratory. It was integrated into the activities of the local Atomic and Molecular Physics group, which aims at studying the electronic structure of isolated systems of increasing complexity such as atoms, molecules and clusters in the gas phase. The GasPhase and Circular Polarization beamlines of the Elettra storage ring cover a wide spectrum of advanced photoionization methods for a thorough description of both energetics and dynamics of isolated systems. The research activity involved an active collaboration with national and international research groups (Assoc. Prof. Vitali Zhaunerchyk, University of Gothenburg, Prof. Stefano Falcinelli, University of Perugia, Prof. P. Decleva, University of Trieste, Dr. M, Alagia, CNR-IOM Institute) and with the research staff of the GasPhase and CiPo beamlines. The collaboration with the department of physics of the Gothenburg University (Sweden) resulted in a series of experiment on gas-phase molecular chiral recognition at the FELIX facility situated in Nijmegen (The Netherlands).
This doctorate thesis reports on a variety of experimental investigations aiming to advance the understanding of fundamental processes in molecules and clusters by exploiting the properties of Synchrotron and FEL radiation: photoionization dynamics, double ionization, dissociation and molecular recognition were subject of investigation. The emphasis of the thesis lies on the application of advanced light sources in the study of photoionization processes in simple gas-phase molecules, with particular attention on chiro-optical properties of chiral systems.
The valence photoionization dynamics of a chiral molecule, namely the epichlorohydrin molecule, was studied for the first time and a peculiar electron correlation effect was observed. The experimental data were supported by state-of-the-art theoretical calculations. VUV direct double ionization was studied for the methyl oxirane chiral molecule by the use of Photoelectron-Photoion-Photoion Coincidence spectroscopy using synchrotron radiation.
The chiral recognition mechanism of 1-methoxy-2-propanol oligomers was studied by FEL based IRMPD-VUV vibrational spectroscopy, a technique that exploits the nature of the photoionization process in order to apply the IRMPD spectroscopy to systems of arbitrary structure.

The collaboration between the Sapienza University of Rome, the CNR-IOM institute, and the Elettra Instrumentation and Detector Laboratory, has resulted in the development of a position sensitive cross delay line electron detector integrated in an experimental apparatus with the flexibility to perform synchrotron radiation (SR) photoemission experiments on gas-phase systems. The improvement of the apparatus detection system has stimulated the collaboration with the Theoretical Chemistry group of the University of Trieste, in a joint experimental and theoretical long-term research activity, whose first part was the study of the photoionization dynamics of the Osmium tetroxide molecule, a highly reactive tetraoxo complex.

Chapter 1

Introduction

Atoms and molecules are the fundamental building blocks of matter. They are the smallest units responsible for the characteristic properties of gases, liquids and solids. For this reason a deeper understanding of their electronic structure and dynamics is of extreme importance for the comprehension of the properties of matter. The discovery of x rays by Röntgen on November 8, 1895, marked the introduction to mankind of a totally new and unexpected phenomenon in nature, ionizing radiations. The original findings were followed rapidly by the discovery of radioactivity and sources of ionizing radiation with properties different from those of x-rays. Ionizing radiation research and use became an extraordinary tool in understanding the nature of matter and its connection with the atomic structure. Photoionization studies of atoms, molecules and clusters by means of VUV and soft X-ray radiation have greatly benefited from the advance in new experimental methods. In particular new generation high-brightness light sources such as Synchrotrons and Free Electron Lasers (FEL) have increased the variety of experiments and also the range of accessible phenomena. Nevertheless a parallel development in experimental techniques and readout systems was needed as well.
The unique features of Synchrotron radiation were exploited with specially designed experimental setups in order to measure total photoionization cross sections, photoelectron angular distributions, the mass and the kinetic energy distributions of ions produced in the photoionization process, as well as their state-selected distribution.
Gas-phase small molecules are suitable model systems in photoionization studies: their simple structure, and the fact that they are isolated molecular systems, are unique conditions for a better understanding of a such a complex process as photoionization, where multi-electron correlation effects can play an important role. Moreover, their limited number of constituent atoms makes them a useful benchmark for the development of state-of-the-art theoretical models.
Among the large number of molecular classes, chiral molecules received a special attention since their discovery. The property that most characterizes these chemical species, and which differentiates them from other

molecular systems, is their ability to interact selectively with each other and/or with other systems on the basis of a certain chirality form. The concept of chirality has therefore always had a wide interest in the field of chemistry, physics and natural sciences; its study has led to scientific and technological progress in various areas, from the pharmaceutical industry to nanotechnology. A well established physically based method for probing molecular chirality, namely, chiroptical spectroscopy, relies upon the interaction between circularly polarized light and chiral molecules[11, 12]. In particular, circular dichroism rests on the differential interaction with a circular polarized light and implies measuring the difference in absorption by a chiral molecule of right-handed and left-handed helicity radiations. Although very small, this effect is well documented in the case of both electronic and vibrational transitions. Because of their limited magnitude (usually of the order of less than 1% of the total absorption), these methods are mostly limited to condensed phase. More recent is the observation, in the gas phase, of the photoelectron circular dichroism (PECD), described in Chapter 2, which is several orders of magnitude greater than conventional absorption, making PECD spectroscopy a suitable tool for studying isolated chiral species in the gas phase. Moreover, there are attempts to explain life's homochirality by asymmetric processes induced by astronomical sources of circular polarized light. PECD, as an asymmetric photon-induced process, could play a role in the origin of life's homochirality. Furthermore, the interaction of cosmic rays, as well as VUV and X-rays radiations, with small organic molecules can trigger ion-molecule reactions, which are very important in the evolution process of interstellar clouds, where chemical reactions between neutral species are hindered by the critical physical conditions characterizing these environments. These processes could be of great interest in the perspective of an induced extraterrestrial homochirality of initial organic matter. For instance, both UV and charged particle irradiation of simple gas mixtures of $H_2O/CH_3OH/NH_3/CH_3CN$ were shown to produce up to 26 racemic amino acids, diamino acids, and N-(2-aminoethyl)glycine[13].
The chemistry of chiral systems is not limited at the atomic scale or at a single molecule, but aspires to understand the processes behind molecular interactions. Most of the chemical approaches are based on chiral discrimination, that is the difference in behavior of the two enantiomers of a chiral molecule when interacting with a chiral surrounding. As previously mentioned such phenomenon plays a key role in life chemistry. The peculiar enantioselectivity displayed in most of the processes involving the interaction of a chiral ligand, such as a drug with enzymes or protein receptors, has been explained in terms of formation of weakly bound contact pairs involving specific interactions[14]. The combination of supersonic jets and electronic, vibrational, or microwave spectroscopy has led to a great number of experimental results that, in conjunction with quantum chemical calculations, brings information on the structure of weakly bound complexes of chiral molecules and the nature of the inter-

actions responsible for chiral recognition. Due to the fact that electronic spectroscopy can only bring indirect structural information, vibrational spectroscopy is nowadays largely applied in the study of molecular complexes: the use of ionizing VUV radiation allows the study of molecular systems of arbitrary structure. The fragmentation mechanisms of chiral molecules after the interaction with energetic radiations has also recently gained attention as a tool for the direct determination of absolute molecular stereochemistry by means of ion imaging[15, 16, 17], highlighting the importance of molecular dissociation upon photoionization.
In the light of these considerations, the development of new possible methodologies in the study of properties of chiral molecules, with particular interest in enantiomeric recognition and chiro-optical properties of new molecular systems, is of considerable interest in the context of basic and applicative research , both at national and international levels. The aim of this doctorate thesis is to apply advanced light sources, such as synchrotron radiation sources and Free Electron Lasers, in order to study the the electronic structure, dissociation mechanisms, and structural information brought by the photoionization process of small gas-phase chiral molecules, supporting the experimental results with state-of-the-art theoretical calculations. Small gas-phase chiral molecules are a suitable model system in photoionization and photofragmentation studies: they are usually liquids with high vapor pressure, making easier their characterization in the gas-phase, and their limited number of constituent atoms makes them a very good benchmark for testing state-of-the-art theoretical models. For such reason we have chosen small model organic chiral molecules, the methyl oxirane and its derivative, the chloromethyl oxirane, as our subjects of study. The methyl oxirane photodissociation by VUV double ionization is of great astrochemical interest, since it was the first chiral molecule discovered in space. The presence of the chlorine atom in the chloromethyl oxirane, on the other hand, makes this molecule a suitable candidate for the study of the photoionization dynamics of chiral molecules in the Cooper minimum region.
The photoionization process was also exploited in the study of chiral recognition of small oligomers of enantiomers, namely those of the 1-methoxy-2-propanol molecule, by applying the FEL radiation based IRMPD-VUV spectroscopy.

Chapter 2

Photoelectron Spectroscopy

2.1 Introduction

Photoelectron Spectroscopy (PES) is the spectroscopic technique related to the study of the abundances, energies, and angular distributions of the electrons emitted from matter when it is exposed to sufficiently energetic electromagnetic radiation[18, 19]. PES is based on a physical process that has been discovered more than a century ago, the photoelectric effect, i.e. the emission of electrons (photoelectrons) when light of appropriate wavelenght shines on a material. In Photoelectron Spectroscopy elemental identification and the information on chemical bonding can be directly derived from the measured electron energy and energy shifts in the binding energies, making this techniques suitable for chemical analysis. Depending on the light sources used, PES can be divided into three main experimental branches: X-ray Photoelectron Spectroscopy (XPS), Ultraviolet Photoelectron Spectroscopy (UPS) and Synchrotron Radiation Photoelectron Spectrosocpy (SRPES). Nowadays, photoelectron spectroscopy is extensively used in many areas of science, and it's considered as one of the most important tools in the study of the electronic structure of free atoms, molecules and clusters, as well as solids, liquids and surfaces.
A simple picture of the photoelectron emission process (photoionization) can be define as follow: if an atom or molecule absorbs a photon with an energy $h\nu$ sufficiently large to excite it to an energy level above the first ionization limit of the neutral species (the continuum states), the molecule/atom will be ionized and an electron (called photoelectron) will be emitted. A schematic representation of the photoemission process is shown in fig.2.1. As specified by eq.(2.1.0.1), as the photon energy $h\nu$ is varied and either the ion or the electron is detected, a photoionization spectrum is obtained. If $h\nu$ is held fixed, and the e^-(KE) is scanned, the peaks in the e^-(KE) spectrum correspond to successive energy levels of the cation. This is known as photoelectron spectroscopy (PES).

$$AB + h\nu \rightarrow AB^+ + e^-(KE) \tag{2.1.0.1}$$

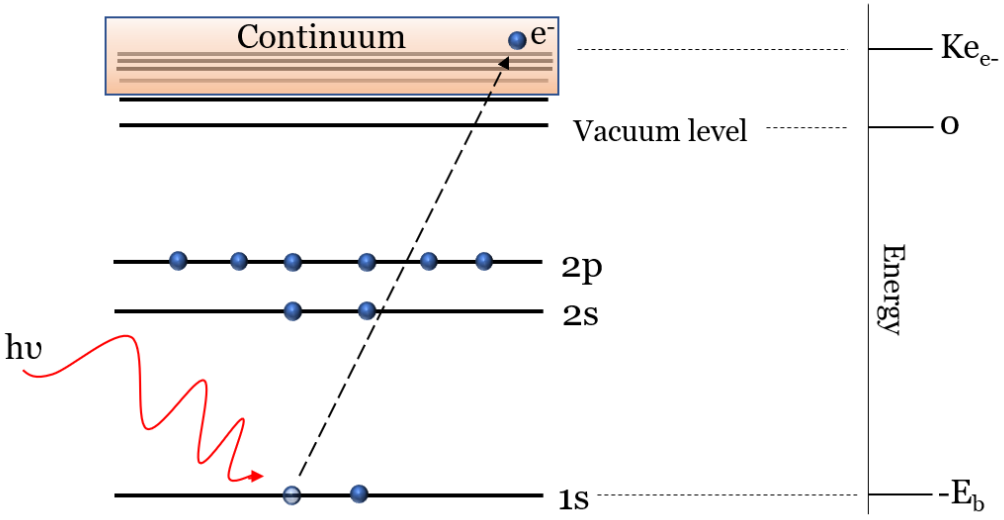

Figure 2.1: Schematic representation of the photoemission process.

2.2 Historical background

The development of photoelectron spectroscopy began over than a century ago[20]: in 1887, the German physicist H. R. Hertz was experimenting on the production and detection of electromagnetic waves, whose existence was predicted by Maxwell[21], using a high voltage induction coil (a Ruhmkorff coil) to cause a spark discharge between two pieces of brass (the electromagnetic wave transmitter), and a small detector circuit as receiver. Hertz found that the small receiver spark was more vigorous if it was exposed to ultraviolet light from the transmitter spark[22]; it was the first observation of the photoelectric effect. The next year Wilhelm Hallwachs continued to work on the observations made by Hertz, but under a much simpler experimental condition[23]: he observed that if a zinc plate is mounted on an insulating stand and wired to a gold leaf electroscope, which is then negatively charged, the electroscope lost its charge very slowly. However, if the zinc plate is exposed to ultraviolet light, the charge leaked away quickly. Moreover, if the plate is positively charged, there is no fast charge leakage, indicating the involvement of a sort of negatively charged particle in the phenomenon. Independently, the same year, also the Italian physicist Augusto Righi was working on the link between these new electric phenomena and the UV radiation: he was the first scientist to use the term "*photoelectric*"[24]. The discoveries of X-rays by Rontgen (1895)[25] and the electron by Thomson (1897)[26] enabled many of these results to be understood in a more complete way. In 1902 Lenard used a carbon arc lamp to study the light intensity dependency of this new photoelectric effect[27]. In his experimental setup, the ejected photoelectrons hit another metal plate, called the collector, winch is connected to the cathode with a wired sensitive ammeter, that

one may measure the produced current. To determine the kinetic energy of the emitted electrons, the collector was negatively charged, in order to repel the incoming electrons: in this way only the photoelectrons with a kinetic energy sufficient to overcome this potential barrier would produce an electric current. He discovered that there was a well defined minimum voltage capable to cease any electron and, with his surprise, Lenard discovered that this "stop" potential does not depend on the light intensity. The effect of increasing the light intensity was only to produce more electron, but was not affecting their kinetic energy. Moreover, he observed that this stop potential (and hence the photoelectrons kinetic energy) was indeed depending on the light wavelenght; the lower the wavelength, the higher the energy of the emitted electrons. Only in 1905 Einstein showed that the new Planck's quantum theory of radiation[28] could be used to explain the photoelectric effect[29]. The radiation is thought as quanta ("packets") of energy $h\upsilon$, the absorption of such a quantum with appropriate frequency causes the emission of one electron, following the relation:

$$E = h\nu - \phi \tag{2.2.0.1}$$

where E is the maximum energy of the emitted electron, h is the Plank's constant (6.626x10^{-34} J·s), ν is the photon frequency, and ϕ is the work function, i.e. the minimum energy required to extract the electron from the material.
In 1907 P. D Innes, working together with J. J. Thomson, performed what can be considered the first XPS experiment[30]. In his experiments Innes used three main components: i) an X-rays source (a Rontgen tube), ii) an electron energy analyzer (the electrons were deflected, and hence velocity selected, by the magnetic field produced by a Helmotz coil), iii) an electron detector (a photographic plate. Innes measured the velocity of the photoelectrons emitted by different metals in order to understand if the photoelectric effect was due to a process similar to those observed for radioactive elements, or if the electrons are extracted by the impinging X-ray radiation. He erroneously concluded that this phenomenon was due to the atom disintegration, ignoring the work of Lenard and Einstein.
The work of Innes and other researchers on the relation between the photoelectric effect and the atomic disintegration had almost surely attracted the attention of E. Rutherford, who was studying the β- and γ rays emitted from radioactive materials; three young scientist working in his lab, H. Moseley, W. Rawlinson and H. Robinson, worked extensively on the photoemission processes, contributing to the birth of the photoelectron spectroscopy. Moseley was interested in the work done by Laue and Bragg on the interference of X-rays reflected by crystals planes[31, 32, 33]. Between 1913 and 1914 Moseley designed and built a X-rays tube for his experiments. In a vacuum tube a cathode filament produces electrons that are accelerated towards the anode target by a high voltage, one or

more electrons are emitted from the anode due to the photoelectric effect and, as a consequence of the atom internal relaxation process, X-rays are emitted. The radiation then impinged on a crystal and the interference pattern was observed on a photographic plate. Moseley discovered[34, 35] that different metal anodes lead to different patterns, associated with a different wavelength of the emitted X-rays, and soon realized that these wavelengths were related to the element's periodic table atomic number, Z, and derived an empirical formula to relate the two quantities, also relying on the new Bohr's atomic model[36]. Moseley's work did not only give a physical meaning to the atomic number as the positive charge on the atomic nucleus, but showed how it is possible to have an unequivocal way to establish if a substance is a pure element or not. After the death of Moseley in World War I, Rawlinson continued, together with Robinson, the work of Moseley. Robinson resumed the work of Innes: using the apparatus built by Moseley, he measured the photoelectron spectra of different metals[37], determining the velocity of the photoelectrons emitted by the internal atomic orbitals, comparing the obtained experimental results with theoretical calculations. In his paper Robinson wrote "*As an accurate knowledge of the energies associated with the different electronic orbits within the atoms is essential to the further development of the theory of atomic structure, it seemed well worth while to proceed with this work, refining the experimental methods wherever possible...There is, therefore, an obvious need for direct measurements of these levels, and in many respects the study of the corpuscular spectra excited by X-rays of suitable frequency is specially adapted to this purpose...*". Photoelectron spectroscopy was thus established as a tool to study the electronic structure of atoms and molecules.
Photoelectron spectroscopy largely disappeared between the two world wars due to the fact that it can not yet compete in accuracy with X-ray absorption and emission spectroscopies. After WWII great technological advances were made, in particular the experimental tools developed in the study of nuclear physics were applied in other scientific fields, including photoelectron spectroscopy. At the beginning of the 50's Steinhardt recognized that x-ray photoelectron spectroscopy could be used for the chemical analysis of samples and developed an XPS spectrometer for the qualitative and quantitative analysis of the surfaces of solids that could compete with X-rat emission and X-ray absorption based techniques[38]. This concept was significantly developed and exploited by the work of Kai Seigbahn and his group in Uppsala. The Swedish physicist was particularly interested in the link between the variations in core-level binding energies and the chemical environment of an element. Starting from the late 50s, it took more than ten years to Siegbahn to refine the instruments used in carrying on his experiments and developed a new technique for chemical analysis, namely the Electron Spectroscopy for Chemical Analysis (ESCA); the results of these studies are marked in his startling article in 1967[39].

At the same time as ESCA was developed, an important work was being done on Ultraviolet Photoelectron Spectroscopy (UPS) by Vilesov, Price and Turner[40]. In the early 1960s Vilesov and his coworkers began to study the photoionization of gases and vapors by vacuum ultraviolet radiation[41, 42]. The same year Turner developed a Helium lamp as a source of ultraviolet light, providing photons of 21.22 eV, and measured the photoelectron ionization energies (IEs) for a large number of gas-phase (or gaseous) molecules, establishing ultraviolet spectroscopy as a new technique to study the electronic structure of free molecules[43, 44]. UPS experimental measurements of IEs and their comparison with theoretical molecular orbital energies from quantum chemistry, which was also extensively developed in the 1960s, led to a better understanding of the valence electronic structure of molecules, which contributes to the unique chemistry of each substance. Photoelectron spectroscopy is nowadays considered the most powerful and versatile technique to study the electronic structure of a large variety of systems.

2.3 Theory of photoionization

The quantum mechanical treatment of the the photoemission process can be found in many text books[18, 45, 46, 47], in the following text I will briefly introduce some key theoretical concepts useful for the comprehension of the next chapters presented in the thesis.
In photoelectron emission, the basic process is the absorption of a sufficiently energetic photon of energy hν by a N-electron atom or molecule, according to eq.(2.3.0.1).

$$\Psi^i_{TOT}(N), E^i_{TOT}(N) \xrightarrow{\text{hv}} \Psi^f_{TOT}(N,k), E^f_{TOT}(N,k) \tag{2.3.0.1}$$

Here $\Psi^i_{TOT}(N)$ is the initial state N-electron wave function, associated with a total energy $E^i_{TOT}(N)$, and $\Psi^f_{TOT}(N,k)$ is the kth final state N-electron wave function with final energy $E^f_{TOT}(N,k)$, in which the final state wave function includes also the emitted photoelectron. The energy conservation law implies that:

$$E^i_{TOT}(N) + h\nu = E^f_{TOT}(N,k) \tag{2.3.0.2}$$

In the simplest case the index k labels the Kth one electron orbital from which the photoelectron has been emitted. Since the cation and the photoelectron In the final state are no more interacting with each other, eq(2.3.0.3) can be rewritten as follows:

$$\Psi^i_{TOT}(N), E^i_{TOT}(N) \xrightarrow{\text{hv}} \Psi^f_{TOT}(N-1,k), E^f_{TOT}(N-1,k) + \\ + \phi^f(1)\chi^f(1), E_{KIN} \tag{2.3.0.3}$$

where $\Psi^f_{TOT}(N-1,k)$ and $E^f_{TOT}(N-1,k)$ refer to the Kth (N-1)-electron ionic state, while $\phi^f(1)$ and $\chi^f(1)$ are respectively the spatial and spin part of a monoelectronic wave function describing the emitted photoelectron. The energy conservation law of eq.(2.3.0.2) can now be written as:

$$E^i_{TOT}(N) + h\nu = E^f_{TOT}(N-1,k) + E_{KIN} \tag{2.3.0.4}$$

and we can define the binding energy of the electron in the initial state as (here the vacuum level reference is implicit):

$$E^v_b(k) = E^f_{TOT}(N-1,k) - E^i_{TOT}(N) \tag{2.3.0.5}$$

From eq.(2.3.0.4) and eq.(2.3.0.5) we obtain the classic formula for the photoemission process, that relates the photoelectron binding energy, its kinetic energy and the incoming photon energy.

$$E^v_b(k) = h\nu - E_{KIN} \tag{2.3.0.6}$$

The total wave function $\Psi_{TOT}(N)$, describing the N-electron system and the cation wavefuntion describing the cation final state, must satisfy the time-independent Schrödinger equation.

$$\hat{H}\Psi_{TOT}(N) = E_{TOT}(N)\Psi_{TOT}(N) \tag{2.3.0.7}$$

$$\hat{H}\Psi_{TOT}(N-1) = E_{TOT}(N-1)\Psi_{TOT}(N-1) \tag{2.3.0.8}$$

In principle, solving the Schrödinger equations allow us to determine the binding energy of the Kth electron in the atom/molecule, but since we have a N interacting electron, we cannot resolve exactly (analitically) the equations, and observables can only be estimated by approximate models. A strong simplification of the problem can be achieved by introducing the independent-particle model, in which in a N-electron system the motion of the i-th electron is considered to be independent from the motions of the remaining N-1 electrons. One of the starting points when approaching the many-body problem by the use of the independent-particle model, is the non relativistic Hartree-Fock (HF) Self-consistent field (SCF) model. In the HF theory the N-electron total wave funcion is approximated as an antisymmetrized single Slater determinant of N mono-electron orthonormalized spin-orbitals.

$$\Psi_{TOT}(N) = \frac{1}{\sqrt{N!}} \sum_p (-1)^p \hat{P} \begin{vmatrix} \phi_1(1)\chi_1(1) & \dots & \phi_N(1)\chi_N(1) \\ . & . & . \\ \phi_1(N)\chi_1(N) & \dots & \phi_N(N)\chi_N(N) \end{vmatrix} \tag{2.3.0.9}$$

By breaking up the electrons into individual wave functions, we can create single-particle Hartree-Fock equations, which can be used as an operator whose eigenvalue is the energy of a particle in a particular orbital.

$$\hat{F}\phi_i(x) = \varepsilon_i\phi_i(x) \tag{2.3.0.10}$$

The Fock operator, $\hat{F}$, is an effective one electron operator that consists of the one-electron Hamiltonian (kinetic energy and Coulomb potential due to nuclei) plus a mean-field Coulomb potential created by all other electrons. Unlike the case of truly non-interacting electrons, the total Hartree-Fock energy is not the sum of one-electron energies, ε_i. One might wonder whether the solutions of (2.3.0.10), that is orbitals ϕ_i and the respective energies ε_i, have any physical significance. The answer is given by Koopmans' theorem[48] (KT) that states that the canonical Hartree-Fock MOs (those that diagonalize the matrix of the Fock operator) can be interpreted as the states from which an electron is removed in an ionization process and the respective energies approximate the IEs:

$$E_b^{KT}(k) = -\varepsilon_k \tag{2.3.0.11}$$

There are, however, three main limitations in this approach, that are source of error in the KT .Briefly, they consist in i) neglecting that the best N/2 doubly occupied orbitals in the initial closed-shell N-electron neutral system are not the best in descibing the N-1 electron cation system in the electronic final state; ii) neglecting the electron correlation energy difference in the neutral and cation states caused by the different number of electrons in the two systems; iii) neglecting the relativistic energy difference between the neutral initial and the cation finale states, since the HF-SCF does not include relativistic effects. This latter effect, however, is rather small and negligible for valence electron ionizations. Despite these limitations, the simplicity and intuitive nature of the theorem had contributed to set the basis of modern chemistry, it is applied in many fields, not only spectroscopic, but also in Lewis acidity/basicity[49], in the concepts of "chemical hardness", affinity and electronegativity[50], among others.

2.3.1 Photoionization dynamics: partial cross section and photoelectron angular distributions

The probability that the absorption of a photon of energy $h\nu$ causes the emission of an electron from an atom, or molecule, is related to the so called photoionization cross section σ. If the direction of emission of the photoelectron relative to the photon propagation direction and polarization is specified, a differential cross section can be obtained, indicated by $\mathrm{d}\sigma/\mathrm{d}\Omega$, where $\mathrm{d}\Omega$ is the differential solid angle in which the electrons are collected. The total angle-integrated cross section will hence be:

$$\sigma(h\nu) = \int \frac{d\sigma(h\nu)}{d\Omega} d\Omega \tag{2.3.1.1}$$

The measurement of the only photoionization cross section contains no information about the distribution of l-values of the ejected electron. However, other measurable observables of the photoionization event can provide information about its mechanism. The frequently measured quantities include the β asymmetry parameter, that describes the angular distribution of the ejected electron, providing crucial information on the nature of the molecular orbital involved in the photoionization process. The differential cross section, and other photoionization observables, can be calculated by the use of the first-order time dependent perturbation theory[51, 52, 53, 54].
The differential photoionization cross section can be written as

$$\frac{d\sigma}{d\mathbf{k}} = \frac{\sigma}{4\pi}\left[1 + m_r b_1 P_1(\cos\theta) + (-\frac{1}{2})^{m_r} b_2 P_2(\cos\theta)\right] \tag{2.3.1.2}$$

A derivation of eq.(2.3.1.2) is given in appendix A.
In eq.(2.3.1.2) σ is the total, angle-integrated, photoionization cross section, $P_2(\cos\theta)$ and $P_1(\cos\theta)$ are the second-order and first order Legendre polynomial in $\cos\theta$ respectively, whose values are

$$P_1(\cos\theta) = \cos\theta \tag{2.3.1.3a}$$

$$P_2(\cos\theta) = \frac{1}{2}(3\cos^2\theta - 1) \tag{2.3.1.3b}$$

The detection angle θ is measured with respect to the laboratory frame z-axys, which is the oscillation direction of the electric field vector for linearly polarized (LP) radiation, and the propagation axis of the radiation in the case of circularly polarized (CP) light.. The coefficient m_r is the photon helicity: in the case of linearly polarized light $m_r = 0$, while for circularly polarized light $m_r = \pm 1$. The parameters b_1 and b_2 depend upon the photoionization target orbital, and on the photon polarization.

Photoionization dynamics studied with linearly polarized light

If we integrate over all possible momenta $\mathbf{k}$ rather than the possible orientations Ω, and consider the LP light case ($m_r = 0$), we obtain the same formula reported in the famous paper of Cooper and Zare[57].

$$\frac{d\sigma}{d\Omega} = \frac{\sigma}{4\pi}\left[1 + \beta P_2(\cos\theta)\right] \tag{2.3.1.4}$$

Here the laboratory frame Z-axis is along the polarization vector, and

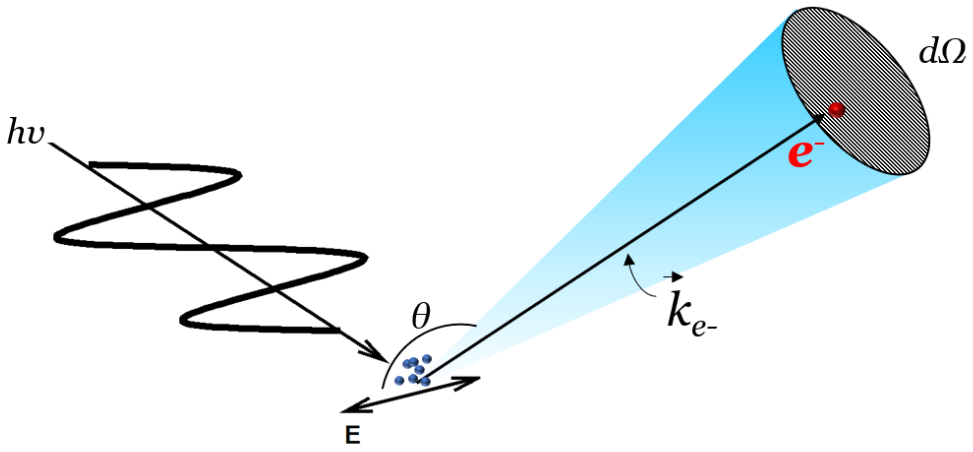

Figure 2.2: Experimental setup to study the differential cross-section $d\sigma/d\Omega$ using linearly polarized radiation. The polarization vector ϵ is parallel to the electric field **E** of the radiation. The detection angle θ is defined with respect to the light polarization vector.

hence the detection angle θ is referred with respect to this axis, as shown in fig.2.4. We can see that the b_2 is the classical β asymmetry parameter that describes the photoelectron angular distribution (PAD)[74]. This parameter can vary between values $\beta = -1$, i.e. a pure $\sin^2\theta$ distribution, and $\beta = -2$, i.e a pure $\cos^2\theta$ distribution; the value of $\beta = 0$ corresponds to an isotropic distribution. This three cases are shown in fig.2.3

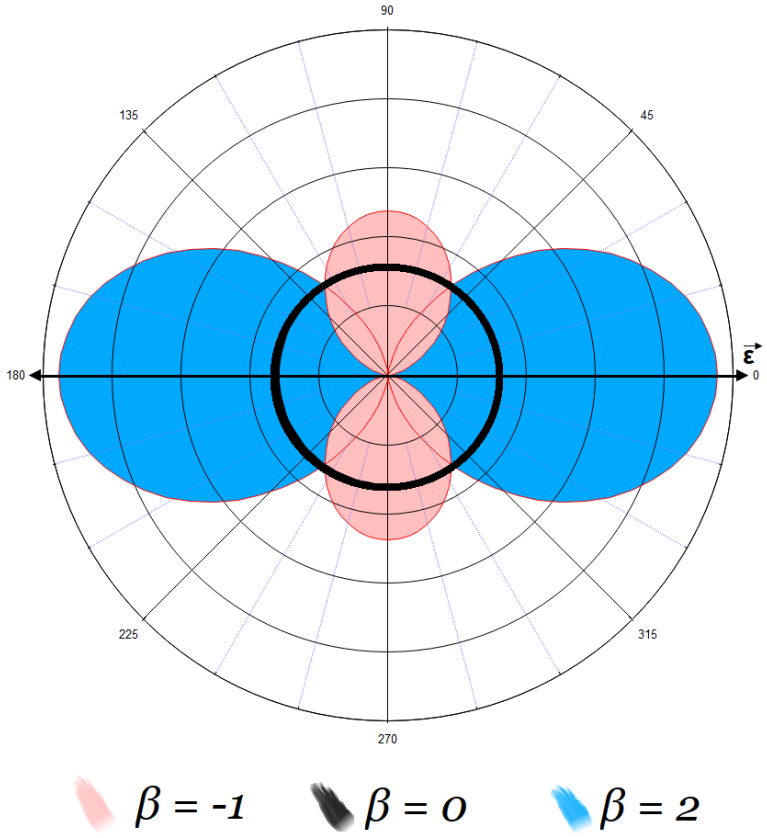

Figure 2.3: Polar plot showing the projection of the photoelectron angular distributions (PADs), with respect to the linearly polarized photon polarization axis ϵ, for $\beta = -1$ (pink), $\beta = 0$ (black) and $\beta = 2$ (blue).

Photoionization dynamics studied with circularly polarized light

In the case of circularly polarized light, both the b_1 and b_2 parameters are present in eq.(2.3.1.2), and the laboratory frame Z-axis is defined as the propagation direction of the the radiation. The condition for the b_1 parameter to vanish requires space-inversion symmetry, and does not follow from any rotation invariance alone[75]. Consequently, this coefficient is expected to be relevant in the case of chiral molecules, that are characterized by an extremely low molecular symmetry. Physically, the absorption of a left or right polarized photon populates selectively a single fine-structure level, according to the selection rules on the magnetic angular momentum $\Delta m = \pm 1$; if the the magnetic sublevels are inequivalent due to the effect of a low symmetry molecular field, as in the case of chiral molecules, the absorption of left or right CPL different gives rise to different radial amplitudes in the matrix elements for the two cases, and no complete cancellation occurs in the summation, and as a consequence all the linear $\cos\theta$ terms survives in eq.(2.3.1.2). The b_1 is hence related to the chiro-optical properties of the target molecular system, and is often referred as "dichroism parameter", labeled as D[77, 78, 76, 79]. It is to point out that this is true only when the sample has a predominance of one chirality, i.e. is enantiopure, otherwise the b_1 will vanish since for each target molecule not in a parity eigenstate (for instance the R enantiomer) there is a target molecule in the corresponding space-inverted eigenstate. Thus, in the case of a racemic mixture, as well as for unoriented achiral molecules, the dichroism parameter is canceled, and eq.(2.3.1.4) is recovered.
The P_1 Legendre polynomial introduces a $\cos\theta$ term to the PAD that is odd with respect to the inversion $\theta \to \pi - \theta$, that is $\cos(\pi - \theta) = -\cos\theta$, introducing a backward-forward asymmetry in the photoelectron angular distribution, that can be a useful information for eneantioselective analysis of molecules. The analysis the photon helicity and molecular handedness in eq.eq.(2.3.1.2) leads to some useful relations.

$$b_2(m_r = \pm 1) = -\frac{1}{2} b_2(m_r = 0) \equiv -\frac{1}{2}\beta \tag{2.3.1.5a}$$

$$b_1(m_r = +1) = -b_1(m_r = -1) \tag{2.3.1.5b}$$

In particular eq.(2.3.1.5)b indicates that the forward-backward asymmetry in the angular distribution is inverted. In the case of handedness inversion, namely on going from one enantiomer to the other, the theoretical work by Ritchie[75] proved that the b_1 preserves its value but with the reversed sign.

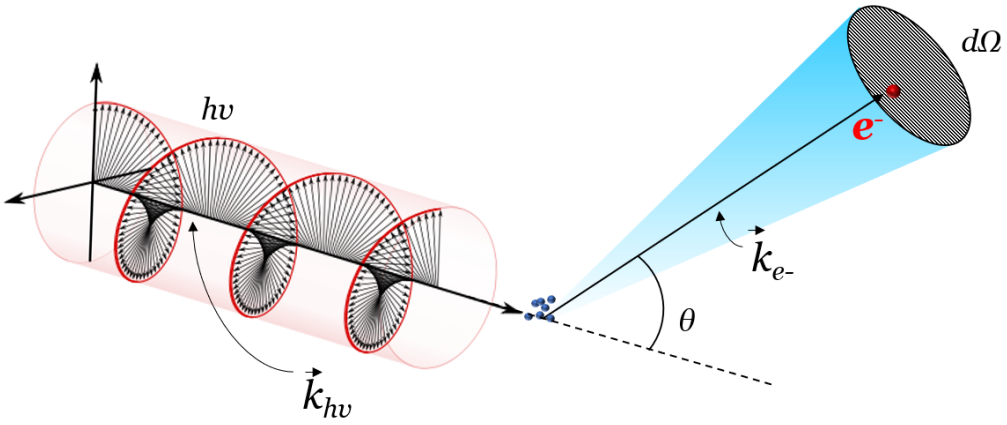

Figure 2.4: Experimental setup for studying the differential cross-section $d\sigma/d\Omega$ using circularly polarized radiation. The detection angle θ is defined with respect to the light propagation vector $k_{h\nu}$.

Cooper Minimum

Comparison between the experimental photoionization cross sections and photoelectron angular distributions, studied as a function of photon energy, becomes extremely important when distinct features can be observed, since one of the main purposes of theoretical support is to have an appropriate description of the physical phenomenon and its behavior as a function of photon energy rather than a point-by-point match between theory and experiment. One of the most informative and striking effects observable in photoionization dynamics its the so called Cooper minimum (CM). This phenomenon shows itself as minimum in the partial photoionization cross section as the photon energy is increased from the ionization threshold. Jointly with this $\sigma(h\nu)$ behavior, the β parameter displays in the same CM energy region a rapid oscillation characterized by a maximum and a minimum. Originally Cooper[58] developed the theory for this effect in the atomic case, and for simplicity the same will be done in the following text. When an atomic orbital has a radial node, i.e. a point at which the radial part in the wave function is zero (not including the origin), the matrix element of eq.(A.0.0.6) describing the transition moment, can change its sign on increasing the photon energy from the ionization threshold. In fact, the radial dipole matrix element of the form $\langle n'l'|\mathbf{r}|nl\rangle$ will change by changing the photon energy if the final state $n'l'$ exists but is not occupied in the initial ground state[59]. In a simple view, the radial part of both the initial and final state wave functions change sign and shape depending on the occupied$nl/n'l'$ orbitals. There will be an energy region in which the wave functions of initial and final states interfere destructively, and consequently the dipole matrix element approaches zero. If this matrix element plays an important role in the overall photoionization cross section, a minimum will be observed in the energy region where the matrix element change sign crossing the zero.
The number of radial nodes in an atomic orbital can be calculated from the simple formula $n - l - 1$: for instance a 1s orbital has (1-0-1=) 0 radial nodes, and no Cooper minimum is expected. Conversely, for a 3p atomic orbital, which has (3-1-1=) 1 radial node, it is expected to see the effect of the Cooper minimum in the cross section. Lets consider as an example the photoionization from the Ar 3p orbital[60] (neglecting the spin-orbit coupling). The photoionization from the 3p orbital leads to two continuum ionization channels (in the dipole approximation, the selection rule for the angular momentum is $\Delta l = \pm 1$), namely the ks and kd channels. In fig.2.5 the radial wave function for the bound 3p orbital, together with the kd continuum wave function at different photoelectron kinetic energies, are shown. It can be noted that as the kinetic energy of the emitted photoelectron in the kd continuum channel increases, the kd radial wave function moves towards smaller radial distances and the matrix element for the 3p orbital decreases in magnitude, becoming zero when the positive and negative parts of the integrands are equal. It is

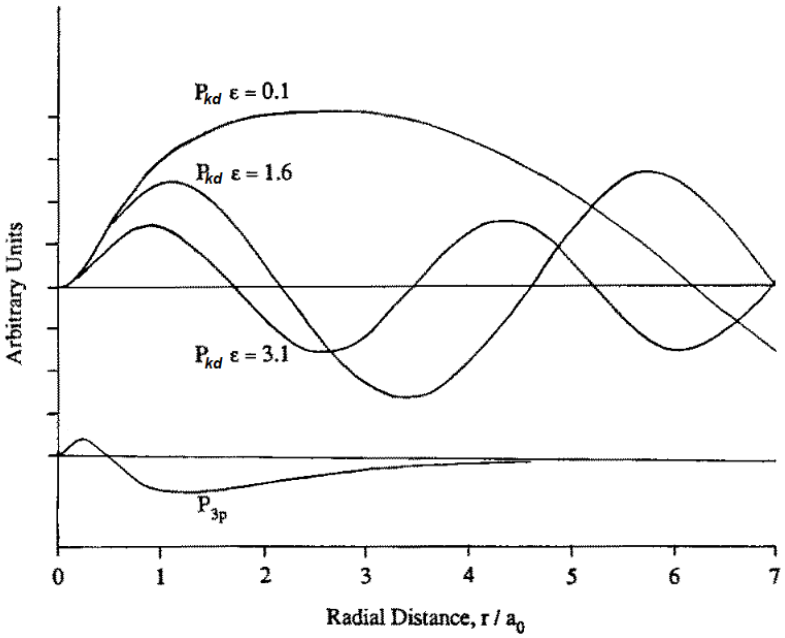

Figure 2.5: Argon bound 3p radial wave function together with the continuum kd radial wave function for photoelectron kinetic energies of 0.1, 1.6 and 3.1 Ry (1 Ry = 13.6056923 eV). Figure adapted from ref.[60].

shown in fig.2.6 that in the case of Argon this happens at an energy of approximately 30eV ($\sim 2Ry$) above the ionization threshold, giving rise to a minimum in the partial photoionization cross section at a photon energy of about 50eV, as displayed in fig.2.7, together with the monotonic ks continuum wave function.

Together with the cross section, also the β asymmetry parameter is strongly affected. At the 3p CM energy region the contributions to the kd channels are eliminated and only the ks channel is available, which has an isotropic angular distribution, i.e. $\beta = 0$. Consequently the Ar 3p asymmetry parameter (shown in fig.2.8) is characterized by a strong oscillation in the CM region, with a maximum and a minimum values of *beta*, underlying that it is a much more sensitive experimental parameter then the cross section in the determination of such CM dynamical effect. Unlike the case of Argon, in the photoionization of Neon 2p orbital the radial matrix element is always positive, i.e. never crossing the zero (see fig.2.6), and no Cooper minimum is expected; as a matter of fact both the partial photoionization cross section and the photoelectron angular distribution, shown in fig.2.9, simply increase monotonically from the ionization threshold as the photon energy increase. Effects analogous to atomic CM are expected also in molecules in which are present lone-pair molecular orbitals, derived from those atomic orbitals known to exhibit the CM effect, e.g. Cl 3p and S 3p. The CM effect has been observed in free atoms and molecules[64, 65, 66, 67, 68, 69, 70] as well as in condensed matter[71, 72, 73].

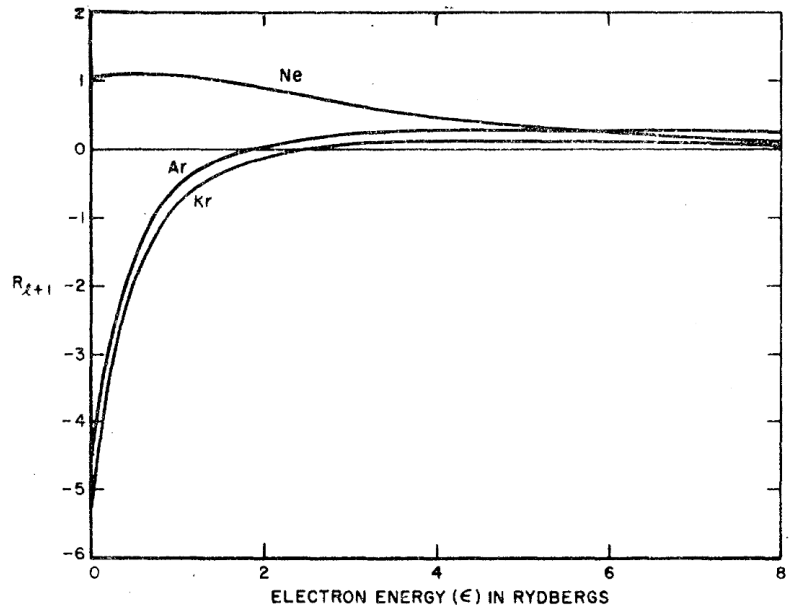

Figure 2.6: Dipole matrix elements for $p \rightarrow d$ transitions in the case of Ar, Ne and Kr. Figure adapted from ref.[58].

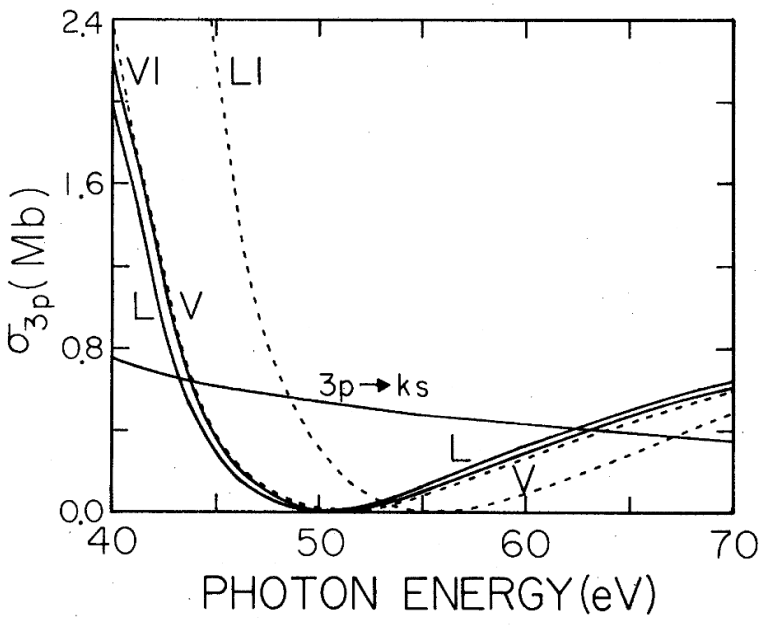

Figure 2.7: Partial photoionization cross section for the Ar 3p orbital. The solid curves I and V represent the length and velocity calculation, respectively.The dotted curves L1 and V1 are the result of the single-particle Hartree-Fock calculation. The contribution of the monotonic wave function for the ks continuum channel is also shown. Figure adapted from ref.[61].

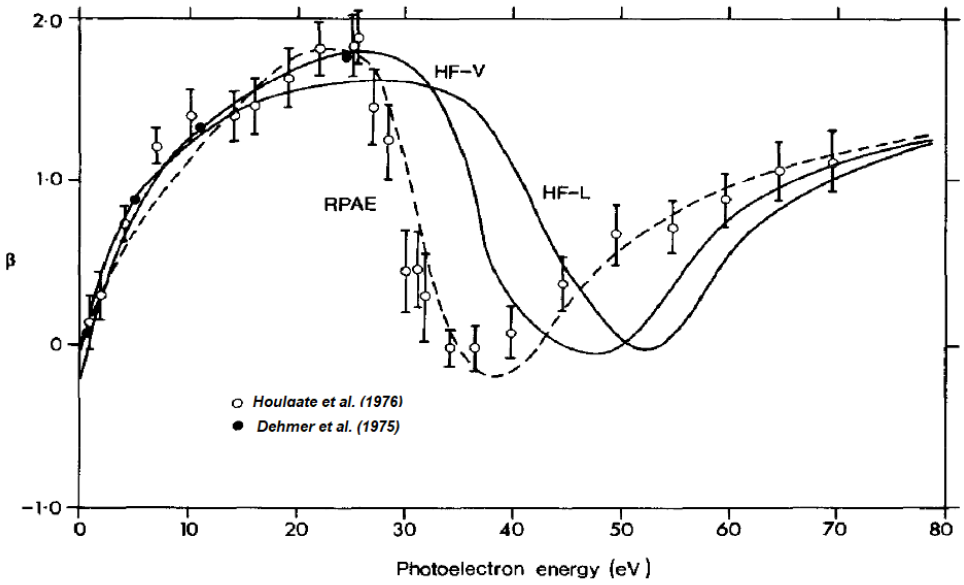

Figure 2.8: The asymmetry parameter β plotted as a function of ejected photoelectron kinetic energy for the Argon 3p orbital. The solid curves are the single-electron Hartree-Fock length and velocity (HF-L and HF-V) calculations of Kennedy and Manson (Phys. Rev. A **5**, 227 (1972))". The dashed curve is the RPAE calculation of Amusia et al. (Phys. Lett. A **40**, 15 (1972)). Figure adapted from ref.[62].

The Cooper minimum is an extraordinary probe of photoelectron dynamics and the nature of atomic and molecular orbitals, moreover it can provide a strong experimental evidence of the many-body interaction effects and can thus be a valuable guide in developing more accurate theoretical methods.

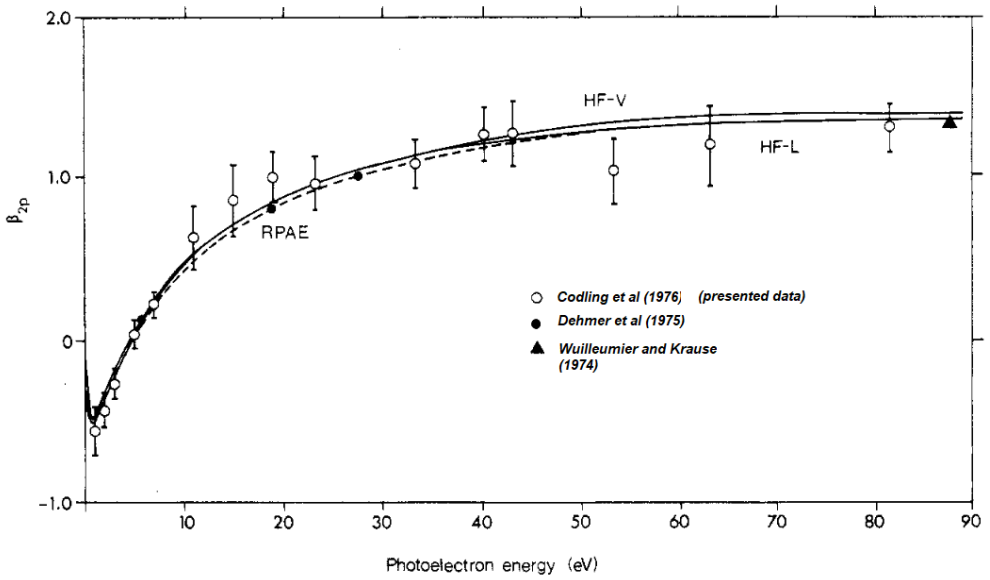

Figure 2.9: The asymmetry parameter β plotted as a function of ejected photoelectron kinetic energy for the Neon 2p orbital. The full curves are the Hartree-Fock (HF) length and velocity calculations of Kennedy and Manson (Phys. Rev. A **5**, 227 (1972)) and the broken curve is the RPAE calculation of Amusia et a1 (Phys. Lett. A **40**, 15 (1972)). Figure adapted from ref.[63].

2.4 Angle-Resolved Photoelectron Spectroscopy (ARPES)

The partial differential cross section and the photoelectron angular distribution can be determined experimentally by measuring the photoelectron intensities iat different detection angles with respect to the polarization axis of the monochromatic linearly polarized radiation. In Angle Resolved Photoemission Spectroscopy (ARPES) experiments, the photoelectron spectrometer is rotated with respect to the axis of polarization of the LP light, collecting the photoelectrons at different emission angles. Experimentally, since in eq.(2.3.1.4) there are two unknown variables, at least two independent equations are needed, that is the photoelectron intensities at two different angles must be recorded. If $I(\theta_1)$ and $I(\theta_2)$ are the photoelectron intensities at two different detection angles, the β asymmetry parameter can be calculated from:

$$\frac{I(\theta_1)}{I(\theta_2)} = R = \frac{(1+\beta P_2(\cos\theta_1))}{(1+\beta P_2(\cos\theta_2))} \tag{2.4.0.1}$$

For instance, if one choose two convenient angles, like $\theta_1 = 0°$ and $\theta_2 = 90°$, for which $\cos(0°) = 1$ and $\cos(90°) = 0$, the asymmetry parameter can be easily calculated.

$$\beta = \frac{2(R-1)}{R+2} \tag{2.4.0.2}$$

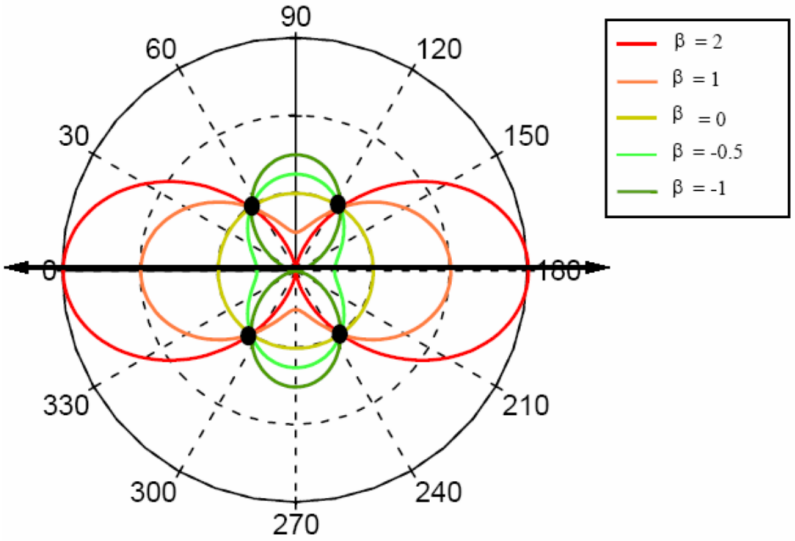

Figure 2.10: Photoelectron angular distribution in polar coordinates for different values of β. Magic angle has been indicated by a black point.

However, in ARPES experiments there is a much more convenient choice of detection angles, which enables to obtain, within the same experiment, not only the asymmetry parameters as a function of photon energy,, but also the partial photoionization cross sections. In fact, from eq.(2.3.1.3) it can be pointed out that the term $P_2(\cos\theta)$ is exactly zero if $\theta = 54.7° = \theta_m$, the so called "*magic angle*" (MA). This is graphically showed in fig.2.10, where it can be seen that there are four points at which photoelectron intensities are expected to be independent from angular distribution effects. By choosing $\theta_2 = 54.7° = MA$, the photoelectron intensity $I(MA)$ will be directly proportional to the partial photoionization cross section, and choosing the second angle as $\theta_1 = 0°$ the asymmetry parameter will simply be

$$\beta = R - 1 \tag{2.4.0.3}$$

Where $R = \frac{I(0°)}{I(MA)}$.

Thus, in such an ARPES experiment all the photoionization observables that characterized the photoelectron dynamics can be measured as a function of photon energy, provided that a tunable monochromatic photon source is used. This techniques has been extensively used in the study of the photoionization dynamics of free molecules. An ARPES experiment requires as ideal photon source a tunable linearly polarized synchrotron radiation. It also requires a photoelectron analyzer, tipically a hemispherical deflector analyzer. ARPES photoelectron analyzers collect emitted electrons within a finite acceptance angle and energy resolution and binning

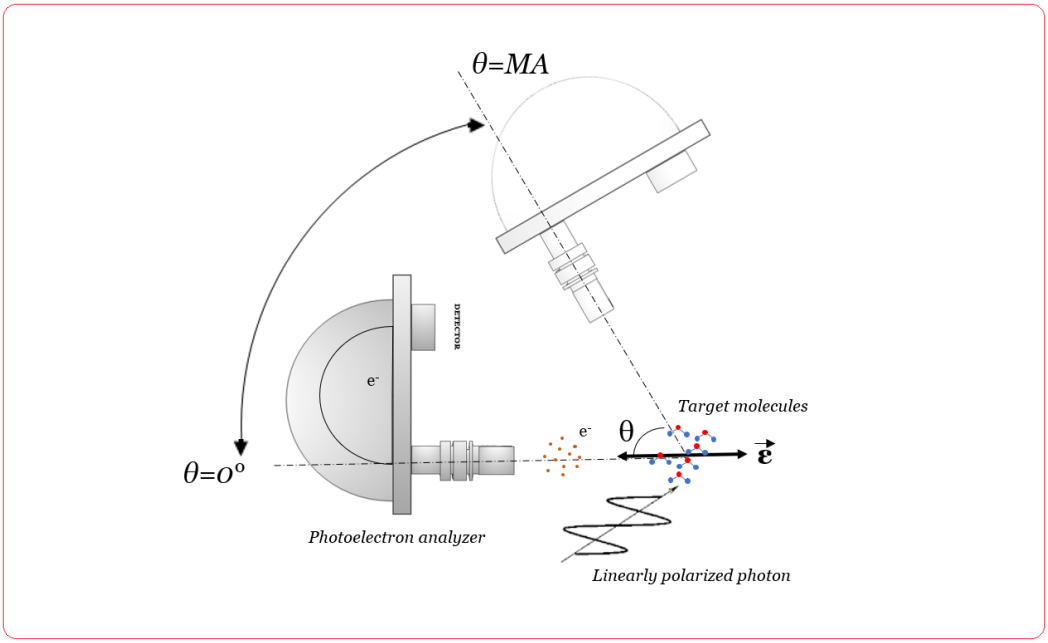

Figure 2.11: Sketch of a classic gas-phase ARPES experiment. The photoelectron analyzer rotates with respect to the polarization vector ε of the ionizing radiation (in the case of LP light), and photoelectron spectra are recorded as a function of photon energy at two different angles.

them according to their energy, with a preset energy resolution. Common ARPES analyzers consist of three parts: input lens, which sorts the electrons according to their ejection angle, hemispherical deflector analyzer, which sorts the electrons by their kinetic energy and, as in the present work, a 2D electron detector, which records the photoelectrons signal. Nowadays, an energy resolution of 1 meV and angular resolution of 0.1° [80] can be achieved with state-of-the-art apparatuses. The acceptance angle depends on the dimensions of the lens aperture and the distance between the sample and the entrance slit. In a classic gas phase ARPES experiment an effusive or supersonic beam of target molecules (or atoms) intersects the monochromatic radiation and the resulting ionization volume is seen by the entrance slit of the analyze.The analyzer rotates with respect to the polarization vector of the ionizing radiation (in the case of LP light), and photoelectron spectra are recorded as a function of photon energy at two different angles, as schematically shown in fig.2.11.

2.5 Photoelectron Circular Dichroism (PECD)

One of the more recently developed techniques in investigating chiroptical phenomena is photoelectron circular dichroism[81, 82, 83, 77, 78]. Due to the fact that this technique is based on photoelectron spectroscopy, and hence there are no restrictive selection rules, PECD can be applied to any chiral species and does not require a specific chromophore to be present in the molecule. Photoelectron circular dichroism arises from asymmetry in the angular distribution of photoelectrons emitted upon ionization with circularly polarized radiation of randomly oriented chiral molecules, as stated in section 2.3.1. The dichroism parameter b_1 of equation (2.3.1.2) is the observable related to the chiro-optical properties of the target molecular system. It can be experimentally determined, for instance, by measuring the photoelectron intensity $I(\theta)$ at the magic angle, either in the forwards or in the backwards hemisphere, using sequentially CP light of both helicity states (I+ and I-)[84].

$$b_1(h\nu) = \frac{I^+(\theta_m, h\nu) - I^-(\theta_m, h\nu)}{\cos\theta_m (I^+(\theta_m, h\nu) + I^-(\theta_m, h\nu))} \tag{2.5.0.1}$$

The PECD effect occurs within a pure dipole approximation theory (E1), in contrast with classic circular dichroism absorption spectroscopy , where the observed weak dichroic effect is due to much smaller electric-dipole/magnetic-dipole (E1-M1) and electric-dipole/electric-quadruple (E1-E2) interference terms. It is for this reason that PECD asymmetries are found to be typically two-three orders of magnitude greater than the conventional absorption CD. The dichroism parameter can be used not only for chiral recognition, but it is extremely sensitive also to its molecular structure; in fact, the b_1 parameter appears to respond sensibly to even comparatively slight changes in the assumed molecular geometry, like in the case of different substituents or even for different conformers of the same molecule[85, 86, 87]. Continuum functions can be represented as an expansion in partial waves of specific angular momentum l, to whom is associated a phase shift resulting from quite subtle interaction with the molecular ion potential[75, 88]. As a consequence, the relative phase shifts between the adjacent l waves enter b_1 as a sine function, rendering this parameter much more sensitive to even small relative phase shifts, this may be due to possibly little changes in molecular structure. The continuum nature of the final state in the photoionization process, combined with the large typicale size and lack of symmetry of chiral molecules, pose a challenging problem in the numerical evaluation of the b_1 parameter. The experimental study of gas-phase model chiral molecules serves as a benchmark for the development of new theoretical model[77, 89], with the aim of obtaining a more accurate description of the physical process involving the emission of photoelectrons from chiral molecules interacting with circularly polarized light. Experimentally, many types of setup have

been emplyed in PECD studies, although most of them are based on the use of VUV/X-rays synchrotron radiation. One approach is to employ Velocity Map Imaging (VMI) design[90]]. The main advantage of this method is the detection capability into the full solid angle of photoelectron emission. With the same setup both asymmetry parameters and D coefficients can be measured. However this technique is limited to a kinetic energy region of few eV, in order to maintain an acceptable spectral resolution, this being a limit in the study of dynamical effect far from the ionization thershold or in investigating inner shell processes. The use of hemispherical electron analyzers can provide high resolution even at higher kinetic energy.

Chapter 3

3D Ion Imaging

3.1 Double photoionization study by molecular dications fragmentation

The interaction of neutral molecules and atoms with energetic electromagnetic radiation, such as x-rays or Extreme Ultraviolet (EUV) light, can lead to the formation of multiply charged ions thorough different mechanism, from Auger decay to direct double photoionization. Molecular dications have been subject of study due to their role in upper planetary atmosphere and interstellar medium (the reader can refer to ref.[91, 92, 93, 94, 95, 96] and references therein), as well as a potential key role played in plasmas and high energy environments. An important process in the planetary atmosphere is the production of doubly charged ions from direct double photoionization.
Double photoionization (DPI) is a phenomenon in which two electrons are removed simultaneously from an atom or a molecule by the absorption of a single photon, with the concomitant formation of a dication. Fundamental information about this process can be extracted from the analysis of the emitted electrons and the ionic fragments arising from the dissociation of molecular dications. In fact, many dication electronic states are purely dissociative and their population results in the formation of traslationally energetic monocations and neutral species[97]. In the case of a small doubly charged parent ion AB^{2+}, containing light elements, the thermodynamic limit for the dissociation channel $A^+ + B^+$ usually lies below the asymptotic limit for the $A^{2+} + B$ formation. This allows the existence of a metastable AB^{2+} configuration, whose stability is given by a potential energy barrier on the pathway to the $A^+ + B^+$ formation, a barrier that arises from the avoided crossing of the diabatic potential surfaces correlating with the $A^+ + B^+$ and $A^{2+} + B$ asymptotes, as shown in fig.3.1. Direct double photoionization is of interest not only because of the role of molecular dications in the planetary atmosphere but also due to the fact that it is a spectacular manifestation of electron correlation, and an extensive

theoretical[98, 99, 100, 101, 102] and experimental[103, 104, 105, 106] work can be found in the literature on this phenomenon. In fact DPI would be a forbidden process unless the electron-electron correlation is considered. The reason is that, since the photoelectric operator is a single-particle operator, the simoultaneous emission of two electrons by the absorption of a single photon must arise purely from electron correlation effects, which are not taken into account in the independent particle model. In the literature DPI is usually described as the result of two processes, a direct simultaneous release of two electrons from the system and an indirect process, where intermediate states are involved. However interference between direct and indirect process must be present to some extent, as they can lead to the same final state[107]. Direct DPI, which is the case presented in this thesis, is sometimes modeled as a combination of two different mechanisms: knock-out and shake-off[108]. The first mechanism describes the correlated dynamics of the two electrons as they leave the atom or the molecule, in which the primary electron is knocking out the secondary electron; in such model the final-state correlation governs the knock-out mechanism. Conversely, the shake-off mechanism accounts for the fact that photon absorption may lead to a sudden removal of the primary electron without any direct interaction with the secondary electron. This causes a change in the atomic field so that the secondary electron relaxes with a certain non-vanishing probability to an unbound state of the remaining ion (the second electron is said to be shaken off). In this second process the initial-state correlation effects are dominant. Based on the qualitative picture described above one may also distinguish knock-out and shake-off by the different energy regimes where they dominate. Shake-off is characterized by a sudden removal of the photoelectron and therefore by a short time of interaction between the ionized electrons. This situation is typical for the high energy regime with photons of short wavelength. On the other hand, knock-out dominates for low photon energies, i.e. near threshold, when the electrons have little energy in the continuum and therefore plenty of time for interaction[109]. Double photoionization of molecules can be studied not only looking at the emitted electrons but also at the product fragments arising from the dications, by means of different ion coincidence spectroscopic techniques[110, 111, 112].

3.2 Electron-ion-ion coincidence measurements

The ion fragments formed from the dissociation of multiply charged molecular ions can be detected and correlated using the fact that they are born at the same instant from the same photodissociation process. A coincidence measurement is a method used to determine whether two or more particles originate from the same event. In a coincidence experiment both two - or more - product ions and the emitted photoelectrons can

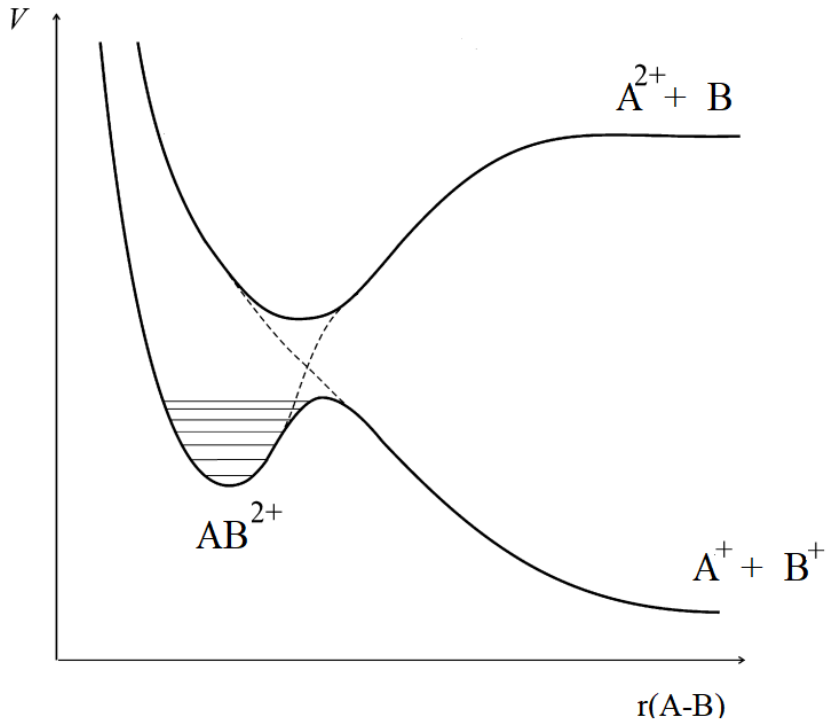

Figure 3.1: Schematic potential energy curves for a diatomic dication AB^{2+}.

be detected and correlated, giving an unique set of information on the energetic and mechanism of the photodissociation process. Many experimental methods based on coincidence spectroscopies have been developed over the past decades[113, 114, 115, 116, 117], although the measurement of the arrival time of each charged particle at the detector is the fundamental principle in a large number of coincidence spectroscopy techniques. Among them, Photoelectron-Photoion-Photion Coincidence (PEPIPICO) spectroscopy[118] has been extensively used in the study of multibody dissociation[119, 120, 121, 122], and in particular in the case of molecular dications[123, 124, 125]. In a PEPIPICO experiment an effusive or supersonic molecular beam crosses the ionizing radiation, usually synchrotron radiation, and the electrons and ions produced in the extraction region are accelerated towards the respective detectors by static electric fields and analyzed separately. The arrival of an electron to the electron detector triggers the time of flight of the ions. The extraction electrodes accelerate the ions towards a time-of-flight (TOF) spectrometer and a position sensitive detector. The arrival time of the ions depends on their velocity and charge-to-mass ratio. Due to the fact that the arrival time of the electrons is usually of the order of several ns, while the arrival time of ions is of the order of μs, one can approximate the formation of the ion with the detection instant of the electron. If two or more ions hit the detector whithin a certain time interval, they are classified as "in coincidence", i.e. coming from the same dissociation event. The electrons can be used as a

simple trigger or analyzed in coincidence with the detected ions, adding information on the electronic states involved in the process. A description of the ARPES 3D ion imaging apparatus used to collect the coincidence data presented in this thesis is given in section 5.5.

Chapter 4

IRMPD-VUV action spectroscopy

High power far/mid-IR free electron lasers (FEL) facilities are used in the application of infrared multi photon dissociation (IRMPD) spectroscopy to the study of biologically relevant molecules in the gas phase, particularly in the case of ionic and protonated species[126, 127, 128, 129]. Recently[130], a new technique based on IRMPD spectroscopy was developed and successfully applied[131, 132] to gas phase molecules by ionizing (and so probing) the molecular dissociation products with vacuum ultraviolet (VUV) photons and analyzing them with a mass spectrometer. The resonant absorption of multiple IR-FEL photons induces the molecular dissociation of the target molecule and its oligomers, then a VUV laser is used to ionize the fragments, that can be analyzed by their mass. Probing these fragments as a function of the IR wavelengths allows the reconstruction of the vibrational spectrum. This technique shows several advantages in the study of jet cooled molecular cluster: i) it enables measuring IR spectra for molecules of arbitrary structure, including molecules that do not contain a chromophore, and ii) the spectra of monomers and oligomers can be recorded simultaneously. In fact, vibrational spectra of homo- and heterochiral oligomers in the far-IR region can provide information about their structure, shedding more light on enantiomer-specific interactions between the moieties. As a matter of fact, the spectral region in the interval of 400 cm^{-1} and 1500 cm^{-1}, the so called fingerprint region, usually contains a series of unique absorption bands, thus allowing an unambiguous identification of molecular structures[133, 134, 135]. In an IRMPD experiment, the target molecules are confined in a small interaction region overlapping with tunable IR radiation. When the IR frequency ν_i coincides with the energy of a transition from the vibrational ground state to an excited vibrational level, resonant absorption of the IR pulse takes place. Between two or more IR excitation pulses Intramolecular Vibrational Redistribution (IVR) effect[136] takes place, redistributing the acquired internal energy over different vibrational modes. If the process is performed in absence of collisions in the interaction region, as in

the case of supersonic jets, the acquired IR multi-photons internal energy leads to molecular dissociation as it exceeds the fragmentation energy threshold. The IVR process that takes place between two IR photons absorption can be more or less efficient, depending on the nature of the excited vibrational states. This implies that the multi-photon IR spectra can be not equivalent to the corresponding spectra recorded using single IR photon absorption; spectral lines can be broadened and shifted, and line intensities can differ from those predicted by the calculated IR spectrum. The study of such small protoype molecules in the gas phase enables combining theoretical calculations with the experimantal measurements, which allows a better understanding of the chirally-selective molecular interactions.

Chapter 5

Experimental Methods

5.1 Hemispherical Deflector Analyzer

5.1.1 Introduction

Among the various electron analyzers[137, 138], one of the most used and commercially available analyzer in high resolution photoelectron spectroscopy experiments, is the hemispherical deflector analyzer (HDA). It consists of two hemispherical capacitors, namely the inner sphere and the outer sphere, of radii R_1 and R_2 respectively, with $R_1 < R_2$, a system of electrostatic lenses that collects and focuses the emitted electrons at the entrance of the hemispherical dispersive elements and an electron detection system.
An electrostatic electron analyzer, such as a HDA, acts in a similar way to a prism: the electrons are deflected in the HDA electric field according to their kinetic energy as a prism disperses light in its component depending on the wavelength. If the entrance and exit points of the electron trajectories are defined by slits apertures it is possible to select electrons with different kinetic energies by scanning the voltage difference between the two hemispheres; electrons with different kinetic energies will be made to fly in a fixed trajectory through the hemispheres gap till the analyzer exit aperture, positioned at 180° with respect to the analyzer entrance, where a suitable electron detector collects all the incoming electrons. In another scanning mode, the so called Constant Pass Energy mode, a constant kinetic energy is selected on the dispersive elements and the electrons are accelerated or decelerated by a retarding-field potential applied on the analyzer base plate, called the Herzog plate. In this way electrons of selected kinetic energies are forced to follow the same central trajectory and reach the detector with a constant energy resolution.
With both scanning modes is thus possible to record the number of detected electrons as a function of their kinetic energy, that is a photoelectron spectrum.

5.1.2 Ideal HDA

In an ideal 180° electrostatic deflector [139] a $1/r^2$ electrostatic field is generated by a voltage difference between two concentric hemispherical capacitors, the inner and outer spheres of radii R_1 and R_2 ($R_1 < R_2$). The electrons enter the deflector at the entrance aperture and are deflected by 180° towards the exit aperture of the analyzer, following a trajectory along the mean radius $R_m = (R_1 + R_2)/2$. A representation of an ideal HDA is shown in fig.5.1. The electrostatic potential between the two spheres (the inner sphere of radius R_1 at potential V_1, and the outer sphere of radius R_2 at potential V_2), obtained from the solution of Laplace's equation, is given by

$$V(r,\theta,\phi) \equiv V(r) \equiv -\frac{k}{r} + c \tag{5.1.2.1}$$

where

$$c = \frac{V_2 R_2 - V_1 R_1}{\Delta R}$$

and

$$k = \frac{\Delta V}{\Delta R} R_1 R_1$$

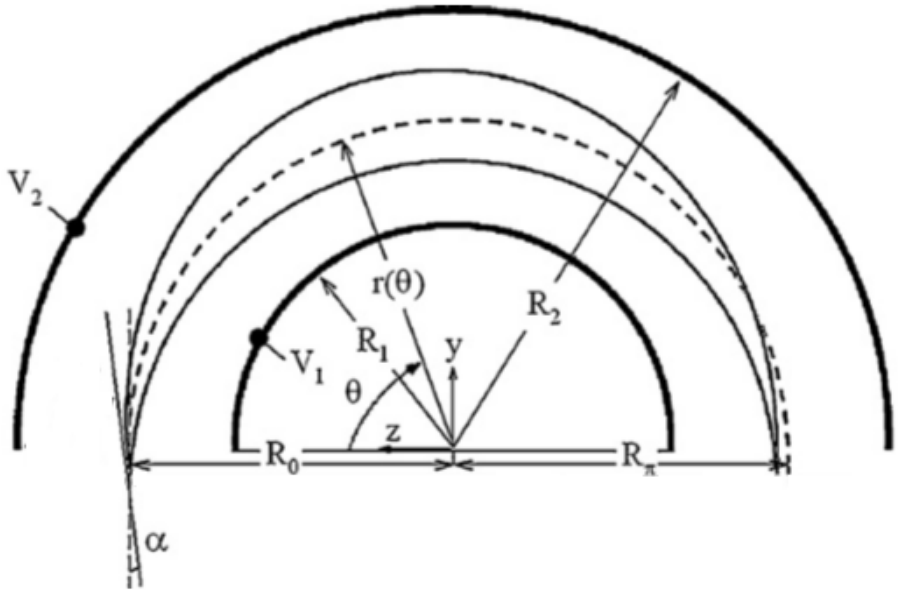

Figure 5.1: Scheme of an ideal hemispherical deflector analyzer.

Since the electric field (and hence the force on the particles) is proportional to $1/r^2$, the trajectory of a particle in the potential V(r) is a Kepler orbit

[139, 140, 141]. The solution $r(\theta)$ of the trajectory of a particle of charge q entering the HDA (r_0, $\theta_0 = 0$) with kinetic energy E_k and entrance angle α is:

$$r(\theta) = r_0 \left[\frac{qk(1-\cos\theta)}{2r_0 \cos^2\alpha(E_k - qc + \frac{qk}{r_0})} + \cos\theta - \tan\alpha \sin\theta \right]^{-1} \qquad (5.1.2.2)$$

and the exit radius r_π at $\theta = \pi$ is

$$r(\pi) = r_0 \left[\frac{r_0(E_k - qc) + qk}{qk \tan^2\alpha - r_0(E_k - qc)} \right] \qquad (5.1.2.3)$$

The potential that must be applied to the sphere is:

$$qV_i = E_k - E_0 \left(\frac{\gamma}{\xi}\right) \left[\frac{R_m(1+\xi)}{R_i} - 1 \right] \qquad (i = 1, 2) \qquad (5.1.2.4)$$

In this formula the parameter $\xi = \mathrm{R_0/R_\pi}$ is called paracentricity and characterized the asymmetry of the HDA, $\mathrm{R_0}$ and $\mathrm{R_\pi}$ are the entrance and exit aperture radii of the electron beam. The parameter γ is the biasing parameter, i.e. a control parameter used to set the voltages of the HDA. The term E_k is the kinetic energy of the electron, while $\mathrm{E_0}$ is the energy in eV of the electrons traveling along the circle of radius R_m and is called the pass energy: $\mathrm{E_0}$ directly depends on the potential difference applied between the hemispheres.

$$E_0 = Cq\Delta V; C = \frac{R_1 R_2}{\frac{\gamma}{\xi}(1+\xi)R_0 \Delta R} \qquad (5.1.2.5)$$

A conventional ideal centric HDA has ξ=1 and γ=1, and eq.(5.1.2.4) is reduced to eq.(5.1.2.6).

$$qV_i = E_k - E_0 \left[\frac{2R_m}{R_i} - 1 \right] \qquad (i = 1, 2) \qquad (5.1.2.6)$$

It follows from eq.(5.1.2.6) that the voltage difference between the two hemispheres depends only on the pass energy and the ratio of the inner sphere/outer sphere radii.

$$\Delta V = E_0 \left[\frac{R_2}{R_1} - \frac{R_1}{R_2} \right] \qquad (5.1.2.7)$$

If $\mathrm{X_1}$ is the radial distance of an electron from the path of radius Rm, at an angle α_0 with respect to the axis perpendicular to the mid-plane of

the hemispheres, the conjugate point at which the electron will leave the analyzer X_2, after being deflected, is given by eq.(5.1.2.8)[142],

$$\frac{X_2}{R_m} = -\frac{X_1}{R_m} + \frac{2\Delta E}{E_0} + 2\alpha_0^2 \tag{5.1.2.8}$$

where $\Delta E = E - E_0$. The first term in eq. (5.1.2.8) shows the magnification of HDA, the second term shows the linear energy dispersion, and the third term shows angular aberration. It is to point out that in real HDA an additional quadratic term in $\Delta E/E_0$ should be taken into account, that arises from non linear dispersion. Because the displacement X_2 depends in α_0 on the second order only, the spherical capacitors exhibit first-order focusing properties. The electron trajectory can also be expressed in term of angular displacement $X(\theta)$[142].

$$\frac{X(\theta)}{R_m} = \left[\alpha_0 \sin\theta + \frac{X_1}{R_m}\cos\theta\right] + \left[\alpha_0 \sin\theta + \frac{X_1}{R_m}\cos\theta\right]^2 + \alpha_0^2(\cos\theta - 1) - \left(\frac{X_1}{R_m}\right) \tag{5.1.2.9}$$

The electrons entering parallel to the central trajectory (α_0=0, θ=0) at a distance X_1 from it, will cross R_m at θ=$\pi/2$ emerging at X_2= - X_1.

The base energy resolution $\Delta E/E_0$ can be obtained from by calculating the transmission of the electron beam as a function of kinetic energy. If we assume equal entrance and exit aperture widths W, a triangular energy distribution function is obtained, with a full width at half maximum (FWHM) of[142]:

$$\frac{\Delta E}{E_0} = \frac{W}{2R_m} + (\texttt{terms in } \alpha_0^2) \tag{5.1.2.10}$$

We can see from eq.(5.1.2.10) that the use of entrance and exit (mechanical) slits can improve the energy resolution of the analyzer.

5.1.3 Real laboratory HDA: electrostatic input lens

In a real hemispherical analyzer[143], before entering the deflector, the electrons pass through a system of apertures and electrostatic lenses, which collect and focus the electron beam into the capacitors gap. In an electrostatic lens at the boundaries between two different potential regions V_1 and V_2, the electron beam is deviated of an amount proportional to the distance of the particle ray from the optical axis, h, and to the inverse of the f-number, defined as the ratio between the focal length of the lens and its pupil diameter. This effect is shown in fig.5.2.
Between the two sections energy conservation must be applied, that is:

$$eV_1 = \frac{1}{2} m_e v_1^2 \tag{5.1.3.1a}$$

$$eV_2 = \frac{1}{2} m_e v_2^2 \tag{5.1.3.1b}$$

And consequently:

$$\frac{v_1}{v_2} = \sqrt{\frac{V_1}{V_2}} \tag{5.1.3.2}$$

Even if the potential changes at the boundary, there is no change in the parallel direction to the latter, so that the tangent velocity component is unchanged.

$$v_1 \sin \alpha_1 = v_2 \sin \alpha_2 \tag{5.1.3.3a}$$

$$\frac{\sin \alpha_1}{\sin \alpha_2} = \frac{v_2}{v_1} = \sqrt{\frac{V_2}{V_1}} \tag{5.1.3.3b}$$

Which is the Snell's law of refraction, where $(\mathrm{V})^{\frac{1}{2}}$ can be considered as a refractive index.

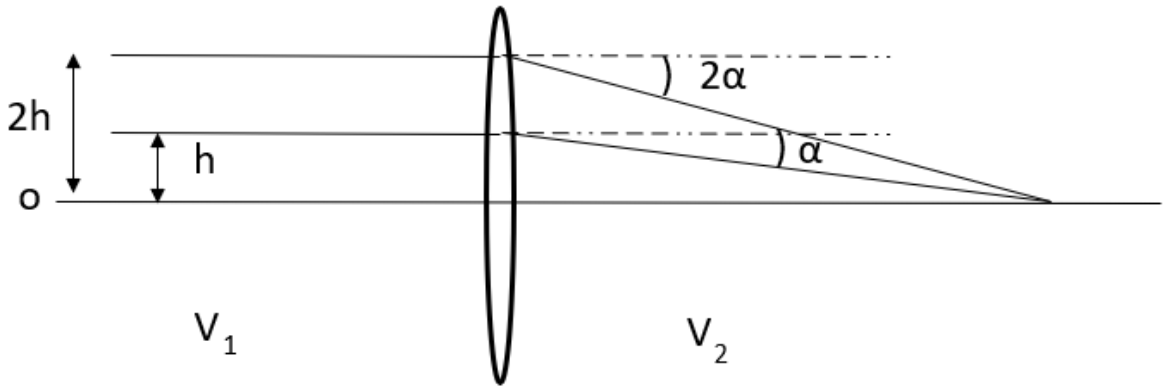

Figure 5.2: Schematic drawing of the focal properties of an electrostatic lens.

among the large variety of lens types, the use of cylinder lenses offers several advantages: they are easy to make and mount, and small inter-electrode gaps can be achieved, an important factor in keeping the potential distribution in the gap at the inner electrode surface close to the calculated one, in order to ensure a good screening from any stray electric field around the lenses. The focal properties of three-cylinder lens depend on two voltage ratios, namely, V_3/V_1 and V_2/V_1, giving to the lens a very useful property, i.e. the overall voltage ratio V_3/V_1 can be varied while

maintaining constant values of object and image distance by a suitable adjustment of the focusing voltage V_2/V_1. It is a very important property since in practical situations the objects and images, e.g. particle sources, detectors, and energy analzyers, are usually fixed in position. One of the simplest lens geometry is the Einzel lens[144], a combination of the accelerating tube lenses with opposite polarity (see Fig.5.3). This lens system has the property of a thick focusing lens for $V_2 > V_1$ as well as for $V_2 < V_1$. Passing trough an Einzel lens does not change the energy of the charged particles. It should be anticipated that in the case of the electron analyzer used to collect the data presented in this thesis, the electrostatic lens system can be considered as a pseudo-Einzel lens, in which the three elements are kept at three different voltages: the first element (the closest to the ionization region) is kept at ground (V_1), the second element is set to a potential V_2, and the third element, mounted on the Herzog plate, has a potential $V_3 \neq V_1$ that is equal to the accelerating/decelerating potential of the Herzog plate. The focusing voltage V_2 is the only optimized parameter of our electrostatic lens system.

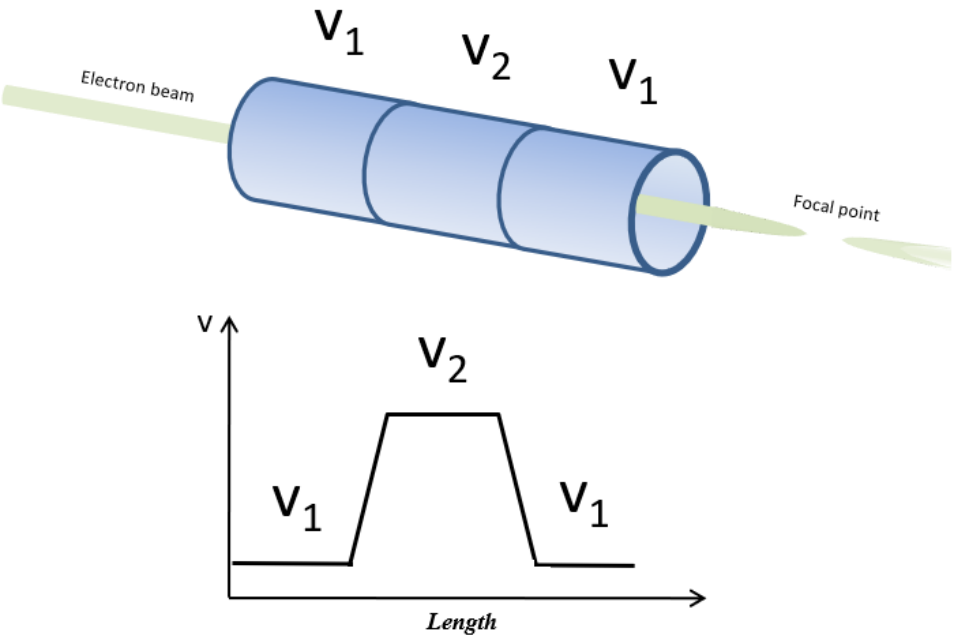

Figure 5.3: Schematic representation of an Einzel lens.

To understand the importance of the lens system we can consider the following example. Lets assume that we have an hemispherical analyzer of mean radius 50 mm and entrance slit of 1mm in diameter, positioned at 25 mm from the ionization region, collects a ray of isotropically emitted electrons with a kinetic energy of 10eV. The electron yield will be proportional to the acceptance solid angle.

$$\texttt{Electron yield} \sim \frac{\pi(0.5)^2}{4\pi(25)^2} \sim 0.01\% \tag{5.1.3.4}$$

If now we insert an electrostatic lens with f number $f/8$ and a diameter of 8 mm (in such way the focal length is $\sim$ 25mm) we have:

$$\texttt{Electron yield} \sim \frac{\pi(2)^2}{4\pi(25)^2} \sim 0.16\% \tag{5.1.3.5}$$

As we can see with the use of an electrostatic lens the electron yield is 16 times better.

5.1.4 Real laboratory HDA: basic electron-optic relations

An electrostatic lens produces images of the physical aperture that define the electron beam. The behavior of the particles passing through the lens system is described by the Helmhotz-Lagrange law[144, 145]. If V_1 and V_2 are the voltages applied to two contiguous sections of the lens, with entrance radius r_1 and virtual window (image) radius r_2. The Helmotz-Lagrange law can be written as:

$$\sqrt{\frac{V_1}{V_2}} = Mm \tag{5.1.4.1}$$

Where $M = r_2/r_1$ is the linear magnification, and $m = \alpha_1/\alpha_2$ is the angular magnification, in which α_1 and α_2 are the pencil angles of the object and image points. This relation states that the electron beam brightness for the object and the image is conserved between the entrance and the exit of the particle trajectories. This law can thus be applied between the entrance and exit slits of a focusing lens.

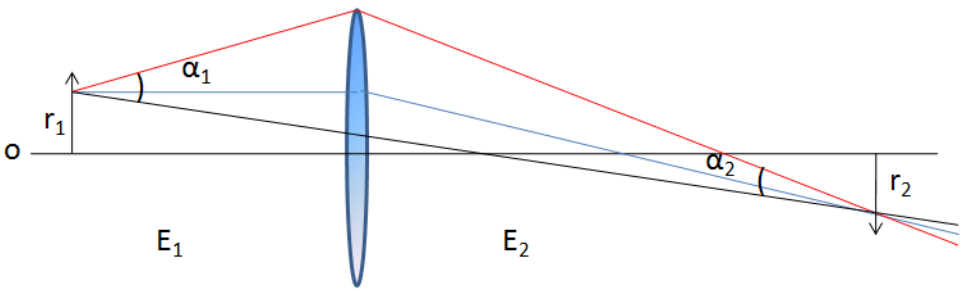

Figure 5.4: The schematic drawing explains Helmholtz-Lagrange Law: $E_1 = qV_1$ and $E_2 = qV_2$ are the electron kinetic energies at the object and image position, respectively.

The Coulomb forces between the electrons in the high-intensity beam going through the analyzer's hemispheres create a self-field which acts on the particles inside the beam. These macroscopic interactions are a consequence of the fact that the electron beam can be considered as a continuum cloud of negative charges, which creates an electric field superimposed on the applied external field, altering the focusing properties of the electron deflector. This space charge effect occurs only in dielectric media, as the vacuum, and it is of importance only when the local beam intensity is very high. One of the most important effects of space charge is the fundamental limit on the current density that can be drawn between two infinite parallel plane electrodes. The space charge-limit current J can be derived from the Child-Langmuir law [146, 147] of eq.(5.1.4.2).

$$J = \frac{4\varepsilon_0}{9}\sqrt{\frac{2e}{m_e}}\frac{V_a^{\frac{3}{2}}}{d^2} \tag{5.1.4.2}$$

In the equation V_a is the anode potential, d is gap between anode and cathode, e and m_e are the electron's charge and mass, respectively, and ε_0 is the vacuum dielectric constant.

5.1.5 Real laboratory HDA: electron detection systems

The electrons are collected at the exit of the analyzer by suitable devices. In both the cases of scanning the hemispheres voltage or accelerating/decelerating the electrons with the Herzog plate, electrons fly across the analyzer's mean radius towards the exit slit; by changing the hemispheres voltage or the accelerating/decelerating (A/R) voltage, electrons with different kinetic energies will be made fly across the mean radius reaching the hemisphere exit slit. A single channeltron detector can be positioned after the exit slit in order to collect the electrons. The main disadvantages of using a single channeltron detector are that the major part of the electrons are lost on the slit in the trajectories outside the mean radius, and only one kinetic energy at the time can be recorded. By removing the exit slit the entire kinetic energy dispersion, or a large fraction of it, can can be recorded at the same instant. Imaging detectors can collect the electron beam at the exit of the analyzer conserving its kinetic dispersion and angular dispersion information[148]. The electron is associated with its kinetic energy depending on the impact position on the detector. Thus, in the case of an imaging detector, the photoelectron spectrum is projected on the exit plane of the analyzer and in such way entire portions of the spectrum can be recorded simultaneously. This makes the Position Sensitive Detector (PSD) much more sensitive to fringing field effects (see next section) and focusing distortions, like for example the distortion of the image at the boundaries of the detector or its rotation with respect to the detector plane.

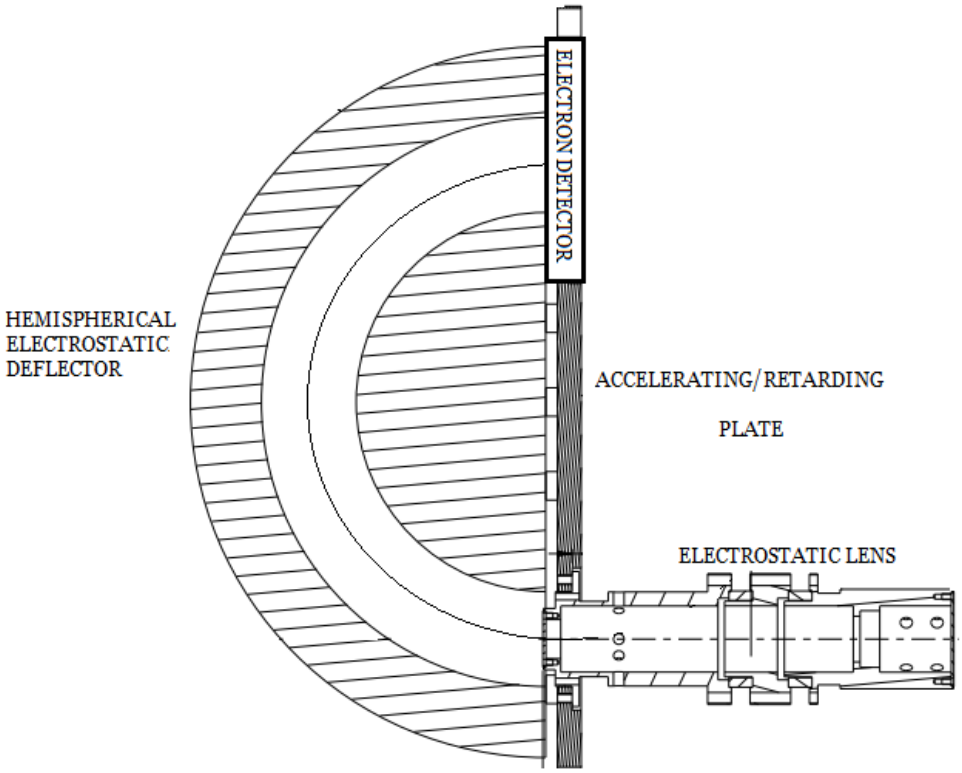

Figure 5.5: Representation of a classic setup for a hemispherical deflector analyzer equipped with an imaging electron detector.

5.1.6 Real laboratory HDA: fringing fields effect

The performances of a real hemispherical deflector analyzer, like the one shown in fig.5.5 are limited by fringing fields at the boundaries of the electrodes, particularly in the region between the A/R plate and the entrance slit of the hemispheres. In particular, slits placed at the entrance and exit of the analyzer, although improve its resolution, distort the $1/r^2$ field, modifying the first-order focusing properties of the electron deflector, deteriorating the energy resolution. Moreover, at the entrance slit, as well as at the exit slit, electrons pass from a constant potential to the spherically symmetric potential. Depending on the radius R_0, electrons therefore are accelerated or decelerated upon entering the analyzer. These fringing field effects are of great importance in the case of an imaging detector: the distortion of electrons trajectories and the effect of the pass energy being not constant over the image (nonisochromaticity) are sources of image aberrations at the 2D detector, such as lost of resolution, defocusing effects, non linear kinetic energy dispersion and image disalignments. Various solutions have been proposed over the years; the Herzog correction[149] is used in many spectrometers by introducing electrode-free space between the electrode fringe and the entrance or exit slit. Other approaches are the Jost correction[150], in which a pair of electrodes connected to the plates of each capacitors are used, and the reduction of the deflecting angle of the hemispheres by the use of tilted input lenses[151]. Baltzer et al.[152] developed an electron analyzer equipped with two fringing field-electrode strips, close to the inner and outer edges of the gaps between the two main hemispherical electrodes. Zouros et al.[153, 154] proposed the use of biased-paracentric entry. All these corrections of fringing fields are summarized in fig.5.6.
In the development of the photoelectron spectrometer used in the experiments presented in this thesis, we used a different approach, poorly treated in the literature, based on a deflecting electrode positioned between the entrance slit and the inner hemisphere of the analyzer. This subject will be discussed later in the text.

5.1.7 Ray tracing simulations: the SIMION software

In many practical cases, the trajectories of an electron beam inside an optical system can not be calculated from analytical equations, and computed similations are needed. One of the most powerful and user-friendly ion-optics simulation software is SIMION[156]. This SIMION Ion and Electron Optics Simulator can be used in order to simulate the trajectories of charged particles flying in a setup consisting of electrostatic and/or magnetostatic elements. In SIMION the object physical space is converted to a 3-dimensional grid, and the potential at each grid point of the volume is calculated for every element. In the case of a hemispherical electron

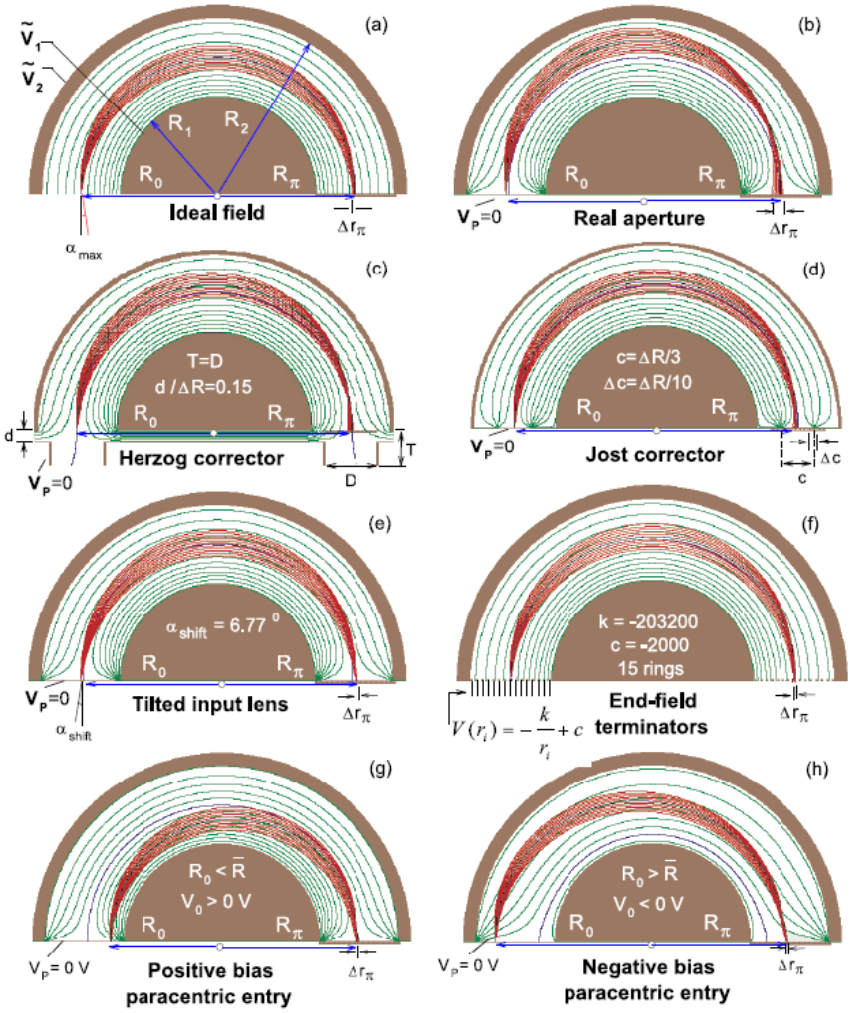

Figure 5.6: SIMION calculations of electron trajectories for (a) Ideal field HDA, (b) real apertures HDA, (c) HDA with Herzog corrector[149], (d) Jost corrector[150], (e) tilted input lens[151], (f) end-terminal electrodes[152], (g)-(h) biased paracentric entry[153]. Image from ref.[155]

analyzer, the electrons will be made fly in the 3-dimensional space by experiencing the electrostatic forces of the estimated potential at each grid point. SIMION provides extensive supporting functionality in geometry definition, user programming, data recording, and visualization. For the electron trajectories simulations presented in this thesis, SIMION v8.1 was used.

5.2 Photoelectron Detectors

The photoelectrons separated according to their kinetic energies can be detected at the exit of the the electron analyzer by a large number of detectors. A photoelectron current of the order of $10^{-14}A$ is typically

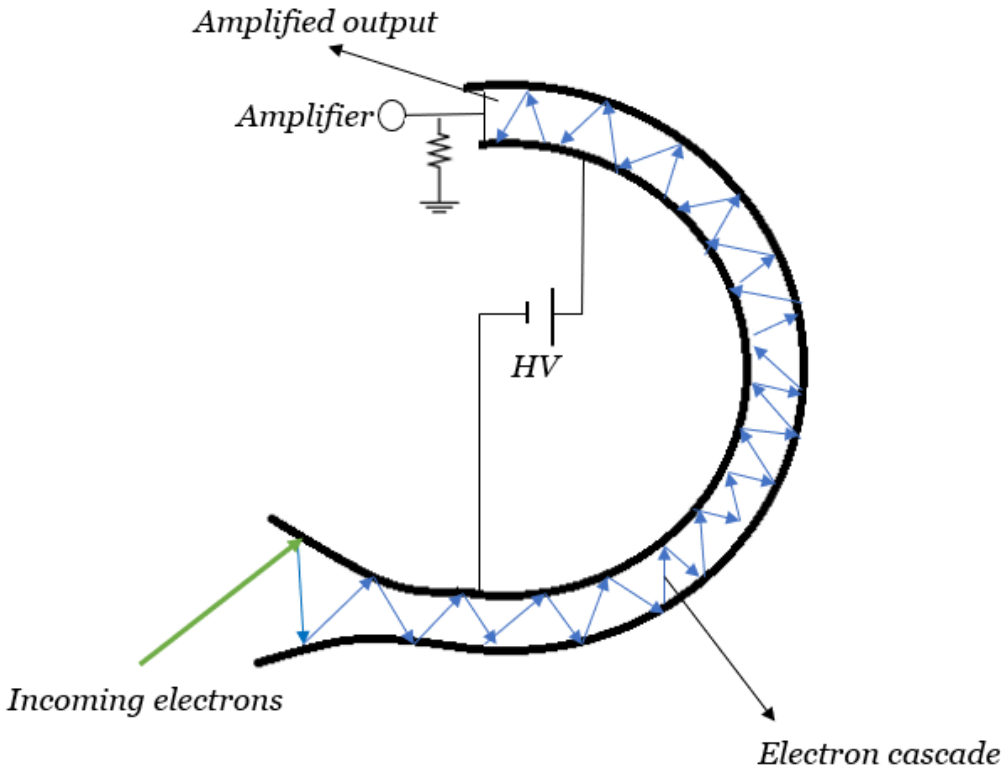

Figure 5.7: Schematic drawing of a channeltron detector.

recorded, this signal can be enhanced by the use of different devices. A brief review of the photoelectron detectors used is presented in the next section.

5.2.1 Channel Electron Multiplier (Channeltron)

One of the most common electron detector used in photoelectron spectroscopy is the single channel electron multiplier, also called channeltron[157]. This electron multiplier is a curved high resistance glass or ceramic tube that acts as a continuous dynode system based on its semiconducting inner surface. When a high voltage (~ 3 kV) is applied between the terminal of the glass capillary, a single electron produced at the low voltage end will be accelerated down the tube and, at every collision with the tube inner wall, will produce a cascade of secondary electrons that continue that process. In this way the signal can be enhanced by a factor $> 10^8$. A scheme of a channeltron device is shown in fig.5.7.

5.2.2 Micro Channel Plate (MCP)

A microchannel plate is a specially fabricated plate that amplifies electron signal, turning a single impinging particle into a cloud of electrons[158]. It is composed by several million of independent channels and each channel works as independent electron multiplier. The channel matrix is usually fabricated from a lead glass, treated in such a way as to optimize the secondary emission characteristics of each channel and to render the channel wall semiconducting in order to allow charge replenishment from an external voltage source. A schematic view of a typical MCP is shown in fig.5.8. Glass composition and reduction processing conditions can control the MCP resistance, which is typically in the range between 20 and 1000 MΩ. For normal operation, a bias of about 1000 Volts is applied across the microchannel plate, with the output at its most positive potential. By applying a strong electric field across the MCP, each individual microchannel becomes a continuous-dynode electron multiplier. A particle or photon entering one of the channels through a small orifice will hit the wall of the channel, being the latter at an angle with respect to the MCP plate (usually from 5° to 15°). The impact starts a cascade of electrons that propagates through the channel, amplifying the original signal by several orders of magnitude depending on the electric field strength and the geometry of the MCP. After the cascade, the microchannel takes time to recover before it can detect another signal. The electrons exit the channels on the opposite side of the plate and are collected by an anode. MCPs are characterized by unique properties, such as high gain, high spatial resolution and high temporal resolution. They are used in a large variety of applications including imaging spectroscopy, electrons spectroscopy and mass spectrometry. In general an MCP based detector consists of three parts: a converter, the mechanism that converts initial particles hit in electrons, an assembly of MCPs, to amplify the initial particle event into electron pulse, and a readout device, in order to detect the electron cascade. The converter is the mechanism that converts initial particles hits in electrons: due to the fact that MCPs are directly sensitive to ultraviolet light, X-rays, charged particles, as well as electron beams, in these cases no converters are usually necessary. MCP's assemblies consist of single, double (called Chevron or V-stack) and triple (Z-stack) of single MCPs adjacent to one another: for example Z-stack MCPs are used in charged particle ion imaging techniques. The choice of electronic readout depends on the experimental requirements. For purely detection and particle counting applications single metal anode can be used, while for imaging applications with high temporal resolution state-of-the art anode configurations are usually used, e,g. crossed delay anode detectors[159].

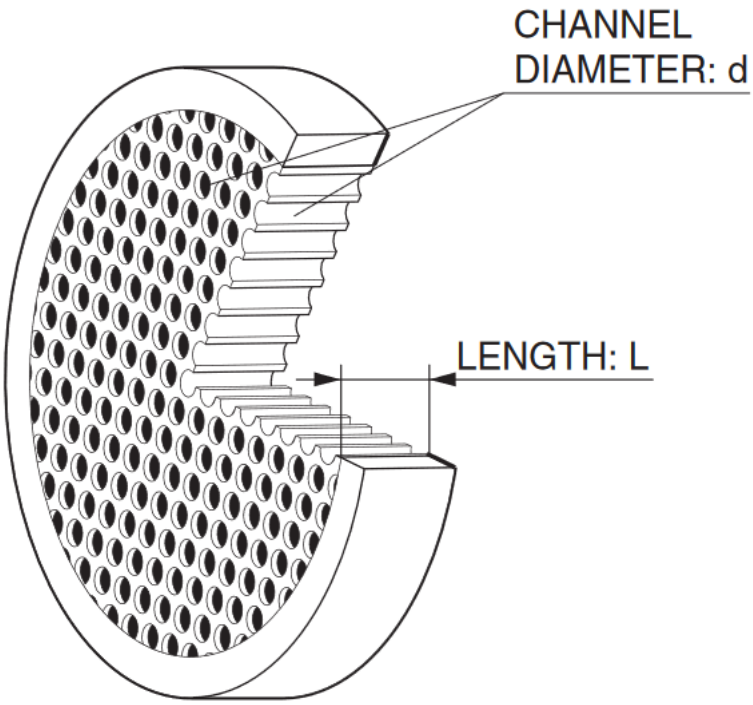

Figure 5.8: Schematic structure of a microchannel plate detector. The ratio of the channel length L to the channel diameter d, together with the inherent secondary emission factor of the channel wall material, determines the gain of the MCP.

5.2.3 Position Sensitive Detectors (PSD)

The purpose of a position sensitive detector is to measure, with high accuracy and speed, the position of light, or particles incident on its surface. The are different systems for obtaining information on the position of a particle impacting on the surface of an MCP: the most straightforward system for the read out of a MCP output is a multianode array placed behind a MCP stack; usually each anode is connected to an individual amplifier and to processing electronics. If the anode takes the form of a two-dimensional sheet of material having a uniform resistivity, the coordinates of the charge cloud impinging on the anode can be determined from measurement of the amounts of charge arriving at three or more points around the periphery of the anode. In this resistive anode setup, the electric signals induced by the MCP electron clouds are picked up from few contacts and the cloud center position is calculated from the relative pulse heights[160]. Resistive anodes do not exhibit great performances in terms of spatial resolution and counting rate, thus in time resolved experiments delay line anodes detectors are preferred[161]. The position is obtained by calculating the time between the start and stop signals coming from the anode ends, making these systems intrinsically suitable for timing information. Moreover, the recent availability of digital Time-to-Digital Converters allows counting capabilities of the order of several MCounts/s.

5.3 Synchrotron Radiation

When charged particles, such as electrons, are accelerated at relativistic speed (i. e. the speed of light) and forced to move along curved trajectories by applied magnetic fields, they lose energy by emitting electromagnetic radiation, the so-called Synchrotron Radiation (SR)[162, 163, 164]. Due to its peculiar characteristics, synchrotron radiation is one of the most powerful tools for investigating the properties of matter in many different fields, from molecular and atomic physics, to medical applications. Many SR sources have been developed all over the world. In third generation synchrotron radiation sources electrons are generated by a Tungsten filament in a linear accelerator (LINAC) and injected in a first circular accelerator, called booster: here the electrons are accelerated through radio-frequency (RF) cavities to a given energy and then are sent into a storage ring, which is a structure made to circulate electrons for as many turns as possible keeping the energy (and the current) stable. The energy lost by the electrons when they emit radiation is recovered making the particles pass into Radio-frequency cavities. The synchrotron light is produced when electrons pass through either conventional bending magnets, or in so-called insertion devices, which are installed in the straight sections of the storage ring. The bending magnets have a double function, keeping the electrons in their trajectory and emitting light; every magnet applies to each electron a Lorentz force perpendicular to its vector velocity that causes a centripetal acceleration that changes the direction of the velocity. The emission peak for a bending magnet in the laboratory frame is:

$$h\nu_c \approx \frac{h\gamma^2 eB}{em_e} \tag{5.3.0.1}$$

where $\gamma = \frac{1}{\sqrt{1-\beta^2}} = \frac{1}{\sqrt{1-\frac{v^2}{c^2}}}$ is the Lorentz relativistic factor and B is magnetic field of the bending magnet. The synchrotron radiation emitted from a bending magnet is a broadband emission, including many different photon energies and wavelengths, that can be filtered with suitable monochromators.
Due to the limits of the bending magnets, in new generation synchrotrons insertion-devices, such as wigglers and undulators, are preferred. A wiggler, consists in a periodic series of magnets, and is inserted in one of the straight sections of the storage ring. The electrons passing through this series of magnets are forced to "wiggle" in the transverse direction, stimulating the emission of synchrotron radiation. Due to the large amplitude these "wiggles", the narrow emission cone periodically enters and exists the device, and the emitted light is observed as a series of short pulses, in contrast to the single pulse from a bending magnet. A wiggler can be thus seen as a combination of several bending magnets. For a wiggler, due to the fact that each "wiggles" have large amplitude and brings the narrow emission cone in and out of the detector, an individual pulse of light is

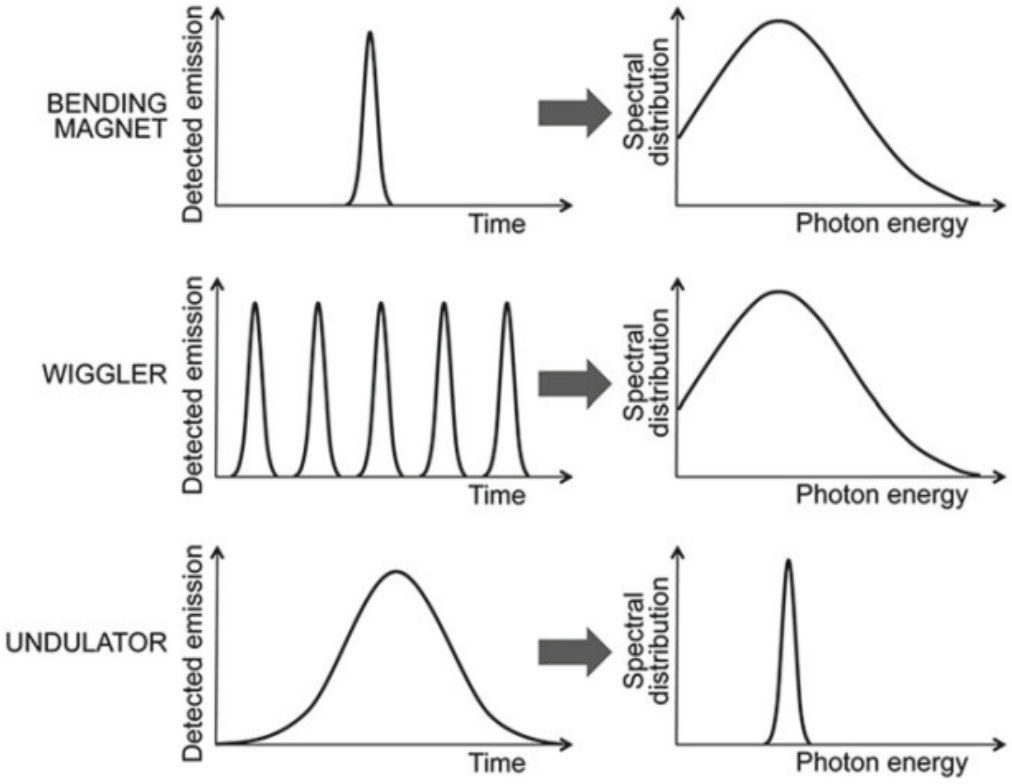

Figure 5.9: Time structure and emission spectrum counterpart for different types of light sources. Top: short pulse and broad emission band from a bending magnet. Middle: series of short pulses from a wiggler, again corresponding to a broad emission band. Bottom: longer pulse from an undulator and narrower bandwidth. Figure adapted from ref.[164]

produced. Conversely, in an undulator, which has a similar structure to the one of a wiggler, the "wiggles" are weak, that is their transverse oscillations keep the emission cone (of amplitude $1/\gamma$) within the detector. As a consequence a single, long pulse replaces the pulse series. and the bandwidth narrows and the emission is almost monochromatic, peaked at an energy of:

$$h\nu_c \approx 2\gamma^2 \frac{nhc}{L_u} \tag{5.3.0.2}$$

where n represents the n-th order, and L_u is the ondulator period. The main spectral features of bending magnets and insertion devices are summarised in fig,5.9

5.3.1 ELETTRA Synchrotron

Elettra Sincrotrone Trieste[165] is a third generation italian storage ring situated nearby the city of Trieste (Italy). It operates in top-up mode in both 2 and 2.4 GeV user energies. Elettra, with his 28 beamlines, has been

optimized to provide the scientific community with photons in the energy range from a few eV to several tens of KeV with spectral brightness of up to $10^{19} photons/s/mm^2/mrad^2/0.1\%bw$ and is continuously upgraded in order to be competitive with the most recent sources.

5.3.2 The GasPhase Photoemission Beamline @ Elettra

The Gas Phase Photoemission (GAPH) beamline[166, 167] of the ELETTRA Synchrotron is specifically devoted to research on gaseous systems and offers a multi-technique approach for investigation of electronic properties of free atoms, molecules and clusters in the photon energy range 13-900 eV. The GAPH beamline is fed by an undulator which delivers linearly polarized light in the range from 13.5 eV to well above 900 eV. The monochromator is a Variable Angle Spherical Grating Monochromator, with fixed positions of the slits and a resolving power (> 10000). The use of two refocusing mirrors provides a roughly circular spot at the sample ($\sim 50 \times 200 \mu m$). The beamline, other than the high-energy main-line, has a branch line dedicated to low energies ($\sim 20 - 200 eV$). The GAPH beamline is equipped with more than 11 different experimental chambers, each one designed for a specific experimental setup.

5.3.3 The Circular Polarization Beamline @ Elettra

The Circular Polarization (CiPo) beamline[168] of the ELETTRA Synchrotron is characterized by its capability of providing synchrotron radiation light of variable polarization (Circular to Linear) in a very broad photon energy range, 11 to 900 eV. The insertion device of the CiPo beamline is the Electromagnetic Elliptical Wiggler (EEW), designed to provide both linearly and circularly polarized radiation over the entire operation photon energy range, and can operate in both undulator and wiggler modes. The request for helicity switching led to a fully electromagnetic design which combines the horizontal and vertical periodic magnets into one open-side structure. In wiggler mode the EEW operates for different values of the vertical and horizontal magnetic field providing an elliptically polarized radiation and a continuum emission spectrum from 40 eV to more than 1000 eV. This insertion device also provides a spectrum of harmonics in the low photon energy side (< 40 eV). The degree of circular polarization changes with photon energy: from 40 % at 8.5 eV to 80% at 575 eV. Full circular polarization condition (90%) is achieved when the EEW works as a pure circular undulator, that is when the horizontal and vertical magnetic fields are equal. The undulator mode allows to produce also linearly polarized radiation with the polarization vector parallel or perpendicular to the orbit plane. The beamline is equipped with two monochromators: a low energies (5 - 35 eV) Normal Incidence

Monochromator (NIM), and a Spherical Grating Monochromator (SGM) for high energies.

5.4 Free Electron Laser (FEL)

A free electron laser (FEL) is an unique type of laser[169] and a suitable radiation source in many applications, including chemistry, structure determination of molecules in biology, medical diagnosis, and nondestructive testing. The main characteristics of FELs are: continuous wavelength tunability, high spectral brightness, narrow light bandwidth. which makes them highly suitable for various applications. In conventional lasers stimulated emission of radiation is achieved by creating a population inversion between higher and lower excited states of an active lasing medium. The emitted radiation, which has a frequency equal to the energy difference between these two states, is amplified in the laser cavity and a coherent laser beam with a narrow bandwidth is produced. The laser frequency tunability is achieved by the use of nonlinear optical processes; the tuning range is thus limited by the choice of the nonlinear media. Conversely, a FEL does not have a principal limitation for the wavelength of emitted radiation, as the active lasing medium in this case is represented by electrons traveling with relativistic speeds. The electrons propagate through a periodic magnetic field created by the undulator, an array of magnets with alternating dipoles, and perform a wiggling motion due to Lorentz forces, emitting radiation of wavelength:

$$\lambda = \frac{\lambda_u}{2\gamma^2}(1 + K^2) \tag{5.4.0.1}$$

in which λ_u is the undulator period, K is a dimensionless parameter proportional to the strength of the magnetic field, and γ is the Lorentz factor. The wavelength of the radiation can be tuned by changing the energy of the electrons, and the strength of the magnetic field B (by changing the gap between the undulator magnets). The FEL principle allows achieving laser radiation from microwaves to X-rays.

5.4.1 FELIX Facility

The FELIX (Free Electron Laser for Infrared eXperiments)[170] light source at Radboud University (Nijmegen, the Netherlands) exploits intense, short-pulsed infrared and THz free electron lasers, and is suitable for IR absorption spectra measurements in extremely diluted gas-phase environment. The tuning region of the FELIX ranges from 3 to 150 μm (3200-80 cm^{-1}).

5.5 ARPES 3D ion imaging end station

The ARPES end station, historically devoted to angular resolved photoeletron spectroscopy, is now devoted ion imaging spectroscopy[171, 172, 173]. The chamber houses a differential pumping system, suitable for supersonic molecular jets, and a two interchangeable molecular beam systems, namely a pyrolitic source and a hypodermic needle.
A schematic view of the 3D ion imaging experimental setup is shown in fig.5.10. A detailed description can be found in ref.[174, 175, 176]. An effusive or supersonic beam of the target molecule crosses the synchrotron radiation at the extraction region. In the case presented in this thesis, an effusive molecular beam is introduced in the interaction region through a stainless steel needle, to whom can be applied a voltage in order to compensate its electrostatic perturbation in the interaction region, which has effects on the angular distribution of the emitted ions. The electrons are accelerated towards an MCP detector, and are used as trigger for the ions time of flight. The ions are extracted, accelerated towards a field-free first-order Wiley-MacLaren TOF spectrometer[177] and mass-selected. The electron clouds produced by the ion impacts on a MCPs Z-stack are collected by a position sensitive detector formed by a XY matrix of 32+32 strips anodes (see fig.5.11), 32 horizontal and 32 vertical, each of one connected with an independent time-to-digital converter (TDC). In our setup the vertical strips are related to the X direction of the linearly polarized light and the horizontal ones to the Y direction. The identification number of the vertical and horizontal stripes is directly related to the X and Y impact coordinates of the ion. The stop signals time distribution, processed by the 64 independent TDCs, is triggered by the same electron extracted and detected by a single anode MCP Z-stack electron detector, producing in this way a mass spectrum with the same time origin for every anode strip.
The use of 64 independent TDCs allows the measurement of several ion fragments and electrons (up to 5 particles in coincidence) coming from the same photoionization event. In addition, each of the 64 independent detector channels is connected to a discriminator. When an event occurs the signal from the TDC is read by a VME (Versa Module Eurocard) computer and sent to the acquisition computer that controls the experimental acquisition setup and registers the data. The ion detector records the x and y coordinates of each particle hit so that for each ion two space and one temporal coordinates are determined. For every start electron the measured ions are sorted in groups of single and multi-body coincidences and the time of flight is coded by the TDCs on a 16 bit string while the X and Y impact positions are encoded in two 8bit strings. As a result for each particle in a coincidence group the (X,Y,t) information are saved in a compact 32 bit string. The ion-ion correlation can be visualized by plotting a two-dimensional histogram, in which the time-of-flight of the first ion is plotted versus the time-of-flight of the second detected ion.

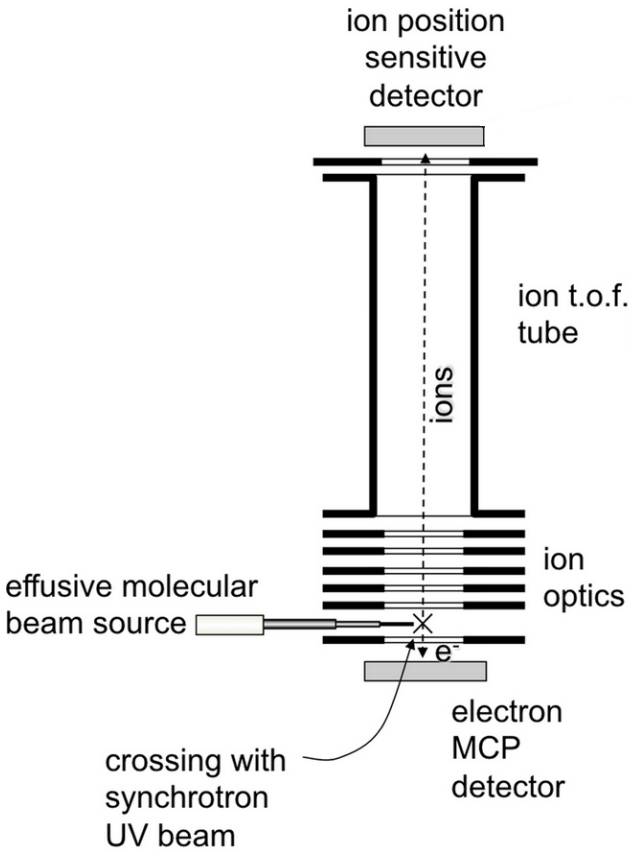

Figure 5.10: Scheme of the experimental electron-ion extraction and detection system installed in the ARPES Ion imaging spectrometer.

This histogram, representing two-body correlation, is usually referred as coincidence map. An example of such bidimensional map is shown in fig.5.12.

In correspondence of the time-of-flight crossing of two correlated ions an "island" can be observed. These coincidence islands, in which each dot represents a coincidence event, contain important information about the dynamics and kinetics of the dissociation process leading to the correlated ions. In fact, the slope and shape od such islands are related to the dissociation mechanism and energetics of the molecular ion photofragmentation[178], while the intensity is related to the ionization probability of the molecular species and can be used to determine double photoionization thresholds and fragments appearing potentials by recording the coincidence maps as a function of photon energy. In all coincidence experiments a random background is present in the coincidence maps, arising from false coincidences. These random coincidences events occur in the case of two not correlated stops signals, or for uncorrelated ion stop and electron start signals, and depends in general to both electrons and ions counting rates. Different methods for the false coincidences subtraction can be used in the

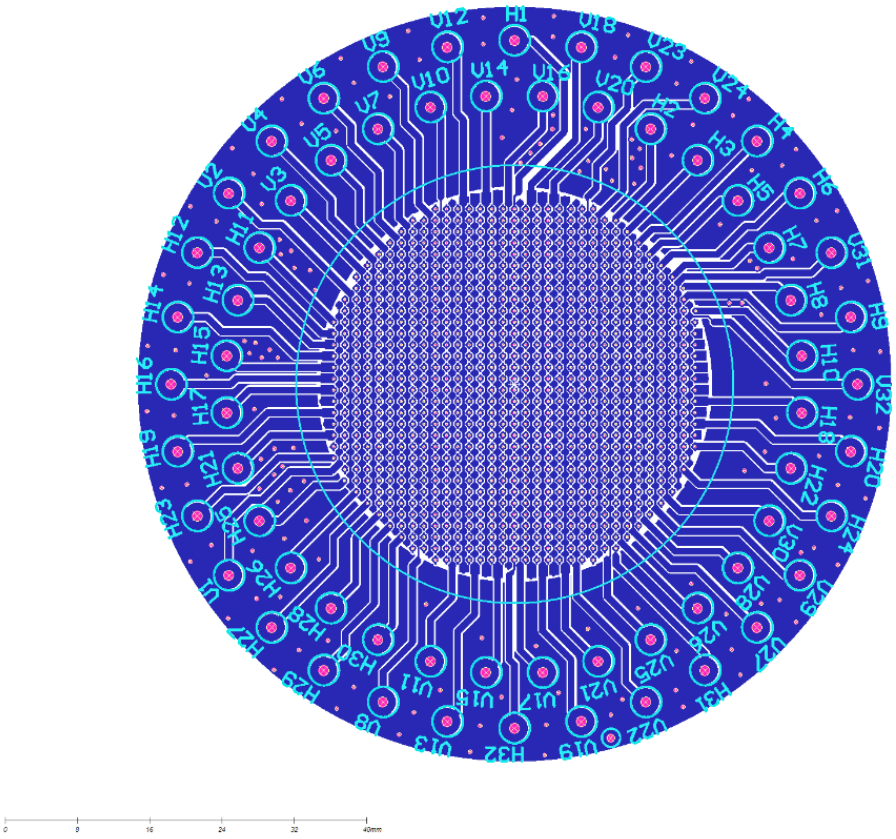

Figure 5.11: Technical drawing of the printed circuit board position sensitive detector of the ARPES 3D Ion Imaging end station. X direction is represented by the Vertical strips while the Y direction is represented by the Horizontal strips

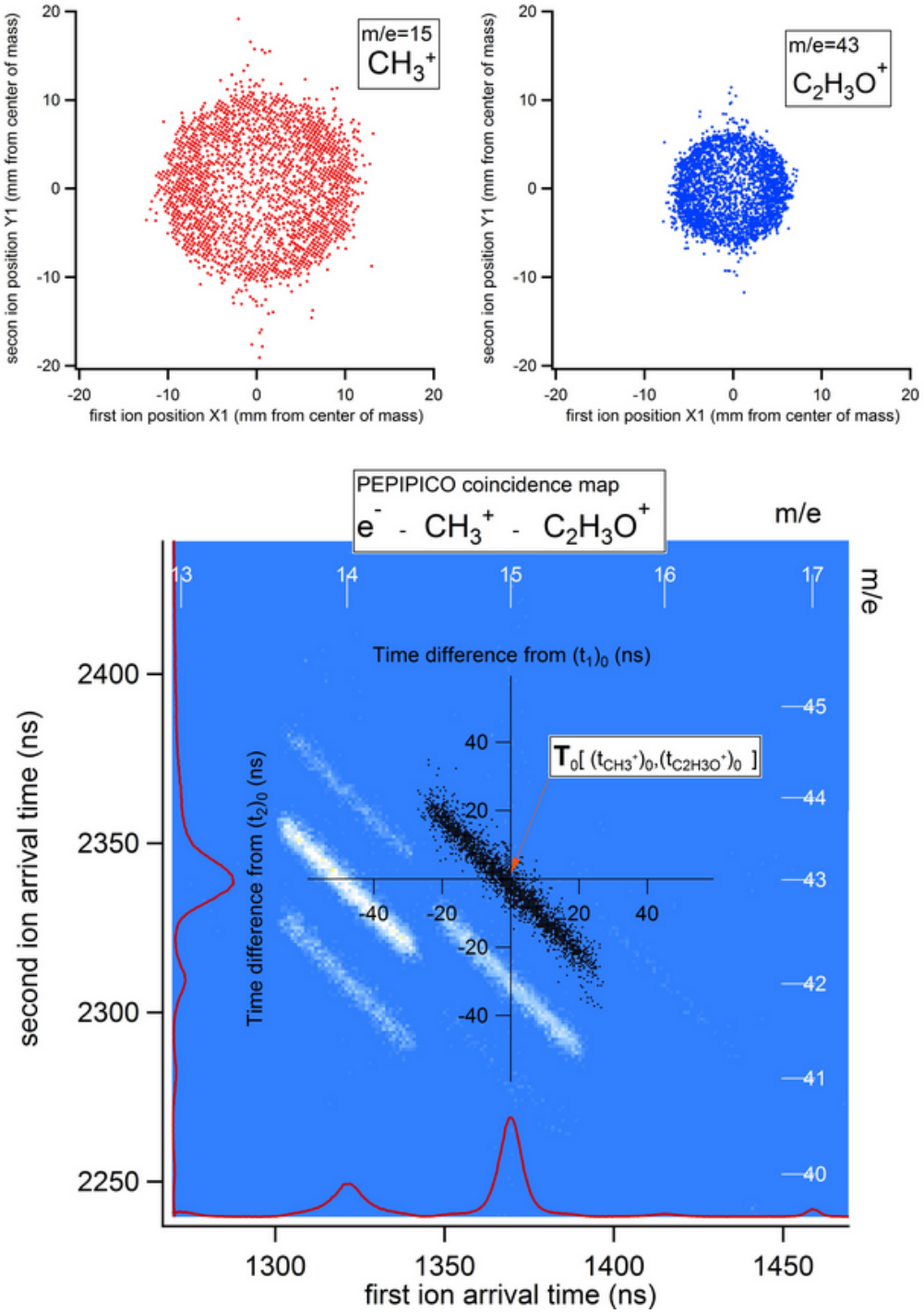

Figure 5.12: A typical coincidence map (bottom) obtained in a photoelectron-photoion-photoion coincidence experiment. The figure refers to the two body $CH_3^+ + C_2H_3O^+$ fragmentation channel in the VUV double photodissociation of the propylene oxide molecule. The space coordinates distribution for the two fragments is also shown (top).

data analysis[179, 180]; an empirical method to reduce false coincidence contribution is to perform the experimental measurements at sufficiently low counting rates.
The measurement of the impact point coordinates and the arrival time for each particle allows to calculate its linear momentum in the laboratory frame, according to[174]:

$$p_{i,x} = p\sin\theta\cos\phi = k_1\frac{m(x_i - x_g)}{t_i} \tag{5.5.0.1a}$$

$$p_{i,y} = p\sin\theta\sin\phi = k_1\frac{m(y_i - y_g)}{t_i} \tag{5.5.0.1b}$$

$$p_{i,z} = p\cos\theta = -k_2(t_i - t_0) \tag{5.5.0.1c}$$

where x_g and y_g are the coordinates of the center of mass of the n-th PEPIPICO dissociation event (z_g coordinate does not enter the equations if the Wiley–MacLaren time focusing is employed), m is the ion mass and t_0 is the arrival time for an ion with no initial momentum along the z axis, p is the magnitude of the momentum, θ and ϕ are respectively the polar and azimuth angles with respect to the radiation polarization vector; k_1 and k_2 are geometrical factors. If a complete two (or more) body dissociation is detected, we have enough measurements to solve the system of kinematical equations. In particular, one can calculate the x_g and y_g coordinates by applying the linear momentum conservation law, that is $\sum p_{i,x} = 0$ and $\sum p_{i,y} = 0$. The knowledge of the center of mass coordinates allows to transform the measured x_i , y_i , and t_i coordinates into the linear momenta components following the previous mentioned equations, and then the laboratory angles and energies can be computed. Thus, from the momenta distribution in the center of mass coordinate system it is possible to obtained the Total or Partial kinetic energy released (KER) in the dissociation process.

$$KER = \frac{p^2}{2m} \tag{5.5.0.2}$$

Moreover, the photofragments angular distribution $P(\theta)$, with respect to the radiation polarization plane, can be obtained from the knowledge of the ion momenta distribution according to eq.(5.5.0.3)

$$P(\theta) = \frac{\sigma}{4\pi}\left[1 + \beta P_2(\cos\theta)\right] \tag{5.5.0.3}$$

However the 2D images measured in this experimental setup appear as the projection on the plane of the detector, so that an integration of eq.(5.5.0.3) is needed, i.e. the measured angular distribution $I(\theta)$ is given by

$$I(\theta) = \frac{\sigma}{2}\left[1 + \beta P_2(\cos\theta)\right]\sin\theta \tag{5.5.0.4}$$

where the term $\sin\theta$ accounts for the projection of the three dimensional product distribution on the detector plane. A fit with eq.(5.5.0.4) of the experimental $I(\theta)$ is sufficient to obtain the ion angular distributions.

5.6 IRMPD-VUV action spectroscopy setup

In this experimental setup the target species are prepared in their rovibronic ground states by means of supersonic-jet cooling and then vibrationally excited by IR photons. The multiple absorption of IR-FEL photons leads to molecular fragmentation. The fragments are then probed with 10.49 eV VUV photons as a function of the IR wavelength, and the resulting ionized IRMPD products are analyzed by a TOF mass spectrometer, in order to obtain mass-selected IR absorption spectra. Low vapor pressure samples are heated in pyrex tube compartment and positioned in front of a pulsed valve nozzle (0.5 mm orifice, Jordan TOF Products Inc.). The sample vapors are then seeded in a supersonic-jet generated by a pulsed valve, using Ar or He, typically at 2-3 bar pressure, as a carrier gas, and admitted in the vaccum chamber region. This jet of electronically, vibrationally and rotationally cooled molecules is further collimated by a skimmer, and directed into the interaction region, where it is crossed by a pulsed IR FEL beam and a delayed VUV laser beam. A scheme of the experimental apparatus is shown in fig.5.13. The VUV laser photons are produced by focusing a 355nm light (3rd harmonic of Nd^{3+}:YAG laser) in a gas cell containing a 10:1 mixture of, respectively, Ar and Xe gases. The resulting 3rd harmonic radiation, with wavelength of 118 nm (10.49 eV) and pulse duration of $\sim$ 2-3 ns, is refocused into the interaction region by a MgF_2 lens. When a molecular vibrational transition resonates with the scanned IR frequency, the molecule dissociates through the IRMPD mechanism. The resulting fragments and parent molecules are then ionized by the VUV laser radiation at the end of each FEL macropulse (6-8 μs), and the resulting ions are detected by a reflectron time-of-flight spectrometer, thus allowing recording the mass-selected IR-spectra. In order to measure reference mass spectra without the IR-FEL pulse at every VUV laser pulse, the VUV ionizing laser and the pulsed valve operate at 10 Hz, while the FELIX laser operates at 5 or 10 Hz. In the study of enantioselective interactions in oligomers of chiral molecules (small clusters of enantiomers), a complete set of measurements is usually obtained for an enantiomerically pure sample and afterwards a second set of measurements is recorded for the racemic mixture. This procedure avoids any possible contamination of the enantiopure sample.

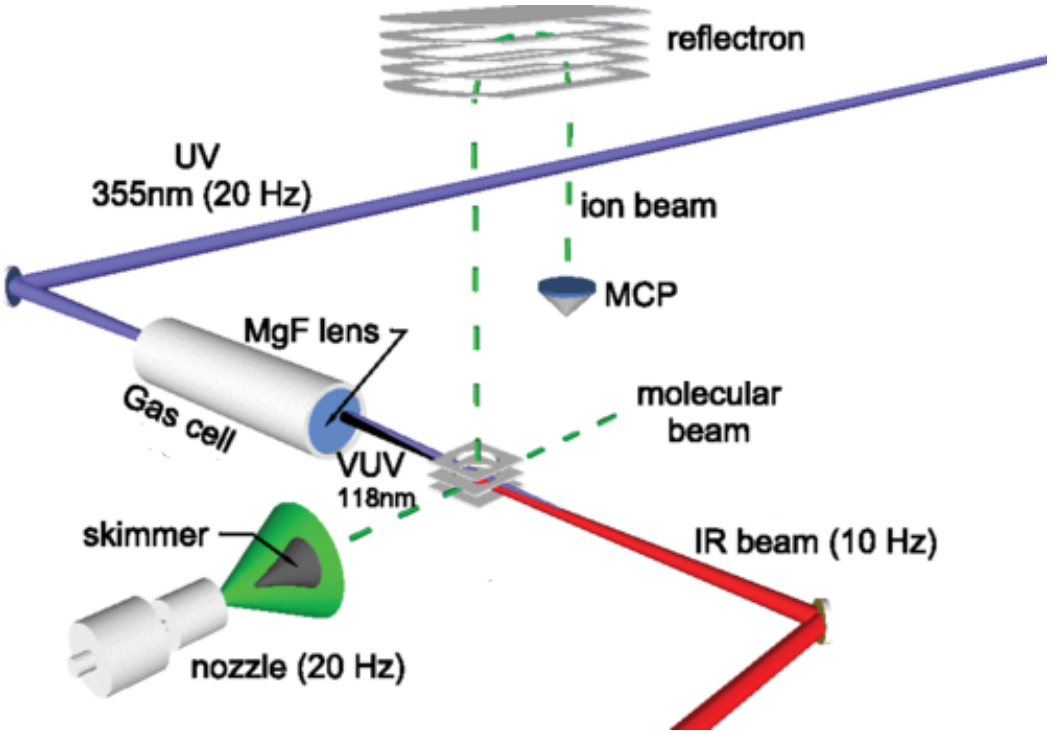

Figure 5.13: Schematic representation of the experimental setup for the IR action spectroscopy of low-temperature neutral gas-phase molecules. For more details see the text. Image adapted from ref.[130]

Chapter 6

Ab initio Methods

All the theoretical calculations presented in this thesis have been performed by Professor P. Decleva and his co-workers of the University of Trieste. Even if I did not performed the calculations by myself, they have a key role in the work presented in the following chapters, and thus a brief presentation of the *ab initio* methods employed is presented here, in order to give to the reader a deeper comprehension of the results. A more completed treatment can be found in many textbooks (see for instance [181, 182]).

6.0.1 Expression of the wave function

Since the photoionization process is a dipole transition between the initial and final states, calculation of the cross sections, as well as of the asymmetry parameters, is related to the calculation of the dipole matrix elements between these states. Thus, the task of computing photoionization observables can be reduced to properly expressing initial and final state wave functions. While the calculation of the initial bound state wave function is straightforward, the calculation of the continuum wave function is extremely difficult, and requires many approximations.

General expression

In the photoionization process open channels are defined as the states accessible at the given energy E, which satisfy the relation (6.0.1.1).

$$IP_I = E_f^{N-1} - E_0^N < h\nu \tag{6.0.1.1}$$

The N-electron final state wave function can be written as (in the so called close-coupling form[183])

$$\Psi_{EIL}^N = \sum_{I'L'} \Psi_{I'}^{N-1} \phi_{EI'L'IL} + \sum_k \phi_{E\alpha k}^N \tag{6.0.1.2}$$

(where $\alpha \equiv I$ collectively includes all the additional quantum numbers necessary to describe the final state).
In eq.(6.0.1.2) the first sum runs over all the possible open channels and includes the antisymmetrized products of the bound ionic final states wave function, Ψ_I^{N-1}, and single-electron continuum wave function, $\phi_{EI'L'IL}$, and automatically satisfies the boundary conditions in the continuum. The second summation is expressed entirely in terms of target orbitals and is necessary to take into account the orthogonalization condition between the target and continuum orbitals. At long range the final state wave function has to reduce asymptotically to a linear combination of products of target states multiplied by a single-particle continuum wave function.

$$\Psi_{E\alpha}^N \xrightarrow{\mathrm{r}\to\infty} \sum_{I'} \Psi_{I'}^{N-1}\phi_{E\alpha I'} \tag{6.0.1.3}$$

Here I' refers to all possible open channels and $\alpha = Ilm$ counts all the possible products of target states I multiplied by all the angular momenta lm of the degenerate continuum particle.

First level approximation

At the single channel level, the final continuum wave function is approximated as an antisymmetrized product of the final ionic state wave function and the continuum orbital describing the outgoing electron, emitted with kinetic energy ε.

$$\Psi_{EIL}^N = \hat{A}\Psi_I^{N-1}\varphi_{\varepsilon IL} \tag{6.0.1.4}$$

In this independent particle approximation, the wave function of the final state can be expressed as a single determinant of single-particle functions.

$$\Psi_{EIL}^N = |\varphi_1, ..., \varphi_\varepsilon, ..., \varphi_N\rangle \tag{6.0.1.5}$$

This wave function corresponds to a single electron excitation in which the i-th orbital has been ionized and the i-th electron excited to the continuum. At this level of approximation there is only the contribution of the emitted particle to the N-particle transition matrix element and the contributions from the other electrons will integrate to unity. This is known as the frozen orbital approximation. Within this approximation the Koopmans' theorem is valid, and it is possible to calculate quantities as the cross sections and dichroic parameters as well as to describe some specific effects such as oscillations in the asymmetry parameters profiles (e.g. the Cooper minima). On the other hand is not possible to describe multiparticle processes, as for instance the autoionization phenomenon.

Second level approximation

Single particle excitation can be included by representing the final state wave function as a mixing of the previously described independent particle functions.

$$\Psi_{Ej}^{N} = \sum_{i} C_{iJ} |\varphi_1, ..., \varphi_\varepsilon, ..., \varphi_N\rangle \tag{6.0.1.6}$$

In this way it is possible to include effects like interchannel coupling (in which a transfer of intensity occurs between one channel and the others) and autoionization resonances due to discrete single excitations. However, the appearance of satellite states and further effects related to the electronic correlation can not be described.

Third level approximation

It is possible to stay at the single channel level, and hence to reduce the dipole matrix elements to the form $\langle\varphi_\varepsilon|D|\varphi_i\rangle$, and still to employ highly correlated bound state wave functions for the initial state and the ionic final state, by substituting to φ_i the function ϕ_{IF}^{d}, called Dyson orbital[184, 185, 186, 187], defined as:

$$\phi_{IF}^{d} = \sqrt{N} \int \Psi_I^N(1, ..., N)\Psi_F^{N-1}(2, ..., N)d2...dN \tag{6.0.1.7}$$

These orbitals represent a superposition between the N-electron initial neutral state wave function, Ψ_I^N, and the (N-1)-electron ionic final state wave function, Ψ_F^{N-1}. All the electron-electron correlation effects (Initial State Configuration Interactions, ISCI and Final State Configuration Interaction, FISCI) can be described at the Dyson orbitals level of approximation, the IPs are not simply calculated by the Koopmans' theorem but are defined as $IP_I = E_f^{N-1} - E_0^N$. This is an overcome of the single-particle picture of the photoemission process, and hence we can speak about the *breakdown of the Koopmans' theorem*.

6.1 Computational methods

Once the level of approximation is established, there are several computational methods that can be used to calculate the initial and final wave functions. In the following text a brief presentation of the methods adopted in this thesis is reported.

6.1.1 Hartree-Fock Method

In the Hartree-Fock (HF) method, each electron is described by an orbital, and the total wave function is given as an antysimmetrized Slater determinant. The best set of orbitals is determined by the variational principle, that is the HF orbitals give the lowest energy within the restriction of the wave function being a single Slater determinant. Since the other electrons are described by their respective orbitals, the HF equations depend on their own solutions, and must therefore be solved iteratively; this is the reason why the HF is also called Self-Consistent field (SCF) method. When the molecular orbitals are expanded in a basis set, that is a set of functions (called basis functions) that is used to represent the electronic wave function, the resulting equations can be written as a matrix eigenvalue problem. The elements in such Fock matrix correspond to integrals of one and two-electron operators over basis functions, multiplied by density matrix elements. The HF equations in a basis set can thus be obtained by repeated diagonalizations of a Fock matrix.

6.1.2 Configuration interaction

The HF method usually gives the 99% of the correct energy. The difference between the exact energy and HF energy is known as the correlation energy. In the Configuration Interaction (CI) approach, these correlation effects can be calculated by the use of wave functions that are a linear combination of Slater determinants. These determinants correspond to electronic configurations in which electrons are promoted into virtual orbitals. Hence, they represent excited states whose contribution to the total wavefunction of the ground state generally decreases with the order of excitation. In this model, the wave function can be written as:

$$\phi_{CI} = a_0\phi_{HF} + \sum_S a_S\phi_S + \sum_D a_D\phi_D + \sum_T a_T\phi_T + ... \qquad (6.1.2.1)$$

where S, D, T, etc. indicate respectively singly, doubly, triply etc. excited determinants relative to the HF configuration. Depending on the symmetry properties of the target system, the linear combination of eq.(6.1.2.1) can be reduced to a basis of states with the same spatial and spin symmetry (Configurational State Functions, CSFs). If the expansion includes all the possible CSFs of the appropriate symmetry, it represents a full CI procedure which exactly solves the electronic Schrödinger equation in the given basis.

6.1.3 Complete Active Space SCF (CASSCF)

One of the most famous multideterminantal approaches is the Complete Active Space Self-Consistent Field (CASSCF) method[188]. It is a spe-

cific type of Multi Configuration self-consistent field (MCSCF) method in which the number of CSFs used in the expansion are defined by dividing the orbitals into three subspaces. In the first subspace, called inactive space, all orbitals are doubly occupied. The second subspace is termed as the active space, in which a full-CI expansion is considered. The electrons and orbitals included in the active space are those that contribute most to the multireference character of the chosen system of study. The occupation number of the orbitals in the active space will be a noninteger number between 0 and 2. Finally, the third subspace, that is the virtual space, consists of unoccupied orbitals. The great advantage of this method is that it decreases the number of CSFs in the CI expansion since it limits the MC wave function within a specific subset of orbitals rather than on all orbitals. The CASSCF method cannot be used as a "black box" method, as a priori knowledge of the chemical system under study is needed; in fact the choice of the appropriate active space represents the main difficulty in the CASSCF method. Another limitation of CASSCF is that the number of electrons and orbitals that can be included in the active space are not infinite, since the CI expansion increases exponentially with respect to the number of electrons and orbitals.

6.1.4 Density Functional theory (DFT)

One of the main problem with the quantum mechanical approach, is that the complexity of the multi-body wave functions grows dramatically with the number of particles (a wave function for an N electron system contains 4N variables, three spatial and one spin coordinate for each electron). The basis for Density Functional Theory (DFT) method is that the ground state electronic energy is determined completely by a new quantity, the electron density $\rho(r)$, that is the square of the wave function, integrated over (N-1) electron coordinates, and each spin density only depends on three spatial coordinates, independent of the number of electrons; thus while the complexity of a wave function increases exponentially with the number of electrons, the electron density has the same number of variables, independent of the system size. The central principle of DFT is the Hohenberg–Kohn theorem[189], which states that the ground-state density, $\rho(r)$, of a system of interacting electrons subject to some external potential, $V_{ext}(r)$, determines this potential uniquely (up to a trivial constant), from which follows that the electron density uniquely determines the Hamiltonian operator. The total energy of the the system will then be a functional of the electron density, and can be written as:

$$E[\rho(r)] = T[\rho(r)] + V_{ext}[\rho(r)] + V_{ee}[\rho(r)] \tag{6.1.4.1}$$

where $T[\rho(r)]$ is the electrons kinetic energy, $V_{ext}[\rho(r)]$ is the interaction with the external potential, and depends on the studied system, and $V_{ee}[\rho(r)]$ includes the electron-electron interactions. Although the

Hohenberg–Kohn approach is in principle exact, the form of the kinetic energy and electron correlation functionals are *a priori* unknown, making this method unpractical. An approximation for the kinetic and electron-electron functionals was proposed by Kohn and Sham (KS)[190],in which a fictitious system of N non-interacting electrons is introduced to be described by a single determinant wave function in N "orbitals" φ_i. In this system the kinetic energy and the electron density are known exactly from the orbitals.

$$T[\rho(r)] = -\frac{1}{2}\sum_{i}^{N}\langle\varphi_i|\nabla^2|\varphi_i\rangle \tag{6.1.4.2a}$$

$$\rho(r) = \sum_{i}^{N}|\varphi_i|^2 \tag{6.1.4.2b}$$

$$V_C[\rho(r)] = \frac{1}{2}\int\frac{\rho(\mathbf{r}_1)\rho(\mathbf{r}_2)}{|\mathbf{r}_2-\mathbf{r}_1|}d\mathbf{r}_1 d\mathbf{r}_2 \tag{6.1.4.2c}$$

In eq.(6.1.4.2) $V_C[\rho(r)]$ is the classical Coulomb interaction part in the electron-electron interaction potential. The functional form of the total energy can be now written as:

$$E[\rho(r)] = T[\rho(r)] + V_{ext}[\rho(r)] + V_C[\rho(r)] + E_{xc}[\rho(r)] \tag{6.1.4.3}$$

We have introduced a new term, the Exchange-Correlation functional $E_{xc}[\rho(r)]$, that contains the difference in energy between the exact solution of the many-particle system and the approximate non-interacting electrons system. the actual form of E_{xc} is not known and thus we must introduce approximate functionals based upon the electron density to describe this term. There are two common approximations (in various forms) in use: the local density approximation (LDA)[191], in which the exchange-correlation energy at a point $\mathbf{r}$ is simply equal to the exchange-correlation energy of a uniform electron gas that has the same density at the point $\mathbf{r}$, and the generalized gradient approximation (GGA)[**?**], attempts to incorporate the effects of inhomogeneities by including the gradient of the electron density. Hybrid functionals improve the total energy determination by using both the electronic density and the individual electronic wave functions to compute the total energy. The exchange part is computed from the electron wave functions and mixed into the LDA or GGA energy.One of the most commonly used hybrid functional for the exchange-correlation term is the B3LYP[193]. On the basis of the found relations the behavior of non-interacting electrons in an effective local potential can be described, in analogy with the Hartree-Fock method, by set of non-linear equations (the Kohn-Sham equations), in the form:

$$\left[-\frac{1}{2}\nabla^2 + V_{ext}(\mathbf{r}) + \frac{\rho(\mathbf{r}')}{|\mathbf{r}-\mathbf{r}'|}d\mathbf{r}' + V_{xc}(\mathbf{r})\right]\varphi_i(\mathbf{r}) = \varepsilon_1\varphi_i(\mathbf{r}). \qquad (6.1.4.4)$$

The price for the re-introduction of the orbitals is in the computational cost of solving the Kohn-Sham equations, that scales formally as N^3(due to the need to maintain the orthogonality of N orbitals). One of the main advantages of DFT is that unlike the Hartree-Fock method, it includes some electron correlation and is thus much more accurate in the energy calculations, but at a similar calculation time. On the other hand, the main limitation of DFT is in the choice of the exchange-correlation functional; many functionals form are available but it is not always clear what the best choice of functional is for the system of interest.

6.1.5 Time-Dependent Density Functional Theory (TDDFT)

Time-dependent density-functional theory (TDDFT) is a universal approach to the dynamical many-body problem. This means that one can use TDDFT to describe non-stationary situations in matter such as atoms, molecules, solids, or nanostructures. As the DFT method is based on the Hohenberg–Kohn theorem, TDDFT rests on the Runge-Gross theorem[194], which establishes a one-to-one correspondence between the time-dependent electron density and a time-dependent external potential. The Kohn-Sham equations are replaced by their the time-dependent analogue of (12). The time-dependent density follows from eq.(6.1.4.2) with the time-dependent orbitals replacing the static ones. The exchange-correlation potential now inherit a time-dependence from the time dependence of the density. If the time-dependent potential is weak, it is possible to use the linear-response theory to study the target system[195]. In particular, within this approximation, TDDFT yields predictions for electronic excitations and it has become, in this research area, a standard tool. On the other hand, if the time-dependent potential is strong, a full solution of the Kohn-Sham equations is required.

6.1.6 Multicenter B-spline static-exchange DFT method

Finite basis sets technique is an important numerical tool in solving quantum mechanical problems. One popular developments in such calculations is the use of B-splines functions, introduced by Schoenberg[196]. The reason to the popularity of the B-splines is due to the fact that they form a sufficiently complete basis set with a reasonably small number of basis functions. B-spline functions are defined as piece wise polynomials and they bridge the gaps left by standard basis functions, such as Gaussian

Type Orbitals (GTOs), or Slater Type Orbitals (STOs) or, in the treatment of specific molecular problems. In particular, the description of the continuum states requires basis sets which could obey to the peculiar continuum boundary conditions and could reproduce the oscillating behavior of the wavefunction to infinity. Traditional GTO and STO functions are not adequate to represent the rapidly oscillating continuum states, since numerical linear dependencies rapidly come up as the basis set increases. B-splines, on the contrary, are very flexible functions and can describe accurately both bound and continuum states without running into numerical dependencies. They produce smooth curves with continuous derivatives at every point. Since B-splines are defined in a restricted space, usually referred to as a box, one has to define a certain knot sequence, depending on the target system. The continuum wavefunctions can be correctly reproduce by using a linear grid of points and a sufficient density of B-splines. The multicenter B-spline static exchange DFT method[197] is based on the use of these B-spline functions in a simple least-squares formulation for the determination of eigenvectors in the continuum spectrum. The method can be summarized in three main steps:

- Standard DFT calculation using the Amsterdam Density Functional (ADF)[198] program to obtain the ground state electron density.
- Construction of the Hamiltonian matrix in the Linear Combination of Atomic Orbitals (LCAO) basis set, followed by a generalized diagonalization for bound states and application of Galerkin[199] approach for continuum states.
- Dipole transition moments are calculated in order to obtain photoionization observables (photoionization cross section and asymmetry parameters).

The main advantage of this method is the complete convergence of the results is obtained with much smaller hamiltonian matrices, that is reflected in a smaller computational effort and also in the possibility to investigate systems which are impracticable with other methods. However, the static-exchange DFT method might be unsuitable when the coupling between different photoionization channels is large, and TDDFT level results are expected to be improved with respect to the simpler KS.

6.1.7 Computational approach in the calculation of the continuum wave function

The method proposed by the group of Professor P. Decleva and presented in this thesis for the treatment of the continuum employs a basis of radial B-splines functions multiplied by spherical harmonics to solve the Schrôdinger equation for the continuum electronic spectrum. B-spline functions have proven a very powerful choice, because are particularly suited to tackle with the boundary conditions obeyed by the continuum

wave-function. Such wave-function does not decay at large distances, but rather oscillates with well defined asymptotic behavior, and this cannot be described with canonical basis sets as GTO or STO functions. For small or highly symmetric molecules the One Center Expansion (OCE) can be used, which consists to set all the functions on the same origin to describe the molecular continuum, but becomes impracticable for large or less symmetric systems, such as chiral molecules. The Linear Combination of Atomic Orbitals (LCAO)method is then used, which consists of the OCE supplemented with off-center basis set elements, this makes the implementation of the code more difficult but the algorithm is very efficient and economic for large systems, so the range of applicability has been much widened. Concerning the Hamiltonian, the DFT-KS approach is, in general, a rather accurate and realistic description of the photoionization, however the agreement with the experiment is not usually quantitative. On the other hand the TDDFT formalism is much more accurate and a quantitative agreement with the measurements is often obtained, though the computational effort is larger with respect to the KS approach. At the TDDFT level, coupling among different ionization channels is actually allowed, this is the reason not only for its better performances but also for its ability to describe properly autoionization (Feshbach) resonances, an effect completely missed at the KS level.

Chapter 7

Results and Discussion

7.1 Epichlorohydrin molecule

Epichlorohydrin, or 2-(Chloromethyl)oxirane, is an chlorine derivative of propylene oxide, belonging to the epihalohydrins chemical class, i.e. any compound having a halogen on the carbon atom adjacent to an epoxide. Epichlorohydrin is an extremely versatile chemical intermediate in the production of epoxy resins and other elastomers[201, 202], in agriculture to produce biologically active compounds, as well as in the pharmaceutical industry.

The assignment of the outer valence photoelectron (PE) bands of the epichloridryn molecule proved difficult since its first valence photoemission investigation[203]. Many authors, in fact, assigned only three bands to the photoelectron spectrum in the 10-12.5 eV ionization energy (IE) region, with the first band (HOMO-1) being well separated from the next largely overlapped bands. Recent investigations[204, 205] could assign the correct number of bands to this spectral region, namely four, on the

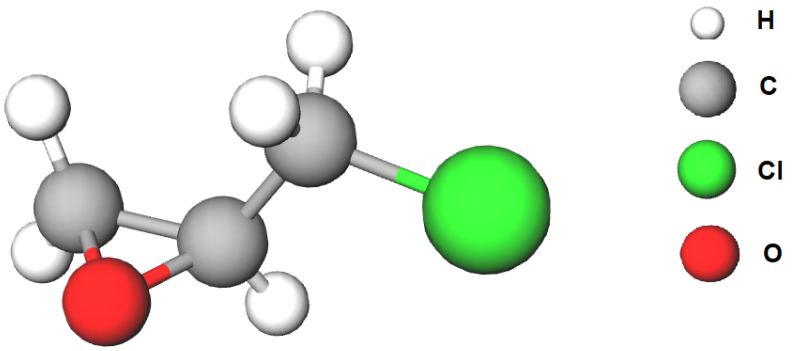

Figure 7.1: 3D molecular structure of the epichlorohydrin molecule.

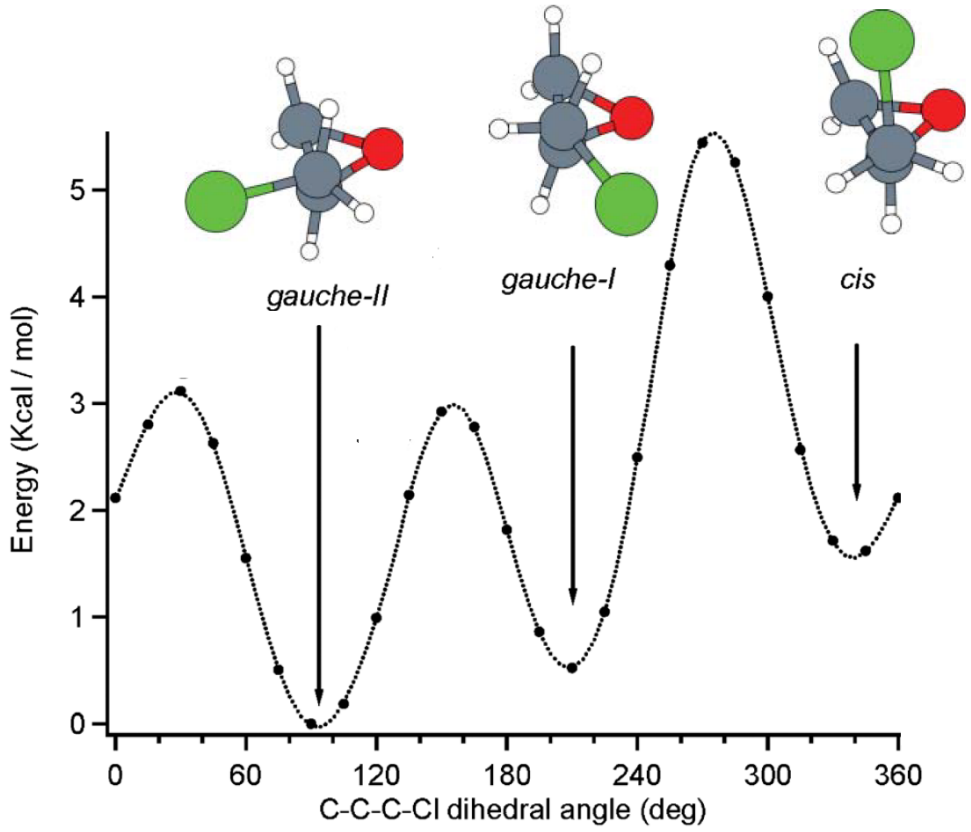

Figure 7.2: Potential-energy curve of (R)-epichlorohydrin for internal rotation of the –CClH2 group calculated as a function of the C–C–C–Cl dihedral angle, and relaxing the whole geometry. The maxima of the potential energy correspond to the eclipsed structures with barriers of 3.12, 2.92, and 5.44 kcal mol^{-1} respectively. Image adapted from ref.[205].

basis of theoretical results obtained by ab initio quantum-mechanical calculations. However, the given detailed assignment of the four cationic electronic states, in terms of photoelectron (PE) bands grouping in the experimental spectrum, was controversial, namely (24a, 23a)-(22a, 21a) in ref.[204] and (24a)-(23a, 22a, 21a) in ref.[205]. The intrinsic difficulty of the spectral description is due to the high density of states of this region (four PE bands within less than 2 eV) and the further spectral complexity caused by the rotational isomerism, namely possible co-existence of the different gauche-II, gauche-I, and cis conformers at the experimental temperatures[204, 205], as shown in fig.7.2.

Moreover, the theoretical description of the photoionization process based on the single particle picture for these bands proved to be inadequate since a strong breakdown of the Koopmans' theorem was found for the four outermost valence ionizations of this molecule[205]. Therefore, the present work aims to fully exploit the photoionization dynamics of the valence cross sections and asymmetry parameters in a large photon energy

range to shed light into the electronic structure and the description of the PE spectrum of epichlorohydrin.

7.1.1 Epichlorohydrin : photoionization cross sections

The epichlorohydrin partial photoionization cross sections, $\sigma(h\nu)$, associated with the outer valence PE bands observed in the 10 - 19 eV IE range, have been studied as a function of photon energy with linearly polarized synchrotron radiation. For this purpose, epichlorohydrin PE spectra measured at the magic angle ($\theta = 54.7°$) have been recorded at selected photon energies in the 14 - 55 eV range. A representative set of these spectra is reported in fig.7.3. The experimental data acquisition procedure and the data analysis procedure is described in appendix B.1.

In agreement with previous investigations[203, 204, 205], the photoelectron spectrum exhibits two well separated groups of bands at low and high ionization energies values, namely the bands 24a - 21a and 20a - 15a, respectively. The relative value of $\sigma(h\nu)$ of the ten photoionization channels is obtained as the peak area of the associated PE band. The relative photoionization cross sections of the first four bands 24a-21a, measured as a function of the photon energy, are reported in fig.7.4, while the same cross sections obtained for the high IE bands are given in fig.7.5. The $\sigma(h\nu)$ values for all the outer valence ionization channels, as generally expected for photoionization of valence electrons in molecular systems, show a large decrease on going from the threshold region (below 15eV photon energy) to several tens of eV above threshold. Although this general trend is shared by all the valence photoionization channels, the 24a-21a PE bands, differently from the other bands (the 20a-15a group), show remarkably large changes in their relative intensities, as manifest in the change of the 10-12.5 eV IE spectral region (see fig.7.3) as the photon energy is increased from 18.5 eV (spectrum *a* in fig7.3) to 54 eV (spectrum *f* in fig7.3). As shown in fig.7.4, the cross sections $\sigma(h\nu)$ of the 24a-21a bands exhibit different behaviors. The relative intensity of the HOMO band (24a) (black squares in fig.7.4) has a strong relative increasing with the increase of the photon energy, and the corresponding photoelectron band, being the second more intense peak at hν = 18.5 eV (panel *a* in fig7.3) and about half intensity of the second peak (23a), becomes the dominant spectral components at high photon energies (panel *f* in fig7.3). The relative intensity of the second band (23a), is the highest at low energies (red circles in fig.7.4) and decreases considerably at high photon energies, becoming of the same intensity as the band associated to the 21a state. The third band (22a, blue triangles in fig.7.4) exhibits a clear decrease of the relative intensity as the photon energy increases, since it is much greater than that of the weakest and partially overlapped fourth band (21a), whilst becomes the weakest band at high energies. The

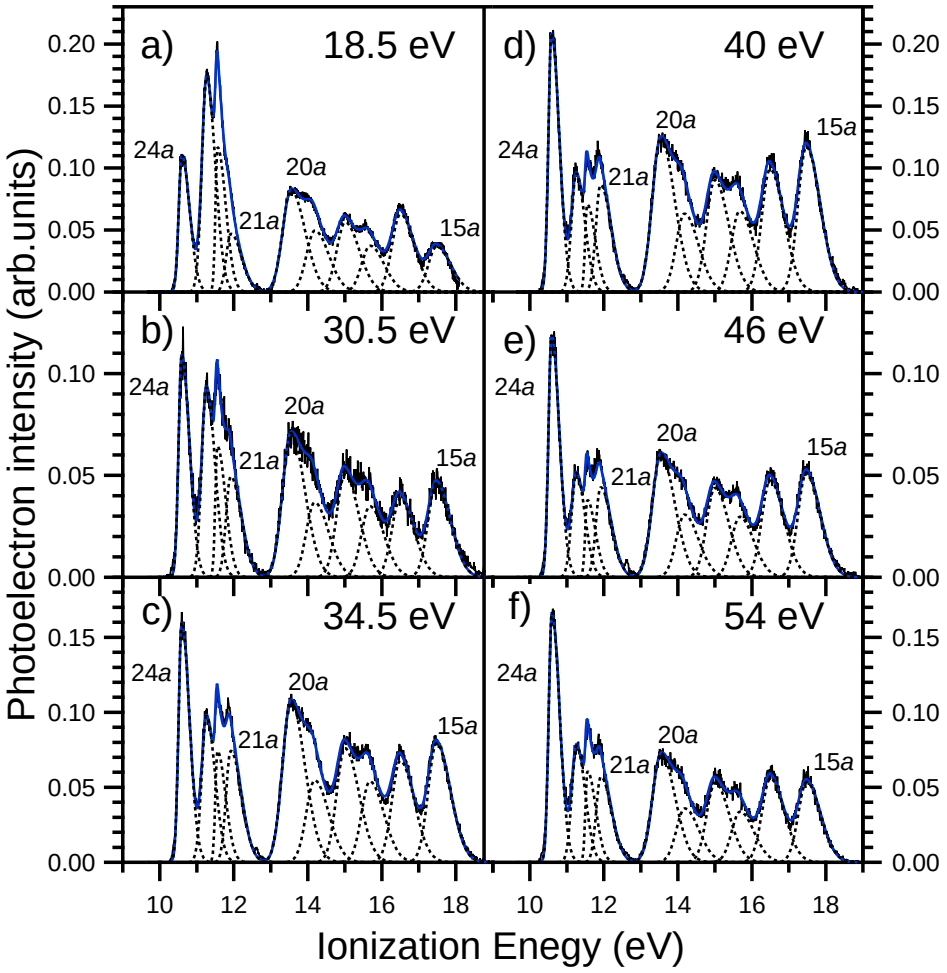

Figure 7.3: Outer valence PE spectra of epichlorohydrin recorded at the magic angle, θ = 54.7°, and at different photon energies (panels a-f). Spectral fit simulation curve (blue solid line) and bi-Gaussian fit components (dotted lines), obtained by the global multipeak fit, are shown with the experimental spectrum (solid thin line).

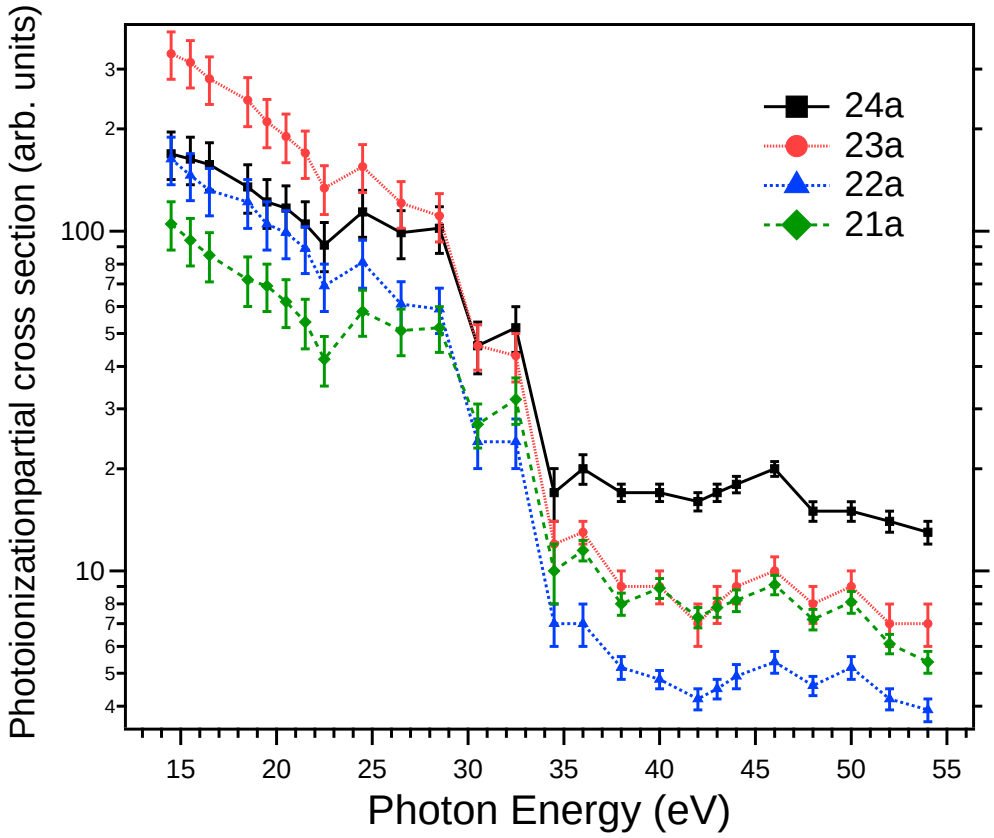

Figure 7.4: Experimental relative photoionization cross sections for the four outermost valence ionizations, 24a - 21a, as a function of photon energy.

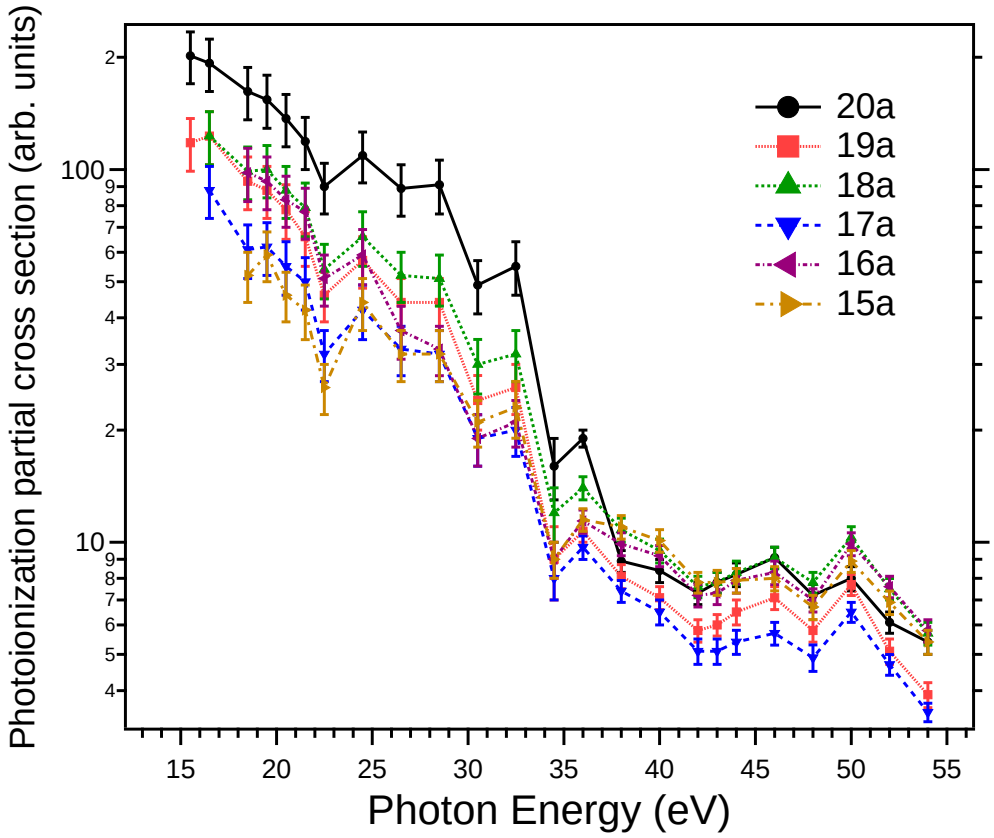

Figure 7.5: Experimental relative photoionization cross sections for the 20a-15a valence ionizations as a function of photon energy.

change in relative intensity of the fourth band has the most striking effect in the valence PE spectrum. A representative low energy photoelectron spectrum, recorded at hν = 18.5 eV, is reported in fig7.3 (panel *a*): the relative intensities of the three overlapped bands, namely (23a), (22a), and (21a) show that the fourth band is much weaker than the other two nearby bands, and is almost totally obscured in the spectrum. It is now clear why this spectral component eluded observation in the previous investigations. The high energy spectra (curves c-f in fig.7.3) point out a much higher relative intensity of the fourth band, which becomes as intense as the second bands and substantially more intense than the overlapped third band, as shown in detail in fig.7.4 by the green, red and blue data points at high photon energies. As a result, all the four photoelectron bands associated with the first four electronic states can be easily discernible at high photon energies.
In contrast with the behavior of the 24a-21a group of bands, the high ionization energy part of the spectrum, namely the 13 - 19 eV IE region, corresponding to the ionization from the 20a-15a group of molecular orbitals, exhibits a rather modest overall change, this being due to the small relative intensity changes of these valence bands. All these cross sections display the expected substantial decrease as the photon energy increases (see fig.7.5) and are not discussed in more detail.
The partial photoionization cross sections, $\sigma(h\nu)$, associated with the outer valence photoemission spectrum of epichlorohydrin have been calculated as a function of photon energy at both DFT and TD-DFT levels. Since the rotational isomerism due to the internal rotation of the -CH_2Cl group might affect the photoionization process, and thus the photoionization observables, the photoionization cross sections, as well as the asymmetry parameters, have been calculated for all the three stable conformers, namely gauche-II ($g-II$), gauche-I ($g-I$), and cis. Room temperature (RT) Boltzmann average values of the cross sections and asymmetry parameters have then been derived to allow a direct comparison between theory and experiment. The calculated TD-DFT photoionization cross sections of the four outermost ionizations for the three conformers are reported in fig.7.6 (panels $a-d$), along with the Boltzmann average curves (black solid lines). In fig.7.7 the RT Boltzmann average cross sections of the 24a-21a bands are also reported together, in order to show the relative intensities theoretically predicted for the first four bands observed in the experimental photoelectron spectra.

The theoretical results in fig.7.6 point out that the cross sections are not heavily affected by the rotational isomerism, and only small differences are visible in the threshold region. It can be seen that at low photon energies the second PE band (RT curve of panel *b*) is predicted to have the highest intensity among the 24a-21a states, whilst the fourth band (RT curve of panel *d*) in the same energy region has a considerably lower intensity than all the other bands. This theoretical finding is more clearly evident in fig.7.7, where only the RT curves are reported. Interestingly, in

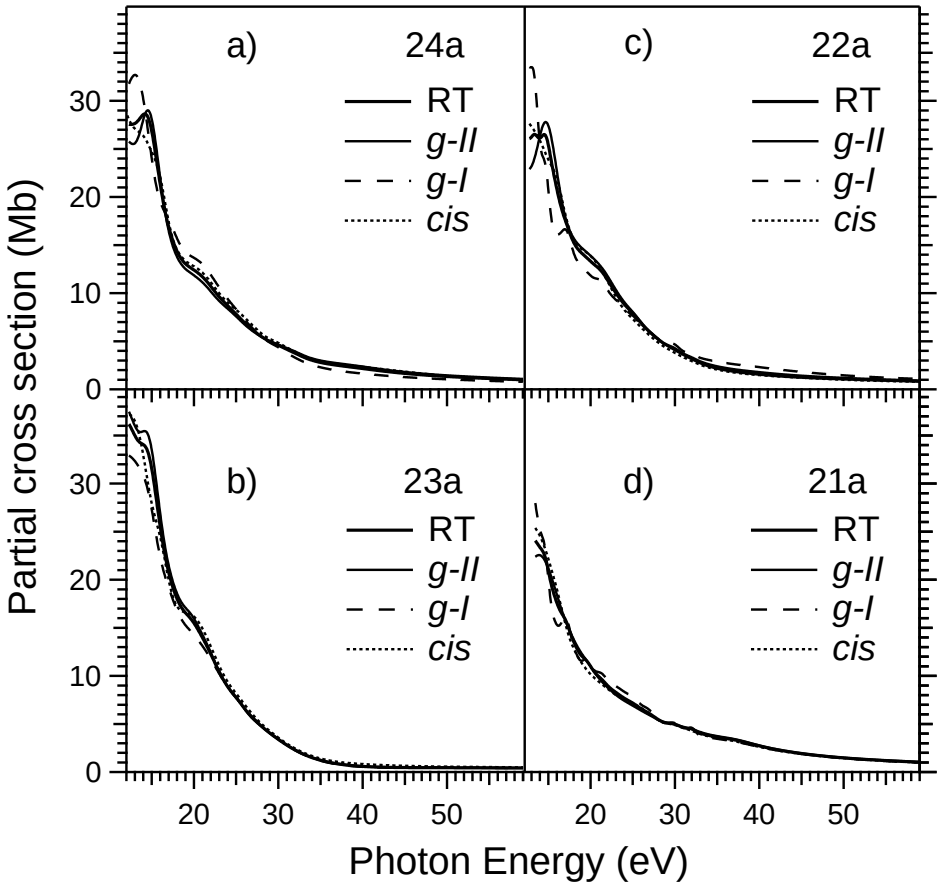

Figure 7.6: TD-DFT calculated photoionization cross sections of the stable rotamers, g-II (solid thin line), g-I (broken line), and cis (dotted line), for the outermost valence ionizations of the epichlorohydrin molecule. The room temperature Boltzmann average (curve RT, solid thick line), is also reported along with the rotamer cross sections.

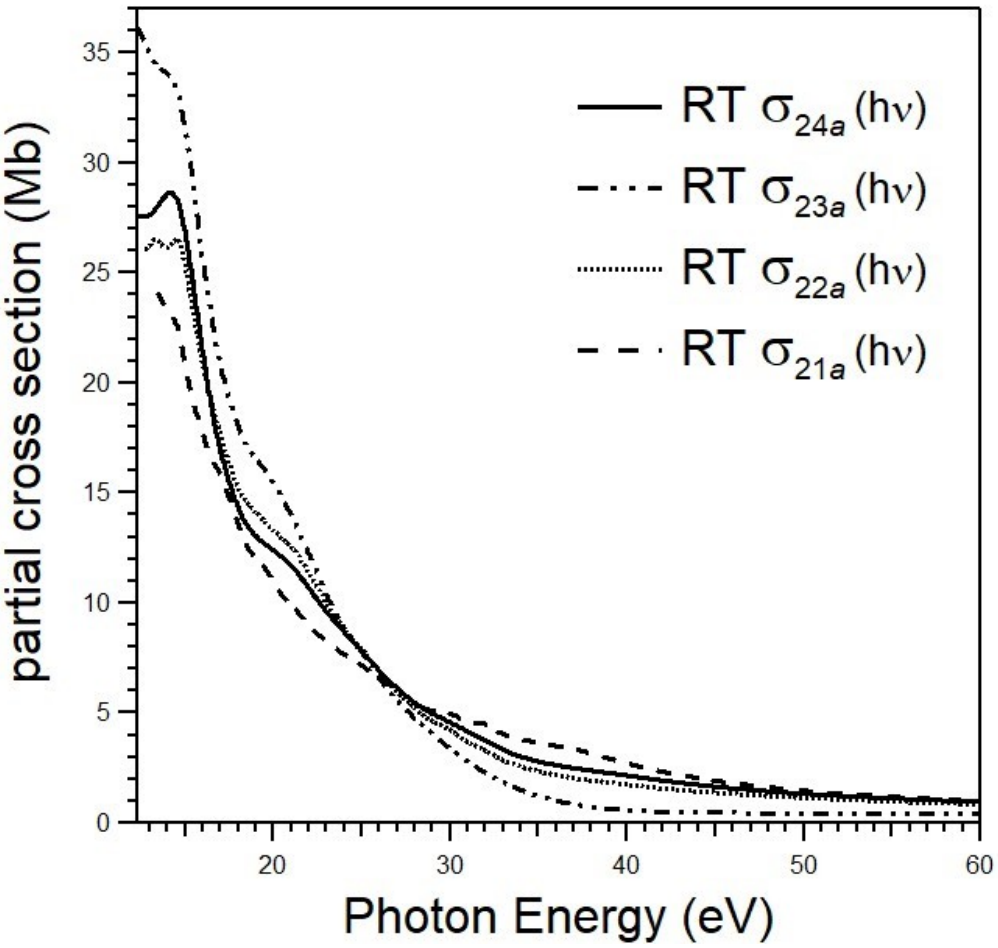

Figure 7.7: Photoionization cross sections calculated at TD-DFT level for the valence outermost ionizations of epichlorohydrin. The reported curves are the Boltzmann average of the three stable rotamer cross sections.

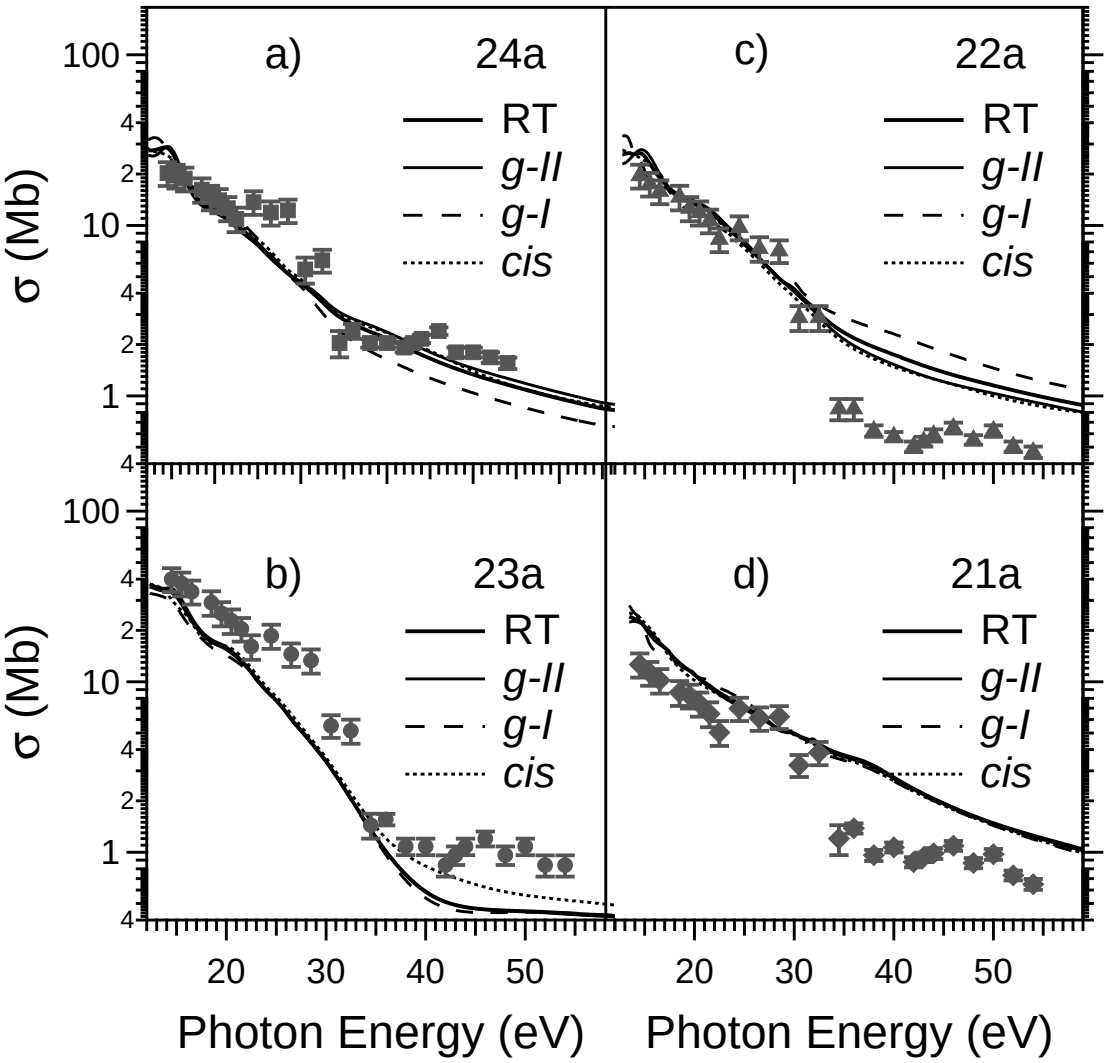

Figure 7.8: Experimental relative photoionization cross sections (markers) and RT rotamers Boltzmann average photoionization cross section calculated at the TD-DFT level(curve RT, solid thick line), for the four outermost valence ionizations, 24a - 21a, as a function of photon energy.

this latter figure the relative intensities pattern becomes dramatically different at high photon energies, where the second band (23a) is the weaker band of the group while the fourth band (21a) exhibits the largest relative increase with respect to the low energy region, becoming as intense as the nearby band (22a) and substantially stronger than the second band (23a). The comparison of the experimental data with the TD-DFT results in fig.7.8 points out that the theoretical calculations are in good agreement with the main experimental findings, providing the correct relative intensities of the first four bands at low photon energies and predicting the large increase in the 24a/23a and 21a/22a intensity ratios on going from the threshold ionization region to the high photon energy region. However, it should be noticed that the strikingly high relative intensity of the 24a band and the clearly lowest relative intensity of the 22a band at high photon energies remain unexplained by the theoretical results, since the 21a and the 23a bands are instead calculated as the most intense and the weakest bands of the group, respectively. This overall good agreement between TD-DFT calculations and experimental cross sections at low photon energy, that is in contrast with the remarkable difference at highest photon energies, is even more evident from the use of a logarithmic scale in fig.7.8. Addressing this issue, which is related to the CM effect, is deferred to the next section. The outer valence photoionization cross sections of epichlorohydrin have also been calculated at DFT level and are shown in fig.7.9. While cross sections are very similar at high photon energies, at lower energies, from threshold to approximately 30 eV, the DFT calculated values are systematically smaller than the TD-DFT ones, due to screening effects important in the presence of the Chlorine atom.

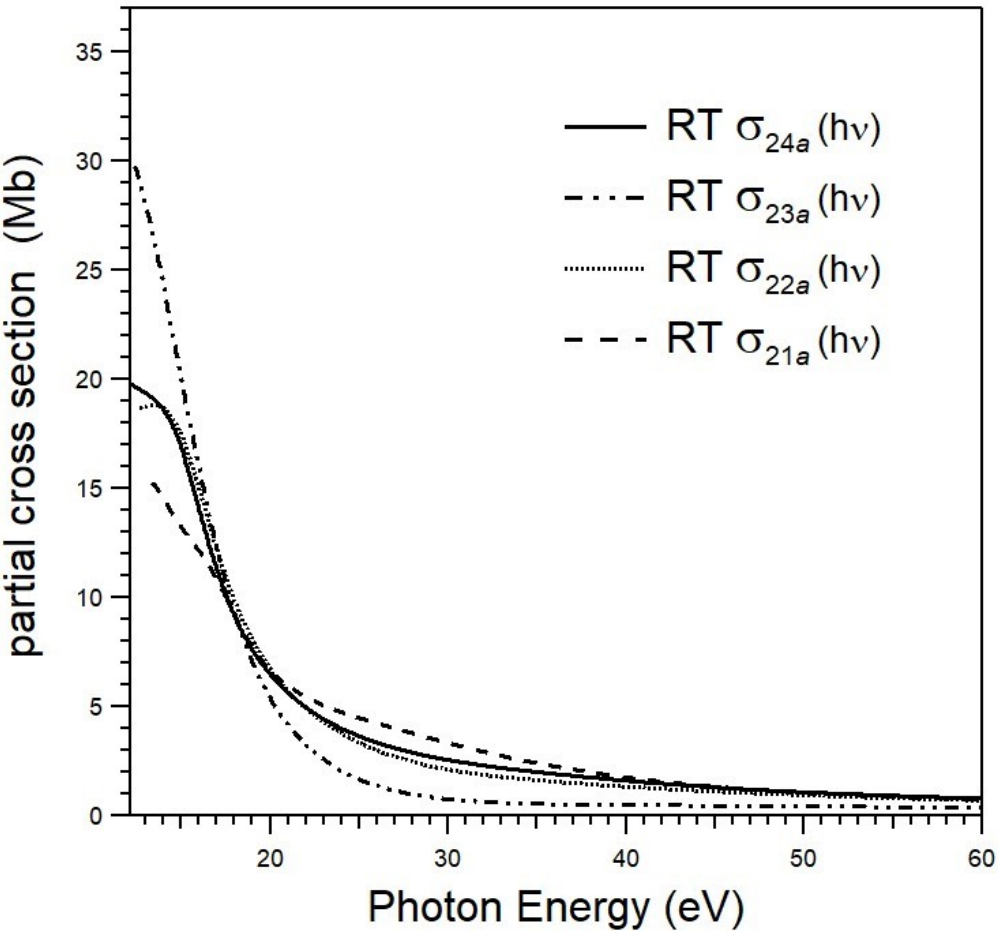

Figure 7.9: Photoionization cross sections calculated at DFT level for the valence outermost ionizations of epichlorohydrin. The reported curves are the Boltzmann avarage of the three stable rotamer cross sections.

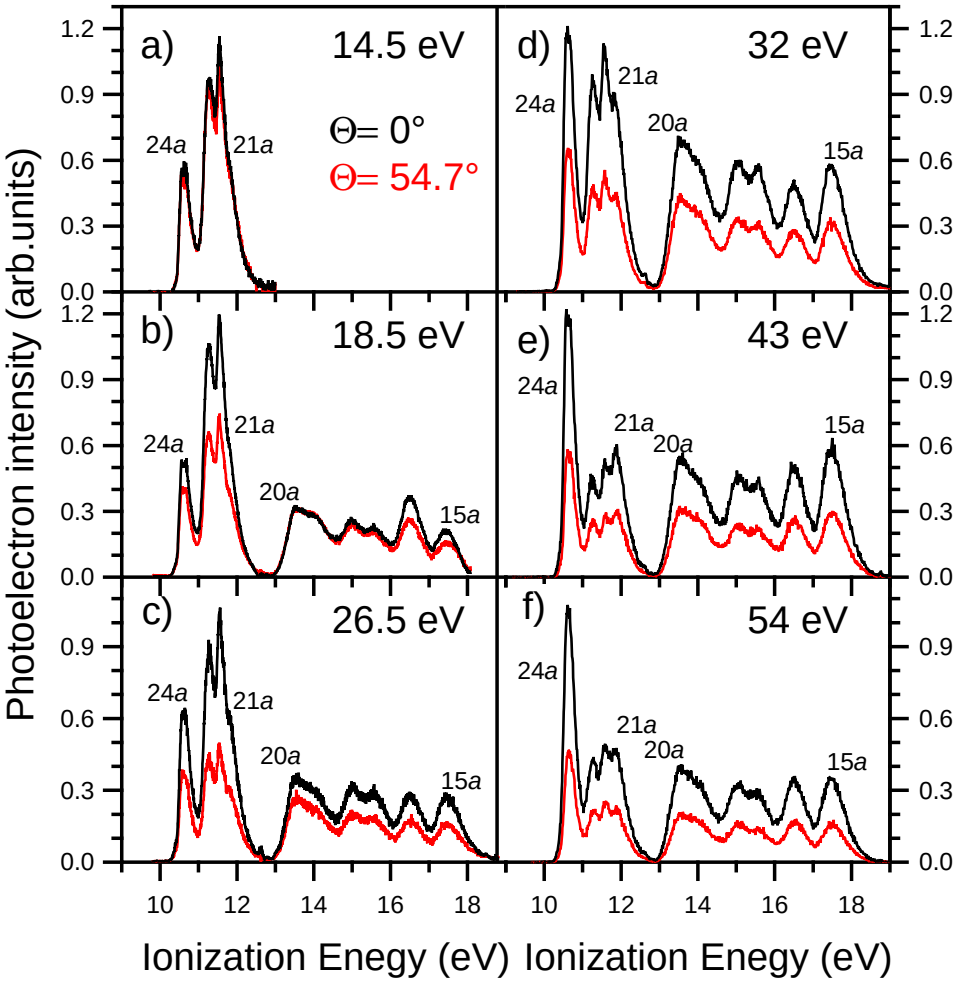

Figure 7.10: Outer valence photoelectron spectra of epichlorohydrin recorded at the magic angle $\theta = 54.7°$ (red curves) and $\theta = 0°$ (black curves), and at different photon energies.

7.1.2 Epichlorohydrin: photoelectron asymmetry parameters

The asymmetry parameters $\beta(h\nu)$ associated with the epichlorohydrin outer valence PE bands have been studied experimentally and theoretically as a function of photon energy. Pairs of PE spectra recorded at $\theta = 0°$ and $\theta = 54.7°$, from which the $\beta(h\nu)$ values have been derived, are reported in fig.7.10 for a representative set of photon energies. The derived experimental $\beta(h\nu)$ values of the outermost valence ionizations 24a-21a are reported in fig.7.11 (panels $a - d$), while the $\beta(h\nu)$ values for the 20a-15a bands are shown in fig.7.12. As in the case of the photoionization cross sections, the asymmetry parameters of the first four ionization bands, 24a-21a, exhibit a much more complex behavior than the 20a-15a ionization bands group. For such reason only for the 24a-21a bands group a more detailed discussion will be presented.

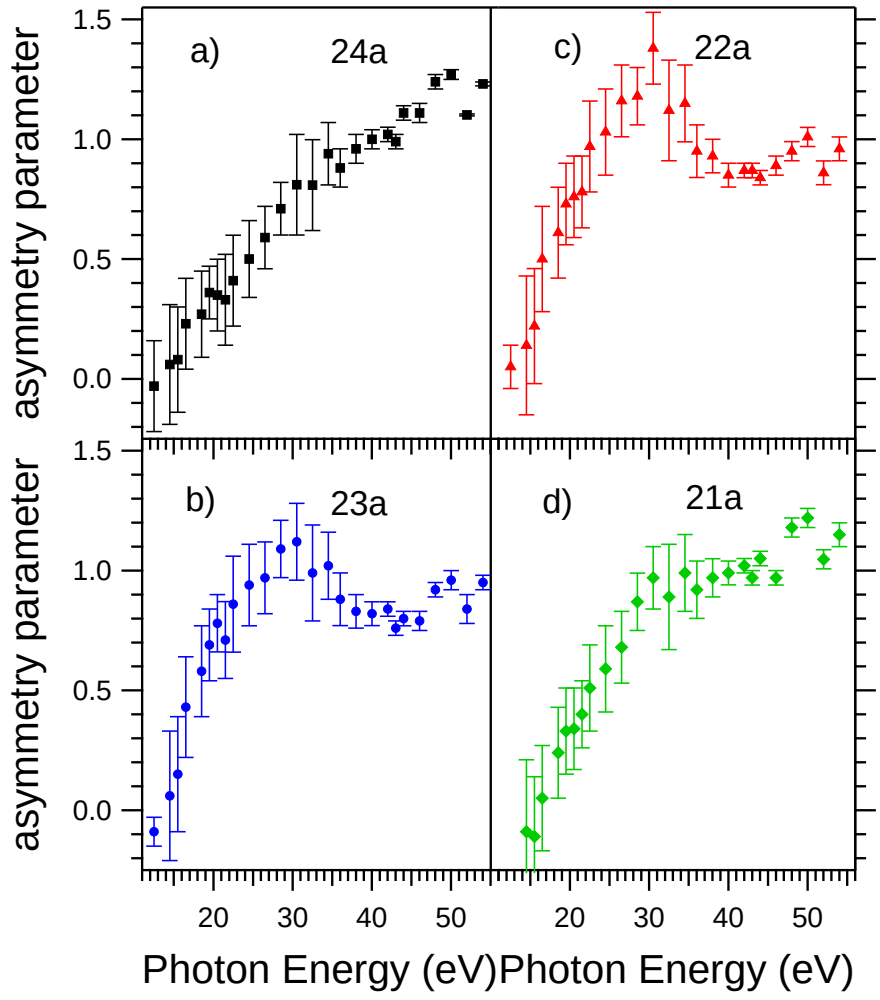

Figure 7.11: Experimental asymmetry parameters for the four outermost valence ionizations, 24a (black) , 23a (blue), 22a (red), 21a (green), as a function of photon energy (panels $a - d$).

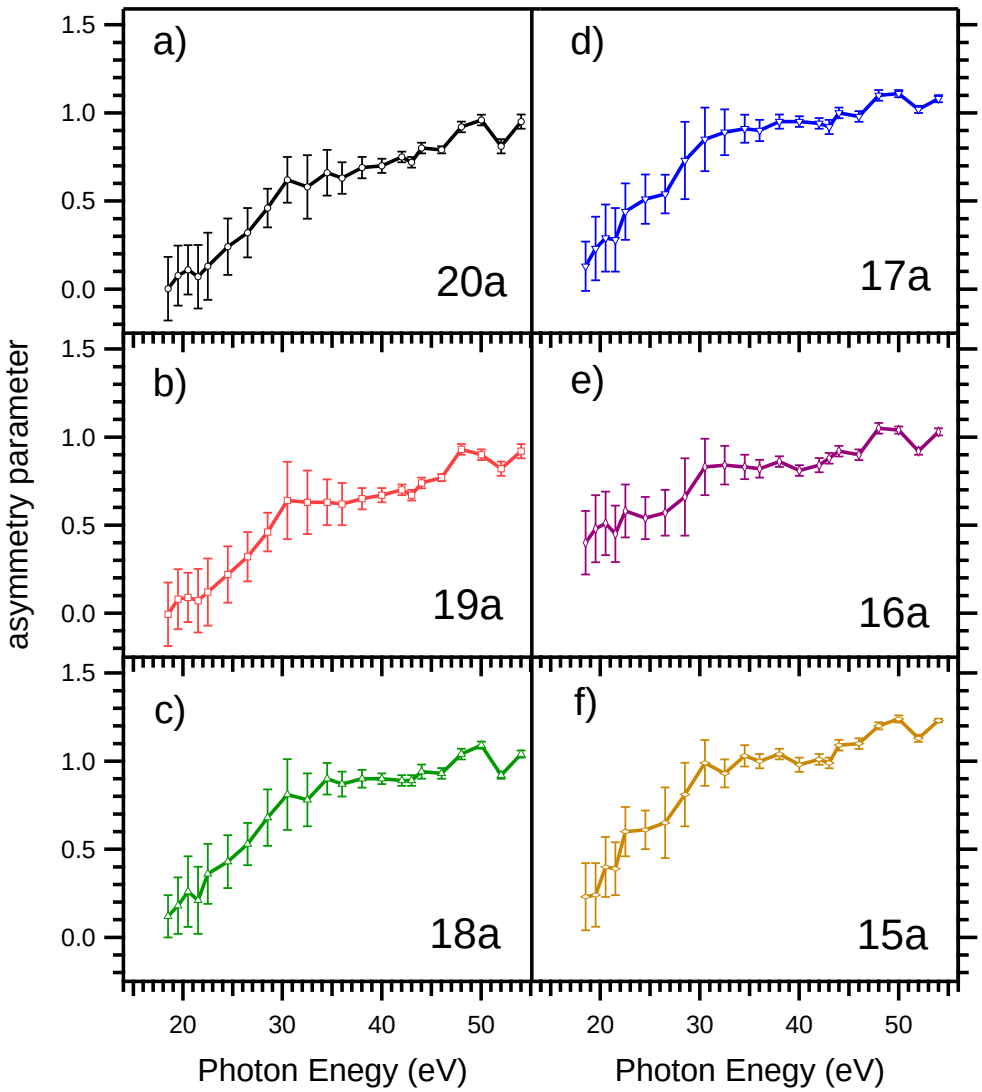

Figure 7.12: Experimental asymmetry parameters for the outermost valence ionizations, 20a (black) , 19a (red), 18a (green), 17a (blue), 16a (purple), 15a (ocher), as a function of photon energy (panels $a - d$).

The dynamical behaviors of the photoelectron asymmetry parameters $\beta(h\nu)$ corresponding to the first four photoelectron bands, as shown in fig.7.11, display clear similarities in the low energy region. All the $\beta(h\nu)$ values are slightly negative or nearly zero at thresholds and rapidly increase with photon energy to reach, at about 30 eV, largely positive values of approximately +1.0. A steeper increase is observed for the 23a and 22a channels with a change in slope around 32 eV, where a maximum is located which corresponds to a $\beta(h\nu)$ values of +1.1 and +1.35 for the 23a and 22a bands respectively. These two curves are the only ones exhibiting an oscillatory behavior. This is characterized by a high energy minimum which is measured for both channels at approximately 43eV (see panels *b* and *c* in fig.7.11). Worth noting is the difference between the two channels in the $\beta(h\nu)$ oscillation amplitude, namely the maximum-to-minimum $\beta(h\nu)$ change, these amplitudes being 0.3 and 0.5 for 23a and 22a, respectively. A change in slope in the $\beta(h\nu)$ curve at 32eV is also observed for the other two photoionization processes 24a and 21a. While the slope change is modest for the 24a channel, the change observed is instead large in the 21a curve, where a clear plateau appears in the 30 – 43 eV photon energy region with $\beta(h\nu) = +1.0$. This $\beta(h\nu)$ parameters behavior for the 24a-21a bands of can be visually seen in fig.7.10. Here, isotropic values, i. e. $\beta(h\nu) \simeq 0$, are measured at 14.5 eV (panel *a*), as the spectra recorded at 0° and 54.7° almost perfectly coincide. On going from 14.4 to 32 eV, from panel a to panel *d*, the relative intensities of these bands in the 54.7° spectrum clearly display a gradual increase which corresponds to the $\beta(h\nu)$ monotonic increase quoted in the panels of fig.7.10 at low energies.

As in the case of the photoionization cross section, in order to understand the experimentally observed asymmetry parameters behavior, theoretical calculations at the TD-DFT level were performed for the three most stable conformers. The results for the 24a-21a states are shown in fig7.13. As stated in section 2.3.1, the asymmetry parameter exhibits higher sensitivity as a dynamical photoionization observable than the photoionization cross section. The presence of the Cooper minimum, in fact, is much more evident in the behavior of the asymmetry parameters as a function of photon energy than in the cross section. This is due to the fact that while the integrated-cross section has no dependence on the relative phase of the final continuum channels, the asymmetry parameter shows a dependence on the cosine of the relative phase shift in the continuum wave functions. Such consideration implies that the behavior of the asymmetry parameter is steadily linked to the nature of the molecular orbitals involved in the photoionization process. It is thus straightforward that in order to have a deeper understanding of the photoelectron angular distribution structure observed in the case of the epichlorohydrin molecule, the discussion should be focused on the nature of the involved electronic states and their atomic orbital composition. We shall first consider the effect of the rotational isomerism on the asymmetry parameters depend-

ing on the calculated molecular orbital composition for each rotamer, and then we compare the theoretical Boltzmann averages to the experimental results. The $\beta(h\nu)$ profiles of the four outermost photoionization channels and their dependency on rotational isomerism can be discussed referring to the ADF-DFT MO composition reported in ref[205], summarized in tab.7.1. The curves of panel d in fig.7.13 show no significant differences with respect to the specific rotamer and no oscillation behavior. This can be explained from the fact that the 21a MO is the only orbital, among the outermost MOs considered, with large ring σ-bonding character and no substantial Cl 3p AO contribution. This is found in all the conformers (see tab.7.1). All curves $a - c$ fig.7.13, at variance with curves d of the same figure, show differences due to the conformer molecular geometry and the associated MOs are characterized by large Cl 3p AO contributions for all the three rotamers. In the case of panel b of fig.7.13, the $\beta(h\nu)$ parameters of the three rotamers exhibit a very similar and striking oscillation behavior with maximum and minimum positions approximately located at 30 eV and 43 eV, respectively. The oscillation amplitude is the largest for the $g - I$ isomer and smallest for the *cis* structure. The involved MO, 23a, has a largely dominant Cl non-bonding character (Cl 3p lone-pair, see tab.7.1), and thus it can be stated that the larger the Cl 3p AO contribution to the MO, the larger the oscillation of the associated asymmetry parameter. Such large $\beta(h\nu)$ oscillations presented in the present thesis and characterized by a minimum located at approximately 43 eV photon energy, have been observed and extensively studied in photoionizations from non-bonding MOs of symmetric simple molecules containing the Cl atom and, in attenuated form (partial Cooper minimum) in ionizations from σ-bonding MOs involving the chlorine atom[66, 67, 69, 70]. In the present case of epichlorohydrin, as well as in the above mentioned molecules, the CM effect is associated with the Cl 3p AOs. The calculated asymmetry parameters of panels a and c in fig.7.13, in the one-particle picture, refer to ionizations from the 24a and 22a MOs, both of mixed O 2p (non-bonding)/Cl 3p (non-bonding) character for all the rotamers. While the 24a MO has a main O lone-pair contribution, 22a MO has instead a Cl 3p lone-pair dominant character, as reported in tab.7.1. The calculated RT Boltzmann average curves of these two latter channels show a barely visible and shallow dip at approximately 37 eV, which is clearer for curve c since it follows a 7-8 eV plateau. It seems that the visibility of the inflection point of the $\beta(h\nu)$ curve depends on the magnitude of the Cl 3p AO contribution to the MO from which the ionization takes place. This would be confirmed, for instance, by observing a clear $\beta(h\nu)$ oscillation only for the $g - I$ curve of panel a, which is ascribable to the significantly larger relative character of Cl 3p AO of $g - I$ than $g - II$ and *cis* for the 24a MO (tab.7.1). Furthermore, the difference between the $\beta(h\nu)$ curves of $g - I$ and $g - II$ isomers in panel c can be explained similarly, since the $g - I$ structure has significantly smaller Cl 3p AO relative contribution to the 22a MO than $g - II$. Still, the simple Cl 3p

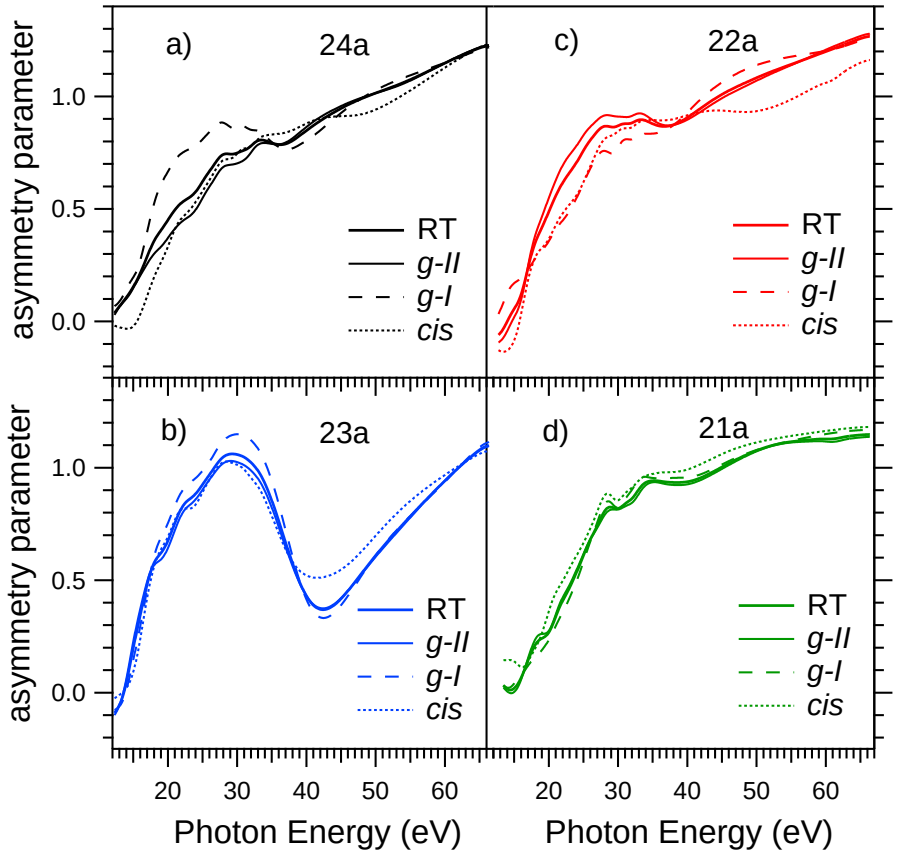

Figure 7.13: Epichlorohydrin asymmetry parameters of the stable rotamers, $g-II$ (solid thin line), $g-I$ (broken line), and *cis* (dotted line), for the outermost valence ionizations (panels $a-d$), calculated at TD-DFT level. The room temperature Boltzmann average (curve RT, solid thick line), is also reported along with the rotamer asymmetry parameters.

percentage contribution to the relevant MOs is a too crude estimate of the magnitude of the asymmetry parameter oscillation, and it does not account for the large difference computed for orbitals 23a and 22a.

Table 7.1: Dominant composition and bonding nature of the 4 outermost DFT Molecular Orbitals (MOs) for the three stable conformers of epichorohydrin, $g-II$, $g-I$, and *cis* (The data reported in the table are taken from ref.[205].)

MO	g-II	g-I	cis	AOs character
24a	56.4%/22.8%	46.6%/32.5%	54.8%/22.9%	O 2p/Cl 3p non bonding (mixed)
23a	80.7%	85.4%	74.4%	Cl 3p non bonding
22a	18.8%/68.2%	28.6%/53.7%	17.7%/66.7%	O 2p/Cl 3p non bonding (mixed)
21a	78%	71%	74%	C-C-O σ-bonding (ring)

The RT Boltzmann average $\beta(h\nu)$ curves shown in fig.7.13 are also reported in fig. 7.14 together with the experimental data for comparison.

In the case of the ionization from the 23a channel (blue curves in 7.14), which is the only MO of Cl 3p lone-pair character, a large amplitude oscillation is calculated in the CM region. The experimental data and the theoretical curve are in excellent quantitative agreement in the rising part of the curve up to the maximum at 30 eV (panel *b* of 7.14). The minimum observed in the experiment at 43 eV is correctly predicted by the TD-DFT calculation, but the magnitude of the calculated oscillation is overestimated by a factor of two. For the ionization from the 22a MO (red curves in 7.14), the comparison between the experiment and theory points out a remarkable difference, since the oscillation experimentally observed in the CM region is the largest among the photoionization processes of epichlorohydrin, and larger than that observed for the 23a MO channel. This experimental finding cannot be explained basing on the calculated MO characters since 22a is described as a Cl lone-pair/O lone-pair mixed orbital and therefore with substantially smaller Cl 3p AO contribution than 23a MO. As far as the ionizations associated with the 24a and 21a MOs are concerned, the trends exhibited by the experimental data, as mentioned above, show a disagreement. In panel *a* of 7.14) the experimental data show a smooth monotonic increase, whilst in panel *d* the asymmetry parameter increase is more rapid and undergoes a change in slope at 30 eV with a plateau, before rising again at higher energies. The calculated RT average curves for the two channels are similar, exhibiting both a change in slope. The agreement between experiment and theory is excellent in the whole investigated energy range for the 21a MO (green curves in fig.7.14), while for 24a (black curves in fig.7.14)the experimental values are systematically larger than the calculated ones in the high photon energy part of the range, since the experimental values increase do not display a slope change. The experimental $\beta(h\nu)$ behavior, on the basis of the calculated O lone-pair/Cl lone-pair mixed character of the 24a MO, seems not to be in agreement with the theoretical predictions, because of the substantial Cl 3p AO contribution to this orbital, which would suggest observing an effect in the CM region.

A key aspect of the present work is that the CM photoionization dynamics has been investigated for the first time in a chiral molecule, where no symmetry constraints prevent orbital mixing upon ionization. To understand how the intrinsic asymmetry possessed by chiral molecules affects their photoionization dynamics, one may refer to the work done by Von Niessen et al. on the ionization spectra of low-symmetrical unsaturated oxo-compounds[206]. Here the authors point out how a change of ordering between hole-states of equal symmetry is not forbidden, and that this phenomenon is indeed expected in particular for large molecules of low symmetry, as in the case of chiral molecules, where orbitals of equal symmetry will be energetically close. Such reorganization and correlation effects modify the original hole configuration towards a more complicated wavefunction with strong mixing of adjacent orbitals of equal symmetry. Such phenomenon is a clear evidence of the breakdown of the

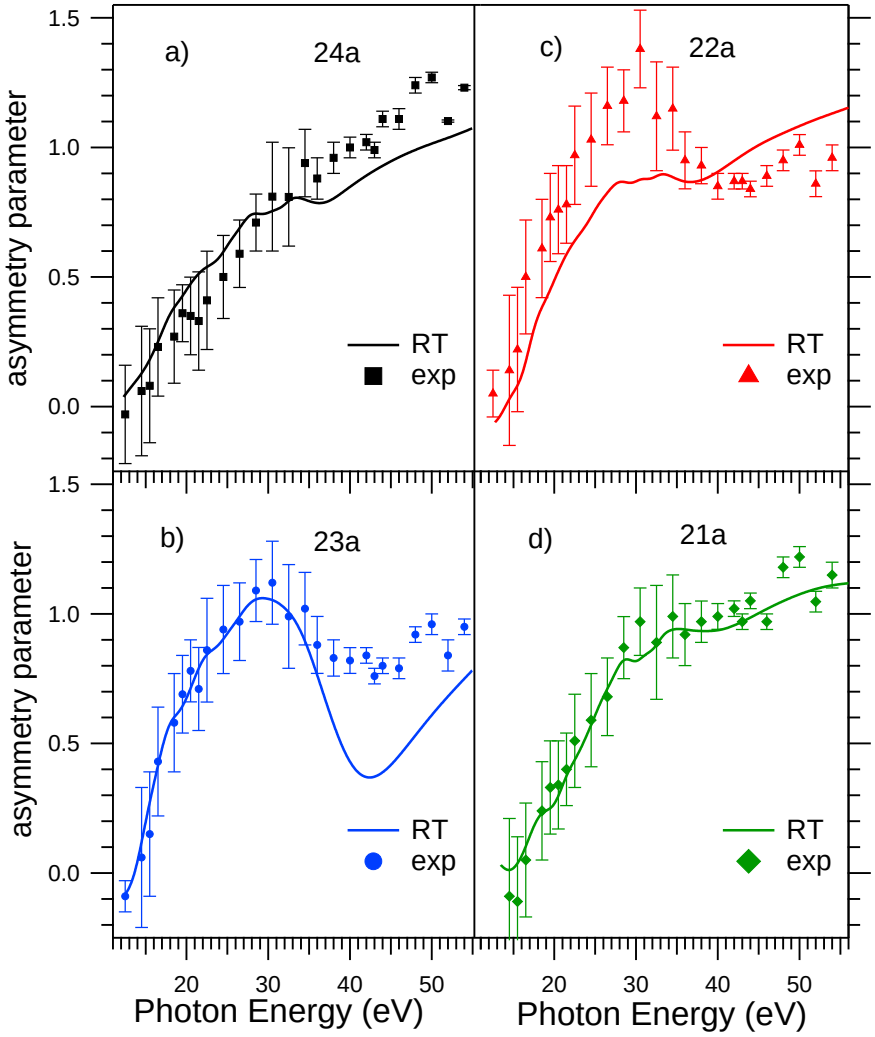

Figure 7.14: Experimental asymmetry parameters for the four outermost valence ionizations, 24a (black) , 23a (blue), 22a (red), 21a (green), as a function of photon energy (panels a-d). Asymmetry parameters calculated at TD-DFT level for the four photoionization channels are also reported as Boltzmann average (RT, solid line) of the calculated asymmetry parameters of the three stable $g-II$, $g-I$, and *cis* rotamers, to allow a direct comparison between experiment and theory.

independent-particle model on which the Koopmans' theorem is based. The hole-mixing for main ionic states is a quite uncommon behavior, especially in the outer valence ionization region. In fact, generally an ionic main state is well approximated by a hole configuration in which the hole is associated with the respective HF orbital of the neutral ground state, because for HF hole-configurations the direct coupling matrix-elements vanish. Mixing different HF hole-configurations occurs only in second and higher order of perturbation theory and is mediated by 2-hole-l-particle (2h1p) excitations and higher excited configurations. However, for energetically close orbitals even a small coupling to 2hlp-configurations can induce an elective hole-mixing for the ionic states. Following the discussion of Von Niessen et al., the perturbation expansion for the ionic wavefunction $|\Phi_p^{N-1}\rangle$ associated with a specific orbital p is given by:

$$\Phi_p^{N-1\rangle} = |p^{-1}\rangle + \sum_{q \neq p} \alpha_{pq} |q^{-1}\rangle + \text{higher excited configurations} \quad (7.1.2.1)$$

In second order the coefficient α_{pq}, of the admixture of another hole configuration $|q^{-1}\rangle$ is given as

$$\alpha_{pq} = \frac{1}{\varepsilon_p - \varepsilon_q} \sum_{jkl} \frac{V_{qj[kl]} V_{pj[kl]}}{\varepsilon_k + \varepsilon_l - \varepsilon_j - \varepsilon_p} \quad (7.1.2.2)$$

In eq.(7.1.2.2) the summation runs over unoccupied one-particle states j and occupied one-particle states k, l. The anti-symmetrized Coulomb matrix element $V_{qj[kl]}$ represents the coupling matrix element between the hole configuration $|q^{-1}\rangle$ and the 2hlp-configuration $|jk^{-1}l^{-1}\rangle$. The energy denominators $\varepsilon_k + \varepsilon_l - \varepsilon_j - \varepsilon_p$ represent the (zero-order) energy differences of the hole configuration $|p^{-1}\rangle$ and the 2hlp-configurations $|jk^{-1}l^{-1}\rangle$. It can be seen how in eq.(7.1.2.2) a small energy separation $\varepsilon_p - \varepsilon_q$ may cause a large mixing coefficient α_{pq} for the considered orbitals p and q. Generally in the case of outer valence states, the orbital energies εp are usually well separated from the 2hlp-energies $\varepsilon_k + \varepsilon_l - \varepsilon_j$ so that these denominators are not small enough to give rise to significant mixing coefficient α_{pq}. However, a significant contribution may arise when there are one or several configurations $|jk^{-1}l^{-1}\rangle$ which simultaneously have large coupling matrix elements to both hole configurations $|q^{-1}\rangle$ and $|p^{-1}\rangle$. Following the arguments presented by Von Niessen et al., it is clear that for large molecules of low symmetries hole-mixing effects should be quite common. As a consequence, for instance, in photoionization of the epichlorohydrin molecule, the first four valence PE bands are associated to four Final Ionic States with strong Configuration Interaction (FISCI) mixing[204, 205]. These CI wavefunctions, for each ionic state, contain more than one dominant single-hole (1h) determinant. Employing the single HF determinant for the ground state, the weight of the 1h determinants in the final wave-

functions is exactly given by the spectral strength, R_k. The calculated spectral strengths of the epichlorohydrin molecule at 2h-1p CI level of theory are reported in Table III of ref[205] and, for convenience, are summarized here in tab.7.2. The value of R_{24a}, for instance, is the weight in the CI wave-function of the determinant referring to the configuration with the electron hole in the 24a MO. This single-hole determinant represents, in the one-electron picture, the final cation state formed by electron removal from the 24a MO. The information gathered about the single-hole configuration mixing of the epichlorohydrin ionic state wave-functions associated with the first four PE bands can allow a deeper understanding of the dynamical behavior of the corresponding experimental asymmetry parameters. Each of the four final states 24a-21a is actually characterized by two dominant single-hole configurations, as evident in tab.7.2, where the spectral strength values R_{24a}, R_{23a}, R_{22a}, and R_{21a}, are reported for the lowest lying ionic states, indicated as roots 1-4, of the three conformers of epichlorohydrin. The $\beta(h\nu)$ oscillation in the Cl 3p CM region is solely observed in two channels, namely it is displayed by the experimental data in panels b and c of fig.7.14 associated with the second and third PE bands, respectively. For the second band, the ionic state CI wave-function (root 2 in tab.7.2) of the most abundant conformer $g-II$ (RT Boltzmann weight of 0.679) has two dominant parts whose weights are R_{24a}= 0.416 (nO/nCl) and R_{22a}= 0.385 (nCl/nO). Both 24a and 22a states have O 2p (non-bonding)/Cl 3p (non-bonding) mixed character, with larger contributions from O 2p AO for 24a MO and Cl 3p AO for 22a MO (see tab.7.1). For the second most abundant conformer $g-I$, which has a RT Boltzmann weight of 0.276, the CI wave-function is similar but with slightly larger R_{24a} character. Owing to the FISCI, the asymmetry parameter of this channel is expected to exhibit only the so-called "partial" CM [tab.7.2] behavior, since the two dominant configurations have a single-hole in a MO of mixed character with partial Cl 3p AO contribution. This is actually observed in the experiment and explains why the large amplitude oscillation predicted by the TD-DFT calculation, typical of ionization from pure Cl 3p lone-pair character MO, is not observed. In the case of the third ionic state, the CI wave-functions (root 3 in Tab.7.2) have single-hole configurations of R_{23a}= 0.583 (nCl) and R_{21a}= 0.283 (σ-ring) for the $g-II$ conformer, and R_{23a}= 0.863 (nCl) for the $g-I$ conformer. Because of the described characters of 23a and 21a MOs the asymmetry parameter of this channel is expected to exhibit a partial CM effect of significantly higher intensity than the previous one, due to the relatively more important role played by the Cl 3p AO through the Cl lone-pair 23a MO. The observed $\beta(h\nu)$ oscillation amplitude of this channel, as already emphasized, is found to be twice as large as that of the second PE band (see data in panels c and b in Fig.7.14). As for the fourth PE band, the CI wave-functions (root 4 in Tab.7.2) have the following dominant single-hole configurations; R_{22a}= 0.479 (nCl/nO) and R_{24a}= 0.425 (nO/nCl) for $g-II$, and R_{21a}= 0.430 (ring), R_{24a}= 0.253 (nO/nCl), and R_{22a}= 0.223

(nCl/nO) for $g-I$. According to the strongly mixed nCl/nO character of the involved 22a and 24a MOs in the single-hole dominant configurations and the dominant R_{21a} term in the CI wave-function of $g-I$, the measured $\beta(h\nu)$ behavior of the RT sample is expected to still show some partial CM effect, but of a lesser extent than for the previous cases, and is indeed confirmed by the change in slope and the plateau in the CM region of the data of panel d in fig.7.13. In the case of the first PE band, the expected global effect on the measured asymmetry parameter behavior is a very small, or even absent, CM effect. This is ascribed to the large value of R_{21a} in both the CI wave-functions of $g-II$ and $g-I$, namely R_{21a}= 0.485 (σ-ring) and R_{23a}= 0.313 (nCl) for $g-II$, and R_{21a}= 0.415 (σ-ring), R_{22a}= 0.282 (nCl/nO), and R_{2a}= 0.137 (nO/nCl) for $g-I$. The electron hole in this dominant configuration is made in the 21a MO which has a σ-C-C-O(ring) character with negligible Cl 3p AO contribution. The experimental asymmetry parameter in panel a of fig.7.14, in fact, is the only curve not showing CM effects among the photoionization channels (curves $a-d$).
In summary, the different dynamical behaviors of the asymmetry parameters of the first four PE bands of epichlorohydrin, as well as the difference between the $\beta(h\nu)$ experimental findings and the TD-DFT theoretical predictions, could be fully discussed and explained in terms of FISCI effects, related to the breakdown of the Koopmans' theorem due to electron correlation effects.
The group of six PE bands in the range 14.7–18.1 eV, namely the 20a-15a states, corresponds to the ionization of molecular orbitals that are largely delocalized over the whole molecular skeleton, with practically no Cl 3p AO contribution, and thus no CM effects are expected. This is confirmed by the monotonic increase, as a function of photon energy, of the experimental $\beta(h\nu)$ parameters for all the six channels, as shown in fig.7.12.

In order to confirm our interpretation of the observed asymmetry parameter behaviors, we have computed Dyson orbitals from CASSCF wavefunctions for the relevant individual states, and computed cross sections coupling them to DFT continuum states[207]. $\beta(h\nu)$ parameters for the four outermost PE bands evaluated at the pure DFT, HF and CASSCF levels are compared in fig.7.15. As expected, results employing HF or CASSCF Dyson orbitals are very different: HF shows prominent cooper minimum $\beta(h\nu)$ oscillations only for the first and second PE bands. DFT in general is closer to CASSCF, but the experimental oscillation for the third PE band is barely visible in the calculated curve (panel c), while it is considerable in CASSCF calculation, which is in agreement with the experimental observation. Due to the relatively limited basis set and CASSCF orbital space employed, and the lack of electron response in the final continuum (treated at the DFT level), the agreement is not quantitatively accurate, but the orbital mixing due to correlation effects is definitively demonstrated. The treatment of the continuum wavefunction at the TDDFT

Table 7.2: Dominant spectral strengths R_k for the three conformers of epichlorohydrin obtained at 2h-1p CI level of theory. Data taken from table III of ref.[205].).

Conformer	Root	R_{tot}	R_{24a}	R_{23a}	R_{22a}	R_{21a}	R_i
$g-II$	1	0.893	0.039	0.313	0.037	0.485	
	2	0.917	0.416	0.001	0.385	0.105	
	3	0.921	0.040	0.583	0.001	0.283	
	4	0.923	0.425	0.007	0.479	0.003	
	5	0.911					$R_{20a} = 0.804$
	6	0.910					$R_{19a} = 0.892$
	7	0.911					$R_{18a} = 0.801$
	8	0.896					$R_{17a} = 0.808$
	9	0.888					$R_{16a} = 0.804$
	10	0.875					$R_{15a} = 0.841$
$g-I$	1	0.893	0.137	0.042	0.282	0.415	
	2	0.918	0.526	0.014	0.352	0.014	
	3	0.922	0.001	0.863	0.034	0.024	
	4	0.918	0.253	0.001	0.223	0.430	
	5	0.906					$R_{20a} = 0.543$, $R_{19a} = 0.281$
	6	0.911					$R_{20a} = 0.342$, $R_{19a} = 0.533$
	7	0.911					$R_{18a} = 0.794$
	8	0.897					$R_{17a} = 0.870$
	9	0.887					$R_{16a} = 0.845$
	10	0.873					$R_{15a} = 0.842$
cis	1	0.895	0.220	0.241	0.122	0.293	
	2	0.919	0.375	0.167	0.319	0.046	
	3	0.923	0.023	0.452	0.436	0.002	
	4	0.920	0.300	0.048	0.021	0.545	
	5	0.907					$R_{20a} = 0.266$, $R_{19a} = 0.609$
	6	0.917					$R_{20a} = 0.3635$, $R_{19a} = 0.270$
	7	0.911					$R_{18a} = 0.860$
	8	0.892					$R_{17a} = 0.572$
	9	0.894					$R_{16a} = 0.610$
	10	0.870					$R_{15a} = 0.844$

level could lead to a more complete description of final state configuration interaction effects. Preliminary results on the calculated asymmetry parameters at the Dyson-TDDFT level are reported in fig.7.16, together with the Dyson-DFT and DFT calculation. Experimental data are also reported for comparison. The Dyson-TDDFT calculations, where the final continuum wave function is treated at the TDDFT level, exhibits a nice quantitative agreement in the case of the 24a and 21a ionizations (panels *a* and *d*). The asymmetry parameter oscillations are predicted for both 22a and 23a bands, and the Cooper minimum position is predicted around 43 eV, in agreement with the experimental evidence. The $\beta(h\nu)$ oscillation amplitude is still overestimated in both cases, even if a significant change in the relative oscillation amplitude is observed for the 22a band with respect to the CASSCF theoretical calculations. Similar results are obtained for the partial photoionization cross sections, as shown in fig.7.17. These results stimulates further theoretical analysis and highlights the complexity of the theoretical treatment of the photoionization process in case of chiral molecules.

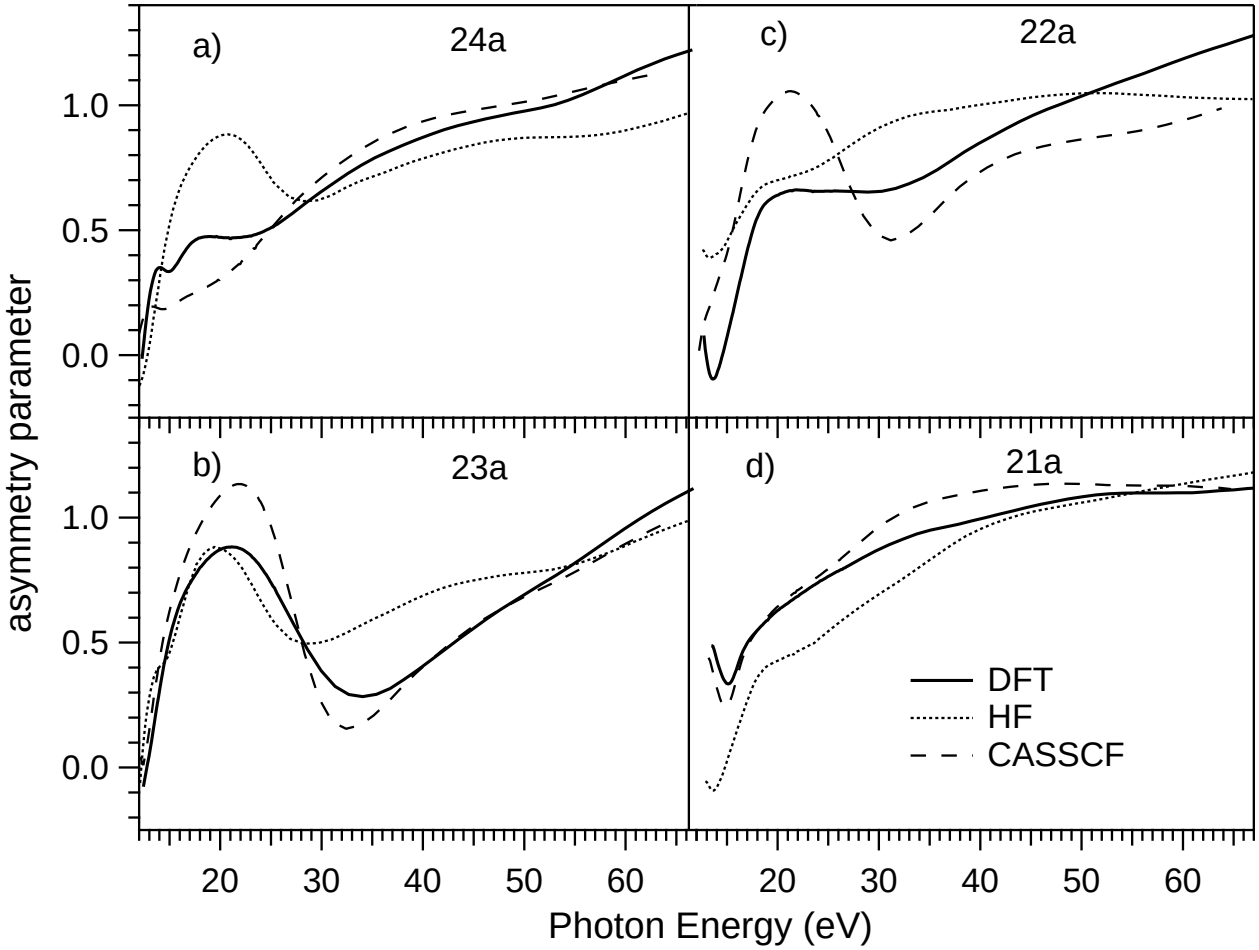

Figure 7.15: Epichlorohydrin asymmetry parameter for the four outermost bands calculated at the DFT (dashed line), HF (dotted line) and CASSCF (solid line) as as Boltzmann average (RT, solid line) of the calculated asymmetry parameters of the three stable $g-II$, $g-I$, and *cis* rotamers.

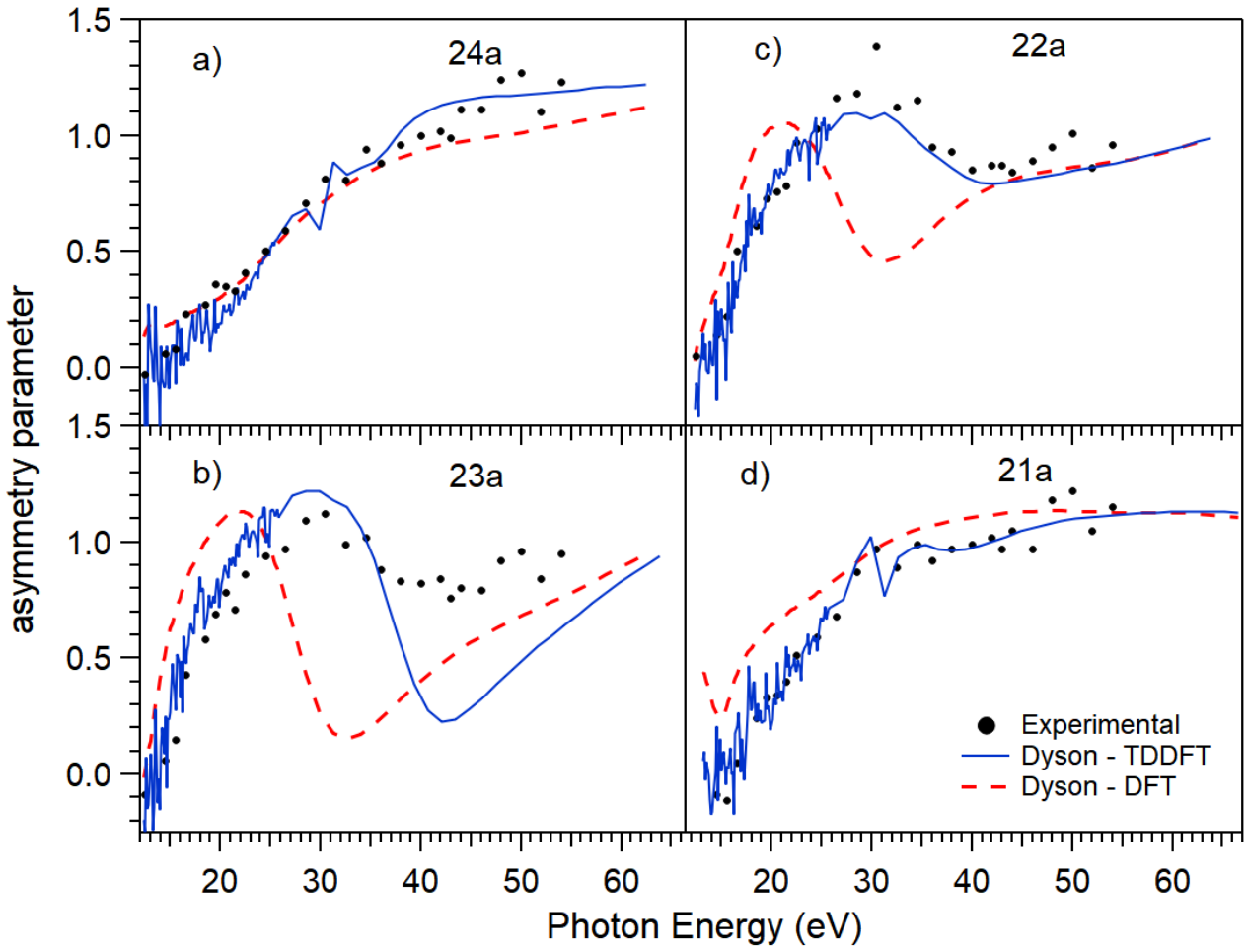

Figure 7.16: Epichlorohydrin asymmetry parameter for the four outermost valence PE bands calculated at the Dyson-TDDFT (blue solid line) and Dyson-DFT (red dashed line) level as Boltzmann average of the calculated asymmetry parameters of the three stable $g-II$, $g-I$, and *cis* rotamers. The experimental values are also reported for comparison (black dots).

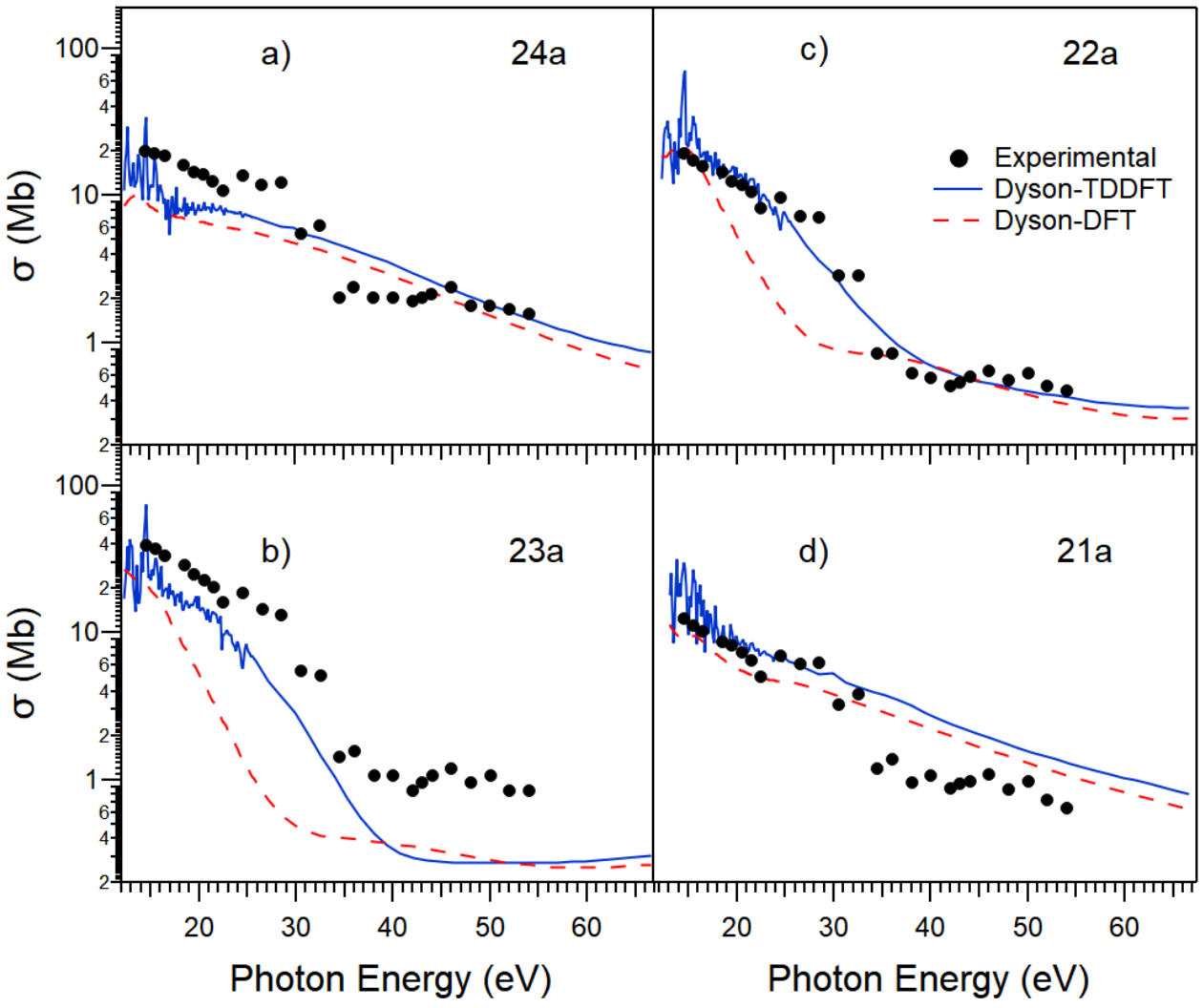

Figure 7.17: Epichlorohydrin partial photoionization cross section for the four outermost valence PE bands calculated at the Dyson-TDDFT (blue solid line) and Dyson-DFT (red dashed line) level as Boltzmann average of the calculated asymmetry parameters of the three stable $g-II$, $g-I$, and *cis* rotamers. The experimental values are also reported for comparison (black dots).

7.1.3 Epichlorohydrin: preliminary results on the photoelectron dichroism parameter

PECD experiments were performed on the epichlorohydrin molecule, and the dichroism pramaters, $D(h\nu)$, associated with the outer valence PE bands observed in the 10 - 19 eV IE range, have been measured as a function of photon energy with circularly polarized synchrotron radiation. For this purpose, epichlorohydrin PE spectra measured at the magic angle ($\theta = 54.7°$) with respect to the radiation propagation axis have been recorded at selected photon energies in the 14 - 30 eV range. At each photon energy and fixed angle (the magic angle) PE spectra were recorded for the two different helicities of the CP radiation and the dichroism parameters were obtained according to eq.(2.5.0.1). The spectra were recorded simultaneously by switching the photon helicity for each scanned kinetic energy point, in order to minimize effects due to changes in photon flux, sample density or other possible effects affecting the spectra intensities. The experimental spectral data were acquired in two separate channels according to the specific radiation helicity. The experiments were performed at the CiPo beamline by the use of the VG-220i end station. The data, collected during the writing of the present thesis, are under analysis, and thus only some preliminary results can be reported. In fig.7.18 the theoretical dichroism parameter of the stable rotamers, calculated at the DFT level for the first PE band, are shown as a function of photoelectron kinetic energy. It is evident the much higher sensitivity of the dichroism parameter to the molecular structure with respect to the asymmetry parameter, as mentioned in Chapter 2, section 5; even small changes in the internal rotation (different conformers) have a significant effect on the dynamical behavior of the photoionization observable. The theoretical room temperature Boltzmann average dichroism parameter (curve RT, solid thick line in fig.7.18) displays a strong oscillation in the 0-10 eV kinetic energy region with a minimum at about 5 eV. The surprisingly large (in particular if compared with the effects observed in absorption dichroism spectroscopy) dichroism effect of ∼10% expected by the theoretical calculations highlights how powerful tool PECD spectroscopy is in the study of chiro-optical properties of gas-phase chiral systems. The dichroic effect is expected to be dumped as a kinetic energy greater than 20 eV is reached. Figure 7.19 shows the experimental dichroism parameter measured for the first PE band, together with the same parameter calculated at DFT level for the same photoionization band reported as Boltzmann average (RT, solid line) of the three stable conformers. In order to match the experimental data a kinetic energy shift of 3 eV was applied to the calculated dichroism parameter. A good agreement was found between the experimental data and the theoretical curve. The theoretically predicted dichroic effect of ∼10% seems to be confirmed by the experimental observations. These preliminary results stimulate a more complete analysis of the experimental and theoretical data.

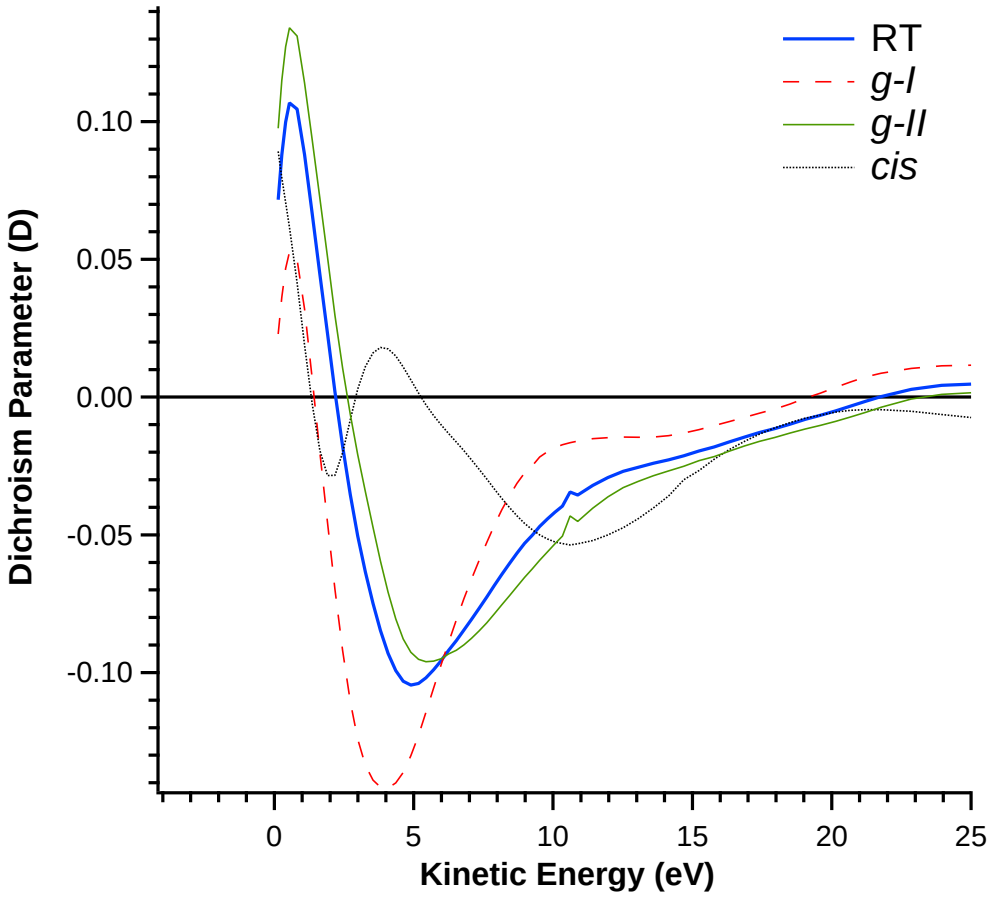

Figure 7.18: Epichlorohydrin dichroism parameters of the stable rotamers, $g-II$ (solid thin line), $g-I$ (broken line), and *cis* (dotted line), for 24a state, calculated at DFT level. The room temperature Boltzmann average (curve RT, solid thick line), is also reported.

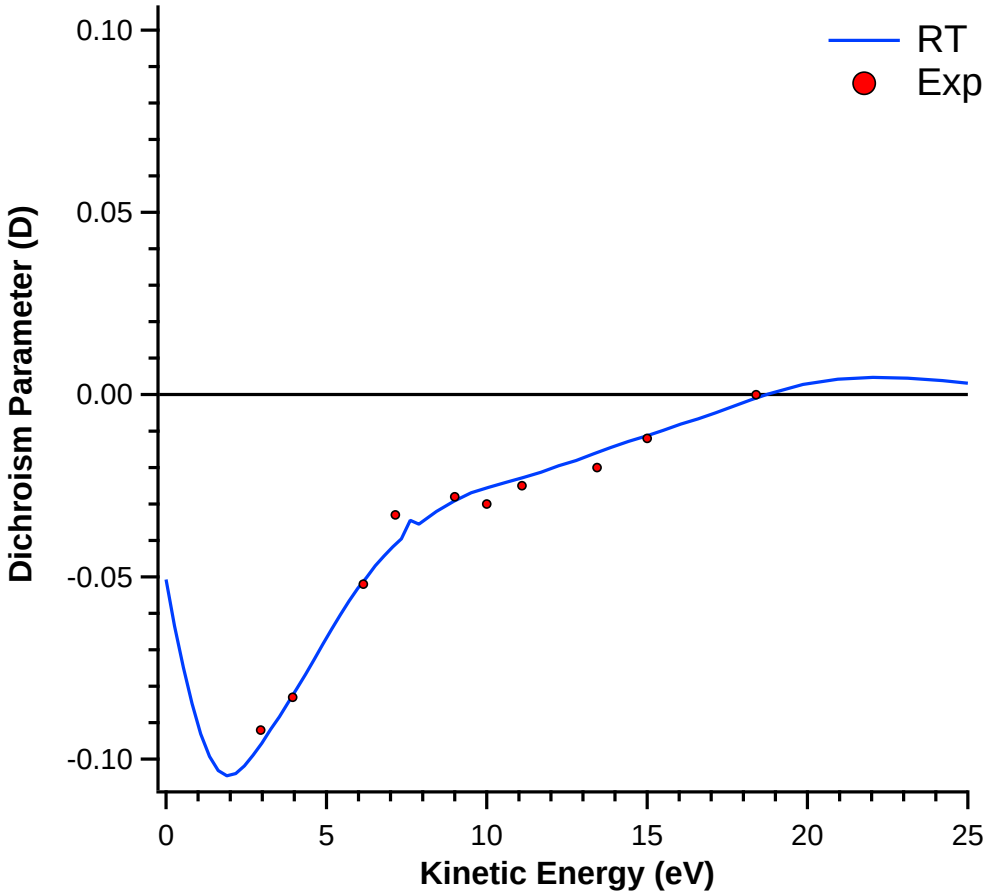

Figure 7.19: Experimental dichroism parameter (markers) measured for the first PE band, together with the same parameter calculated at DFT level for the same photoionization band reported as Boltzmann average (RT, solid line) of the three stable conformers. In order to match the experimental data a kinetic energy shift of 3 eV was applied to the calculated dichroism parameter.

7.2 Development of the new two-dimensional position sensitive electron detector of the ARPES-TPES end station

Part of the work performed in the Ph.D. project was focused on the upgrade of the electron detector of the ARPES-TPES end station. The study of gas phase chiral molecules, which are very often available in very low amounts as enantiopure species (this is the case when the enantiomer is not commercially available and need to be synthesized in laboratory), requires very sensitive, fast and high performance electron detectors, in order to obtain high statistics spectra with the minimum amount of substance. Moreover, a detector capable of recording a photoelectron spectrum in a short time is highly desired when measuring observables that are very sensitive to changes in the experimental conditions, such as photoionization cross section or the asymmetry parameters. For these reasons, the single channeltron detector was replaced by a two-dimensional cross delay line anode detector. Part of the Ph.D. project involved the installation and characterization of the new detector, as well as the upgrade of the acquisition software.

7.2.1 General description of the ARPES-TPES End Station

The experimental spectra of the OsO_4 and epichlorohydrin molecules were recorded with the ARPES-TPES end station. The ARPES-TPES spectrometer, devoted to photoionization experiments on reactive and short lived species, was described in detail elsewhere[208, 209, 210, 211]. Briefly, in the spectrometer the samples investigated in this work were introduced in the ionization region by a 1 mm diameter copper needle. The ionization region (region B in fig.7.20) is surrounded by two differentially pumped boxes equipped with two 400 l s^{-1} turbomolecular pumps(Leybold Turbovac 361C) and N_2 purging valves in order to reduce bearing contamination by reactive species. The vacuum in the chamber housing the two differential pumped boxes, the light guide from the monochromator, and the analyzer lens system (region A in fig.7.20) is provided by a 1000 l s^{-1} turbomolecular pump (Leybold Turbovac 1000). The analyzer section (region C in fig.7.20) is pumped by a 600 l s^{-1} turbomolecular pump (Leybold Turbovac 600). The spectrometer is equipped with a 180° electron energy hemispherical analyzer with a mean radius of 100 mm and a sector gap of 40 mm. This type of analyzer, with a well-defined focal plane, is suitable for housing a micro-channel plate based detector. The analyzer operates in a constant-pass-energy mode and is equipped with a three-element cylindrical lens positioned between the ionization region and the analyzer. The lens has an entrance and an exit slits, which are

typically rectangular slits of 1.2mm×12 mm: such long longitudinal dimension of the slit along the photon beam axis allows to maximize the photoelectron signal. The exit slit of the lens coincides with the entrance slit of the analyzer. Magnetic shielding of the ionization region, lens system, analyzer and detector is achieved by using two continuous layers of 1-mm-thick μ-metal. The synchrotron radiation enters the ionization region from a 6 mm diameter light guide mounted perpendicularly with respect to the axis of the electron input lens; a photon flux monitoring system is placed on the opposite side after the ionization region. The electron analyzer sector can rotate with an angular excursion between $\theta = 0°$ and $\theta = 73.5°$. A picture of the ARPES-TPES chamber is shown in fig.7.21

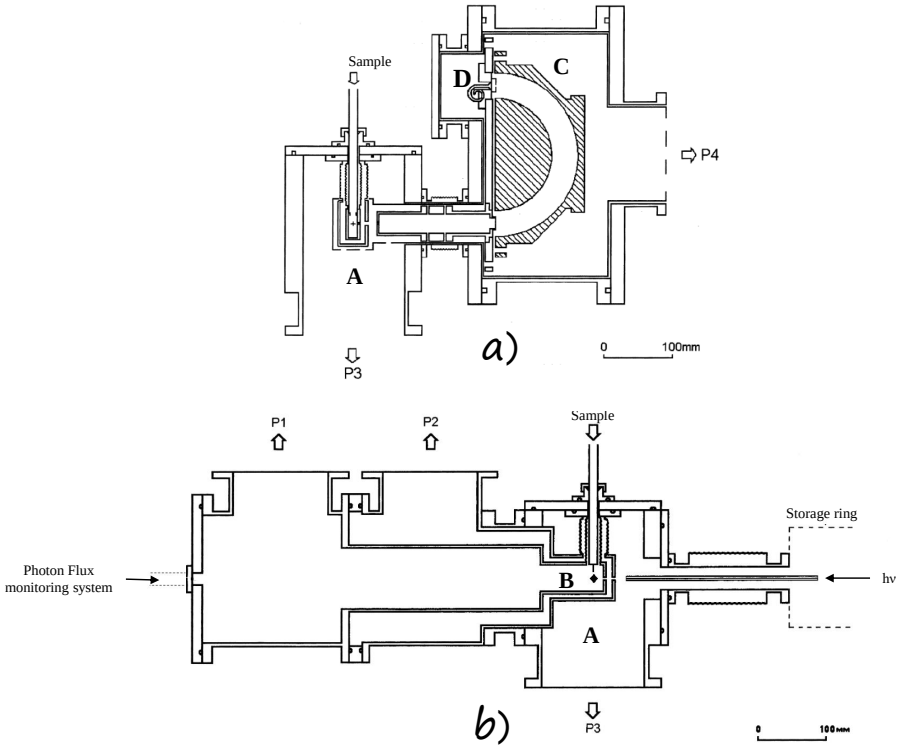

Figure 7.20: *a*) The cross-sectional view of the spectrometer in the direction of the photon beam showing the ionization region and the hemispherical analyzer; *b*) the cross-sectional view of the sample pumping system of the spectrometer.

7.2.2 General description of the implemented 2D detector

The single channel (channeltron) detector (region D in fig.7.20), used in previous experiments[212, 213, 214] was replaced by a two dimensional position sensitive detector, based on the cross delay line technology[215, 216], built in a joint project involving the CNR-IOM institute, "Sapienza"

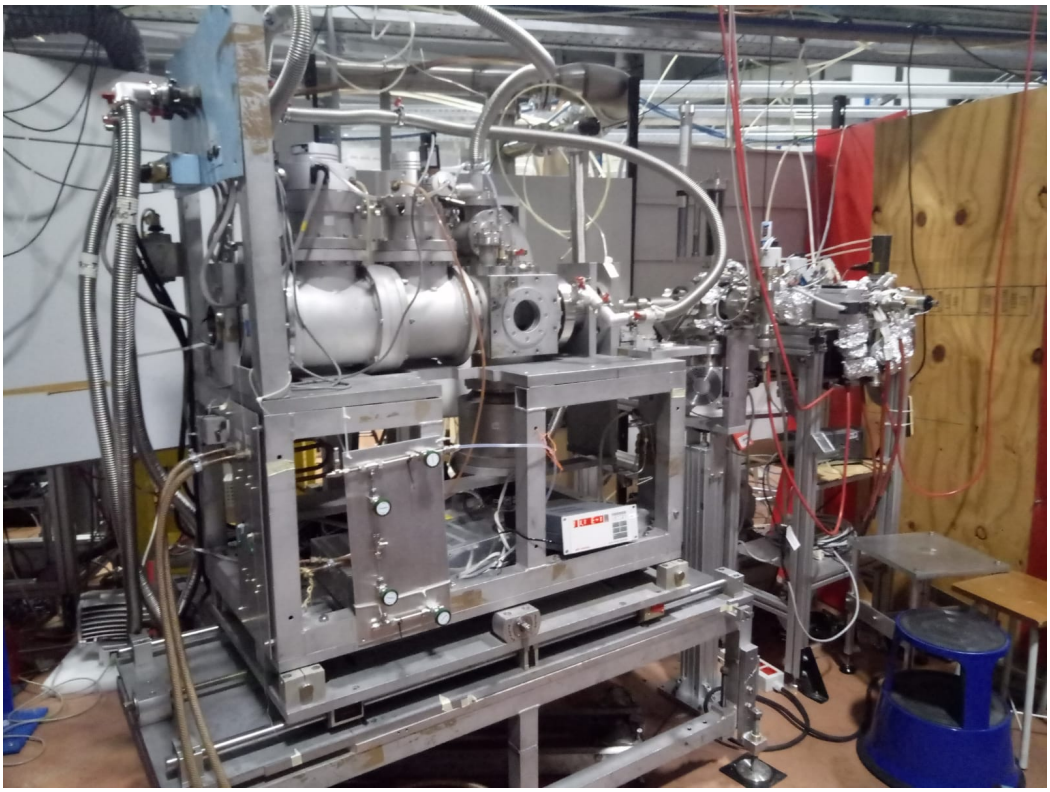

Figure 7.21: The ARPES-TPES end station operating on the Gasphase beamline.

University of Rome, and the Elettra - Sincrotrone Trieste S.C.p.A.. An exploded view of the detector assembly is shown in fig.7.22. The detector consists of a 40mm diameter Chevron MCPs stack (Hamamatsu, 60 Ω impedance) followed by a high voltage decoupling system, based on a resistive anode, and a printed circuit board (PCB) two cross delay lines system; this type of system is based on the work by G. Cautero et al. and is described elsewhere[217, 218]. The assembly is mounted on the exit plate of the 180° electron energy hemispherical analyzer, as shown in figures 7.23 and 7.24.

The distance from the gold mesh element and the analyzer exit plane is of ∼1mm. The gold mesh is kept at the accelerating/decelerating (A/R) voltage of the analyzer's Herzog plate. The "front" MCP is usually kept at +20V with respect to the A/R potential, while the "back" MCP is set to +1650 V higher than the "front" MCP. The resistive anode is at +200 V with respect to the MCPs. The detector voltages are provided by three floating high voltage bipolar power supplies. The heart of the detector consists of two "microstrip" transmission lines in a meander shape. The position of the charge centroid from the MCPs is calculated by measuring the times of arrival of the pulses that propagate up to the ends of the delay line. A ground plane is deposited on the back side of a 630 μm thick alumina substrate, while the lower meander line is deposited on the front side. A layer of dielectric material, an intermediate metalization, a

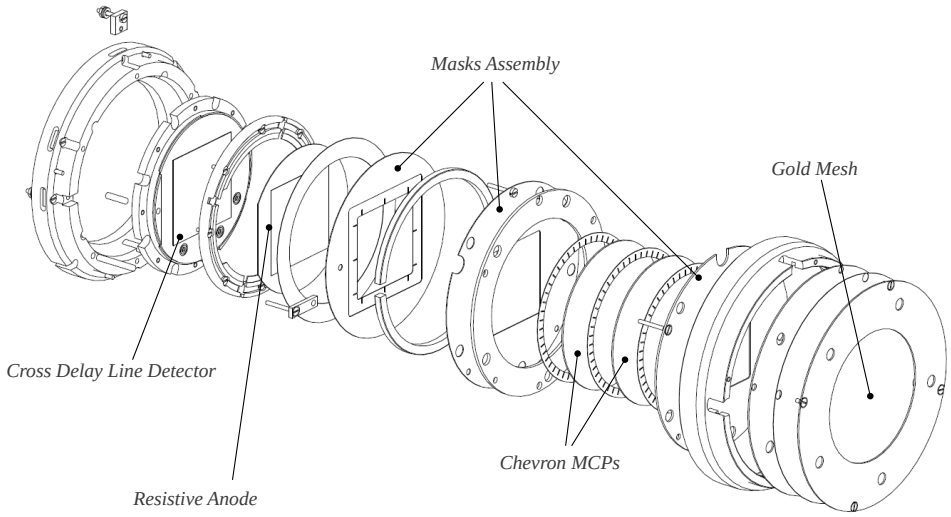

Figure 7.22: Exploded view of the two-dimensional cross delay line detector assembly mounted on the ARPES-TPES end station.

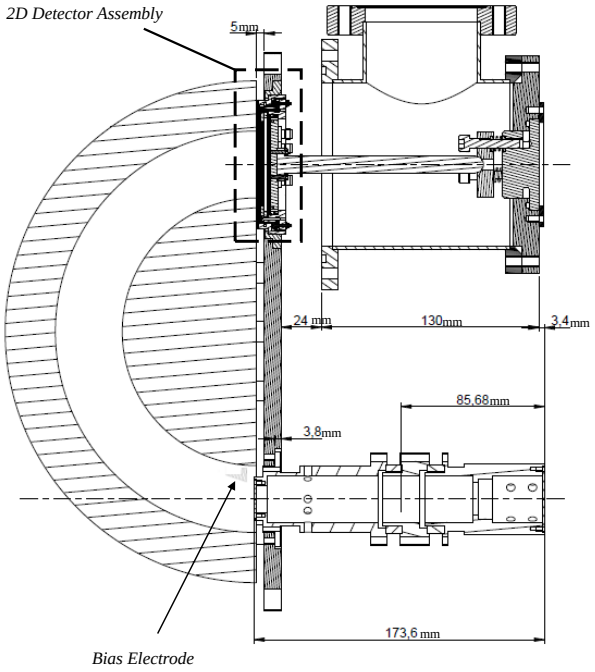

Figure 7.23: The cross-sectional view of the hemispherical analyzer housing the new 2D detector assembly.

second dielectric layer, and finally the metalization of the second meander line are deposited on top of the first one. The X and Y start and stop

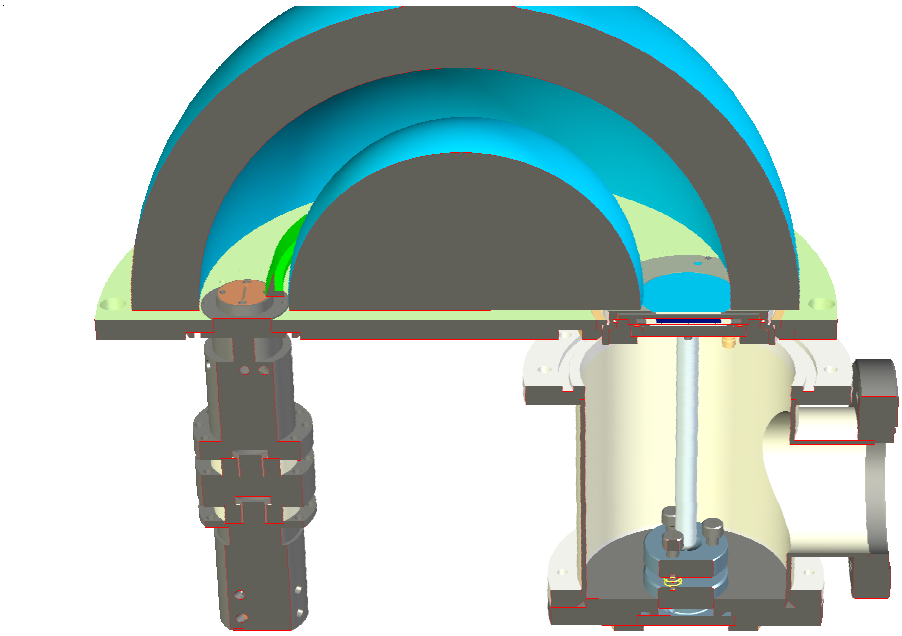

Figure 7.24: The 3D cross-sectional view of the hemispherical analyzer housing the new 2D detector assembly.

signals coming from the detector are carried out of the UHV section by means of four SMA connectors and immediately amplified by four properly customized preamplifiers, reducing in this way the possibility of noise pick-up. The signal from the detector is processed by a THR02-TDC advanced 4-channel time converter, provided by Elettra Sincrotrone Trieste S.C.p.A.
In its classical configuration the THR02-TDC is configured for a 2D delay line detector, in such a way that for each detected particle the instrument can compute the XY position and exact arrival time with respect to a trigger signal, that can be external or internal to the acquisition system. The THR02-TDC has 4 independent input channels, with four separate time converters, coupled with four Constant Fraction Discriminator (CFDs). In fact, the amplitude and width of the pulses coming out from an MCP assembly can vary appreciably depending, in our setup, on the distance between the MCP and the anode, on the voltage applied between them and the counting rate of the events. Moreover, a further spreading of the pulse width is introduced by the amplifier section, which always contains a high frequency noise filter; the width of the final pulse is around 4ns. The use of CFDs in a *fast crossover* configuration, instead of simple threshold discriminators, is needed in order to measure delay signals almost unaffected by peak amplitude variations. The start and stop ECL (emitter-coupled logic) signals coming from the CFDs are

fed to the Time-to-Digital converter (TDC) devices implemented in the THR02-TDC. The CFDs receive an analog input which is converted by the discriminators to a digital pulse, preserving the temporal information; the task of the TDCs is to establish in which instant the event occurred and provide a digital representation of the event elapsed time. The TDC board hosts two ACAM TDC-GPX chips, one for each detector dimension. The THR02-TDC system hosts an ethernet controlled Altera Cyclone II FPGA motherboard, which controls the TDCs, handles the flux of events, controls their logical consistency, elaborates the (x, y, t) coordinates, and menages the transfer of the digitalized data to the acquisition PC through a fast PCIe board connection. A scheme of the acquisition system is shown in fig.7.25.

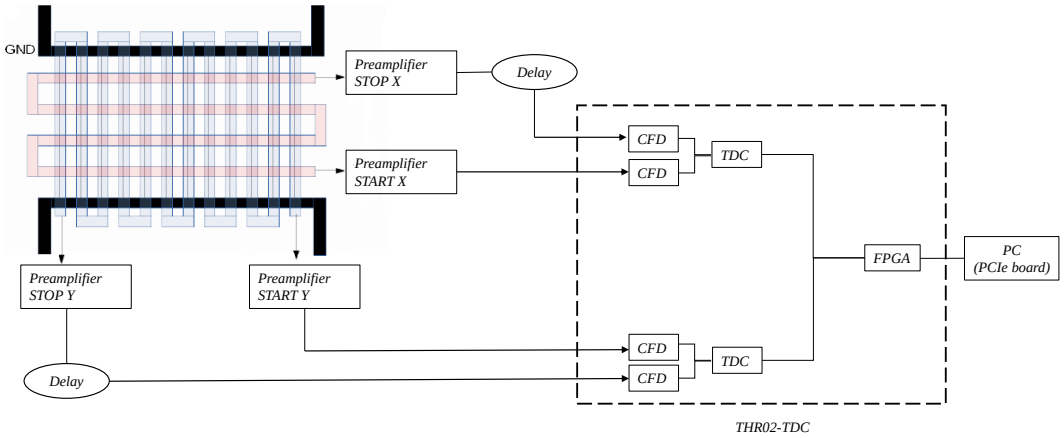

Figure 7.25: Simplified block diagram of the data acquisition system.

The THR02-TDC electronics is controlled in remote by a client-host server protocol. The "raw" data are sent to a host PC, which is directly connected to the THR02-TDC electronics through an ethernet bus. A client PC (the main acquisition computer) receives the analyzed data from the host PC via a point-to-point connection, without interfering with the data transfer between the host PC and the THR02-TDC module. The data exchange between the THR02-TDC, the host computer and the client computer is managed via a software developed by Elettra-Sincrotrone Trieste S.C.p.A. based on the LabVIEW programming code. The LabVIEW code responsible for the parameters setting of the THR02-TDC module and data transfer between host and client PCs, has been integrated in the spectrometer acquisition general software, also based on the LabVIEW programming code. The software has also been upgraded in order to efficiently record and process the imaging data produced by the

two-dimensional detector. The particles hit positions and times recorded by the cross delay anode are processed by the THR02-TDC hardware and the host PC software are converted into a bi-dimensional image that represent the photoelectron spectrum projection on the analyzer's exit plane. The image is represented in the software as 1000×1000 temporal bins matrix. The adopted detector is a 30 mm×30mm cross delay line and a set of three 29mm×29mm masks is placed between the MCPs and the resistive anode; such setup correspond to an active image of 800×800 temporal bin out of the 1000×1000 bins sized matrix. Each temporal bin corresponds to ∼27 ps (30 μm), i. e. the digital time resolution of the TDCs; the temporal precision (FWHM) is of approximately 3 bins, which corresponds to a spatial resolution of about 0.1 mm. One dimension of the 2D image is associated to the kinetic energy dispersion of the electron beam, while the other dimension is the angular dispersion of the beam. Through a calibration procedure based on recording photoemission spectra of different gases at different pass energy, the bin time scale can be converted to kinetic energy scale. The 2D image is analyzed by the acquisition software in the following way: for each kinetic energy scanned by the electron analyzer a single snapshot image, centered at the selected kinetic energy, is acquired and integrated in a 1D histogram by selecting a ROI (region of interest) of 700×700 temporal bin, in order to minimize the small distortions in intensity and space linearity that occurs at the detector edges that can affect the resolution of the reconstructed spectrum. The temporal bin scale of the 1-D histogram is then converted to the corresponding energy scale depending on the energy dispersion at the selected pass energy. The histograms are summed according to their kinetic energy and the intensity corresponding at each kinetic energy value is weighted for the number of times that it has been acquired. The 2D image histograms are also saved in a matrix and can be analyzed afresh by a data analysis software based on the Igor Pro programming code. For each acquisition raw images, the reconstructed photoelectron spectrum, and the matrix containing all the 1D-histograms are saved. The user can choose the binning of the images as well as the reconstructed spectrum, independently from the central kinetic energy step of the energy scan.
The use of a 2D position sensitive detector allowed a significant improvement in the counting rate with respect to a single channeltron. The active area of the latter was limited by a 1mm×15mm rectangular slit to 10mm^2. In the case of a position sensitive detector no exit slits are used, and the entire active surface can be exploited. The use of a 40 mm radius MCPs and a mask of 29mm×29mm increased the active detection area of a factor ∼84 with respect to the channeltron detector; this factor is however reduced by the gold mesh transmission (90%) and the MCP open area ratio of 60%. This factor has been recently improved by the use of funnel type MCPs, characterized by an open area ratio of 90%, with an improvement of a factor ∼2 in the counting rate. While in principle a channeltron detector can collect all the impinging particles

(depending on its efficiency) regardless the events time scale, in a cross delay lines detector the counting rate is limited by the the propagation speed of the signal in the two meander lines, namely 10 ns and 12 ns for the upper and lower meanders respectively. Moreover, a particle hit is classified as a real event only if all the four signals from the delay lines are recorded, and if the (X, Y) coordinates time difference fall in a time window between 3ns and 10 ns, depending on the detector settings. This data processing produces an non negligible fraction of discarded particle hits as false events. However, the use of two-dimensional cross delay line anode detector exhibits several advantages with respect to a channeltron device. The high spatial and temporal resolution makes it simple to integrate counts over the desired distance along the non-dispersive direction. The real time direct observation of the projection on the detector of the particle beam image at the exit plane of the analyzer is an useful tool to monitor the behavior of the electronic optics, in particular during the experimental conditions optimization. The most important feature of a 2D detector is the possibility of acquiring entire spectra in a single shot, by exploiting the energy dispersion of the analyzer; in our case, the energy range covered by the detector ranges from 0.7eV at a 5 eV pass energy, to approximately 2eV at 15eV pass energy . The acquisitions can take place in a single shot mode, exploiting the detector energy dispersion, or in a scan mode, where lenses and hemispheres potentials are changed in steps, extending the acquisition over the desired energy range. In the latter case, single-shot data are scaled and summed, according to the voltage settings. The improvements in detection sensitivity, acquisition time and resolution of such bidimensional detectors are of great importance in gas-phase experiments, particularly when dealing with very low sample densities, where the counting rate with conventional devices can be of the order of 10-50 c/s, such as in the case of transient and reactive species, as well as for enantiopure chiral samples, were in some cases a very small amount of sample is available.

The fringing field effects typical of electron hemispherical analyzers has been partially corrected by the use of a bias electrode positioned in an asymmetric configuration immediately after the entrance slit, between the latter and the analyzer inner sphere; in this way the first order focusing conditions of the analyzer are restored and energy resolution of approximately 30-35meV, 40-45 meV and 60-65 meV respectively at 5 eV, 10 eV, and 15 eV pass energies is achieved in the entire kinetic energy range investigated.

The ARPES-TPES end station can operate in three different modes: Angle Resolved Photoemission Spectroscopy mode, Constant Ionic State Spectroscopy mode and Threshold Phototoelectron Spectroscopy mode, covering a kinetic energy range from 0.5eV up to 100eV. The experimental apparatus can be interfaced with the CiPo and Gasphase beamlines of the Elettra Synchrotron in Trieste.

7.2.3 Detector implementation and characterization

The 2D detector mounted on the ARPES-TPES analyzer is shown in fig.7.26. The A/R plate was modified in order to accommodate the detector assembly. The detector, hosted in a T-piece at the analyzer's exit (see fig7.23 and fig.7.24) is mounted on a special aluminum support and kept in position on the A/R plate by a spring between the support and the T-piece flange (see fig.7.24). The three-element electrostatic lens has been modified in a more compact design and all the isolation PEEK (Polyether ether ketone) spacers responsible for the electric insulation and the internal alignment of the analyzers elements (lens, inner and outer spheres, A/R plate etc.) were redesigned.
The 2D detector system (power supplies, acquisition electronics, preamplifiers etc.) was tested with both laboratory sources (He lamp) and synchrotron radiation by recording UPS spectra of noble gases (Ar, He), N_2 and O_2, in order to characterize the detector performance, and determine the energy dispersion functions of the detector, i.e the relationship between the photoelectron kinetic energy and the impact position on the detector as a function of pass energy. A linear relation was found of the type $E_k(meV/bin) = a + b \times E_0$, with a =0.072256 and b =0.15758.
Fringing field effects became evident in phenomena such as the distortion of the electron beam images at the detector, non linearity in the kinetic energy scale and lost of resolution. In order to reduce these effects electron trajectory simulations were performed using the SIMION Ion and Electron Optics simulator and a deflecting electrode was developed in order to restore the first-order focusing conditions of the analyzer.
Moreover, the experimental apparatus was modified in order to use a new dichroic setup, were the electrons are detected at the magic angle with respect to the circularly polarized radiation propagation axis; this latter setup allows to perform PECD experiments, and thus the experimental determination of the dichroic parameter D. It is therefore possible with the same end station to measure all the three photoionization dynamical observables using linearly and circularly polarized synchrotron radiations available at Elettra.

7.2.4 Deflecting electrode

After studying the feasibility of the fringing effects corrections proposed in the literature on our experimental apparatus, we developed a specifically designed electrode for fringing field correction. The electrode is machined in aluminum with a trapezoidal profile over a 60° arc of circumference, as shown in fig.7.27. The electrode is mounted on the A/R plate, between the inner hemisphere and the analyzer entrance slit, and electrically isolated by two PEEK spacers; a voltage referred to the inner sphere potential can be applied to the electrode by a home made bipolar floating ±2.5V power supply. The effect of the shape and position of the deflecting electrode was

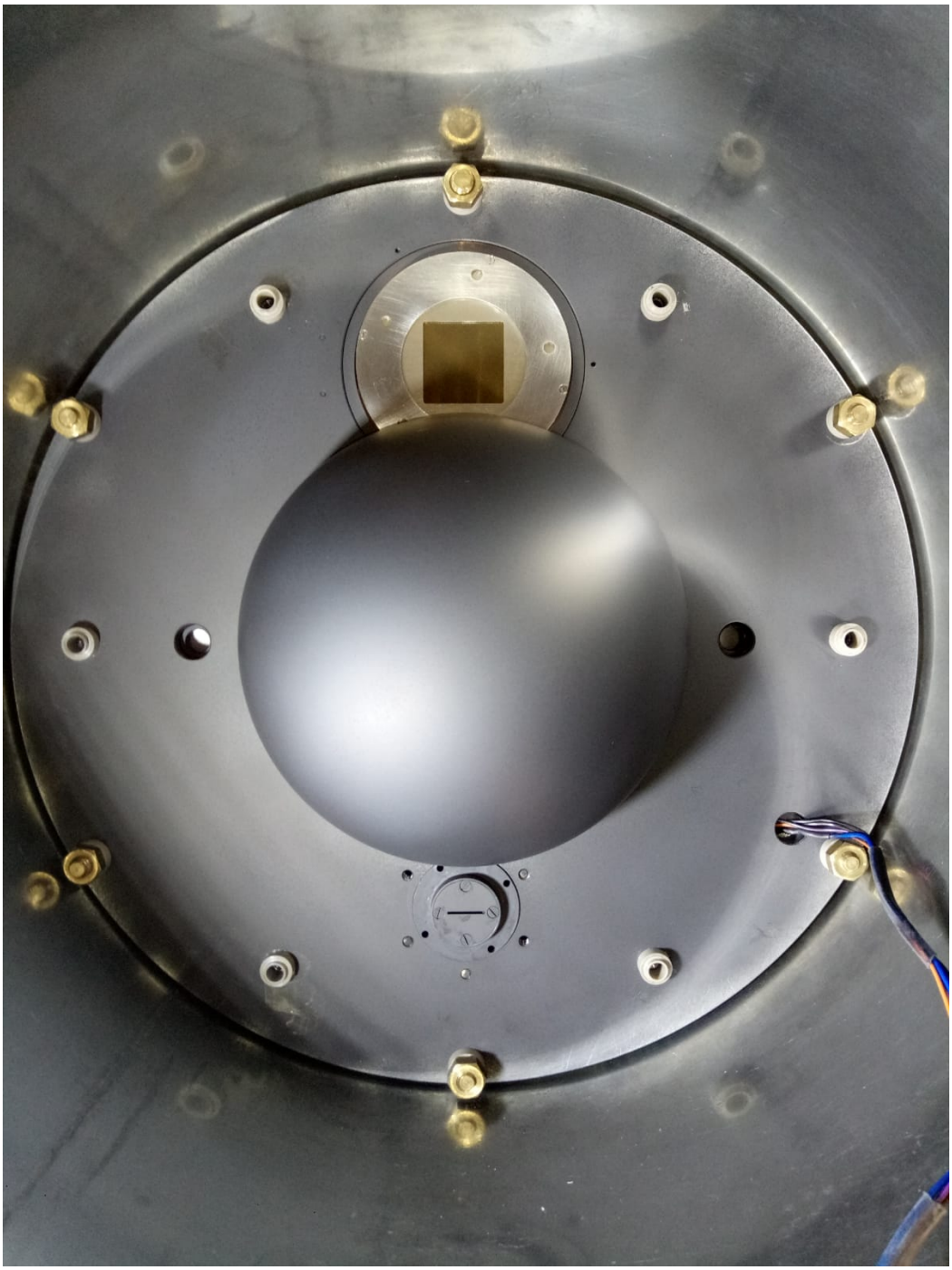

Figure 7.26: Front view of the 2D detector assembly mounted on the ARPES-TPES chamber analyzer. The outer hemisphere has been removed in order to make visible the detector (in the upper part it is possible to see the squared gold mesh of the detector) and the analyzer's entrance slit.

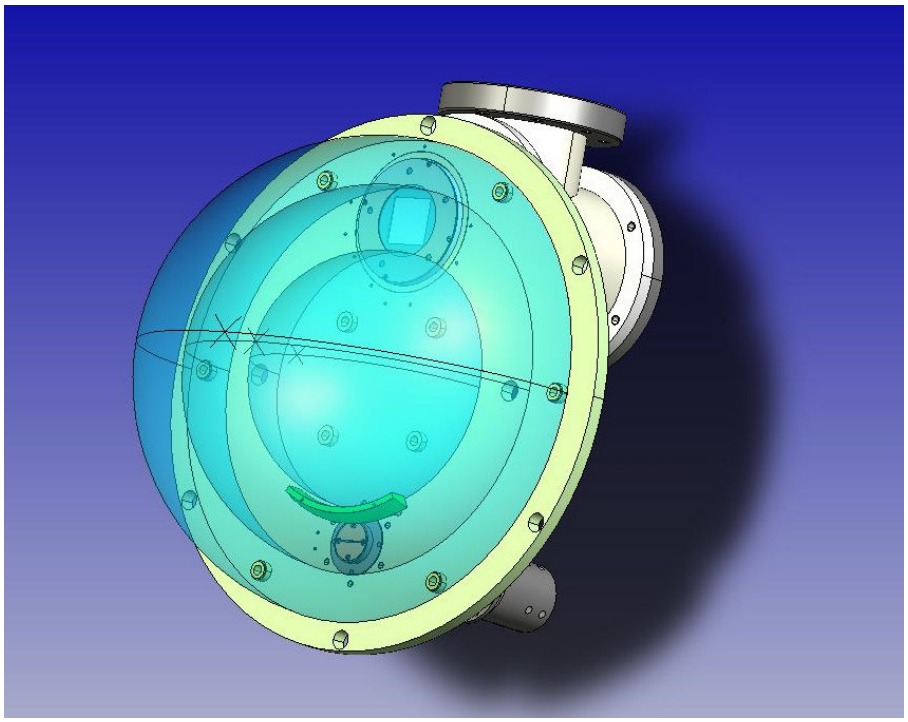

Figure 7.27: The deflecting electrode (green component) developed for the ARPES-TPES end station analyzer and its mounting in the analyzer.

studied by ray tracing simulations with the SIMION software. In fig.7.28 are compared trajectories of electrons flying in the analyzer without the deflecting electrode (panel *a*) and with it (panel *b*). In absence of the electrode, due to the fringing field effect in the region where the electrons experience the transition from the electrostatic lens potential to the $1/r^2$ potential of the hemispheres, the trajectories are distorted and do not follow the analyzer mean radius path, as expected in the case of an ideal analyzer. Moreover, the focal point of the electron beam does not correspond to the exit plane of the analyzer, and a lost in energy resolution is expected as a result. In principle, the losses in the focusing properties of the analyzer can be compensated by defocusing the electron beam at the analyzer entrance by changing the electrostatic lens voltage; however this implies a significant lost in the analyzer transmission. If we now insert in the simulations the deflecting electrode after the entrance slit and apply an attractive potential, the electrons trajectory can be corrected and the focusing properties of the analyzer restored.

Figure 7.29 shows the effect of the deflecting electrode on the 2D image of the detector expected by SIMION ray tracing: the electron beam exhibits a better focusing on the detector plane (see panel *a*) and hence an improvement in the energy resolution. This is clear in the histograms of

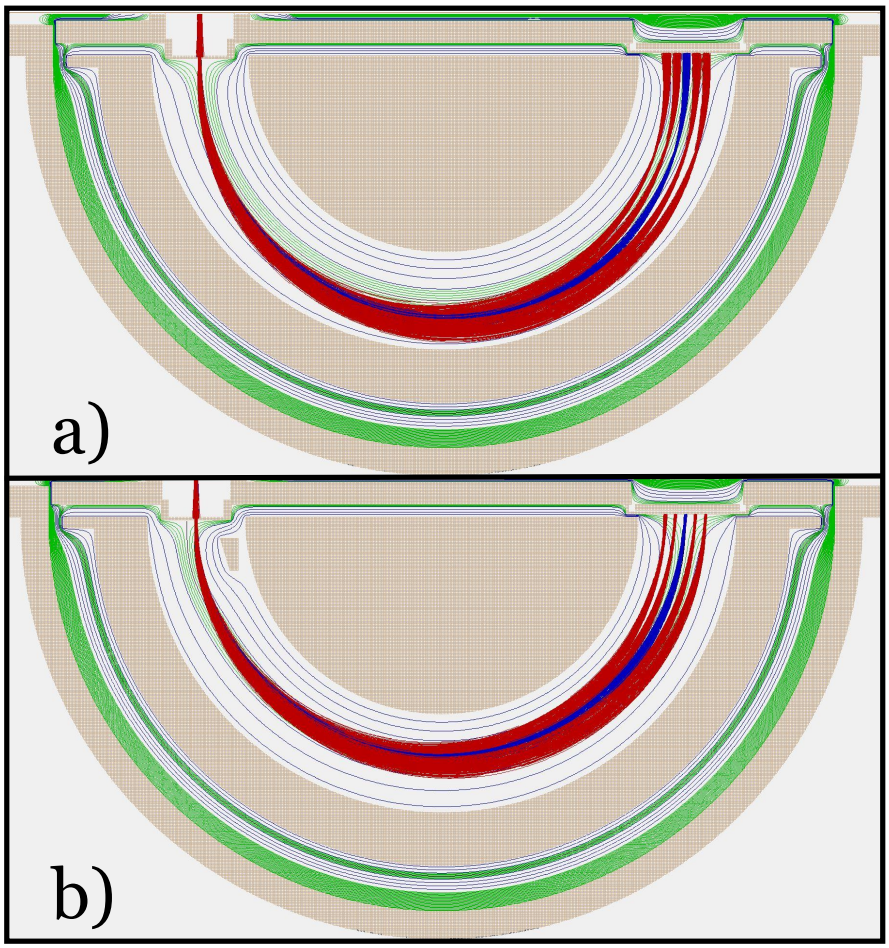

Figure 7.28: Cross-sectional view of the electron beam trajectories in the hemispherical analyzer without the bias electrode (panel *a*) and with the deflecting electrode (panel *b*) , with a pass energy of 5eV, central kinetic energy 10eV, particles energy separation 100 meV, optimum focusing lens voltage 20V, deflecting electrode voltage -2.5eV (same voltage as the inner sphere). It can be seen (panel *a*) how the electron beam (red) trajectories in the analyzer does not follow the central trajectory (blue) and is not focused on the detector due to the distortion of the static electric fields (green). Panel *b* shows how the bias electrode acts as a trajectory corrector deflecting the electron beam, thus improving the energy resolution, focusing conditions and energy dispersion linearity.

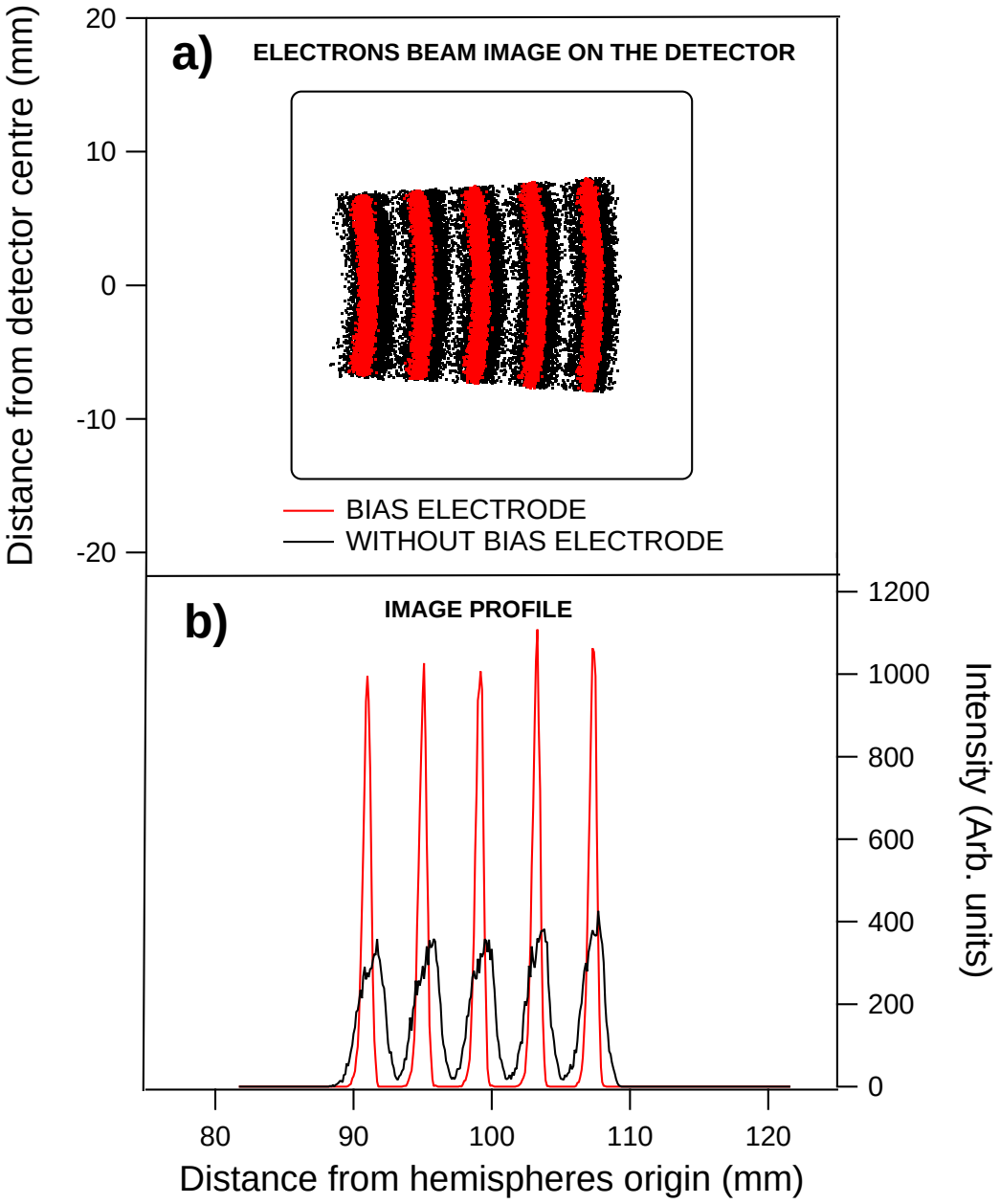

Figure 7.29: Trajectory simulation of an electron beam (Pass energy 5eV, central kinetic energy 10eV, particles energy separation 100 meV, optimum focusing voltage 20V) in the ARPES-TPES hemispherical analyzer, with and without the deflecting electrode (red and black dots/lines respectively). In panel *a* is shown the projection of the trajectories on the 2D image, while in panel *b* are shown the image profiles. It can be noted from the image profiles the dramatic improvement in the resolution in the case of the deflecting electrode. The best bias voltage of the electrode in this case has been found to be -2.5eV, i.e. the same potential of the inner sphere, in accordance with the value obtained by ray tracing simulations.

the image profiles in panel *b* where the same peaks integral is obtained. Hence, with the use of a bias voltage applied to the electrode, an improvement in resolution without a lost in the analyzer transmission is obtained. The bias voltage of the deflecting electrode and the best (maximum transmission) focusing voltage were optimized with the SIMION programming code in order to have the best optimum values for the entire kinetic energy range for different pass energies. The improvement in energy resolution was also observed experimentally. This is shown in fig.7.30, where the reconstructed photoelectron spectra of an Ar/N_2 mixture (recorded at pass energy 15 eV and photon energy 50 eV) are compared: it is evident from the better peak separation in the images, as well as in the spectra, the significant improvement in the detector resolution gained with the use of the bias electrode, as expected by the electron trajectories simulations. The SIMION trajectory simulations, shown in fig.7.31, show how the distortion in the analyzer electric field generated by the electrode deflects the electron trajectories towards the inner sphere. As a consequence the electron trajectories are deflected towards the mean radius of the analyzer. This bending in the trajectories is confirmed by simulating an electron that enters the analyzer with an angle of 5°, as shown in fig.7.32, obtaining the same effect as in the case of the chosen bias voltage of the deflecting electrode. The effect caused by the electrode is thus similar to the case of fringing filed correction by the use of tilted input lens axis, with the advantage of a much simpler geometry.

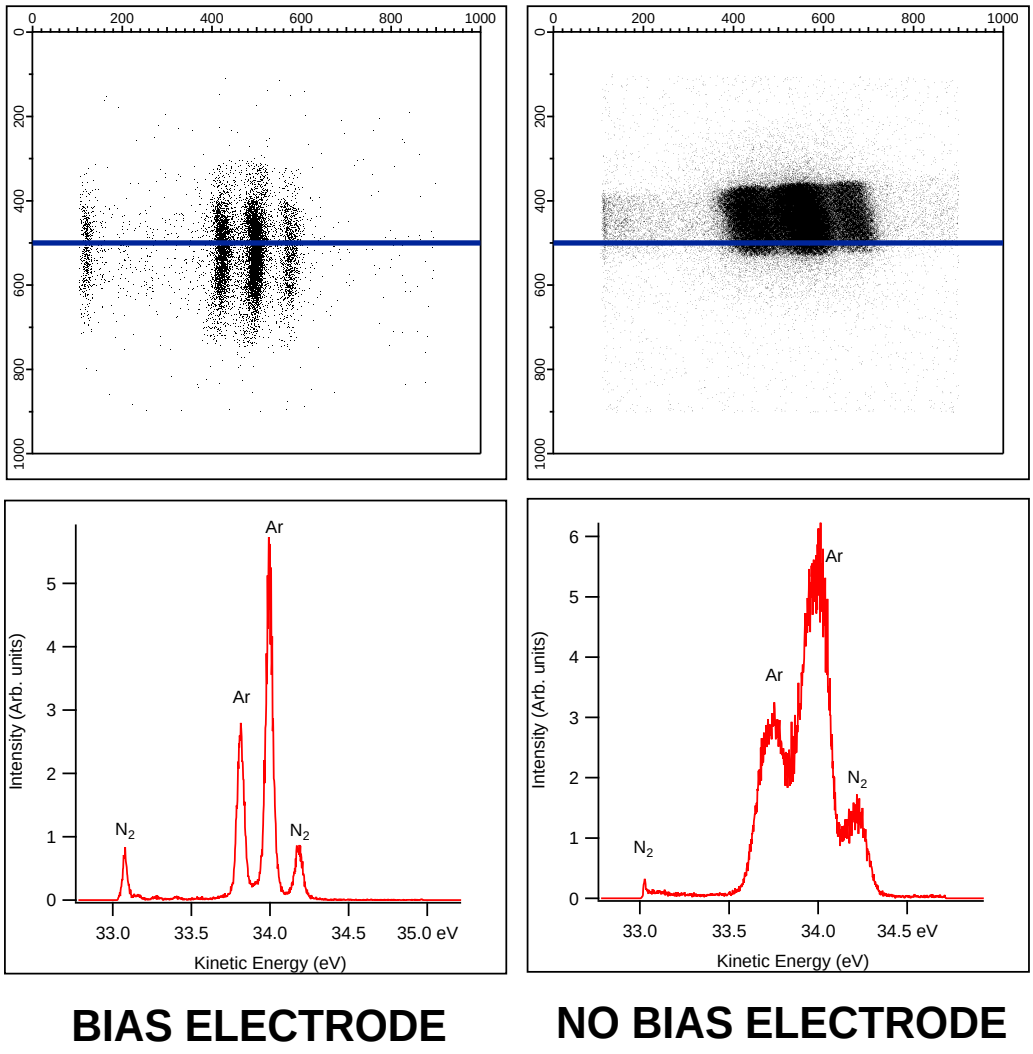

Figure 7.30: Photoelectron spectra of a Ar/N_2 mixture recorded at 50eV photon energy with 15eV of pass energy, rectangular slits size of 1.2mm×12mm, with the bias electrode (left panels) and without the bias electrode (right panel). It can be noted the improvement obtained by using of the bias electrode (kept at the same potential of the inner sphere).

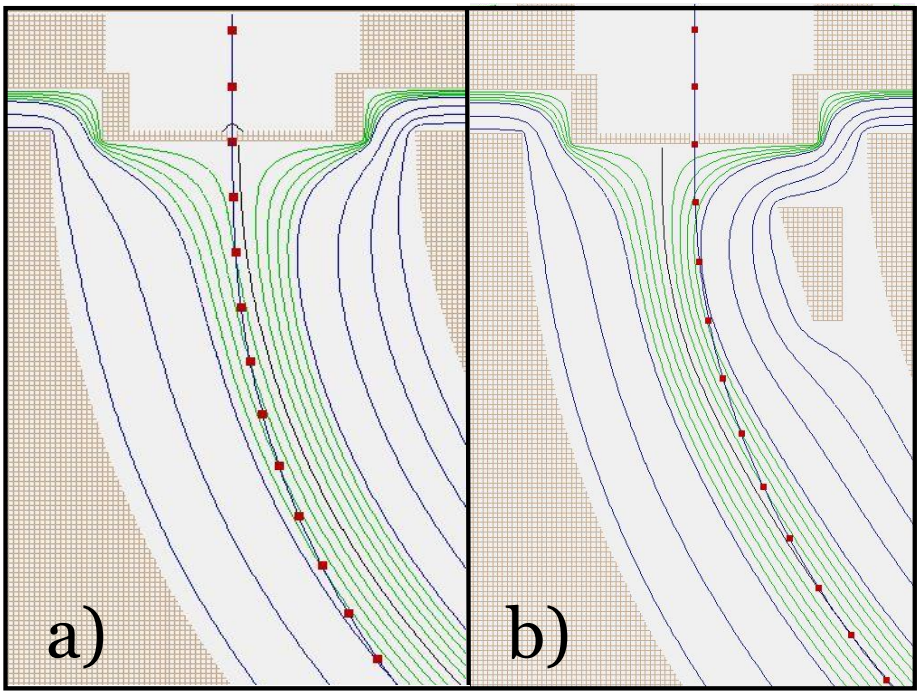

Figure 7.31: Zoom of the Cross-sectional view of a single electron trajectory (dotted line) in the hemispherical analyzer without the deflecting electrode (panel *a*) and with the bias electrode (panel *b*), with a pass energy of 5eV, central kinetic energy 10eV, optimum focusing voltage 20V, bias electrode voltage -2.5eV (same potential as the inner sphere). It can be noted how the bias voltage of the electrode deflects the electron trajectory towards the analyzer's mean radius.

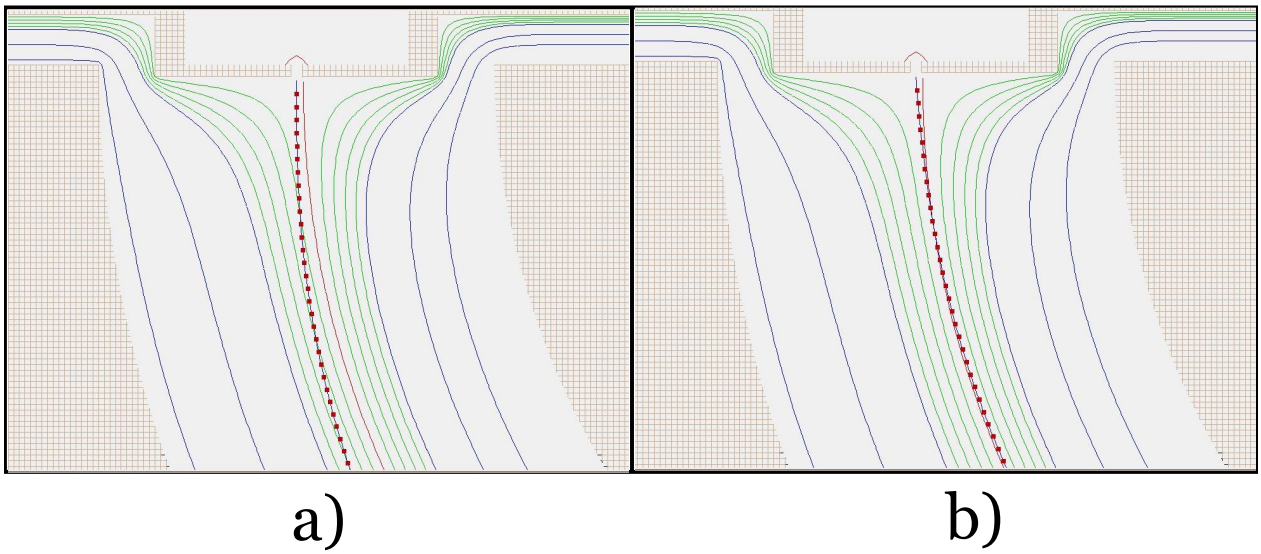

Figure 7.32: Zoom of the Cross-sectional view of a single electron trajectory (dotted line) entering the hemispherical analyzer with an angle of 0° (panel *a*) and with an angle of 5° (panel *b*), with a pass energy of 5eV. The tilted entrance angle of the electron reproduces the effect of the deflecting electrode.

7.2.5 Software development

The hemispherical analyzer voltages, the analysis of the 2D images from the cross delay line anode detector, and the THR02-TDC parameters are controlled via an acquisition software based on the LabVIEW programming code. The original software based on a single channeltron detector has largely been upgraded in order to be compatible with the new data format of a two-dimensional detector and was interfaced with the CiPo and Gasphase beamlines of the Elettra Synchrotron. The main issue in the software upgrade was the detector signal processing, since a single channeltron device and a two-dimensional detector have a completely different data format. In the case of a single channeltron, at each scanned kinetic energy, the analog signal from a counter is acquired through a PCI board; at each pass energy, only the central kinetic energy electrons reach the detector and thus for each kinetic energy scanned by the analyzer the correspondent electron signal is recorded, and the photoelectron spectrum is built simply by a one-to-one correspondence between electron counts and central trajectory kinetic energy. The case of a bidimensional detector is more complex, since for each central kinetic energy scanned by the electron analyzer, the entire kinetic energies dispersion of the electron beam, defined by the chosen pass energy, is recorded by the detector. The data received from the detector are thus in the form of a 2D image of the spectrum projection on the exit plane of the an-

alyzer, and they need to be further processed in order to extract the one-dimensional photoelectron spectrum. The LabVIEW code package provided by the Elettra-Sincrotrone S.C.p.A responsible of the data exchange between the THR02-TDC electronics and the acquisition PC (the client PC in the host-client protocol) was implemented in the general acquisition software of the ARPES-TPES end station; in this way the data from the detector are displayed as a 800×800 bin 2D image. The software can operate essentially in five different modes.

- Continuous time scan: this function is used to monitor in real time the images at the detector, and is used during the experimental conditions optimization procedure. This function can also be used to record a fixed portion of the spectrum by simply changing the kinetic energy of the central trajectory of the snapshot window.
- ARPES mode: this function permits to record the photoelectron spectra by scanning the desired kinetic energy range at different detection angles. The central kinetic energy of the snapshot is scanned by the analyzer at fixed pass energy; the central kinetic energy is the kinetic energy of the electrons that exit at the detector center.
- Constant Ionic State (CIS) mode: this function allows to record CIS spectra, in which a selected ionization state (constant binding energy) is studied as a function of photon energy.
- Threshold Photoelectron Spectroscopy (TPES) mode: the collection energy of the electron spectrometer is tuned to accept electrons of nominally zero kinetic energy (less than ∼1meV). Unlike in conventional PES where the kinetic energy of the photoelectrons is varied, in the TPES technique the kinetic energy is fixed while the photon energy is scanned.
- Focusing Voltage Scan mode: in this function it is possible to monitor the detector image as a function of focusing lens potential, in order to obtain the best focusing curve suitable for the experimental conditions as a function of pass energy and the selected kinetic energy range.

Depending on the operating mode the bidimensional image has to be processed in different ways by the acquisition software. In the case of the ARPES mode, in order to reconstruct the photoelectron spectrum, the software code was written in the following way: a ROI defined by free cursors on the 2D image is selected by the user and a 1D-histogram (intensity scale of the photoelectron spectrum is built by integrating along the angular dispersion direction. The image temporal bin x-scale is converted into the kinetic energy scale by the appropriate energy dispersion conversion formula; the bin is converted to a fixed energy value according to the selected pass energy and the scanned central kinetic energy. Each kinetic energy value is then sorted depending on the energy scale

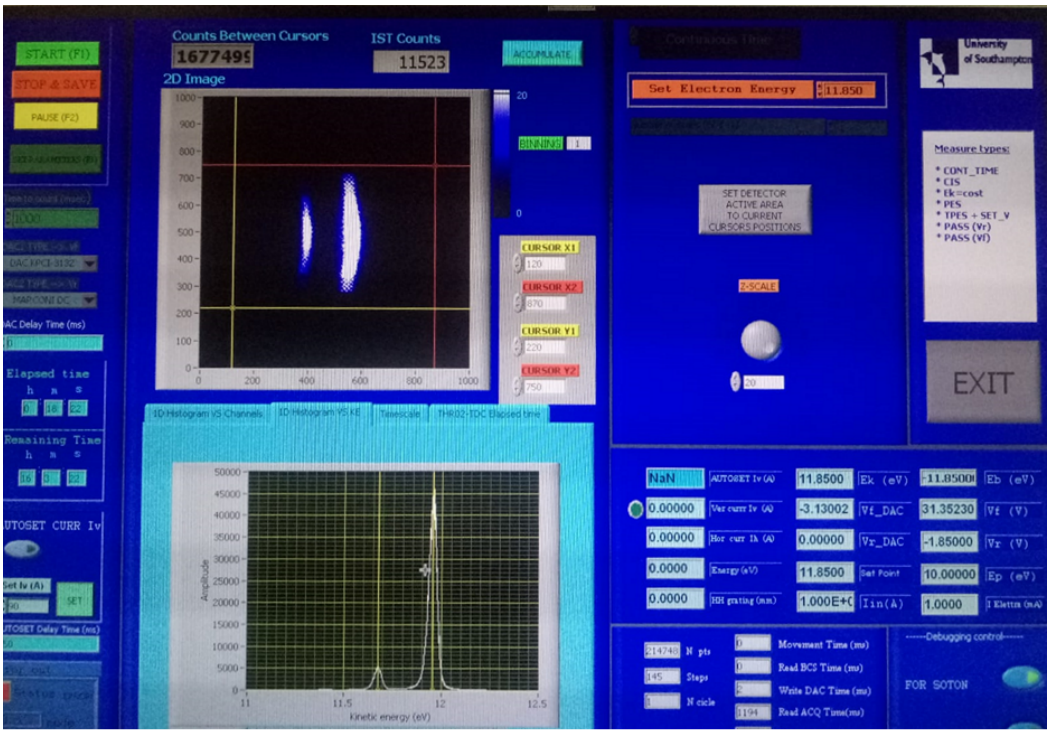

Figure 7.33: User interface of the LabVIEW acquisition software of the ARPES-TPES chamber. It can be noted the 2D image projection of the N_2 photoelectron spectrum and its 1D-histogram as a function of photon energy.

binning chosen by the user and projected on the final spectrum kinetic energy scale. The histograms of each single image are sorted with the same procedure and summed; a weighting procedure based on the number of recorded snapshots ensures the same statistics for each kinetic energy value of the reconstructed spectrum. This image analysis procedure is based on the LabVIEW code adopted by the ALOISA beamline of the Elettra Synchrotron. The final results are: a real time reconstructed photoelectron spectrum, a matrix containing all the histograms and scanned kinetic energies for a refined post-acquisition analysis. All the acquired images are also saved. In the CIS mode a ROI is used to select a specific ionic state and the spectrum is built simply by plotting the signal integral in each ROI delimited snapshot versus the scanned photon energy. The same procedure is applied in the TPES mode. In both cases the raw images and the matrix containing the 1D histograms are saved for a post-acquisition analysis based on a code written in the IGOR Pro programming language. The software has been upgraded in order to to be interfaced with the GasPhase beamline of the Elettra Synchrotron. An example of the ARPES-TPES acquisition software user interface is shown in fig.7.33.

7.2.6 Acknowledgments for the 2D detector development

I would like to thanks G. Cautero, L. Stebel, R. Sergo and C. Dri of Elettra-Sincrotrone Trieste for their support in the hardware and software development of the the two-dimensional cross delay line anode detector, D. Benedetti of the CNR-IOM institute for the technical drawings of the hemispherical electron analyzer, D. Vivoda of Elettra-Sincrotrone Trieste for his contribution in the chamber alignment procedure on the beamlines, F. Salvador and P. Bertoch of the CNR-IOM institute for the mechanical processing. L.S. thanks A. Cossaro and G. Kladnik of the CNR-IOM institute of the ALOISA beamline for their contribution in the acquisition and analysis software developments. I also thanks M. Alagia for his support in the SIMION electron trajectories simulations.

7.3 Osmium Tetroxide

The implemented 2D electron detector system was tested in the measuring of the asymmetry parameter of the valence photoionization process of $OsO4_4$ molecule, using linearly polarized synchrotron radiation. This molecular system was chosen as experimental model molecule for several reasons. First of all, mononuclear and polynuclear organometallic clusters containing heavy metals are a class of interesting and technologically relevant species due to their large use in catalysis[219], the elucidation of the nature of metal-metal bonding in polynuclear complexes, is of interest both for the rationalization of the relative stability and reactivity of these complexes, and for the understanding of their ionization and fragmentation processes[220]. From a theoretical point of view, the study of both mononuclear and polynuclear metal clusters poses several challenges due to their complex electronic structure for the presence of strong correlation effects and the need of relativistic corrections for the heavy metal centers[221, 222]. Moreover, osmium tetroxide is a highly corrosive species, and is thus suitable for testing the performance of the photoelectron spectrometer in extreme conditions, as it will operate in the case of other reactive species, such as radicals. The OsO_4 reactivity required to operate in a very low sample concentration regime, that is conditions similar to those required for investigating enantiopure chiral species. Most importantly, only one experimental study of the valence photoionization dynamics of OsO_4 is present in the literature[223, 224], where the photoionization cross sections are reported for the first five ionization PE bands. Although the asymmetry parameter is consider far more sensitive observable for studying dynamical aspects then relative integral cross sections, this kind of study has not yet been performed. Our work thus fill this gap in the photoionization dynamic of osmium tetroxide by reporting for the first time the experimental measurement of the asymmetry parameters for the outer valence ionization channels and performing theoretical calculations of both cross section and asymmetry distribution at the DFT and TDDFT level, highlighting the importance of correlation in the electronic continuum spectrum. The experimental data acquisition procedure and the data analysis procedure are described in appendix B.3.

7.3.1 Osmium tetroxide: valence photoionization

The valence PE spectrum of OsO_4 recorded at $h\nu = 40$ eV and $\theta = 54.7°$ (magic angle) is reported in fig.7.34. Linearly polarized radiation and the magic angle of detection avoid including photoelectron angular distribution effects in studying partial cross sections as a function of photon energy. The five bands, denoted as features A-E in the figure, are in excellent agreement with the published PE spectra of OsO_4[225, 226], and exhibit all but band E vibrational structure, which has been suggested to be mainly due to the $\nu_1(a_1)$ "breathing" vibrational mode excitation.

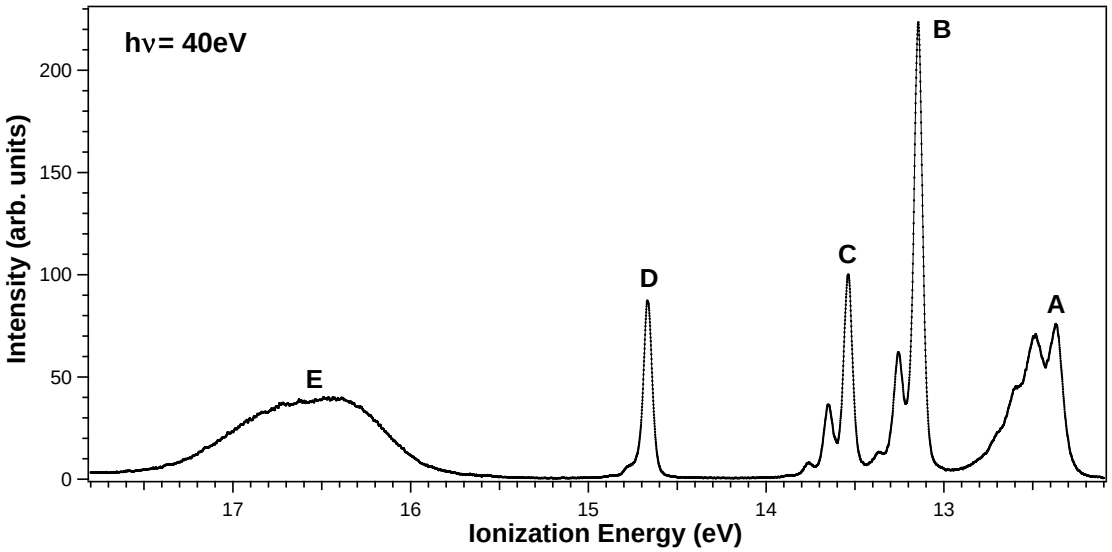

Figure 7.34: Outer-valence PE spectrum of OsO_4 recorded at hν = 40 eV and $\theta = 54.7°$ (magic angle), using 15 eV pass energy, and linearly polarized synchrotron radiation.

Osmium tetroxide has the following valence electronic structure:

$$(1a_1)^2(1t_2)^6(1e)^4(2t_2)^6(2a_1)^2(3t_2)^6(1t_1)^6$$

The assignment of the five photoelectron bands is reported in tab.7.3. The first band, A, is assigned to the $^2T_1$ ion state, which corresponds to the ionizations from the $1t_1$ MOs, the bands B and C, separated by 0.4 eV, to the spin-orbit components associated with ionizations from the $3t_2$ MOs with strong contribution of O 2p atomic orbitals (AOs), namely the $^2T_2$ spin-free ion state. The fourth band, D, is assigned to the $^2A_1$ ion state, while the last band E, includes the remaining outer valence MO ionizations (^2E and $^2T_2$ ion states). Finally, the valence MOs $1a_1$ and $1t_2$ are essentially symmetry adapted linear combinations of O 2s AOs, whose ionizations are energetically not accessed by He-I radiation. This assignment has been put on a firm basis by a theoretical fully relativistic Xα calculation based on the transition-state method (TS)[227], and also confirmed by more recent high level ab-initio EOM-SOCCSD calculations [228].

Table 7.3: Comparison between ZORA LB94/TZP MO energies, ΔSCF IEs from this work, theoretical (TS[227] and EOM-SOCCSD [228]) and experimental IEs for OsO_4, from ref.[227], [226], and this work. All energies are in eV. AO contributions to the MOs calculated at the LB94/TZP level are also reported.

Band	Ion state (MO)	ΔSCF[a]	$-\varepsilon_{KS}^{LB94}$[a]	TS[b]	EOM-SOCCSD[c]	IE_{exp}[d]	IE_{exp}[a]	AO character[e]
A	4U′ ($1t_1$)	12.61	15.14	13.315	12.41	12.35	12.37	O_{2p}
A	2E′ ($1t_1$)	12.78			12.47			
B	3U′ ($3t_2$)	13.26	15.84	13.684	13.23	13.14	13.14	96% O_{2p}/2% Os_{6p}
C	2E″ ($3t_2$)	13.62			13.50	13.54	13.54	
D	1E′ ($2a_1$)	14.97	17.26	14.986	14.86	14.66	14.67	85% O_2p/7% O_2s/8% $Os_n s$[f]
E	1E″ ($2t_2$)	16.78	19.26	17.823	17.30	16.4–16.8	16.33–16.78	47% O_2p/9% O_2s/39% Os_5d
E	2U′ ($2t_2$)	16.89			17.35	16.4–16.8	16.33–16.78	
E	1U′ (1e)	17.35	19.42	18.512	17.92	16.4–16.8	16.33–16.78	56% Os_5d/44% O_2p

[a] from this thesis;
[b] from ref.[227];
[c] from ref.[228];
[d] from ref.[226];
[e] calculated in this work at scalar relativistic LB94/TZP level
[f] n = 6, 7, 8.

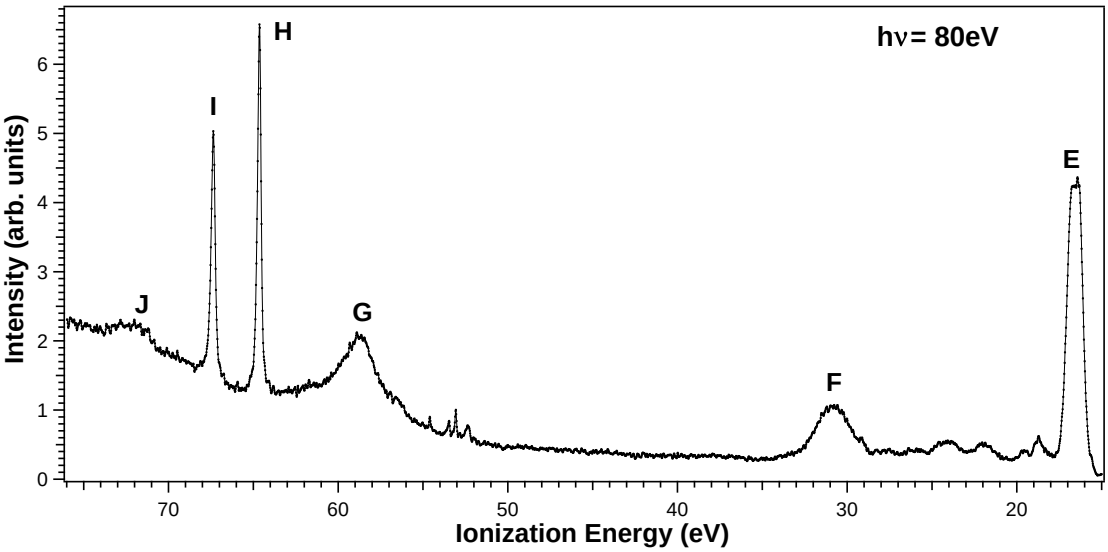

Figure 7.35: High-energy valence PE spectrum of OsO_4 recorded at hν = 80 eV and θ = 54.7° (magic angle), using 15 eV pass energy.

It is possible to note from tab.7.3 that the ΔSCF KS procedure can provide good estimates of the valence IEs since discrepancies with the available experimental data are of the order of 0.2 eV, even tough the accuracy varies with the ionic state considered, and gets worse for the higher-energy states. Moreover, the KS ΔSCF estimates a spin-orbit splitting of the $^2T_2$ ionic state (bands B and C in Fig.7.34) as large as 0.36 eV, in good agreement with the corresponding experimental one of 0.40 eV, indicating that spin-orbit effects are rather accurately described at the ZORA-KS level. The accuracy of the ΔSCF estimates given in this work is, on average, higher than the TS values reported in ref.[227], and comparable to the best ab-initio values[228]. Regarding to the AO composition of the ionized orbitals, calculated at the TZP/LB94 level, the results are in broad agreement with past investigations[224]. In particular, the $1t_1$ MO is non-bonding, $3t_2$ and $2a_1$ have dominant contributions from the O 2*p* AOs, while the metal *d* orbitals are heavily hybridized with ligands O 2*p* AOs in the two innermost MOs $2t_2$ and 1e of the valence shell, which have a strong bonding character. This last remark has strong implications in the departure of the cross-section behavior of ionization from these MOs from a pure atomic behavior characteristic of ionizations from atomic Os 5d orbitals.

The unusual width and shape of band E in the IE region 16.33-16.78 eV, although comprising two (or three relativistically) ionizations, appears to be heavily affected by vibronic excitations or alternatively is a consequence of a strong breakdown of the one-particle picture, with a dense manifold of satellite states, predicted in ref.[229], which however seems to significantly overestimate such effects for the outer ionizations, and does not describe accurately this region. A clear presence of satellites is however seen in the experimental spectrum at higher energies shown in fig.7.35, where the

full valence ionization range is reported. The prominent F band centered at 30.85 eV is clearly assigned to main O2s ionizations, possibly broken by many-body effects, while two sharp peaks due to Os $4f_{7/2}$ and $4f_{5/2}$ ionizations, located respectively at 64.65 eV and 67.37 eV (features H and I) are in the middle of the broad Os $5p_{3/2}$ and $5p_{1/2}$ peaks (G and J), observed at 58.80 and 71.98 eV and showing a very large spin-orbit splitting.

7.3.2 Osmium tetroxide: photoionization cross sections

The partial photoionization cross sections for the outer-valence orbitals of OsO_4 computed at the DFT and TDDFT level are displayed in fig.7.36, together with the experimental data from ref.[224]. A general good agreement between the calculated values and the available experimental data can be observed in the entire photon energy range investigated. Although the TDDFT approach is expected to be more accurate, it does not overcome the simpler and computationally cheaper KS method, which is good in perspective, since a KS treatment of the photoionization dynamics could be the only feasible approach for the study of more extended polynuclear metal clusters. The only noticeable instance where TDDFT is clearly needed for a quantitative agreement with the experiment is the high-energy behavior (above 70 eV photon energy) of the cross section for the ionization of the metal-based d orbitals 1e and $2t_2$, where the KS profile is seen to underestimate the experimental intensity. Although the super Coster-Kronig decay[230, 231] of the $5p \rightarrow 5d$ singly excited state into the available open continua ($5p^6 5d^n + h\nu \rightarrow 5p^5 5d^{n+1} \rightarrow 5p^6 5d^{n-1} + e^-$)[223] can be gathered from the scatter of the experimental points around 50-60 eV, the cross section modulation is much more pronounced in the TDDFT profiles. This is a clear indication of p-d giant resonant enhancement of the cross section of this band, coinciding with the Os 5p subshell ionization energies ($^2P_{3/2}$=49eV, $^2P_{2/2}$=61eV[232]). This behavior is expected from molecular orbitals (MOs) having significant Os5d character. Moreover, the "double hump", visible in the experimental cross section for band E (ionizations from the 1e and $2t_2$ MOs) and exhibiting an energy separation close to the spin-orbit splitting of the two ^{2}P thresholds (Os $5p^{-1}$), cannot be reproduced by our non-relativistic TDDFT method. However, the method can represent (although damped by the convolution procedure) the first few members of the $5p \rightarrow n$d Rydberg series converging to the Os $5p$ threshold, which cannot be resolved in the experimental data due to their limited energy resolution. We should also point out that our DFT/ZORA scalar relativistic treatment cannot provide an accurate reproduction of the energy position of 5p $\longrightarrow$ nd excitations. This explains why the agreement of the theoretical predictions with the experimental data can be expected to be at best semi-quantitative in resonant regions. Compared to the other outer valence ion states, the partial cross section

for the ionization from the $2a_1$ MO (band D of the experimental PE spectrum) exhibits a distinctly different behavior, in the predicted magnitude, as well as for the presence, in the KS profile, of a maximum at around 45 eV photon energy, which is also predicted at the TDDFT level, only superimposed on modulations due to the decay of the $5p \longrightarrow nd$ excitations. We ascribe this resonant enhancement to the occurrence of a shape resonance in the t_2 continua, and which does not affect the other ionization channels in a noticeable way, in agreement with the experimental observations[223, 224]. In fig.7.37 are reported the experimental photoionization cross section branching ratios (obtained from the data measured in this thesis at the magic angle $\theta = 54.7°$) for the A-E PE bands of OsO_4 as a function of photon energy, together with the same experimental branching ratios derived from the relative cross sections measured in ref.[224]. It is evident the very good agreement between the two independent sets of data, this confirming the high accuracy of both experimental measurements. Moreover, in the same figure, the corresponding branching ratios calculated at DFT and TDDFT level of theory in this work are reported for comparison, and also show a good agreement with both experimental data sets.

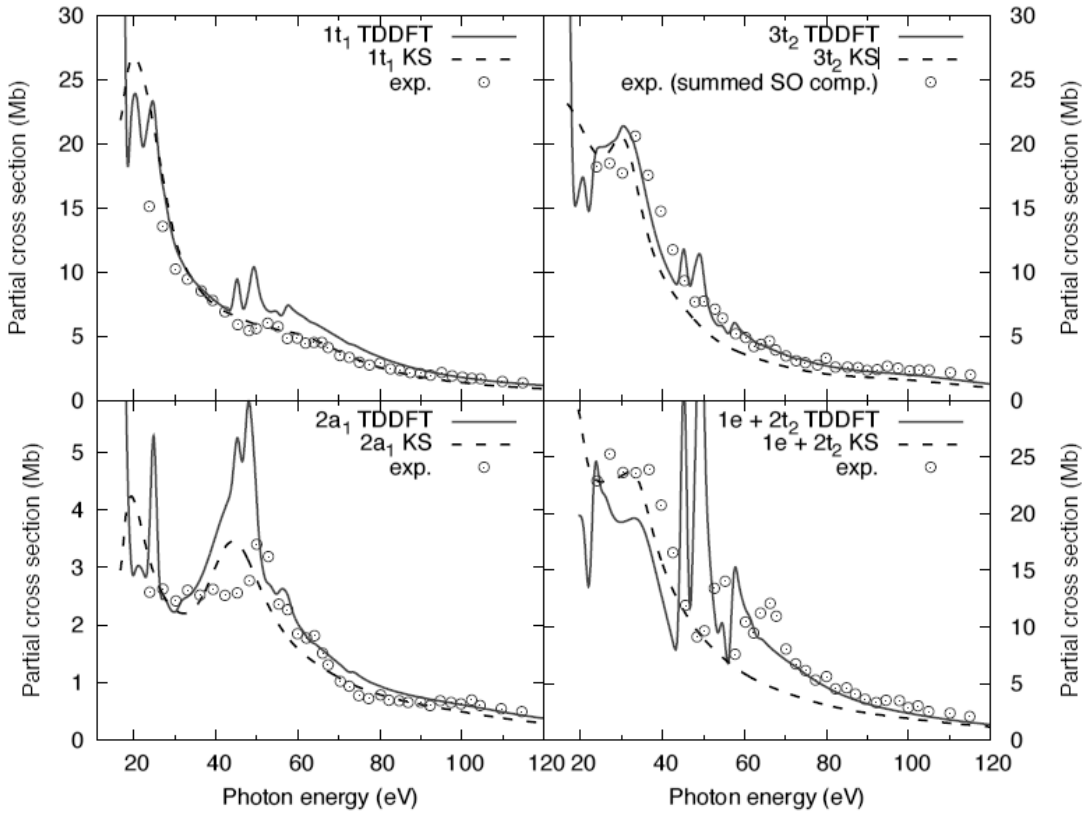

Figure 7.36: DFT (dotted line) and TDDFT (solid line) partial cross sections for the outer valence ionizations of OsO_4, compared with the experimental data (circles) taken from ref.[224].

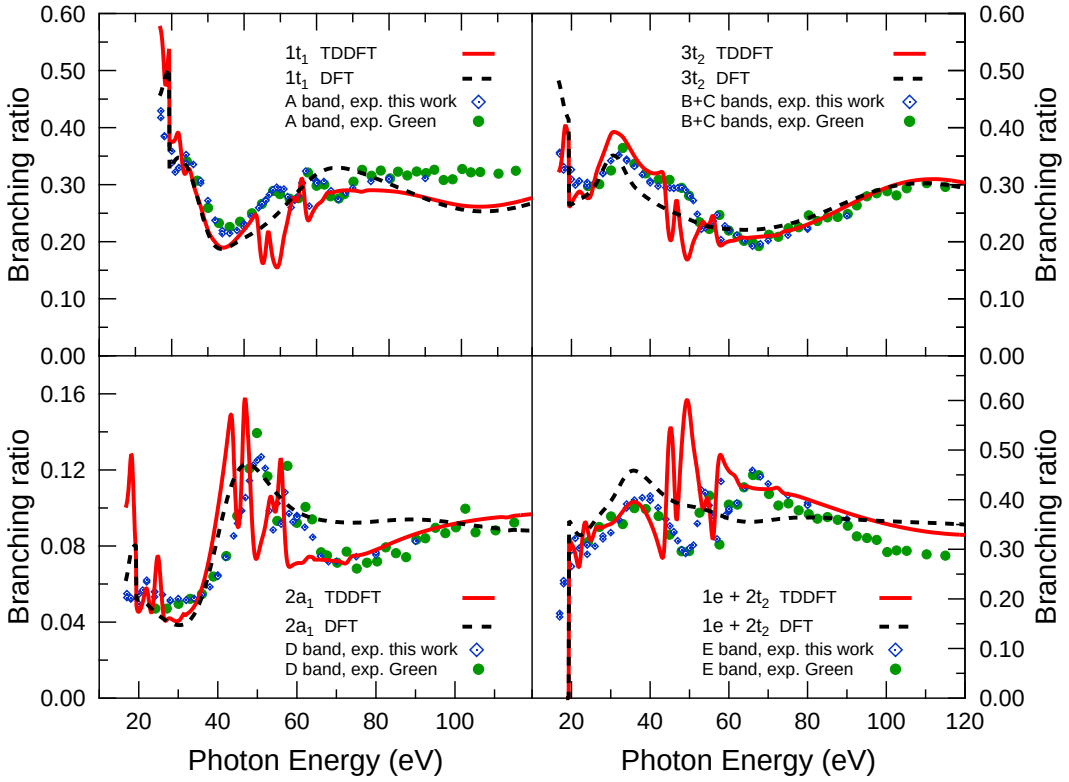

Figure 7.37: Experimental and theoretical photoionization cross section branching ratios for the outer valence ionizations (bands A-E) of OsO_4 as a function of photon energy. The two set of experimental data are from this work (red circles), and derived from Green et al.[224] (green circles). The theoretical data are obtained in this work and calculated at different levels of theory, DFT (black broken line) and TDDFT (blue solid line)

7.3.3 Osmium tetroxide: photoelectron asymmetry parameters

The asymmetry parameters $\beta(h\nu)$ associated with the OsO_4 outer valence PE bands have been studied experimentally function of photon energy in the 17-90 eV energy range. Pairs of PE spectra recorded at $\theta = 0°$ and $\theta = 54.7°$, from which the $\beta(h\nu)$ values have been derived, are reported in fig.7.38 for a representative set of photon energies.
The experimental β parameters for the outer valence ionizations of OsO_4 measured in this work are reported in fig.7.39 together with the calculated theoretical values. All the curves are characterized by a rise, from negative values close to the ionization thresholds, to positive values, except for the $2a_1$ MO, where a very pronounced oscillation in the asymmetry parameter profile is observed. The agreement between the DFT/TDDFT estimates and the experimental β data is overall very satisfactory for all PE bands, with the exception of narrow energy windows corresponding to resonant regions: the agreement can be considered quantitative for the E band ($1e^{-1}$ + $2t_2^{-1}$ ionizations), while the theoretical predictions underestimate the experimental β values for the $1t_1^{-1}$ (band A) and $3t_2^{-1}$ (band B) ionization, although the shape of the experimental profiles is closely reproduced by the calculated curves. The agreement between theory and experiment seems to be less accurate for the $2a_1^{-1}$ (band D) ionization in the threshold region, and the experimental data suggest for this ionization a more damped β oscillation in the energy interval of the shape resonance, in somewhat closer agreement with the TDDFT predictions. Above 60 eV photon energy the experimental β values are instead consistently underestimated by both DFT and TDDFT. The high-energy behavior of the asymmetry parameters profiles are somewhat MO dependent: very flat for the $1t_1$ ionization, with a broad maximum in the case of the $3t_2$ and for the ionization from the 1e and $2t_2$ MOs, while damped oscillations are superimposed on a rising background for the $2a_1$ ionization.

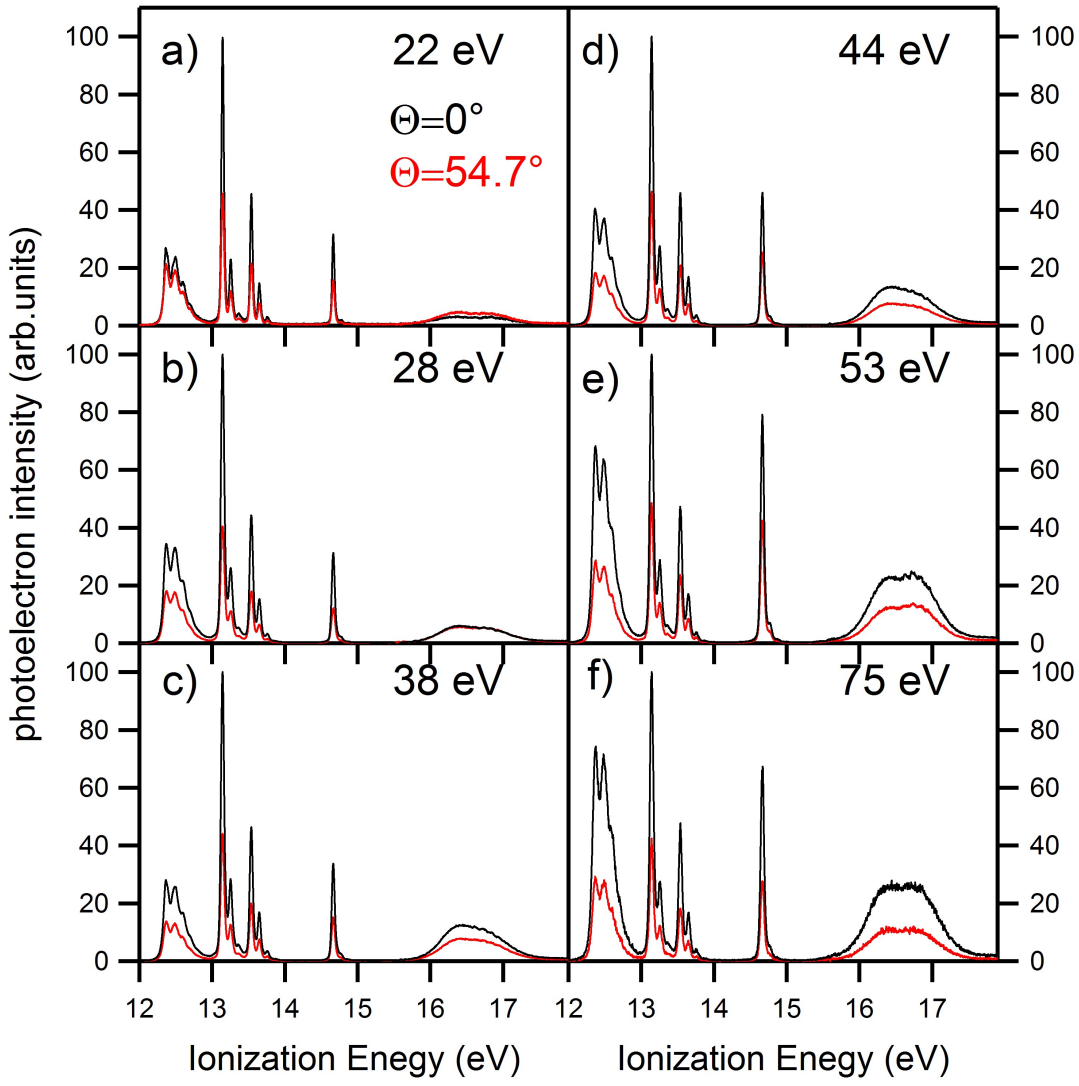

Figure 7.38: Outer valence photoelectron spectra of OsO_4 recorded at the magic angle $\theta = 54.7°$ (red curves) and $\theta = 0°$ (black curves), and at different photon energies (panels a-f).

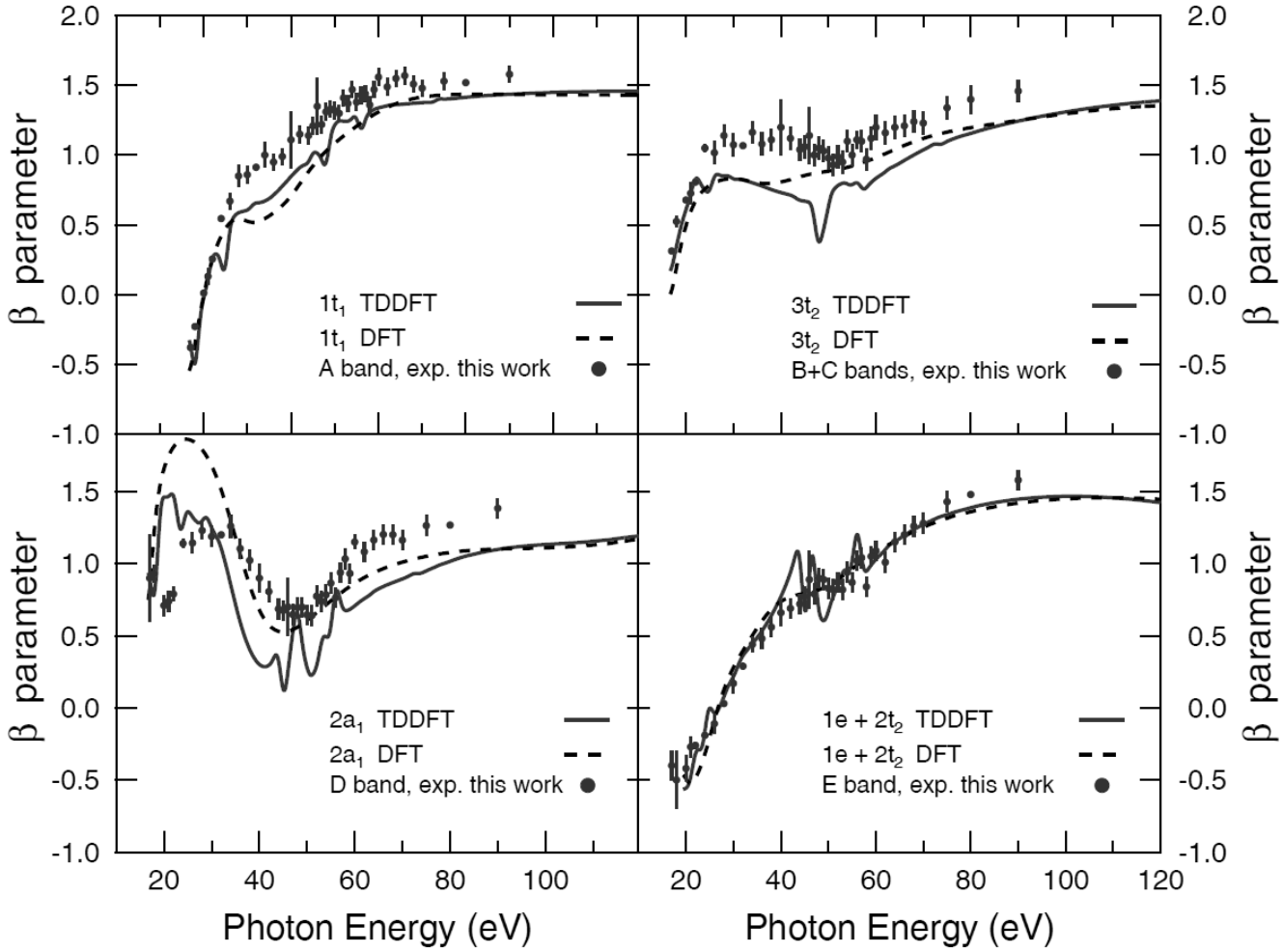

Figure 7.39: Experimental asymmetry parameter profiles for the outer valence ionizations of OsO_4 together with the calculated by DFT (broken line) and TDDFT (solid line).

7.4 Propylene Oxide

Propylene oxide is an organic compound industrially produced on a large scale, whose main application is in the production of polyether polyols in making polyurethane plastics[233]. Besides its industrial applications, propylene oxide is an important model chiral molecule and unique in having been characterized in previous experiments for directional and aligning properties by electrostatic hexapole techniques[235]. In 2016 propylene oxide has been discovered as the first chiral molecule in space by McGuire et al. by means of astronomical detection in absorption toward the Galactic center[234]. This important result highlights the relevance of a deep understanding of radiation-chiral molecule interaction since it has been suggested that enantiomers of chiral molecules can interact differently with circularly polarized radiation of define helicity, and that this mechanism can potentially generate in space an enantiomeric excess, which is considered the first step towards the evolution of life on Earth in abiotic theories[236]. Little is known on the dissociation energetics and dynamics of chiral molecules in the high energy regimes. This prompted us to investigate on the formation and dissociation processes of propylene oxide dications.

7.4.1 Propylene Oxide: dissociation channels and threshold energies

The fragmentation dynamics of the propylene oxide following single photon double photoionization were investigated in the 18-37 eV photon energy range by PEPIPICO spectroscopy with linearly polarized synchrotron radiation. The data acquisition and data analysis procedures are described in appendix B.2. As an example of the fragmentation pattern of the C_3H_6O molecule, the mass spectrum recorded at 32eV photon energy is shown in fig.7.40. The total ion mass spectrum (black solid curve in fig.7.40) exhibits several mass peaks associated with different dissociation ion products (the most relevant fragments are highlighted in the figure), as well as the mass peak of the parent ion, $C_3H_6O^+$. The experimental mass spectrum has been compared to a previously published spectrum[237] (red histogram in fig.7.40), and a very good agreement has been found.
In fig.7.41 a coincidence map recorded at 37eV photon energy is shown, together with the the total ion time of flight mass spectrum. The coincidence islands observed correspond to the various two-body fragmentation channels: for instance, at the crossing of the time of flight of the $C_2H_4^+$ ion (first ion) and the time of flight of the CH_2O^+ ion (the second ion) a coincidence map can be seen. This indicates that the two ions were produced in the same fragmentation event. Moreover, the shape and slope (45°) of the island suggest that it is a complete two-body dissociation mechanism.

A similar discussion can be done for other coincidence events.
The analysis of the coincidence maps recorded in the 18–37 eV photon energy range indicate that double photoionization of propylene oxide, produces mainly the following two-fragment ion channels:

$$C_3H_6O + h\nu \rightarrow C_3H_6O^{2+} + 2e^- \rightarrow C_2H_4^+ + CH_2O^+ \quad (1)$$
$$C_3H_6O + h\nu \rightarrow C_3H_6O^{2+} + 2e^- \rightarrow C_2H_3^+ + CH_3O^+ \quad (2)$$
$$C_3H_6O + h\nu \rightarrow C_3H_6O^{2+} + 2e^- \rightarrow CH_2^+ + C_2H_4O^+ \quad (3)$$
$$C_3H_6O + h\nu \rightarrow C_3H_6O^{2+} + 2e^- \rightarrow CH_3^+ + C_2H_3O^+ \quad (4)$$
$$C_3H_6O + h\nu \rightarrow C_3H_6O^{2+} + 2e^- \rightarrow C_3H_6^+ + O^+ \quad (5)$$
$$C_3H_6O + h\nu \rightarrow C_3H_6O^{2+} + 2e^- \rightarrow OH^+ + C_3H_5^+ \quad (6)$$

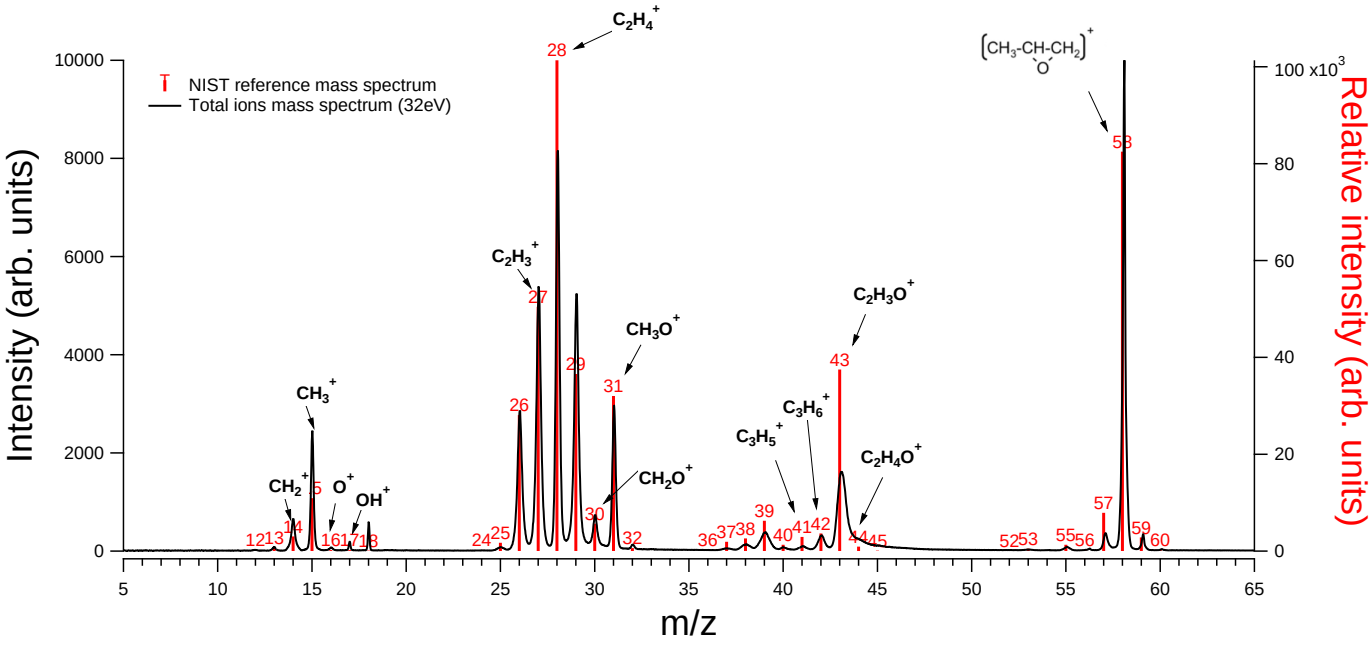

Figure 7.40: Total ions mass spectrum of propylene oxide recorded at 32eV photon energy (black curve) and its comparison with the NIST[237] reference electron impact mass spectrum (red histogram). The ion products of the main dissociation channels are also highlighted.

The relative abundance for each dissociation channel is reported in tab.7.4. The most abundant fragmentation reaction (∼67% of the total average yield) is the channel (1) in tab.7.4 arising from the C1-C2 and C2-O bonds breaking in the $C_3H_6O^{2+}$ molecular dication (see fig.7.42). The lighter ion $C_2H_4^+$ (m/z = 28) is the most abundant in the mass spectrum of propylene oxide published by NIST[237], while the heavier one (CH_2O^+, m/z = 30) is also present but with lower abundance, as confirmed by previous experimental results[238, 239]. The second most abundant channel is reaction

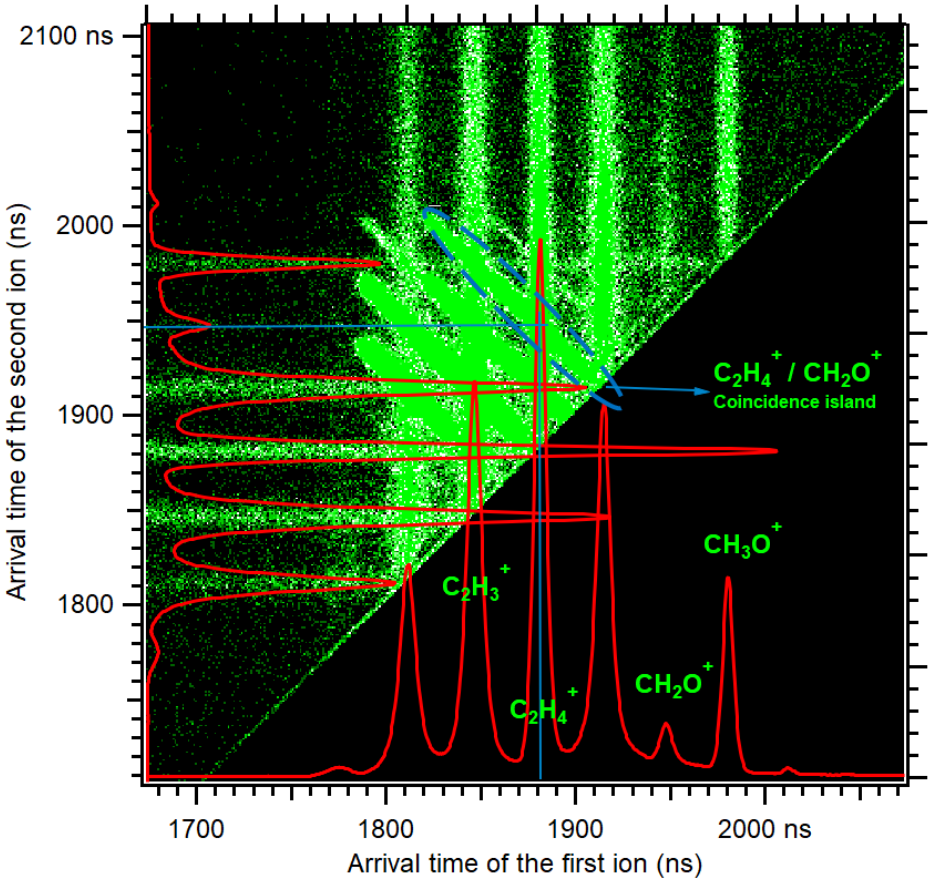

Figure 7.41: A portion of the mass spectrum and ion–ion time-of-flight correlation of ions produced by single and double photoionization of propylene oxide at 37.0 eV. The coincidence plot is related to the main recorded fragmentation channels leading to $C_2H_4^+/CH_2O^+$ and $C_2H_3^+/CH_3O^+$ product ions. In such type of bidimensional plot, which is typical of double photoionization experiments, the two time-of-flight values of a couple of ions produced in the same photoionization event define a point.

(2), with a relative abundance of ∼18%, arises from the same bond breaking as reaction (1) but with a hydrogen atom migration from the C_2H_4 moiety to the CH_2O^+ moiety. Reactions (3) and (4) in tab.7.4, namely CH_2^+ + $C_2H_4O^+$ (m/z=14 and m/z=44) and CH_3^+ + $C_2H_3O^+$ (m/z=15 and m/z=43), with relative yields of ∼8% and ∼5%, respectively, are also related by H-exchange, even if also a direct bond breaking can occur (refer to fig.7.42). In reaction (5), $C_3H_6^+$ + O^+ (m/z=42 and m/Z=16), an oxygen atom is lost after the C1-O and C2-O bonds breaking with charge separation, while reaction (6) in tab.7.4 arises from a similar dissociation mechanism with a hydrogen atom migration on the oxygen atom, leading to the two $C_3H_5^+$ (m/z=41) and OH^+ (m/z=17) fragments. Both channels are characterized by a very low abundance, ∼2% for channel (5) and ∼0.2% for channel (6).

More information can be thus extracted from a coincidence experiment

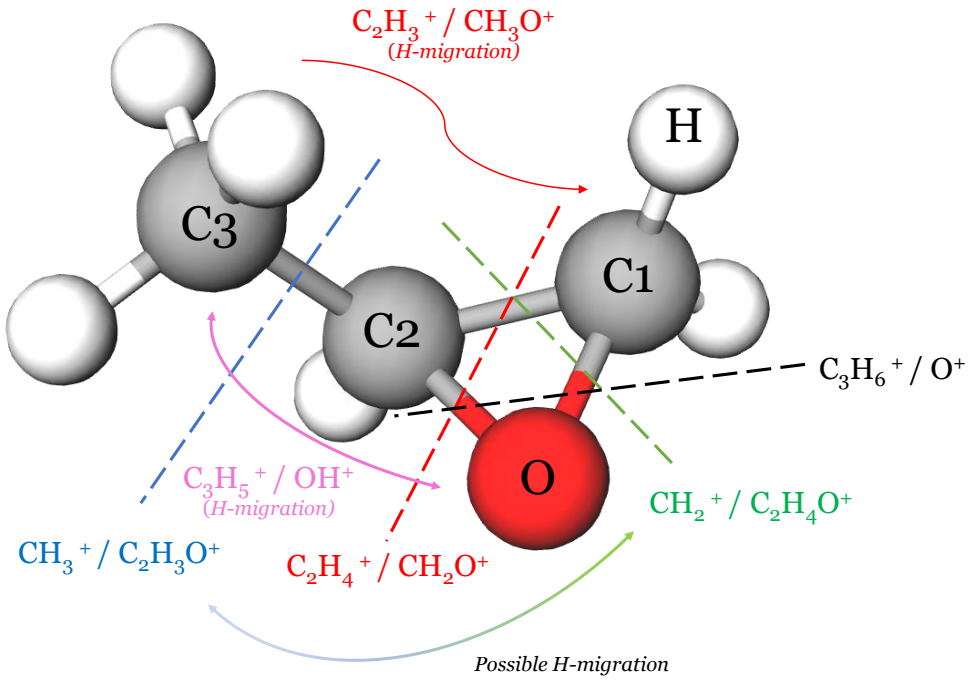

Figure 7.42: Scheme of the possible fragmentation patterns in the VUV double photoionization of propylene oxide based on the results of tab.7.4.

Table 7.4: Product ions of the double ionization of propylene oxide, their average abundance at the photon energies investigated, Kinetic energy released (KER) and the relevant threshold energies.

Dissociation channel	Average abundance (%)	E^a_{max}, KER of the heavier ion (eV)	E^a_{max}, KER of the lighter ion (eV)	E^a_{max}, total KER (eV)	Threshold energy (eV)
1 $C_2H_4^+ + CH_2O^+$	66.70	2.3±0.2	2.5±0.2	4.9±0.3	28.3±0.1
2 $C_2H_3^+ + CH_3O^+$	18.70	2.4±0.2	2.8±0.2	5.3±0.3	29.2±0.1
3 $CH_2^+ + C_2H_4O^+$	7.84	1.0±0.2	3.1±0.2	4.2±0.3	28.5±0.1
4 $CH_3^+ + C_2H_3O^+$	5.00	1.5±0.2	4.5±0.2	6.1±0.3	29.0±0.3
5 $C_3H_6^+ + O^+$	1.59	1.2±0.2	3.3±0.2	4.7±0.3	29.0±0.2
6 $OH^+ + C_3H_5^+$	0.17	*	*	*	32.1±0.3

[a]: value of the KER at the maximum of the distributions.
*: too weak to extract the KER distributions.

such as the one performed on the propylene oxide with respect to a simple ion mass spectrum. At each photon energy, the total counts of ion pairs (coincidence islands in fig.7.41) triggered by the electrons produced in

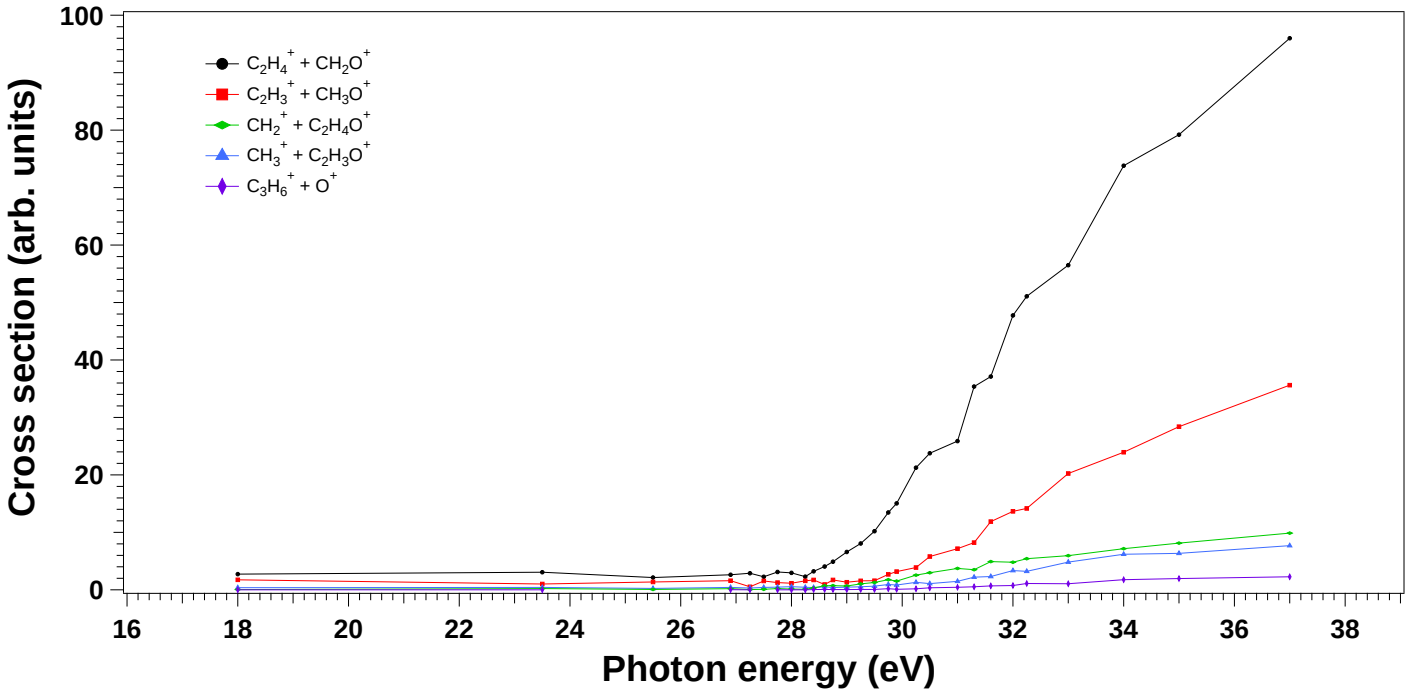

Figure 7.43: Relative cross section for the ion-ion fragmentation channels from the double photoionization of propylene oxide in the 18.0–37.0 eV photon energy range. The process leading to $OH^+ + C_3H_5^+$, also observed, has not been reported in the graph because of too low intensity.

the double photoionization process and detected in coincidence give the intensity and the cross section of the two-body fragmentation channels. In order to study the threshold and the energy dependence of the two-body dissociative channels (see tab.7.4), we have integrated the density of the ion pair coincidence events, normalized with respect to the total ion yield, as a function of the photon energy. The results are plotted in Fig.7.43 for all fragmentation channels of tab.7.4 (except the least intense one that is reported in the sixth row) while in Fig.7.44 the relative cross sections for the same channels with their relative threshold energies are shown separately.

For each open dissociation channel, the threshold energy were determined by using the Wannier threshold law[240], which has the form:

$$\sigma^{++}(E) = \sigma_0^{++}(E_\gamma - IE^{++})^n \qquad (7.4.1.2)$$

in which σ_0^{++} is the constant of proportionality ($\sigma_0^{++} = \sigma^{++}$ for $(E_\gamma - IE^{++}) = 1\text{eV}$), E_γ is the photon energy, IE^{++} is the double photoionization threshold, and n is the Wannier parameter. For systems with high number of electrons, the threshold law is usually approximated by a linear function, i.e. n=1[242]. The Wannier function has been applied in many experimental works in order to extract the double photoionization thresholds[243, 244, 245]. The appearing potential for the main dissoci-

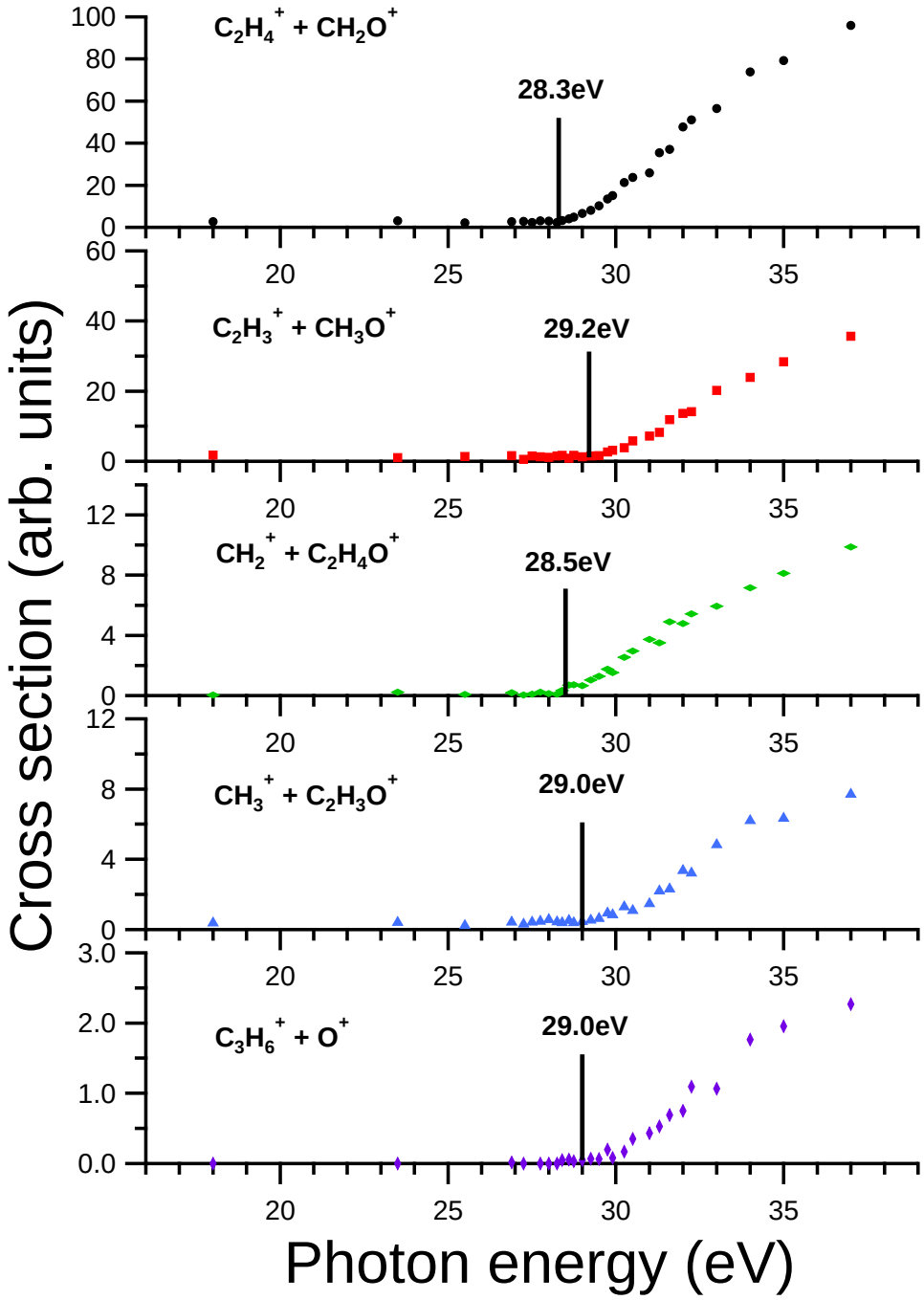

Figure 7.44: Threshold energy for the ion-ion dissociative processes following the double photoionization of propylene oxide. The process leading to OH^+ $C_3H_5^+$, also observed, has not been reported in the graph because of too low intensity.

ation channels are reported in tab.7.4. An indirect estimate of the first double photoionization potential of propylene oxide, which can be compared to the lowest threshold energy of the ion-ion dissociation channels, can be extracted from the analysis of the core-level photoelectron and normal Auger spectra, reported by Piancastelli et al.[246]. In fact, the interpretation of the Auger spectra can be achieved by using a procedure developed by Cini et al.[247], which is based on the calculation of the self-convoluted local density of state (LDOS) at the C and O atoms, in the case of propylene oxide. In this model, the adiabatic DIP is given by the following formula.

$$DIP = IE_{v1} + IE_{v2} + U \tag{7.4.1.3}$$

Where IE_{v1} and IE_{v2} are the binding energies of the valence orbitals in which the final holes are located, in the specific case both at the HOMO, while U is the effective hole-hole interaction energy in the model. For the adiabatic DIP both IE_{v1} and IE_{v2} can be substituted by the value of 10.44 eV (the first ionization energy of propylene oxide from reference 8 in [246]), while U is estimated from Piancastelli et al. to be 10eV in the case of the C KVV normal Auger spectrum. Considering an additional energy shift of -1.7eV, necessary to have a quantitative match between the calculated LDOS Auger spectrum and the experimental one, from the work of Piancastelli et al. we estimated a double photoionization threshold of 29.2 eV. Such a result was confirmed by Alberti et al.[248] in C 1s excitation and ionization of propylene oxide studied by means of photoabsorption, photoemission, and photoelectron-Auger electron coincidence experiments using linearly and circularly polarized synchrotron radiation. Another method to estimate double photoionization thresholds has been given by Molloy et al.[249] in the form of an empirical formula which relates the lowest double ionization energy to the lowest single ionization potential of the same molecules (IE^+ in eq.(7.4.1.4)).

$$DIP = 2.8 \times IE^+ \tag{7.4.1.4}$$

Equation (7.4.1.4) works surprisingly well for a wide range of closed shell molecules. Using this "rule of thumb", where in our case $IE^+ = 10.44$eV, again a DIP value of 29.2eV is obtained.
In the experiment presented in this thesis, we directly estimate the first double photoionization energy as the lowest threshold energy for the propylene oxide molecule of 28.3±0.1eV (reaction (1) of tab.7.4), which is in reasonable agreement with the indirect estimate of 29.2eV. Moreover, we identified and measured the threshold energies for each opened two-body dissociation channel presented in tab.7.4.

7.4.2 Propylene Oxide: KER distribution

The KER distributions of the two ion products of the main decay channels, reported in tab.7.4, have been analyzed as a function of photon energy [see appendix B.2]. The results are reported in figures 7.45, 7.46, 7.47. An important result is that the intensity of the KER peaks depend on the photon energy, but their positions and shapes do not change appreciably. It is well known that all microscopic photochemical processes leading to two-body fragmentations are driven by the dynamics on multidimensional potential energy surfaces, leading to both ionic and neutral fragment products which involve avoided curve crossing, saddle points, and various non adiabatic couplings, determining the opening toward the exit channels. On the basis of the present experimental findings, some qualitative considerations on the dynamics associated with the ion-ion separation coordinates can be made. Particularly, the observation that the peak position and shape of KER do not change with the photon energy suggests that the excess energy, that is the difference between the incident photon energy and the appearance energy of the considered channel, is distributed either in the internal degrees of freedom of the fragment ions or in the kinetic energy of the ejected electrons, or both. The KER peak positions for the various channels are reported in tab.7.4, while in figures 7.45, 7.46, 7.47 the KERs for reactions (1)-(5) are shown. It was not possible to determine KER distributions related to product ions of reaction (6) due to the too low intensity of recorded signals for OH^+ + $C_3H_5^+$ coincidences.

The symmetric shape of the KER distributions makes easy fitting by a simple Gaussian function. This can be considered as a clear indication that each fragmentation channel involves a well-defined single specific region on the multidimensional potential energy surface,associated with the effective intramolecular interaction within the $C_3H_6O^{2+}$ molecular dication frame and responsible for the opening of the various two-body fragmentation channels, at all investigated photon energies. Therefore, for all investigated fragmentation reactions, the excess of the used photon energy with respect to the double ionization threshold energy should be released as the kinetic energy of ejected electrons. The only exception is constituted by the recorded total KER distribution for CH_3^+ + $C_2H_3O^+$ product ions, shown in fig.7.47 for the investigated photon energy range, and in fig.7.48 for two selected above threshold photon energies, namely 35.0eV and 37.0eV. It is evident that these total KER distributions are characterized by a bimodal behavior, previously observed also in the fragmentation of other molecular dications. such as CO_2^{2+} and $C_2H_2^{2+}$[250, 251]. In fig.7.48, the data are best fitted (full line) by the combination of two Gaussian functions (dashed lines), clearly indicating a bimodal behavior, depending on two possible microscopic mechanisms for the two-body fragmentation of this channel. This is an indication that the reaction CH_3^+ + $C_2H_3O^+$ may occur by two different pathways: in one case (the most

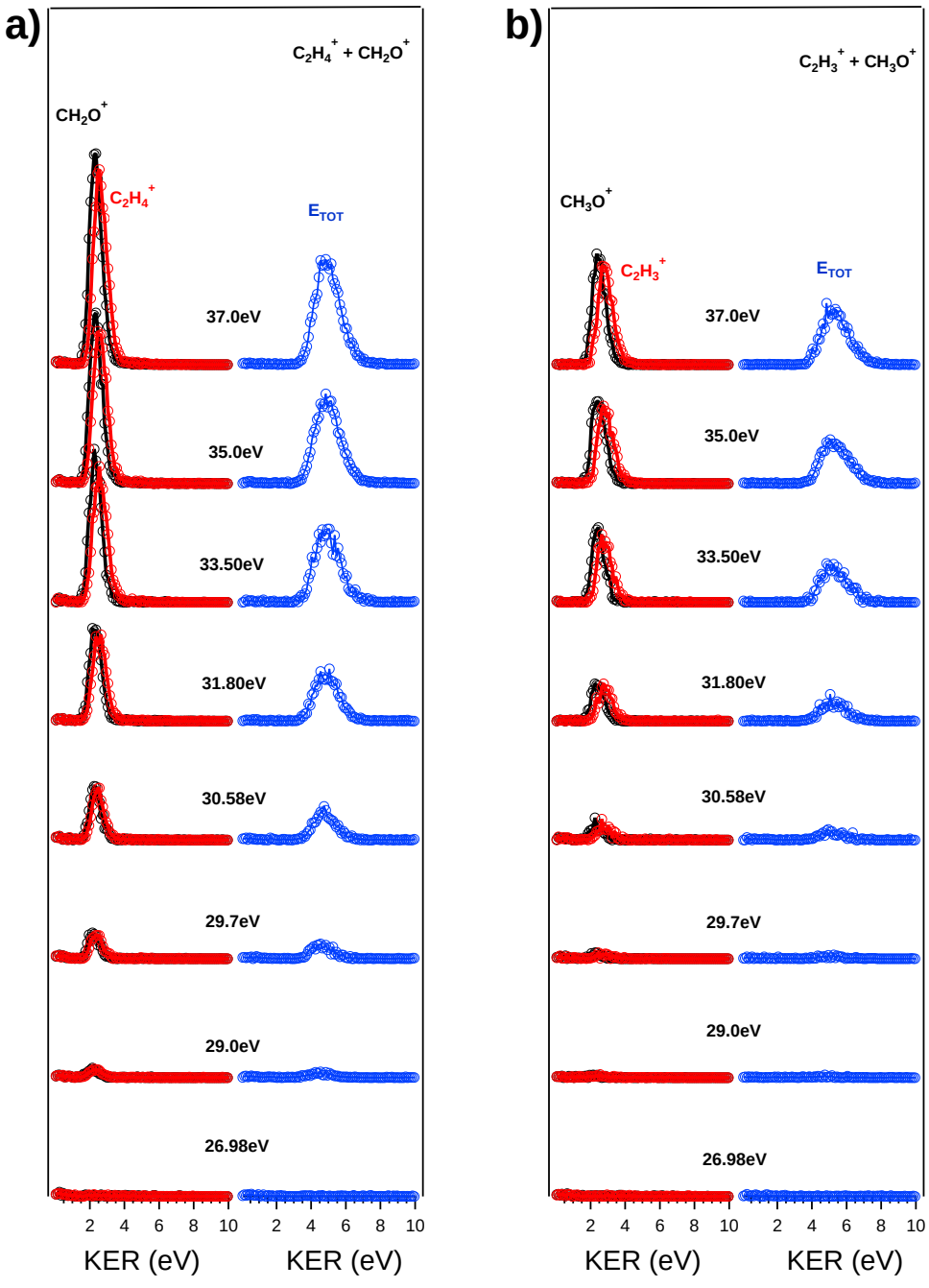

Figure 7.45: The KER distributions of the $C_2H_4^+ + CH_2O^+$ (blue line panel *a*) and $C_2H_3^+ + CH_3O^+$ (blue line panel *b*) formed in the double photoionization of propylene oxide, at different photon energies. The KER distribution for the heaviest ion (black line) and the lightest ion (red line) of each channel are also reported in function of the photon energy.

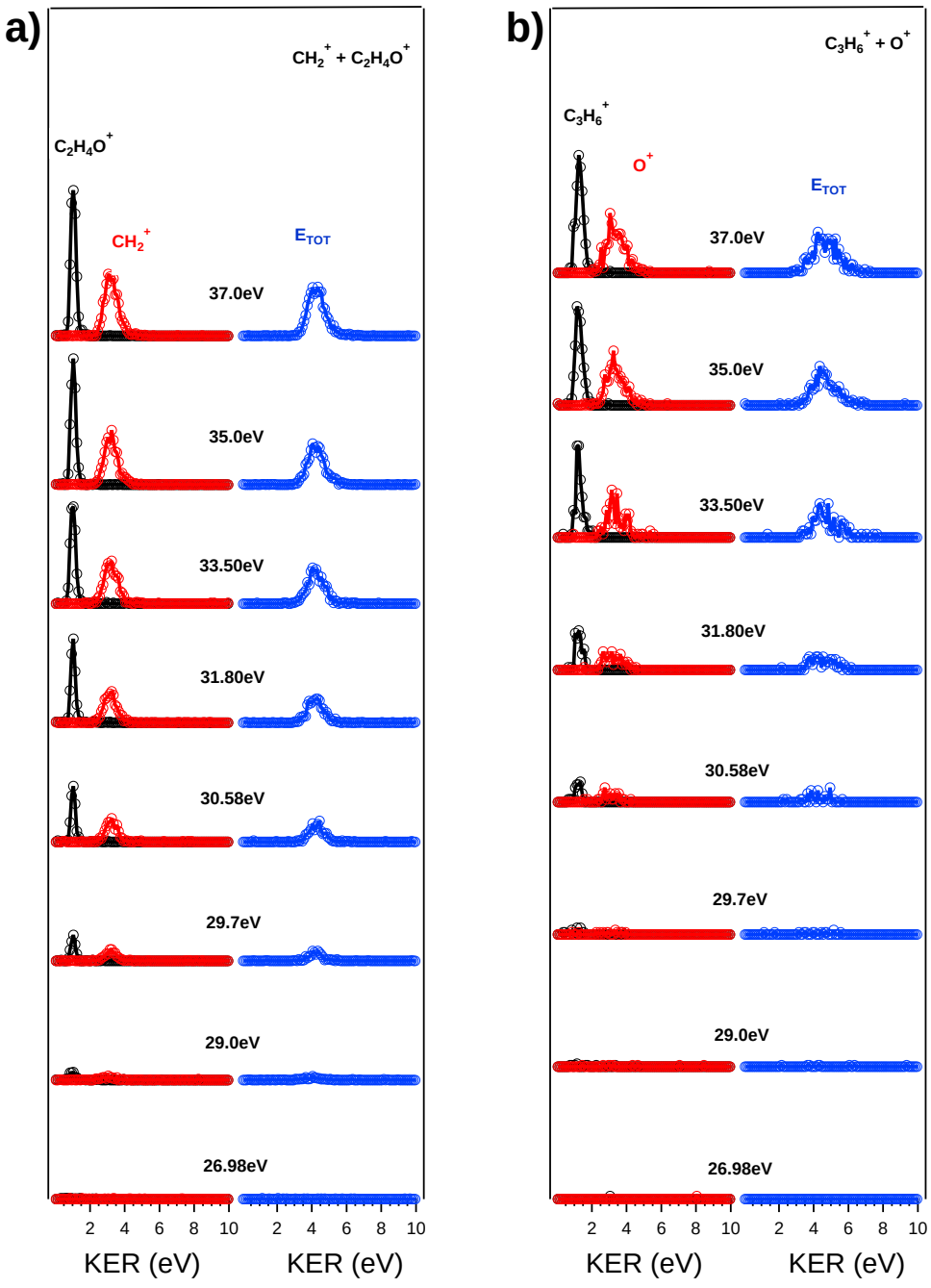

Figure 7.46: The KER distributions of the $CH_2^+ + C_2H_4O^+$ (panel *a*) and $C_3H_6^+ + O^+$ (panel *b*) formed in the double photoionization of propylene oxide, at different photon energies. The KER distribution for the heaviest ion (black line) and the lightest ion (red line) of each channel are also reported in function of the photon energy.

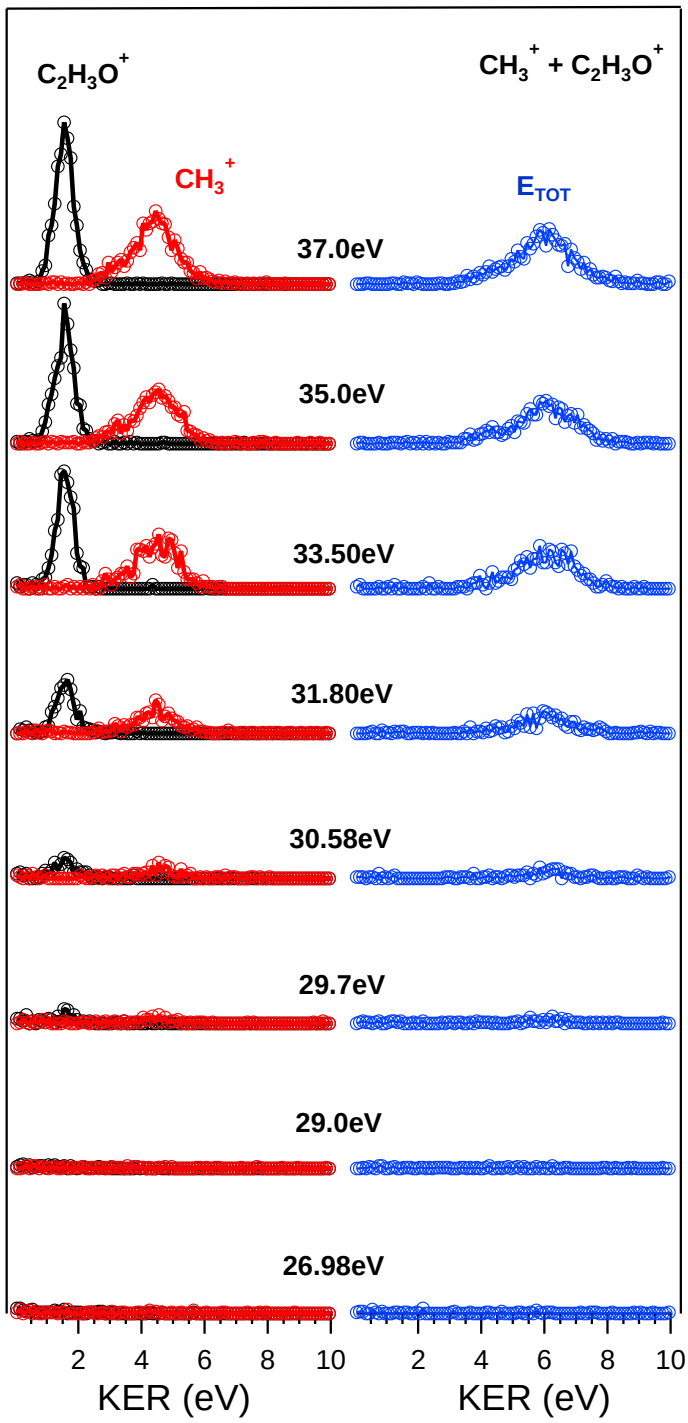

Figure 7.47: The KER distributions of the $CH_3^+ + C_2H_3O^+$ formed in the double photoionization of propylene oxide, at different photon energies. The KER distribution for the heaviest ion (black line) and the lightest ion (red line) of each channel are also reported in function of the photon energy.

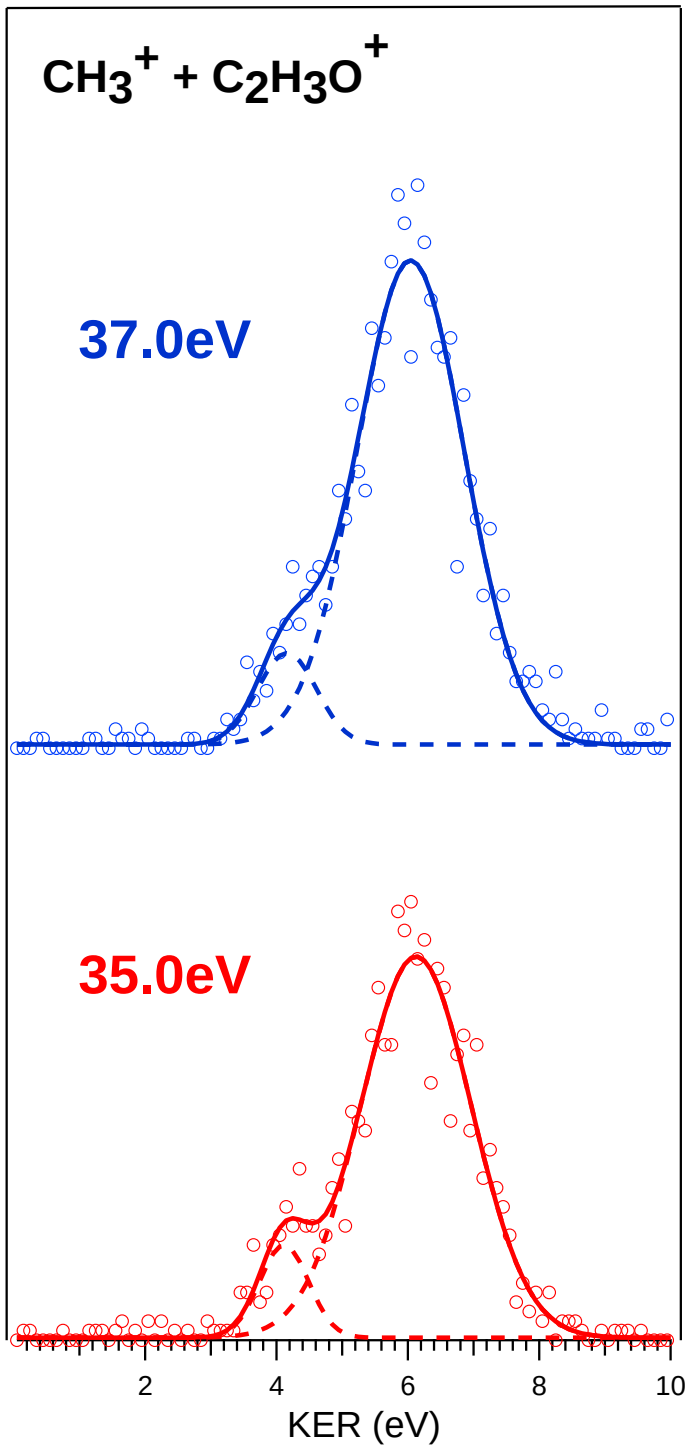

Figure 7.48: The KER distributions of the $CH_3^+ + C_2H_3O^+$ formed in the double photoionization of propylene oxide, at two different photon energies, namely 35.0eV (red line) and 37.0eV (blue line). In the figure, the data (markers) are best fitted (full line) by a sum of two Gaussian functions (dashed line), indicating a bimodal behavior fingerprint of two competing microscopic mechanisms.

important one), the two microscopic mechanisms can involve a direct fragmentation of the molecular dication into CH_3^+ and $C_2H_3O^+$ products and different internal energy states of $C_2H_3O^+$. In the second mechanism, the fragmentation can also involve an internal rearrangement of the molecular bonds of the dication and possible atom migration. Moreover, it should be pointed out that CH_3^+ and $C_2H_3O^+$ fragments can also be formed in an electronically excited state. Therefore, two distinct mechanisms occur for the dynamics along paths in multidimensional potential energy surfaces of the intermediate dication produced in the double photoionization process, accompanied by its breaking in two fragments. Moreover, from the measured KERs, assuming that the KER is coming simply from the Coulomb repulsion (being the dominant interaction component), it is possible to estimate that the main and the less important channels start from 2.4 and 3.6 Å separation distances between ionic fragments. For the other ion-ion dissociation channels (reactions 1-5), the same KER analysis suggests that only one critical distance is operative, intermediate between two values given above.

For a deeper insight into the dissociation yielding the reaction products $CH_3^+ + C_2H_3O^+$ it is worth considering the work by Nobes et al.[252] on the structure and stability of the gas-phase $C_2H_3O^+$ ion. These authors found that only three different isomers of $C_2H_3O^+$, shown in fig.7.49, can be stable and observable species in gas-phase experiments. This was also confirmed experimentally by Burges et al.[253]. In order of their decreasing energetic stability, the most stable is the acetyl cation $[CH_3CO]^+$ (structure I in fig.7.49) which is followed by the 1-hydroxyvinyl cation $[CH_2CHOH]^+$ (structure II in fig.7.49), and finally the less stable is the cyclic oxiranyl cation $[CH_2CHO]^+$ (structure III in fig.7.49). The first two isomers are characterized by a linear structure, while the oxiranyl is a cyclic isomer with a triangular $[C\cdots O\cdots C]$ ring. It has to be noted that the difference in the relative energy between the most stable acetyl cation and the two other isomers is not very different. The acetyl cation is 181 $KJmol^{-1}$ ($\approx$ 1.87eV) more stable respect to the 1-hydroxyvinyl cation, while the oxiranyl cation is located at 244 $KJmol^{-1}$ ($\approx$ 2.53eV) above the more stable acetyl cation[252]. The experimentally measured energy difference between peak maxima of the two Gaussian functions used to best fit the recorded KER of the $CH_3^+ + C_2H_3O^+$ channel, is equal to $\approx 2.1 \pm 0.3$ eV, and corresponds within the quoted error to the difference in the translational energy of the two possible $C_2H_3O^+$ ion isomers produced via two different microscopic mechanisms, following the Coulomb explosion of the intermediate $[C_3H_6O]^{2+}$ dication. Even tough the experimental value of 2.1 eV is very close to both the energy differences between the 1-hydroxyvinyl cation and the acetyl one, and the oxyranil and acetyl ions (the energy difference of $\approx$0.7eV between the oxyranil and 1-hydroxyvinyl cations is too small to be considered in the discussion), it seems to fit better with the formation of the most stable linear acetyl cation with a higher translational energy content, to which we can associate the KER distribu-

tions centered at about 6.1eV in fig.7.48, and the formation of the cyclic oxiranyl isomer, to which we can relate the less intense KER distributions of fig.7.48 located at about 4.0 eV, which is produced with a lower kinetic energy respect to the previous one, being ≈2.53eV less stable than the other. Of course, we cannot exclude completely the possible formation of the 1-hydroxyvinyl cation, but the fact that its production by Coulomb explosion of the molecular dication should involve a hydrogen shift toward the Oxygen atom, resulting in a ring opening, and the fact that the 1.87 eV energy difference in stability between acetyl and 1-hydroxyvinyl isomers, as calculated by Nobes et al., do not fit properly with the difference in the translational energy characterizing the formation of $C_2H_3O^+$ ions from the two different recorded mechanisms, make this hypothesis less probable.

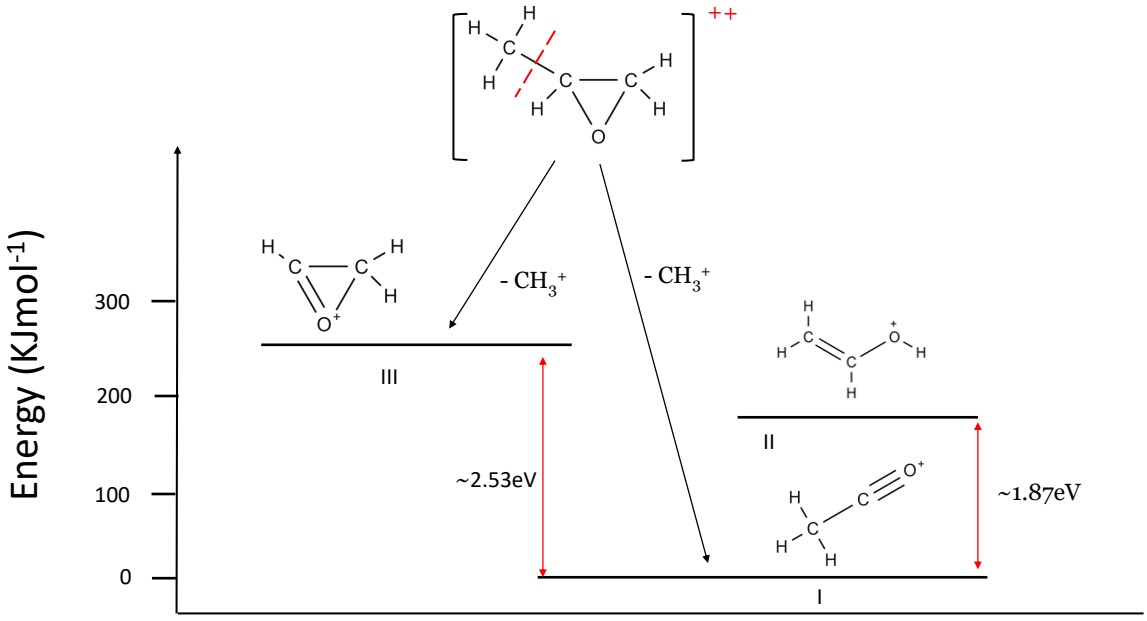

Figure 7.49: Semiquantitative energetic schematic diagram showing the two competing microscopic mechanisms for the unimolecular fragmentation of the intermediate propylene oxide dication forming the two more probable $C_2H_3O^+$ isomers of channel (4) in tab.7.4: the oxiranyl cation (structure III) and the acetyl cation (structure I). In the figure is reported also the third possible stable isomer, the hydroxyvinyl cation (structure II).

7.4.3 Propylene Oxide: photoions angular distribution

The angular distributions measured with respect to the polarization axis of the linearly polarized synchrotron radiation of all ion pairs of reactions 1-5 have been measured as a function of photon energy. The projection of the 3D ion distributions on the plane of the MCP (2D images) have been analyzed, and their best fit allowed to obtained the symmetry parameter of the ion pair angular distribution. These results are reported in figures 7.50, 7.51 and 7.52, at selected photon energies, namely 29.7, 30.6, 31.8, 33.5, 35.0, and 37 eV. The red curves in the figures are obtained as best fit of the experimental data (black dots) using a procedure based on eq.(5.5.0.4), and satisfying the total angular momentum conservation condition of the two fragment ions (see appendix B.2). The derived β values and the associated errors are also reported. Panel *b* of fig.7.52 shows that at photon energies sufficiently above threshold, i.e. 37.0 eV, all the dissociation channels exhibit an anisotropic value of β, that ranges from 0.59 to 0.65, the only exception being the channel $C_3H_6^+ + O^+$ who shows an isotropic distribution ($\beta \sim 0$) in the entire investigated photon energy range (see panel *a* of fig7.50). This difference is an indication that channel (5) proceeds with a different mechanism with respect to the other dissociation reactions, which instead show an anisotropic behavior of the asymmetry parameter. It is worth noting that the anisotropy in the angular distribution of the emitted fragment ions can appear only if the separation of the two ionic fragments in the dissociative double ionization takes place in a period shorter than the rotational period of the molecular dication involved in the Coulomb explosion. At variance with reaction 5 the other two-body fragmentation channels, reactions (1)–(4), appear to be characterized by two different contributions being active in their respective angular distributions of ion pair products (see figures 7.50,7.51 and 7.52): an isotropic contribution which is dominant near the ionization threshold (low photon energies) with $\beta \sim 0$, and an anisotropy component (with ions emission preferentially in a parallel direction with respect to the polarization vector of the light) increasing as the photon energy increases, reaching the maximum values at 37.0 eV, the highest investigated photon energy, equal to 0.63 for the $C_2H_3^+ + CH_3O^+$ reaction (panel *b* of fig.7.50), 0.59 for channel $CH_3^+ + C_2H_3O^+$ (panel *a* in fig.7.51), 0.63 for the channel $C_2H_3^+ + CH_3O^+$ (panel *b* in fig.7.51), and 0.61 for the channel $CH_2O^+ + C_2H_4^+$ (panel *a* in fig.7.52). This observation is an indication that for reactions (1)-(4) the intermediate molecular dication of propylene oxide at low photon energies, i. e. near threshold (on average up to about 31.0 eV), should be formed in its ground electronic state characterized by a lifetime longer than its typical rotational period of the order of 10^{-10}-10^{-12} *s*[254] with a consequent isotropic fragment ions emission by a slow charge separation mechanism ($\beta \approx 0$) in the related recorded angular distributions. At higher photon energies it should be possible to

form excited vibronic states of the propylene oxide dication characterized by shorter lifetimes, that can lead to the opening and progressive increase of an anisotropic component in the recorded angular distributions. The experimental setup used in this PEPIPICO experiment can probe a time window from about 50 ns up to 2.5 μs, depending on the used experimental set up. Thus, in the absence of evidences in the recorded coincidence maps of any traces due to metastable dications (see next section), it is only possible to fix an upper limit of ∼50 ns for the lifetime of the intermediate propylene oxide molecular dication formed in our experimental conditions. The reaction yielding $CH_3^+ + C_2H_3O^+$, although displays an increase of the asymmetry parameter as a function of photon energy, is characterized by a different behavior with respect to dissociation channels (1), (2) and (3). It can be seen from fig.7.51 (panel a) that the angular distribution of the ion products of this channel preserves a clear isotropic character ($\beta \approx 0$) up to the recorded distribution at a photon energy of 31.8 eV. Such observation is consistent with the bimodal behavior observed in the KER dostributions of the channel, and could be due to two different microscopic mechanisms involved in the two-body fragmentation process, as discussed in the previous section.

7.4.4 Propylene oxide: metastable ions

Molecular dications are usually thermodynamically unstable and tends to dissociate into two singly charged fragment ions because of the coulombic repulsion which dominates the long range interaction between the two fragments. However, stable and metastable molecular dications can be experimentally observed due to the fact that at short range covalent bonding can overcome the repulsive coulombic forces within the molecule. The interplay between these forces determines the stability of the molecular dication; the forces are finely balanced in metastable states where molecular dications are stable for nanoseconds or longer and then fragment. Many metastable molecular dications have been experimentally observed with the same PEPIPICO techinques presented in this thesis[245, 255, 256, 257].
The typical signature of metastable decay of a doubly charged ion is a "stripe" of intensity distribution extending across the coincidence map, from the island of the ion pair to a point on the map diagonal (where the times of flight of the two ions are equal) that correspond to the flight time of the doubly charged parent ion. A second branch of intensity extends upwards from the same diagonal point, making a complementary angle to the diagonal itself. This pattern forms a "V" shape near the diagonal and the lengths of the two arms of the "V" are related to the kinetic energy released in the charge separation process[258]. The coincidences along the "tail" are due to the fragmentation of the metastable molecular dication in the ionization source and acceleration regions of the time-of-flight mass spectrometer, whereas the coincidences in the "V" are due to metastable

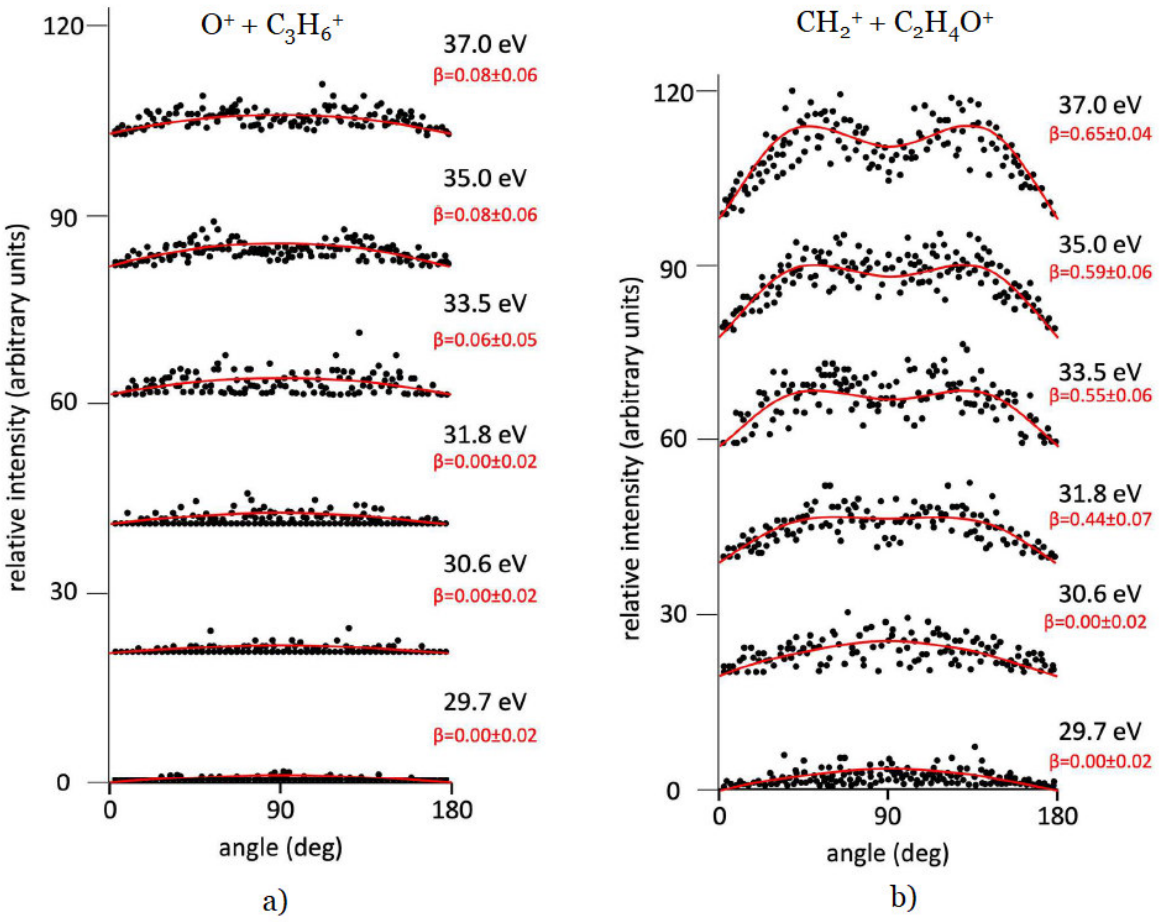

Figure 7.50: Angular distributions of the $C_3H_6^+ + O^+$ (panel *a*) and $CH_2^+ + C_2H_4O^+$ (panel *b*) channels as a function of the photon energy. Dots intensity in the ordinate axis are in arbitrary units, and the error bars are omitted for clarity being of the same order of magnitude of the dot dimensions. On the right side is also reported the anisotropy parameters referred to related photon energy.

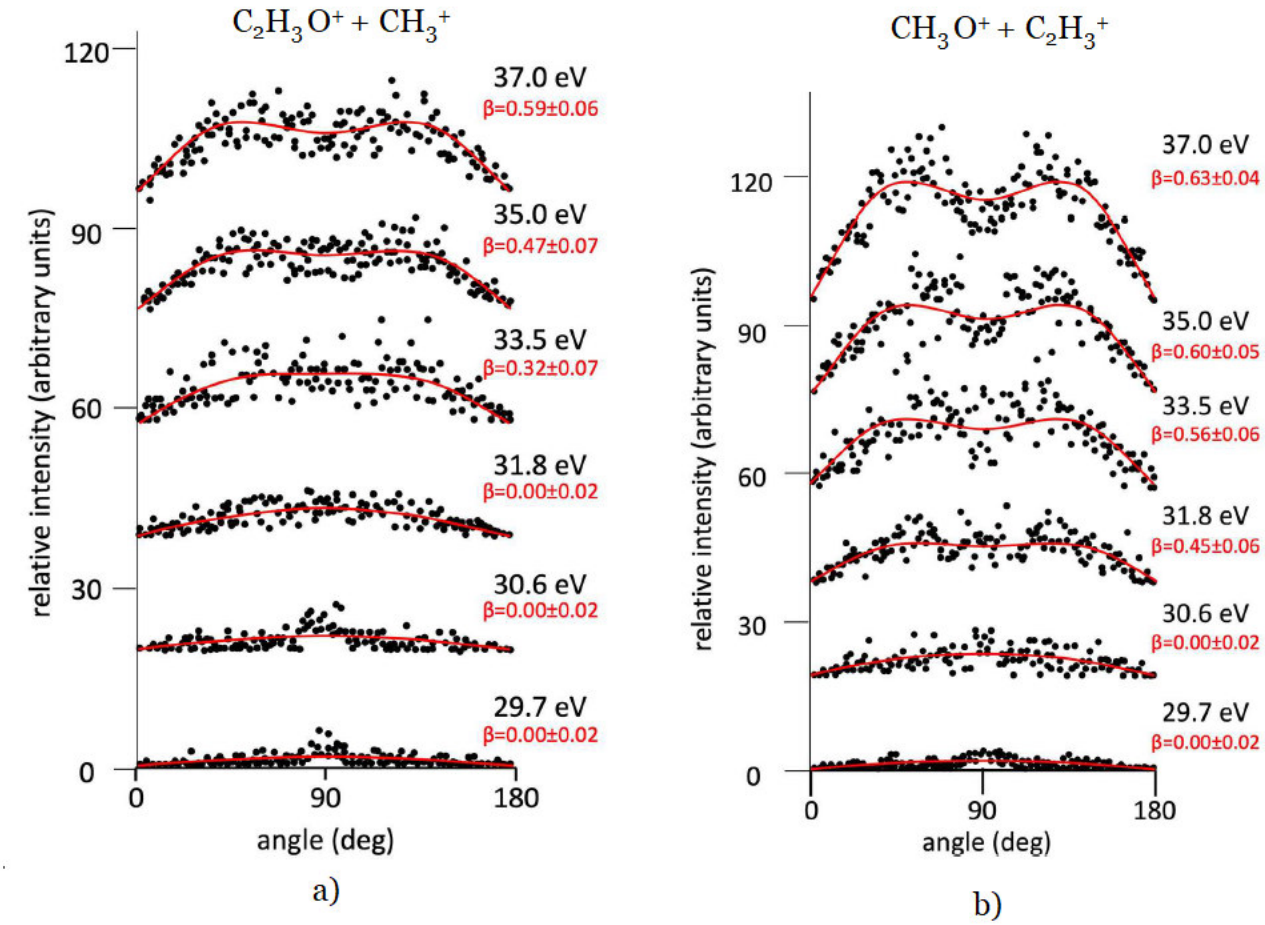

Figure 7.51: Angular distributions of the $CH_3^+ + C_2H_3O^+$ (panel *a*) and $C_2H_3^+ + CH_3O^+$ (panel *b*) channels as a function of the photon energy. Dots intensity in the ordinate axis are in arbitrary units, and the error bars are omitted for clarity being of the same order of magnitude of the dot dimensions. On the right side is also reported the anisotropy parameters referred to related photon energy.

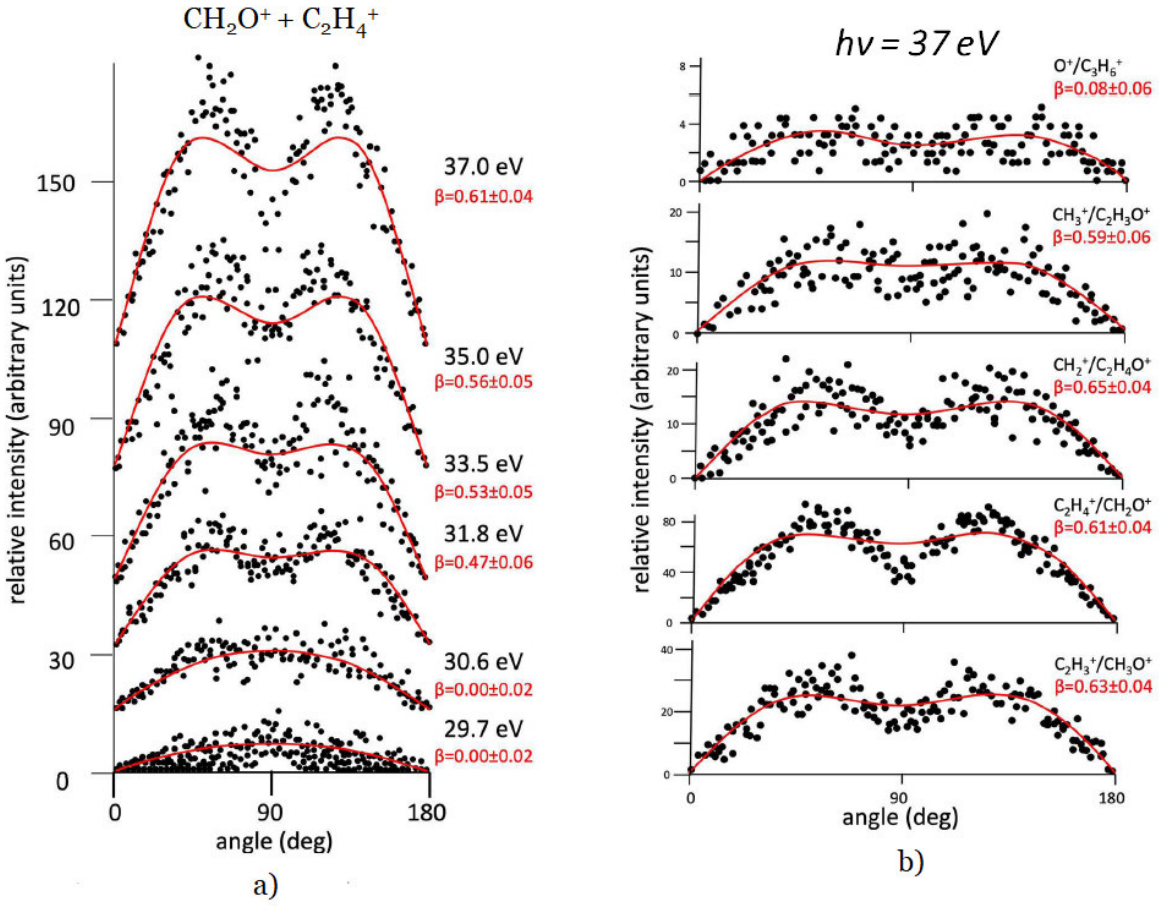

Figure 7.52: Angular distributions of the $CH_2O^+ + C_2H_4^+$ (panel *a*) channel as a function of the photon energy. In panel *b* a comparison of the angular distributions of ion pair products formed by main recorded two-body fragmentation reactions (reactions (1)–(5)) following the double photoionization of propylene oxide at a photon energy of 37.0eV is reported. Dots intensity in the ordinate axis are in arbitrary units, and the error bars are omitted for clarity being of the same order of magnitude of the dot dimensions. On the right side is also reported the anisotropy parameters referred to related photon energy.

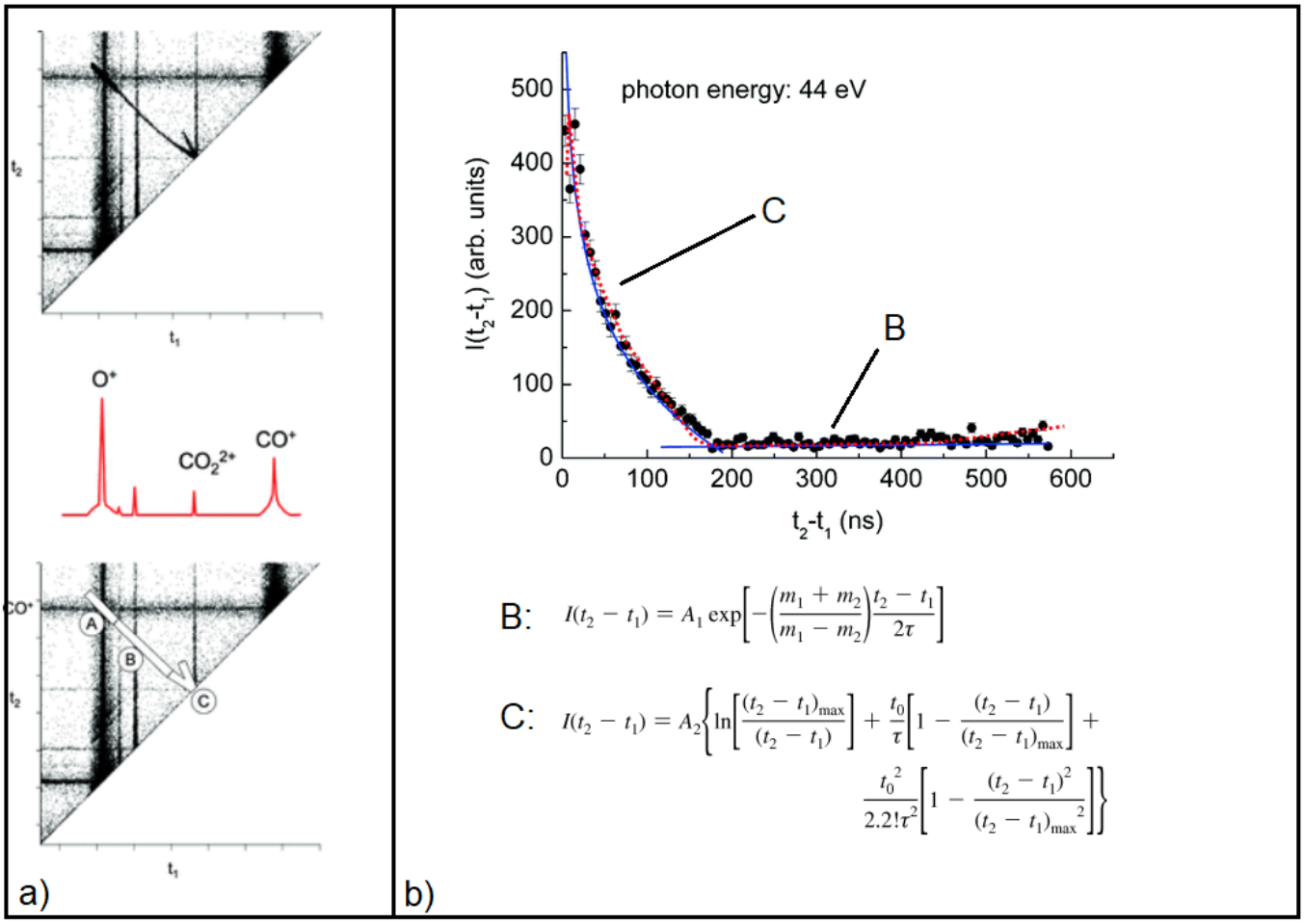

Figure 7.53: Panel *a*: Spectra of coincidences for the double photoionization of CO_2 at 44 eV photon energy, where the different areas for the analysis of the lifetime of metastable $(CO_2^{2+})^*$ dication are indicated as A, B and C. Panel *b*: density of coincidences between one photoelectron and two photoions within the areas B and C, as a function of the time difference $t_2 - t_1$. The dotted line represents a Monte Carlo simulation with $\tau = 3.1\ \mu s$ and KER = 4 eV. The image is adapted from from ref.[257].

dissociation in the drift region. The lifetime of the molecular dication can be derived in several ways: one is to fit the whole intensity distribution pattern using a Monte Carlo simulation for a chosen set of decay parameters. This procedure was adopted in ref.[257], and the result is reported in fig.7.53.

In the case of propylene oxide dication, such metastable "tail" in the coincidence map is not observed. In fact, looking at fig.7.41 no clear evidence of an intensity trace starting at an ion pair and reaching the dication mass peak at ∼1915 *ns* (m/z = 29, the half with respect to the singly charged $[C_3H_6O]^+$ ion at m/z = 58) is observed. This is also the case at all other photon energies investigated. The absence of such peculiar structure clearly indicates that, in the double photoionization of propylene oxide in the 18.0–37.0eV energy range, the intermediate molecular molecular dication is a short-lived transient species having a lifetime shorter than 50 *ns*

(the minimum time window in our experimental setup). Thus, the quite intense mass peak visible at m/z = 29 (1915 ns) in figures 7.40 and 7.41 is more likely to be associated with the CHO^+ fragment, which is one of the most abundant ion products in the single ionization of propylene oxide (∼55% relative abundance)[238], rather than to the the $[C_3H_6O]^{2+}$ dication since no fingerprint traces of metastable fragmentation is observed, even if a small percentage of the molecular dication can still overlap with the CHO^+ ion signal.
Although there are no clear evidences of the presence of a metastable dications, some peculiar metastable fragmentation features are observed in the coincidence map for the propylene oxide molecule, as shown in fig.7.54. In the figure four distinct metastable traces can be observed, labeled as 1 to 4: the first three metastable tails are all converging to the singly charged propylene oxide ion ($[C_3H_6O]^+$) peaked 5440 ns (m/z = 58) (see the total ion mass spectrum, red solid line in fig.7.54). This is an evidence of the existence of a metastable singly charged propylene oxide molecular ion, that dissociates in an ionic product plus a neutral energetic fragment. This neutral fast fragment is also detected by the 2D position sensitive detector due to its high impact energy onto the MCP detector. The presence of a "tail" and the absence of a "V" shape feature near the molecular ion trace points out that the fragmentation of the metastable ion occurs in the ion extraction region or in the accelerating stage, but not in the time of flight tube. In the case of trace "4" the tail converges to the m/z = 57 peak, i.e the metastable $[C_3H_6O]^+$ formed by a neutral hydrogen atom loss that further dissociates into an ion product and a neutral fragment. Future Montecarlo simulations on the trajectories of such metastable ions could shed more light into the lifetimes, dissociation mechanism and energetics of these metastable singly charged ions.

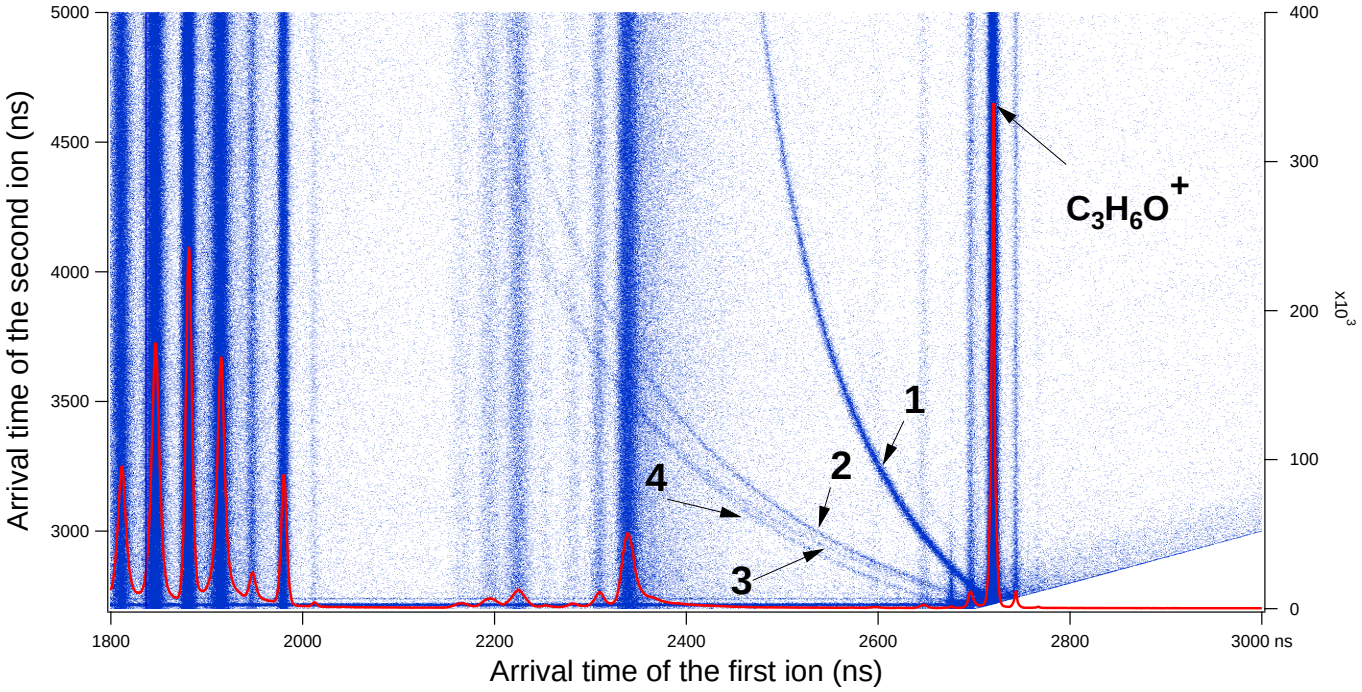

Figure 7.54: Coincidence map (sum of all recorded photon energies) in the 1800 - 3000 *ns* time window of propylene oxide. Four metastable traces (label 1-4) can be observed converging to the $[C_3H_6O]^+$ and $[C_3H_5O]^+$ ion signals. The total ion mass spectrum is also reported (red solid line).

7.5 1-methoxy-2-propanol

The data presented in the next section are part of a research project, to which a part of the Ph.D. program was dedicated, in an international collaboration with Associate Professor V. Zhaunerchyk of the Department of Physics of the University of Gothenburg. The project was focused on the study of chiral recognition mechanism in gas phase molecules by the use of IRMPD-VUV spectroscopy. Vibrational spectroscopy has been extensively used for the characterization of jet cooled chiral complexes [259, 260, 261, 262, 263], providing information on local binding sites, in particular for hydrogen-bonded systems, and can thus allows a better understanding of the chiral recognition mechanisms. High power far-IR free electron lasers (FEL) facilities are used in the application of infrared multi photon dissociation (IRMPD) spectroscopy to the study of biologically relevant molecules in the gas phase, particularly in the case of ionic and protonated species [126, 127, 264, 129].
Recently [265], a new techniques based on IRMPD spectroscopy was developed and successfully applied to gas phase molecules by ionizing (and so probing) the molecular dissociation products with vacuum ultraviolet (VUV) photons and analyzing them with a mass spectrometer. The resonant absorption of multiple IR-FEL photons induces the molecular dissociation of the target molecule and its oligomers, then a VUV laser is used to ionize the fragments, that can be analyzed by their mass. Probing

these fragments as a function of the IR wavelengths allows the recording of the vibrational spectrum. This technique shows several advantages in the study of jet cooled molecular cluster: i) it enables measuring IR spectra for molecules of arbitrary structure, including molecules that do not contain a chromophore, and ii) the spectra of monomers and oligomers can be recorded simultaneously.
We have applied IRMPD-VUV spectroscopy in the study of the 1-methoxy-2-propanol (Meth-Prop) chiral dimers, embedded in supersonic jets, in order to probe the possibility of this technique in studying the chiral recognition mechanisms in biomolecules. Vibrational spectra of homochiral (formed by only S-enantiomer units) and heterochiral (formed by both S-enantiomer and R-enantiomer units) oligomers in the far-IR region can provide information about their structure, shedding more light on enantiomer-specific interactions between the moieties. In fact, the spectral region in the interval of 400 cm^{-1} and 1500 cm^{-1}, the so called *fingerprint region*, usually contains a series of unique absorption bands, thus allowing an unambiguous identification of molecular structures [133, 134, 135]. Moreover, the study of such small protoype molecules in the gas phase enables combining theoretical calculations with the experimental measurements, which allows a better understanding of the chirally-selective molecular interactions.

7.5.1 IRMPD-VUV spectroscopy of 1-methoxy-2-propanol

The IR spectra measured for both the enantiopure and racemic mixture were analyzed using the same procedure. The data acquisition procedure is described in appendix B.4. A detailed description of the data analysis procedure can be found in ref.[132]. Briefly, the raw IRMPD spectra, expressed as fragmentation efficiency upon IR photons absorption, were normalized to the FELIX laser power. In addition to the dimer parent ion, corresponding to m/z = 180, also the m/z = 119 and m/z = 135 fragments, whose gain spectra match the depletion spectrum of the parent dimer ion, has been added to the m/z fragmentation yield, in order to improve the data statistics. Spectra recorded at different power attenuation were corrected for accordingly. The frequency scale has been calibrated measuring the output wavelength of each FELIX pulse, with an accuracy of $\sim \pm 2$ cm^{-1}. The spectra have been corrected for background events measured in absence of IR pulse, i.e. deriving only from VUV laser. The sample density was checked to be constant in each set of data, using the integrated mass spectrum for the 1-methoxy-2-propanol monomer (m/z = 90) when the IR pulse was off.
The experimental IR absorption spectra of the 1-methoxy-2-propanol dimers in the range of 540 cm^{-1} - 1510 cm^{-1} for the enantiopure and racemic samples are shown in fig.7.56. Both spectra show a large number of vibrational bands in the investigated frequency range; the two spectra are quite similar in this spectral region, though significant differences can be

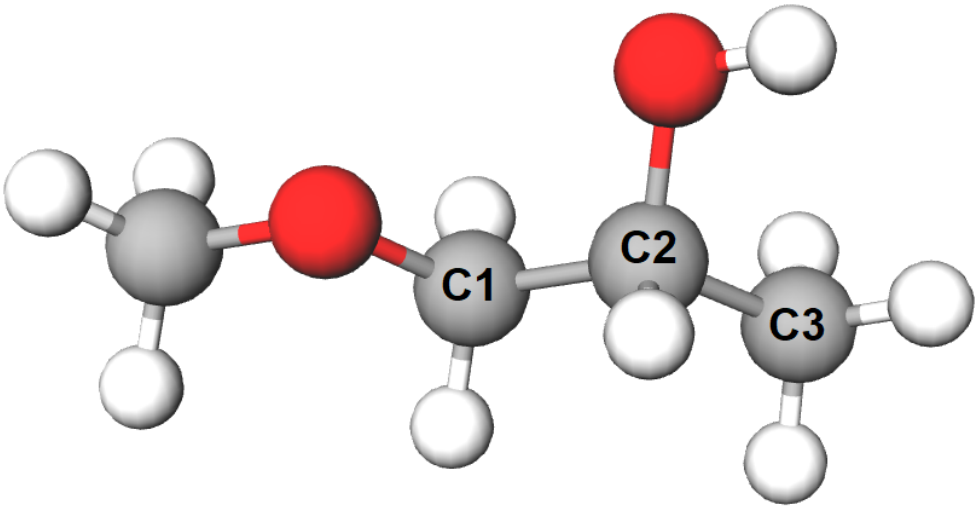

Figure 7.55: 3D molecular structure of the 1-methoxy-2-propanol molecule.

observed in the 1320-1500 cm^{-1} range and more clearly in the spectral feature around 1084 cm^{-1}, shifted to higher frequencies in the case of the racemic mixture. The frequency range between 800 cm^{-1} and 1000 cm^{-1} is characterized by three strong features, namely at 864 cm^{-1}, 927 cm^{-1} and 986 cm^{-1}, that are very similar in intensity and frequency in both spectra. The spectral region 530-750 cm^{-1} is the one that shows the most prominent differences between the enantiopure and racemic samples spectra. In the pure SS dimer spectrum two main vibrational bands are observed at 566 cm^{-1} and 587.6 cm^{-1} respectively. The IR spectrum of the racemic mixture dimer, in addition to the same two intense bands observed in the case of the enantiopure sample, exhibits a strong vibrational band peaked at 627 cm^{-1}. Since aliphatic alcohols are flexible molecules, the 1-methoxy-2-propanol molecule may exist in different conformers and this gives rise to different patterns in the IR spectra. Hence, in order to interpret the IR features observed in the experimental IRMPD-VUV spectra, a theoretical conformational analysis of the homo- and heterochiral dimers has been performed. The Gibbs free energies and Boltzmann distributions for the lowest energy dimer's conformers have been calculated using the G4MP2 method[278]. Only the lowest energy conformers with a Boltzmann distribution greater than 0.05 at 300 K were taken into account. The six conformers found for the SS dimer are shown in fig.7.57, while the five conformers found for the RS dimer are shown in fig.7.58. Each B3LYP harmonic frequency line has been convoluted with a gaussian function, with a full width at half maximum (FWHM) equal to 1% of the wavelength. The convoluted theoretical spectra were compared with the experimental ones, in order to assign conformer-specific features in the measured spectra, as shown in fig.7.59 and fig.7.60 for the homochiral case and the homo/heterochiral mixture respectively.

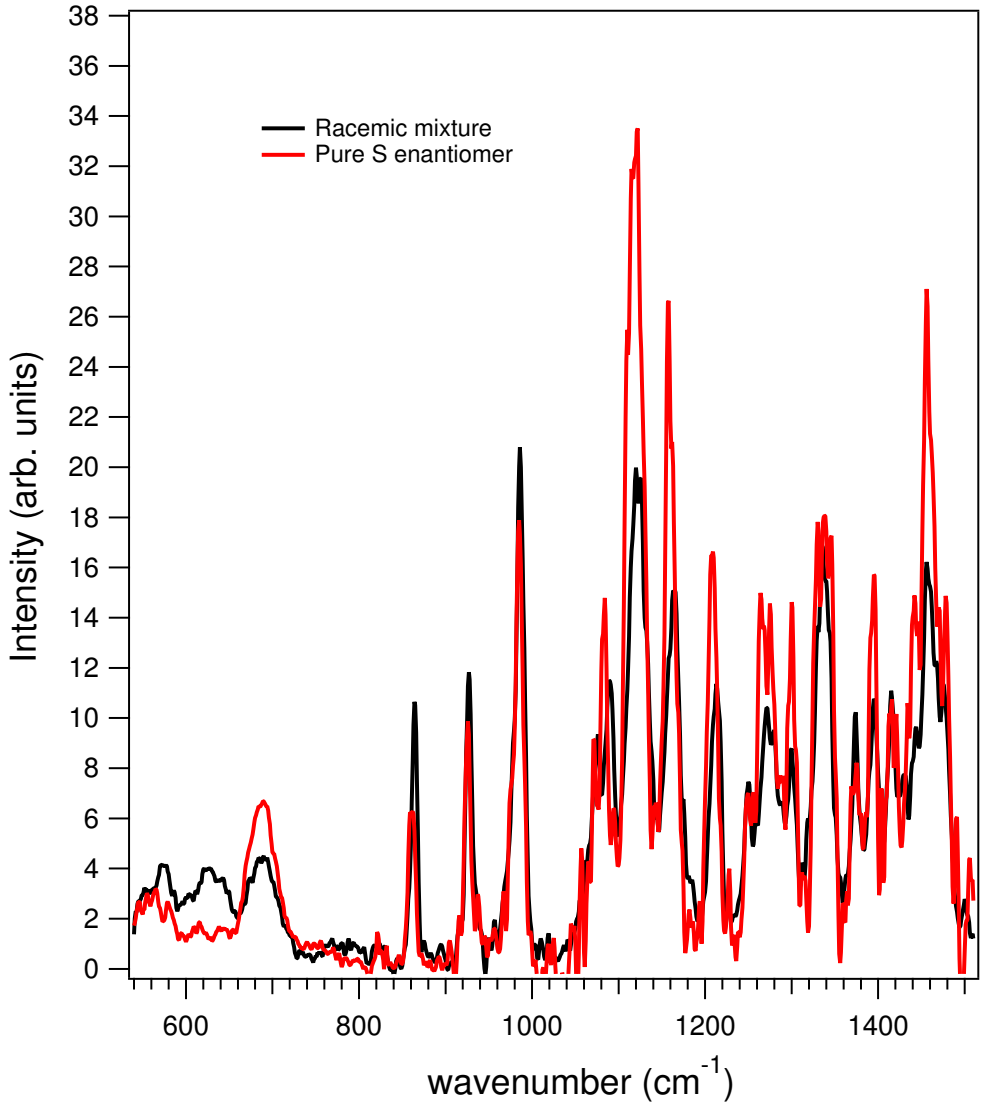

Figure 7.56: IRMPD spectra of pure enantiopure (red solid line) and racemic mixture (black solid line) of 1-methoxy-2-propanol dimers.

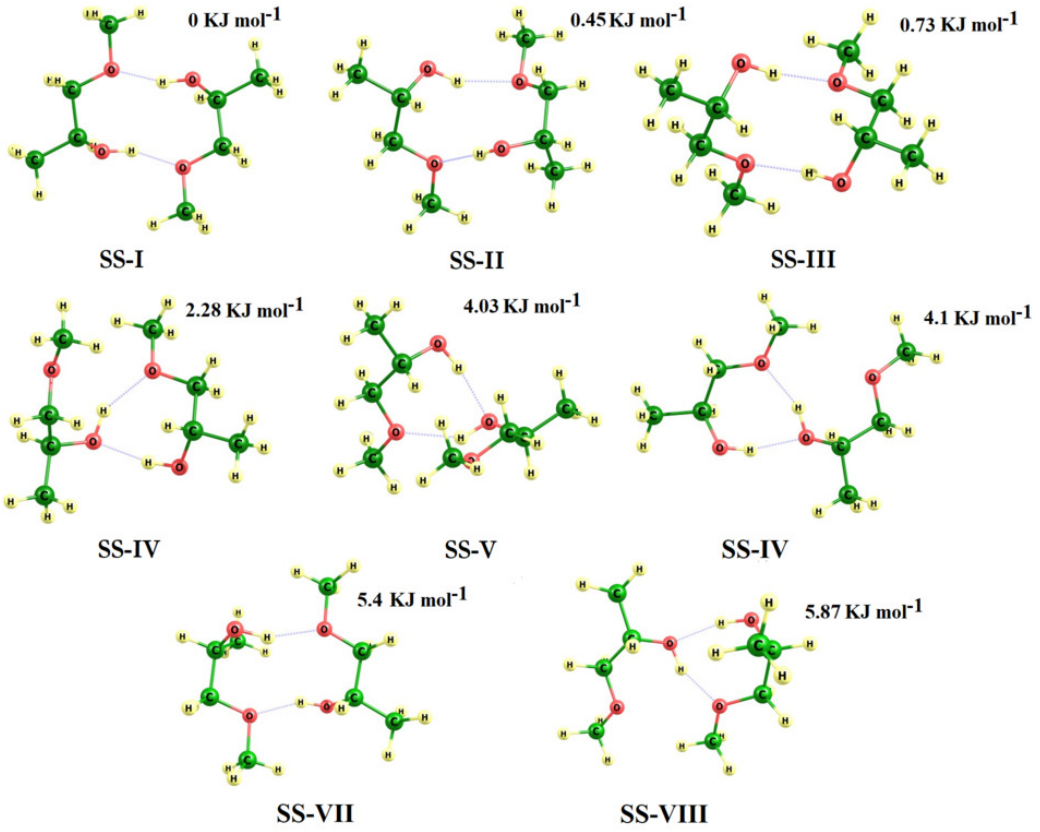

Figure 7.57: Stable conformations of the SS dimer calculated with the B3LYP functional. The reported Gibbs free energies are relative to the lowest energy conformer (SS-I)

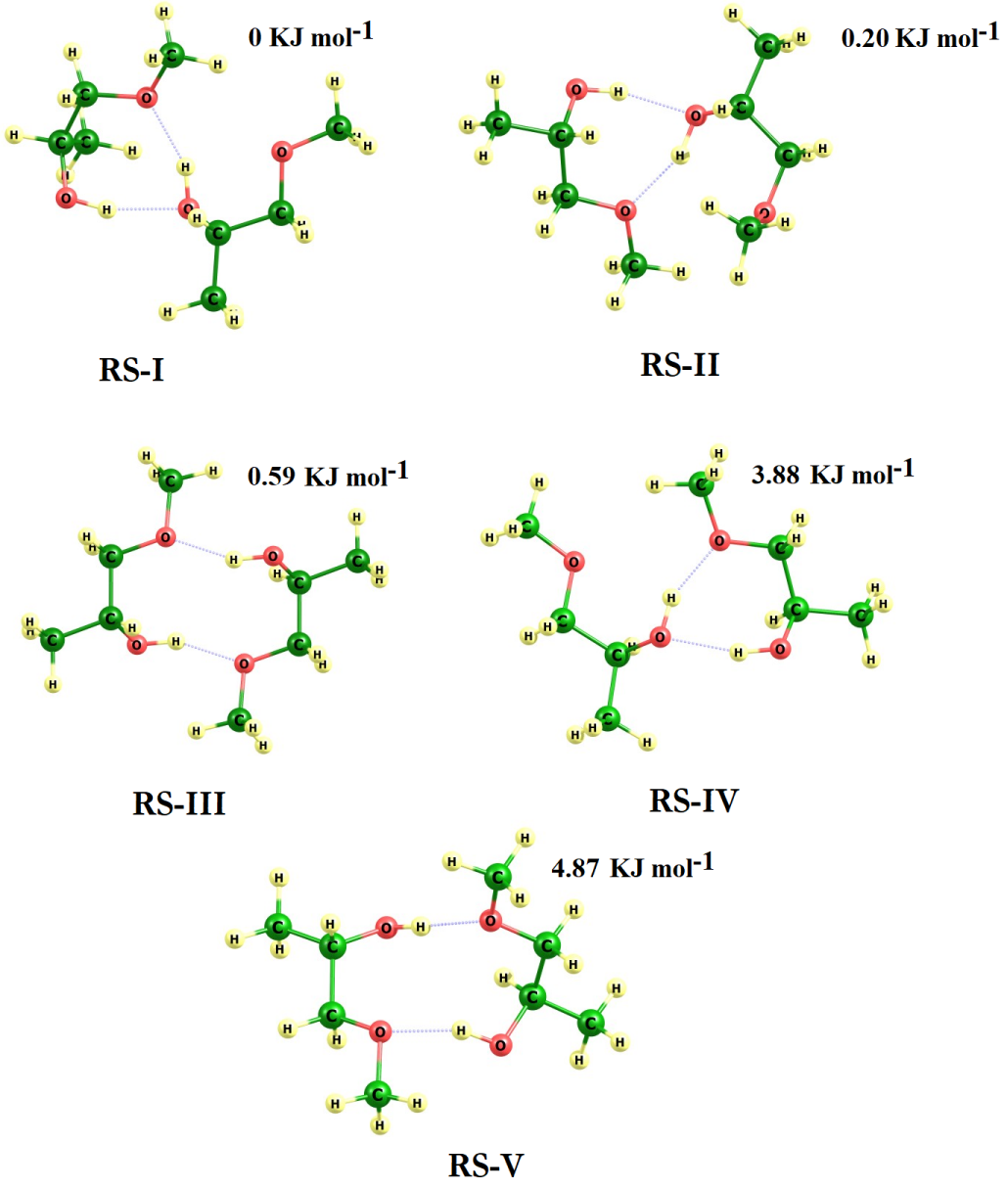

Figure 7.58: Stable conformations of the RS dimer calculated with the B3LYP functional. The reported Gibbs free energies are relative to the lowest energy conformer (RS-I).

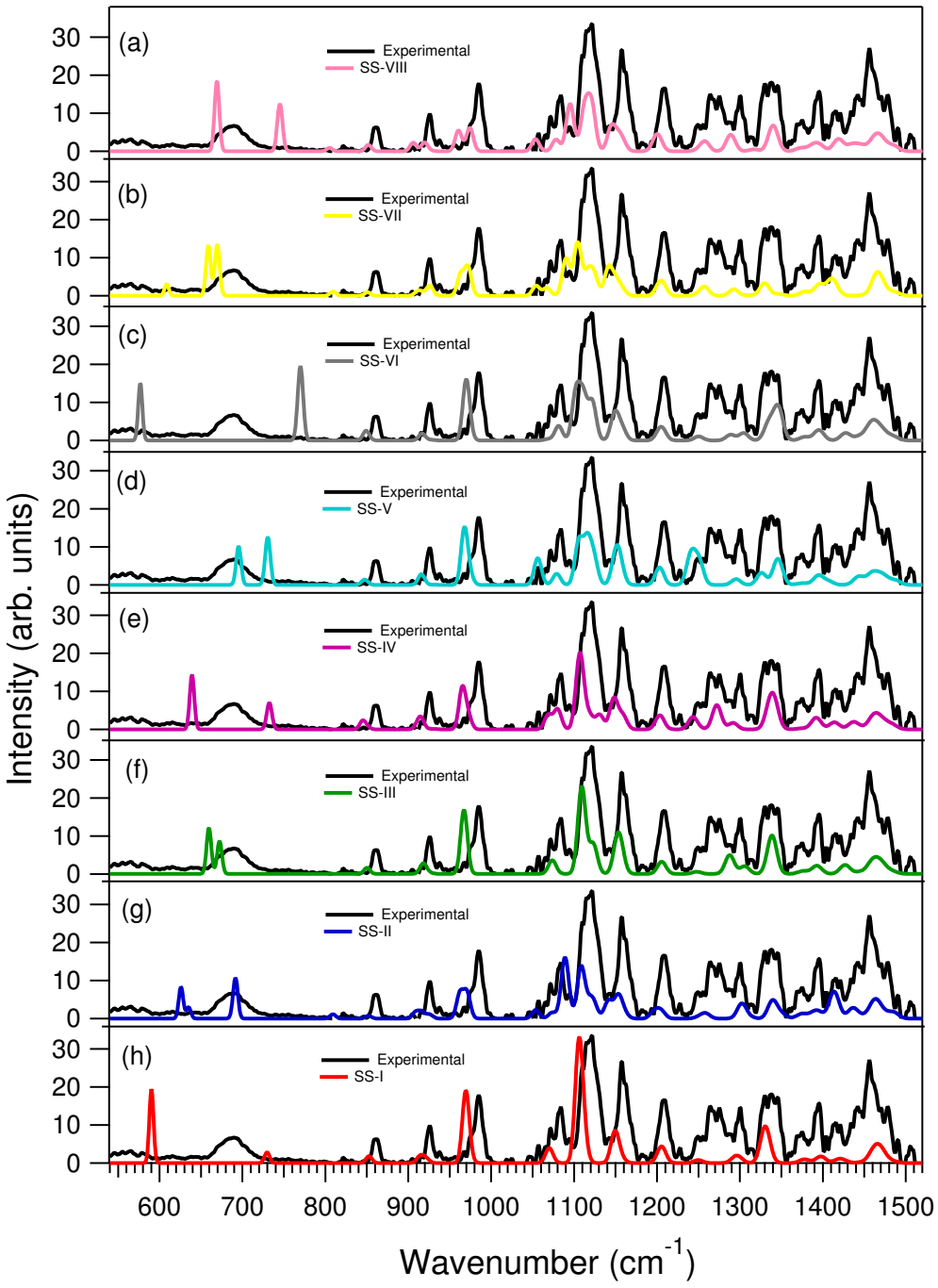

Figure 7.59: Comparison between the experimental enantiopure sample spectrum (black solid line) and the calculated harmonic spectra of the lowest energy SS conformers at the B3LYP level (panel *a*-*h*). A scaling factor of 0.98195 is applied to the calculated frequency scale.

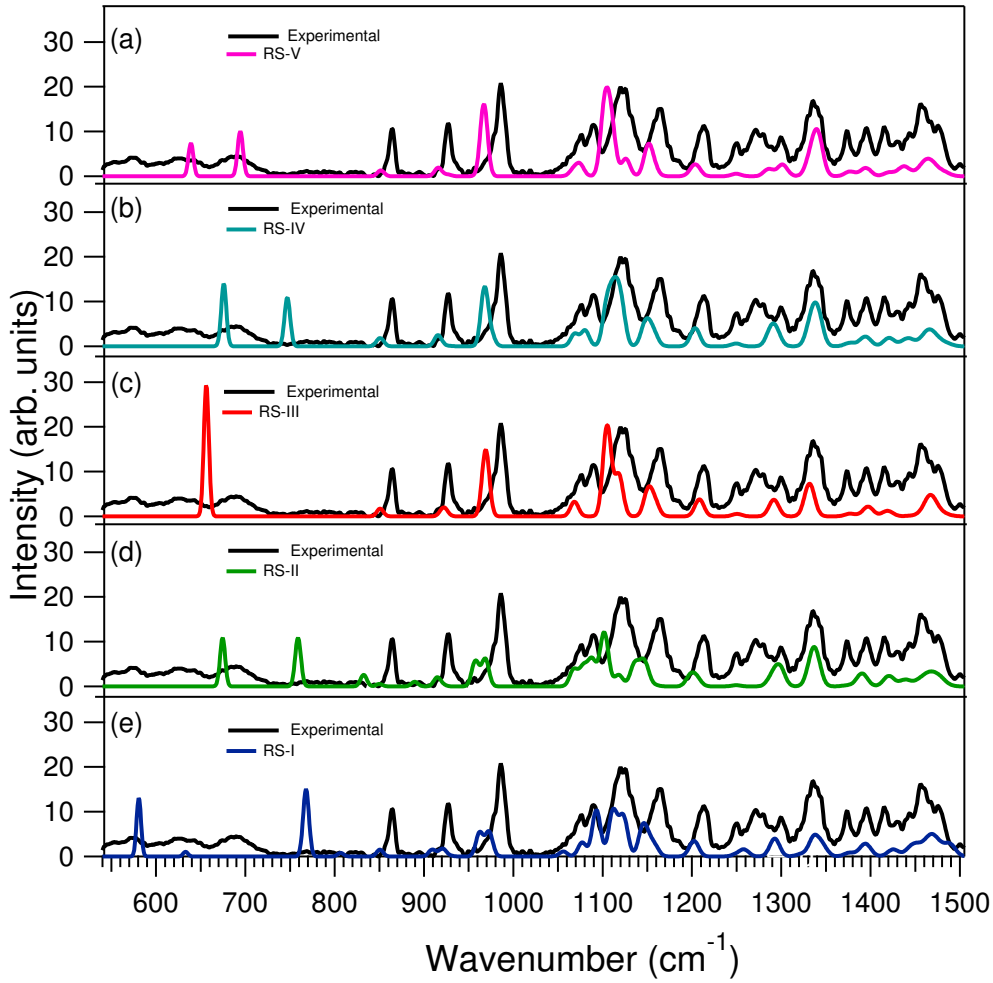

Figure 7.60: Comparison between the experimental racemic sample spectrum (black solid line) and the calculated harmonic spectra of the lowest energy RS conformers at the B3LYP level (panel *a*-*e*). A scaling factor of 0.98195 is applied to the calculated frequency scale.

The theoretical IR spectra of the lowest energy conformers for the SS dimer are shown in fig.7.59), together with the experimental spectrum of the enantiopure sample. The spectra of the six conformers are very similar in the whole range between 1000 cm^{-1} and 1500 cm^{-1}, while they differ significantly in the far-IR region, i.e. below 800 cm^{-1} . By comparing the theoretical results with the experimental data, conformer-specific spectral features can be identified, if any. The calculated spectrum for the SS-IV conformer (panel *e* in fig.7.59) shows an overall good agreement with the experimental one, reproducing almost all the absorption bands in the spectrum. Moreover it is the only conformer that can reproduces the strong features at 1270 cm^{-1}. The S-II conformer (panel *b* in fig.7.59) exhibits a strong absorption feature at 1420 cm^{-1}, in accordance with the experimental results, and a relative strong feature in correspondence of the broad vibrational band at 690 cm^{-1}. The S-I and S-VI conformers (panel *h* and panel *a* in fig.7.59 are the only two species for which a strong feature below 600 cm^{-1} is expected, in agreement with the experimental spectrum, but the S-VI conformer shows a strong spectral component at 769.8 cm^{-1}, that is not clearly observable in the spectrum, also considering the relatively good agreement in the peak position between the experimental data and the harmonic theoretical spectra. On the basis of the previous considerations, it can be stated that the greatest contribution to the measured IR spectrum of the SS dimer is given by the conformers S-I, S-II and S-IV. As shown in fig.7.57, in conformer S-I the two 1-methoxy-2-propanol units are bonded together by a double hydrogen bond, involving both hydroxyl groups and the two ether oxygen atoms. The two molecular units present a linear structure, with a $\widehat{CCC}$ angle of 110.6°, while the $\widehat{COC}$ angle and $\widehat{COH}$ are 110° and 108.7° respectively. The conformer S-II is also characterized by a double hydrogen bond, but in this case, while one of the molecular units is planar, the other unit shows a C3-C2-C1-O dihedral angle of 57°, causing an helix-shape hydrogen bond (see fig.7.55 for the carbon atoms enumeration). The SS-IV conformer shows only one hydrogen bond between the hydroxyl group of one molecular unit and the methoxy group of the second 1-methoxy-2-propanol molecule. Both the molecular units in the dimer have a linear structure, but unlike the SS-I conformer, the dimer is not planar.

All the three conformers are characterized by an intense vibrational band at 1490 cm^{-1}, arising from the four methyl groups antisymmetric bending motion. Conformers S-II and S-IV exhibit an intense feature at 1440 cm^{-1}, associated with the C2-C3 stretching coupled with the OH bending motion, that is not present in the calculated spectrum of conformer S-I. Only in the case of conformer SS-II a strong absorption features is expected by theory at 1413 cm^{-1}, arising from the relatively localized C2-C3 stretching mode, that implies also a strong H-C-O-H in-plane bending motion, while in the case of the SS-IV conformer this vibrational normal mode is more delocalized in a C1-C2-C3 antisymmetric strething. The two intense features observable in the experimental spectrum at 1395

cm^{-1} and 1374 cm^{-1}, predicted for all the conformers, are associated with the C1-C2 stretching mode and the C2-C3 stretching mode respectively. The strong vibrational band observed at 1337 cm^{-1} is also reproduced by all the selected conformers, and can be associated with an *OH* bending motion, Due to the fact that the hydroxyl group is involved in the hydrogen bond between the two molecular units in the dimer complex, is expected that this normal mode is very sensitive to the dimer structure. In fact, a frequency shift of several wavenumbers can be observed in the harmonic spectra of the various homochiral conformers. The intense peak at 1300 cm^{-1} is observed for all the selected conformers and can be associated with a H-C-O-H torsional vibration, involving, also for conformer S-IV, a hydroxyl group in a single hydrogen bond. The strong features observed at 1270 cm^{-1} can be reproduced only by conformer S-IV. This feature is associated with the H-C-O-H torsional vibration of the hydroxyl group involved in two different hydrogen bonds. This normal mode is thus characteristic of the single-hydrogen bond structure of this conformer, in contrast with the double hydrogen bond of conformers SS-I and SS-II. Even if also conformers SS-V and SS-VI exhibit the same single-bond structure, the peculiar conformation of the SS-IV dimer can be held responsible for the clearly evident features in the experimental spectrum. The last component of the broad band around 1300 cm^{-1}, visible at 1250 cm^{-1}, is common to almost all the conformers and it originates from the $-CH_2$ twisting motion. All the vibrational progression between 1250 cm^{-1} e 1320 cm^{-1} is thus associated with vibrational normal modes that involve the -OH group, and is thus expected to be very sensitive to dimer structure, and indeed this is the spectral region in which the theoretical calculations predict the larger differences between the various conformers. Also the strong absorption band is a common feature in all the conformers. This feature is associated with C-O stretching involving the C1 carbon and the oxygen atom of the methoxy group, and in effect the theory shows a significant frequency shift between the conformers with a double hydrogen bond, and the S-IV conformer in which only one of the oxygen atom in the methoxy groups is involved in a hydrogen bond. The region in the spectral range 1000-1200 cm^{-1} shows three intense broad and overlapped vibrational bands, in agreement with the theoretical harmonic calculations. The feature at 1157 cm^{-1} corresponds to a relatively localized C-C stretching vibration between the C1 and C2 carbon atoms in the case of the S-I and S-IV conformers, with the two stretching motions of the two different molecular units being out of phase, while in the case of the S-II conformers it arises from a C-C-O antisymmetric stretching, involving the C1-C2 bond and the -OH group, with a difference of 8 wavenumbers between the two motions in the two molecular units. In addition, both S-IV and S-II conformers show a series of less intense features between 1130 cm^{-1} and 1160 cm^{-1}, related to a strongly coupled C-O stretching at the C2 atom, and C2-C3 stretching modes. All three conformers are characterized by a strong absorption band peaked at 1225 cm^{-1}, in

agreement with the experimental spectrum. For all the conformers this feature is associated with an antisymmetric C-O-C stretching mode, at the methoxy oxygen atom, that involves a strong deformation of the entire molecular backbone. Also in this case a substantial frequency shift can be observed for the the S-II conformer. The spectral region 1100-1030 cm^{-1} is characterized by a strongly coupled C2-C3 stretching vibration, with a peculiar out of phase motion in the two molecular units for the S-IV dimer. All three conformers show three strong absorption features in the region 800-1000 cm^{-1},that can be associated with the features at 985 cm^{-1}, 926 cm^{-1} and 860 cm^{-1} observed in the experimental spectrum. The first feature can be attributed to a strong C-O-C symmetric stretching vibration, the second one to a C-C-O antisymmetric stretching, strongly coupled with methyl group in C3 antisymmetric bending motion, and the third feature arising from a C-C-C stretching vibration coupled with a methyl group bending motion. The strong vibrational coupling of the normal modes associated with the spectral features observed between 800 cm^{-1} and 1200 cm^{-1} suggests a strong anharmonic nature of these vibrational modes [266], that could explain the discrepancy between the calculated harmonic frequencies and the experimental ones, while a better agreement is observed in the spectral region 1200-1500 cm^{-1}, this latter characterized by more localized vibrational normal modes that can be threatened in the harmonic approximation. The region below 800 cm^{-1} exhibits two intense broad absorption bands at 560 cm^{-1} and 690 cm^{-1} respectively. The latter can be assigned to an out-of-phase OH wagging motion of the two hydroxyl group of the molecular units in both the SS-I and SS-IV conformers (at 730 cm^{-1}), and the lower frequency OH wagging involving only one hydroxyl group of the S-II conformer. The band at 560 cm^{-1} can be attributed to the S-I conformer, which shows an intense feature at 590 cm^{-1} arising from an in-phase OH wagging, that involves both the hydroxyl groups in the double hydrogen bond. Also the small features at 615 cm^{-1} in the enantiopure experimental spectrum can be assigned to an OH wagging of the SS-II and SS-IV conformers. As the spectral region in the 500-700 cm^{-1} range is associated with vibrational modes that involve the hydrogen bond, this spectral region is expected to be a finger-print region for the different interactions between S-S enatiomers and R-S enantiomers, being the chiral center at the carbon atom bonded to the OH groups involved in these hydrogen bonds, with thus a different spatial orientation of the latter. In order to estimate the relative percentage of each conformer, the experimental spectrum was fitted with a linear combination of the three selected conformers, minimizing the root mean square between the experimental data and the theoretical ones. Furthermore, this procedure allowed to find the proper scaling factor for the calculated harmonic frequencies. The comparison between the averaged theoretical spectrum and the experimental data is shown in fig.7.61. A very good agreement is observed between the theoretical calculations and the experimental spectrum. Almost all the features observed in the

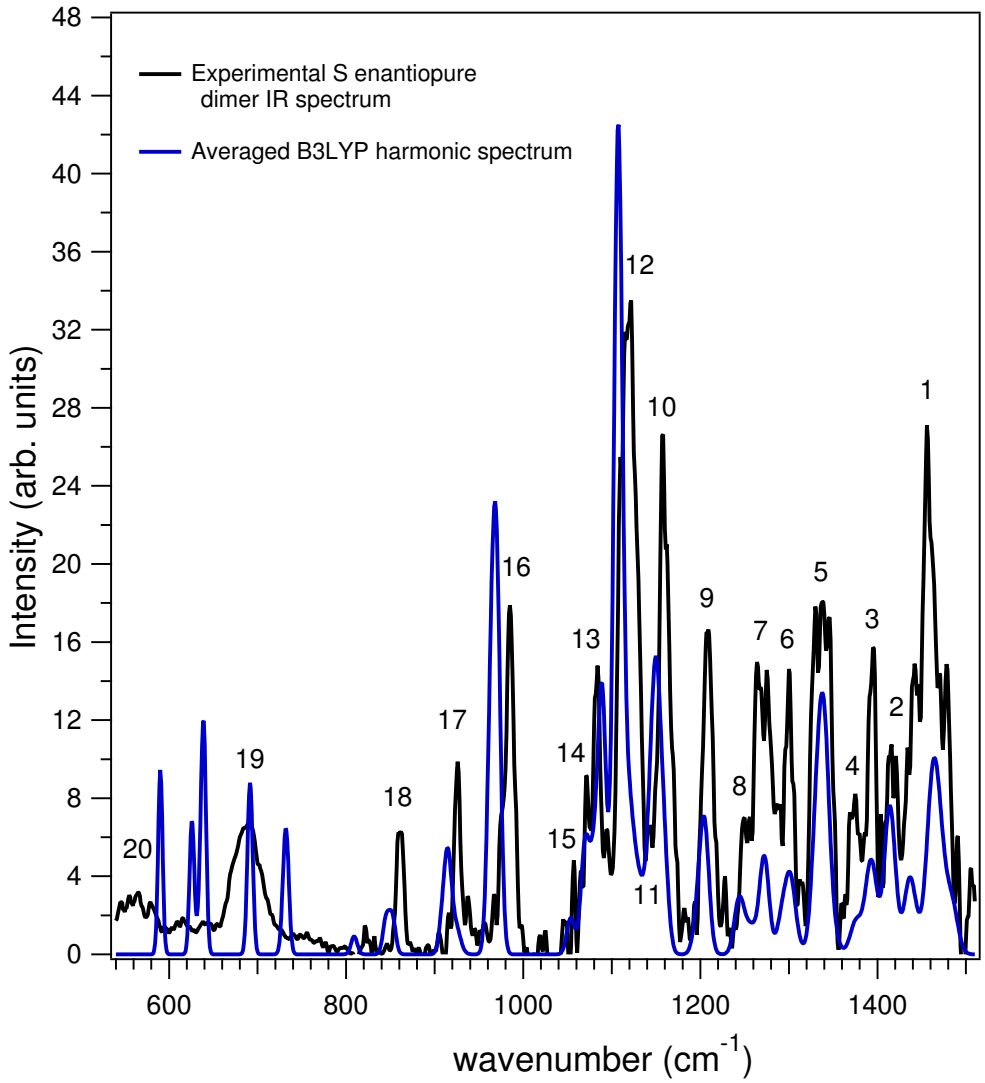

Figure 7.61: Comparison between the experimental IR spectrum of the pure S enantiomr dimer (black solid line) and the averaged B3LYP harmonic spectrum (blue solid line). The theoretical spectrum is multiplied by a scaling factor of 0.2266. See tab. 7.5 for peaks assignment (numbers 1-20).

IR spectrum can be reproduced by the harmonic calculations. It is worth noting that, though an overall good agreement in the frequency position can be observed, a strong difference between the calculated spectral line intensities and the experimental relative intensities can be noted; this can be related to the multi-photon nature of the IRMPD process, in which the intensity and line profile of the absorption band depend on the IVR effect efficiency[267].

The IR spectrum of the racemic mixture, shown in fig. 7.56, contains spectral features arising from both the homochiral dimer and the heterochiral dimer. Although the contribution of the SS dimer can in principle be estimated in the spectrum, since by definition in a racemic mixture there is 50% of each of the two enantiomers, the multiphoton nature of the

IRMPD process makes a quantitative comparison of the relative fragmentation yields difficult to implement, since the IVR efficiency, and hence the fragmentation yield, do not always follows a linear relation with the laser power, which was not constant in the whole set of data. However, the comparison between the pure homochiral spectrum and the racemic mixture spectrum highlights clear differences in various spectral features, that can be explained on the basis of the various RS conformational structures. A clear blueshift and peak broadening can be observed in the 1000-1200 cm^{-1} spectral region in the racemic mixture spectrum respect to the enantiopure one. In 7.60 it can be noticed that only the RS-I (panel *e*)and RS-II conformers (panel *d*) exhibit a series of strong absorption features that can take into account the observed frequency shifts. Both these conformers possess one single hydrogen bond between the methoxy group of one molecular unit, whose antisymmetric stretching is responsible of the spectral features at 1092 cm^{-1}, and the hydroxyl group on the other molecular unit, whose bending motion is coupled with a strong C2-C3 stretching motion giving rise to the spectral component at 1076 cm^{-1}. The major differences between the two experimental spectra of fig.7.56 can be observed in the 540-750 cm^{-1}; a new intense absorption band can be seen at 630 cm^{-1}. This feature could be explained by the dominant spectral component predicted at 657 cm^{-1} for the RS-III conformer (panel *e* in fig.7.60), whose structure is analogue to that of conformer SS-I (as shown in 7.57 and fig.7.58). Both conformers are characterized by a double hydrogen bond, but while in the case of the SS-I dimer both the hydroxyl groups are orientated on the same direction with respect to the molecular plane identified by the two planar 1-methoxy-2-propanol units, in the case of the RS-III conformer, because of the configurational inversion at the C2 chiral center of the OH group in the (R)-1-methoxy-2-propanol unit, the two hydroxyl groups are facing on opposite sides of the dimer molecular plane, giving rise to a strong in-phase OH wagging, at a significantly higher frequency respect to same vibrational motion observed for the homochiral SS-I conformer. This phenomenon is a manifestation of the chiral recognition mechanism, as the different spatial orientation of the functional groups involved in hydrogen bonds between the two dimer molecular units, due to the different configuration of the molecules bonded together in the diasteromeric complex, could lead to different vibrational modes and hence to fingerprint patterns in the far-IR spectral region, as observed in the case of the 1-methoxy-2-propanol molecule. An analogous phenomenon can be observed comparing the OH wagging motion of the RS-I conformer and the SS-IV conformer, in which the configurational inversion in one of the the molecular units leads to a strong shift in the OH in-phase wagging motion, that appears at lower frequencies for the heterochiral dimer, in agreement with the prominent shoulder at 575 cm^{-1} over the broad band observed at 560 cm^{-1} in the case of the homochiral dimer IR spectrum.
Although the experimental investigation carried on the vibrational spectra

Table 7.5: Experimental and theoretical frequencies of main vibrational bands. The harmonic theoretical frequencies are scaled by a factor of 0.98915. All frequencies are reported in cm^{-1}. Notes: [1] = Involving both monomers, [2] = The two monomers show different vibrational frequencies for the same vibrational mode.

Mode	Exp.	SS-I	SS-II	SS-IV
CH_3 asym. bend[1]	1456	1466	1463	1464
C1-C2-C3 asym. stretch.	1440+1416	1451[1]	1437+1413[2]	1438+1414
+OH bend. (2)				1392
CH_2 wagging (3)	1395	1398	1393	1392
CH_3 sym. bend (4)	1374	1377	1374.7	1400.3
OH bending (5)	1337	1330.5	1341	1339.4
H-C-O-H torsion (6)	1300	1296.2	1303	1292
H-C-O-H torsion (7)	1270	•	•	1272
CH_2 twisting (8)	1254	1250	1258	1243.1
C1-O stretching (9)	1209	1205.5	1201	1203.9
C1-C2-O asym. stretch. (10)	1157	1149.9	1147	1153
C2-O stretch.	1144	112.5	1122	1131
+ OCH_3 stretch. (11)				
C-O-C asym. stretch. (12)	1121	1105	1129+1109	1108
out-of-phase C2-C3 streth. (13)	1084	•	•	1080.1
in-phase C2-C3 streth. (14)	1070	1070.3	•	1069.3
C1-C2-C3 bending (15)	1058	•	1052.7	•
C-O-C sym. stretch. (16)	985	969.2	970+963	982
C1-O stretch.	925	916.2	312	914
+ C2-O stretch. (17)				
C1-C2-O sym. stretch. (18)	860	853	852.3	845.5
out-of-phase OH wagging (19)	690	729.6	691.3	732.5
in-phase OH wagging (20)	560	590.2	632	639.2

of the 1-methoxy-2-propanol homo- and heterochiral dimers highlighted clear spectral differences that could be associated with the chiral properties of the two diastomers (RS- and SS-dimers), the nature of the multiphoton absorption process, that could lead to frequency shifts, peak broadening and intensity saturation effects, and the high number of possible conformers, together with the impossibility of separates the RS-dimer IR spectrum from the SS-dimer spectrum, makes the interpretation of the experimental results very challenging. Since the IRMPD-VUV spectroscopy is a mass selective techniques, the use of isotopically labeled molecules in the case of one of the two enantiomer, permits to obtain separated IR spectra for the all the possible oligomers, and further experiments are thus planned. Moreover, the results obtained stimulates the improvement of the theoretical methods, in both the conformational analysis and in anharmonic frequencies calculations.

Chapter 8

Conclusions

In this work, a joint experimental and theoretical study of photoionization processes in small gas-phase molecular systems is presented. The emphasis was placed on processes occurring in the VUV photon energy regime. The peculiar properties of synchrotron and FEL radiation were exploited in order to study the photoionation dynamics, photodissociation and chiral properties of different molecular systems.
The photoionization dynamics for the epichlorohydrin, as a simple prototype of chiral molecule, was investigated for the first time. The $\beta(h\nu)$ asymmetry parameters and photoionization partial cross sections for the outer valence ionizations of epichlorohydrin have been measured as a function of photon energy by ARPES in the Cl 3p Cooper minimum region. The $\beta(h\nu)$ dynamical behavior displayed a wide oscillation only for the second (23a) and third (22a) PE bands, where the oscillation of the third band was found to be twice larger than that of the second band, while a $\beta(h\nu)$ monotonic increase, although differently structured, was observed for the first and fourth PE bands. Both the asymmetry parameters and cross sections have also been theoretically calculated, as a function of photon energy, at DFT and TD-DFT levels, for the three stable molecular conformers of epichlorohydrin, and the corresponding Boltzmann average curves, derived at room temperature, could be properly compared to the experimental data. The dynamical behavior of asymmetry parameters for the PE bands calculated at TD-DFT level were found in partial agreement with the experimental results. While the low energy behavior was accurately reproduced, important disagreement were found in the region of the Cooper Minimum, although, at variance with DFT, its energy position, notably the minimum in $\beta(h\nu)$ displayed at 43 eV, was predicted in excellent agreement with the experiment. The most important deviations were found in the high energy behavior, namely the lack of $\beta(h\nu)$ oscillation in the third band, while that in the second was predicted of amplitude twice larger than the observed one. A similar effect was also seen in the case of the photoionization cross sections: the qualitatively good agreement achieved in the low photon energy region deteriorates at higher photon energies, in particular for the second and third PE bands. This findings

were consistently interpreted as clear evidence of FISCI correlation effects not accurately described by Kohn-Sham DFT orbitals, due to orbital mixing upon ionization, favored by the absence of symmetry constraints in a chiral molecule like epichloridrin. This interpretation has been further confirmed by correlated ab initio CASSCF/Dyson orbital calculations. It is expected that what observed here is a peculiar effect in the photoionization dynamics of chiral molecules containing second row or heavier atoms. The study of the photoionization dynamics in chiral molecules, although the data are still under analysis and hence are not reported in this thesis, is continuing on other oxirane derivatives containing heteroatoms, in particular the $\beta(h\nu)$ and $\sigma(h\nu)$ observables were also measured for the methyl thiirane molecule and a similar dynamical behavior was observed in the Cooper minimum region. Parallel to the experimental activity, an improvement of the theoretical methodology is carried on, with the aim of giving a more accurate description of the final state effects observed in the photoionization of such chiral systems.

The double photoionization in the VUV energy region of a simple chiral molecule of astrochemical interest (the propylene oxide) was studied by Photoelectron-Photoion-Photoion Coincidence Spectroscopy with the use of linearly polarized synchrotron radiation. The main two-body dissociation channels were identified and the double ionization threshold energy of 28.3 ± 0.1 eV of for the propylene oxide molecule was estimated for the first time. The threshold energies, the related branching ratios, the KERs and the photofragment angular distributions were determined for all the different ionic products as a function of the photon energy. The observed bimodality in the measured KER distribution for the $CH_3^+ + C_2H_3O^+$ channel suggests that the formation of the CH_3^+ ion may involve two different microscopic mechanisms in the Coulomb explosion fragmentation dynamics of the intermediate $C_3H_6O^{2+}$ dication. Further experiments performed using isotopically labeled precursor molecules could clarify the relative importance of the competing different pathways. Moreover, theoretical efforts will be done by our group in order to calculate the energy and structure of dissociation ion products to provide additional information on the dynamics of the charge separation reactions following the double photoionization event. The results obtained on the propylene oxide are of interesr not only for its atrochemical importance, but also because such data on the molecular dication energetics, and nuclear dissociation dynamics are mandatory information for further experimental and theoretical investigations of the interaction between chiral species and linearly or circularly polarized light.

The chiral recognition mechanism in 1-methoxy-2-propanol oligomers was studied by IR-FEL based IRMPD-VUV spectroscopy. The vibrational spectrum of both the SS-dimers and RS-dimers were measured and compared. Significant spectral differences can be observed in the low wavenumbers region (below 600 cm^{-1}), suggesting a different chiral-specific interaction mechanism in the two diastereomers that is reflected in the fingerprint

region of the spectrum, a spectral region extremely sensitive to the molecular structure. The experimental results were compared with theoretical harmonic spectra calculated at the DFT-B3LYP level for different conformers. The comparison highlighted a possible manifestation of a chiral recognition mechanism, as the different spatial orientation of the functional groups involved in hydrogen bonds between different dimer molecular units, due to the different configurations of the molecules bonded together in the diasteromeric complex, can lead to different vibrational modes, and hence to fingerprint patterns in the far-IR spectral region. Further investigations performed by using isotopically labeled enantiomers can lead to more conclusive considerations, since the two possible diastomers (SS- and RS- dimers) can be identified by different masses.
Finally, a position sensitive cross delay line anode detector and a bias voltage deflecting electrode where developed for the ARPES-TPES end station. The upgraded experimental apparatus was used in the study of the photoionization dynamics of the OsO_4 tetraoxo compound. The asymmetry parameter and photoionization cross section branching ratios of the outer valence ionizations of OsO_4 has been measured as a function of photon energy by linearly polarized synchrotron radiation. The photoionization dynamics was calculated by the time-dependent density functional theory (TDDFT) that is implemented in a linear combination of atomic orbitals (LCAO) scattering code, which uses a basis set of B-spline functions. The theoretical results have been compared with the available experimental data and a very good agreement has been found.
In conclusion, the photoionzation processes involving small gas-phase molecules have been studied with advanced light sources, and new experimental and theoretical data on the dynamics, dissociation and molecular interaction mechanism were obtained for the chosen molecular systems. The experimental work performed in this thesis lead to a significant technological advancement in the electron detection system of the ARPES-TPES end station, as well as provided a strong motivation for developing more efficient theoretical models describing the photoionization process in chiral molecules.

Appendices

Appendix A

Differential photoionization cross section

The following discussion is based on ref.[55]. The Hamiltonian perturbation term H' on a N-electron system interacting with an electromagnetic radiation can be approximated (in the weak field limit) as:

$$H' = \sum_{i=1}^{N} -\frac{e}{mc}(\mathbf{p}_i \cdot \mathbf{A}(\mathbf{r}_i, t) + \mathbf{A}(\mathbf{r}_i, t) \cdot \mathbf{p}_i) \tag{A.0.0.1}$$

Here $\mathbf{A}(\mathbf{r}_i, t)$ is the vector potential of the incoming wave and $\mathbf{p} = -i\hbar\nabla$ is the momentum operator.
The Hamiltonian in eq.(A.0.0.1) can be simplified considerably: first we can choose the Coulomb gauge for $\mathbf{A}$, which fixes the divergences as $\nabla \cdot \mathbf{A} = 0$. Furthermore now $\mathbf{p}$ and $\mathbf{A}$ commute, and the first and second term in eq.(A.0.0.1) can be combined. The field $\mathbf{A}(\mathbf{r}_i, t)$ can be represented as a superposition of monochromatic plane waves, in the form:

$$\mathbf{A}(\mathbf{r}_i, t) = \sum_{k,\omega} \hat{\varepsilon_k} a_{k,\omega} e^{(i\omega t - i\mathbf{kr})} + c.c. \tag{A.0.0.2}$$

In eq.(A.0.0.2) $\mathbf{k}$ and ω are the wave vector and angular frequency of the incident radiation, and $\hat{\varepsilon_k}$ its polarization unit vector. $a_{k,\omega} = c\sqrt{2\pi/\omega}$ is an expansion coefficient. A third approximation can be done if we consider that in general the wavelength of the absorbed radiation is much greater than the typical atom/molecule size (for instance, in the methane molecule the C - H distance is $\sim 1\mathring{A}$ and the wavelength corresponding to the energy to overcome the first ionization limit is $\sim 985\mathring{A}$), and hence if we expand the exponential term in eq.(A.0.0.2) using the Taylor - McLauren series

$$e^{i\mathbf{kr}} = 1 + ikr + \cdots \tag{A.0.0.3}$$

we note that $|\mathbf{k} \cdot \mathbf{r}| << 1$ and only the first term can be considered,

i.e. the unity. This simplification is known as the electric dipole (E1) approximation. The differential transition probability, between the initial state of energy E_0 and the final state E_f, can be then calculated according to eq.(A.0.0.4).

$$dW = 2\pi |F_{Ef,E0}|^2 \delta(E - E_0 - \omega) df \tag{A.0.0.4a}$$

$$F_{Ef,E0} = -\frac{1}{c} \sum_{i=1}^{N} a_k \int \Psi^*_{E0}(x_1 ... x_N)(\varepsilon_k \cdot P_n)\Psi_{Ef}(x_1 ... x_N) d_{x1} ... d_{xn} \tag{A.0.0.4b}$$

Where the $\delta(E - E_0 - \omega)$ Dirac delta function expresses the energy conservation law. Being the cross section defined as the transition probability per unit incoming photon flux density, it can be directly derived from eq.(A.0.0.4).

$$\sigma(\omega) = \frac{\pi^2}{\omega c} |D_{f,0}|^2 \delta(E - E_0 - \omega) df \tag{A.0.0.5a}$$

$$D_{f,0} = \int \Psi^*_0(x_1 ... x_N)(\varepsilon_k \cdot P_n)\Psi_f(x_1 ... x_N) d_{x1} ... d_{xn} \tag{A.0.0.5b}$$

In eq.(A.0.0.5) $D_{f,0}$ is the electric dipole transition matrix element. In the long-wave approximation the "velocity" form of $D_{f,0}$ of eq.(A.0.0.5) can be equivalently written in its "length" form.

$$D_{f,0} = \omega \int \Psi^*_0(x_1 ... x_N)(\varepsilon_k \cdot r_n)\Psi_f(x_1 ... x_N) d_{x1} ... d_{xn} \tag{A.0.0.6}$$

It follows that (pointing out that the term 1/c in (A.0.0.5) is the fine-structure constant α in a.u.)

$$\sigma(\omega) = 4\pi^2 \alpha \omega |D_{f,0}|^2 \delta(E - E_0 - \omega) df \tag{A.0.0.7}$$

The expressions derived are valid in both the bound-bound transition and photoionization cases. For the latter case the transition will be from an initial bound state, Ψ_0^N, to a final state characterized by a well defined ionic bound state, Ψ_I^{N-1}, and a photoelectron with a well defined asymptotic momentum $\mathbf{k}$. Thus, the final state, $\Psi_{Ik}^{(-)}$, is characterized by the quantum number I, the momentum $\mathbf{k}$, and the boundary conditions of the incoming wave (indicated by the symbol (-)). The scattering theory[56] tells us the form of the asymptotic boundary conditions for a multichannel continuum wave function, i.e. a plane wave associated with the final chan-

nel considered plus incoming spherical waves in all channels, as described in eq.(A.0.0.8).

$$\Psi_{Ik}^{(-)}(r^{N-1},r) \xrightarrow{\mathrm{r}\to\infty} \frac{1}{(2\pi)^{\frac{3}{2}}}\left[\Psi_{I}^{N-1}\exp^{ik_I\cdot r}+\sum_{I'}^{noc}\Psi_{I'}^{N-1}\frac{\exp^{-ik_{I'}\cdot r}}{r}\right] \tag{A.0.0.8}$$

Here $\Psi_{I'}^{N-1}$ are the wave functions that describe the final ionic states I' and *noc* is the number of open channels at ω. The electron wave function Ψ_{EIL} (where L is the angular momentum) in the (x, y, z) coordinate system can be expressed in polar coordinates (r,ϑ,ϕ) by the use of a partial wave expansion of the form

$$\Psi_{EIL}=\sum_{I'L'}\Psi_{I'}^{N-1}R_{EI'L'IL}(r)Y_{L'}(\hat{r}) \tag{A.0.0.9}$$

where $Y_{L'}(\hat{r})$ are spherical harmonic functions, and $R_{EI'L'IL}(r)$ is the radial part of the partial wave, whose asymptotic behavior can be expressed as a linear combination of irregular spherical Bessel functions.

$$R_{EI'L'IL}(r) \xrightarrow{\mathrm{r}\to\infty} f_{l'}(k_I r)A_{I'L'IL}+g_{l'}(k_I r)B_{I'L'IL} \tag{A.0.0.10}$$

Multiplying by the A^{-1} matrix leads to K-matrix normalization

$$\Psi_{EIL}^{k}=\sum_{I'L'}\Psi_{EI'L'}A_{I'L'IL}^{-1} \qquad K=BA^{-1} \tag{A.0.0.11}$$

and multiplying by $(1+iK_l^{-1})$ we get the so called S^{+}-matrix boundary condition.

$$\Psi_{EIL}^{(-)}=\sum_{I'L'}\Psi_{EI'L'}^{k}(1+iK)_{I'L'IL}^{-1} \tag{A.0.0.12}$$

Finally, a transformation from the angular momentum to the linear momentum conditions gives the final form of the wave function.

$$\Psi_{Ik}^{(-)}=\sum_{L}C_{Lk}\Psi_{EIL}^{(-)} \tag{A.0.0.13a}$$

$$C_{Lk}=\frac{1}{\sqrt{m}}i^{l}\exp^{-i\sigma_l}Y_{L}^{*}(\hat{k}) \tag{A.0.0.13b}$$

The dipole matrix elements computed from the continuum wave function Ψ_{EIL} is then defined by

$$D_{EIL_\gamma} = \int \Psi_{EIL} D_{1\gamma} \Psi_0 \tag{A.0.0.14}$$

and can be transformed to the linear momentum asymptotic boundary condition in the same way as Ψ_{EIL}.

$$D^{(-)}_{Ik\gamma} = \sum_L C_{Lk} D^{(-)}_{EIL\gamma} \tag{A.0.0.15}$$

Because calculations are best performed employing full point group symmetry and symmetry adapted angular functions $\chi_{lh\lambda\mu}$, so that $L \equiv lh\lambda\mu$. another transformation to the angular momentum basis Y_{lm} is needed.

$$D^{(-)}_{Ik\gamma} = \sum_{lm} Y_{lm} D^{(-)}_{EIlm\gamma} \tag{A.0.0.16}$$

The dipole operator in the laboratory frame (LF), D_{1m_r} has to be expressed through its component in the molecular frame (MF), $D_{1\gamma}$ by the use of a rotation matrix $R^1_{\gamma m_r}$.

$$D_{1m_r} = \sum_\gamma D_{1\gamma} R^1_{\gamma m_r} \tag{A.0.0.17}$$

Here the LF(Z', X', Y') coordinates system is rotated to the MF(X, Y, Z) coordinate system ; this rotation is define by the Euler angles $\Omega = (\alpha, \beta, \gamma)$, where α and γ are the polar angles which define the photon orientation in the MF. Furthermore we assume the LF Z' axis defined by the electric vector **E** in the case of linearly polarized light (LP), for which $m_r = 0$, or by the photon propagation direction in the case of circularly polarized light (CP), for which $m_r = \pm 1$.

We can now write the differential form of the cross section in eq.(A.0.0.7) (normalized to the energy Dirac delta function)as:

$$\frac{d\sigma_I(\omega)}{dk d\omega} = 4\pi^2 \alpha\omega |D^{(-)}_{Ik\gamma}|^2 =$$

$$= 4\pi^2 \alpha\omega \sum_{lm\gamma l'm'\gamma'} Y_{ml}(\hat{K}) Y^*_{m'l'}(\hat{K}) R^1_{\gamma m_r}(\Omega) R^{1*}_{\gamma' m_r}(\Omega) D^{(-)}_{lm\gamma} D^{(-)*}_{l'm'\gamma'} \tag{A.0.0.18}$$

Here

$$Y_{ml} Y^*_{m'l'} = (-1)^m \sum_L \sqrt{\frac{(2l+1)(2l'+1)(2L+1)}{4\pi}} \begin{pmatrix} l' & l & L \\ m' & -m & M \end{pmatrix} \begin{pmatrix} l' & l & L \\ 0 & 0 & 0 \end{pmatrix} Y_{LM}(\hat{K}) \tag{A.0.0.19}$$

where M = m-m', and

$$R^1_{\gamma m_r} R^{1*}_{\gamma' m_r} = (-1)^{\gamma' m_r} \sum_J (2J+1) \begin{pmatrix} 1 & 1 & J \\ \gamma' & -\gamma & \gamma - \gamma' \end{pmatrix} \begin{pmatrix} 1 & 1 & J \\ m_r & -m_r & 0 \end{pmatrix} R^J_{\gamma-\gamma',0}(\Omega) \tag{A.0.0.20}$$

$$R^J_{M0}(\alpha\beta\gamma) = (-1)^M \sqrt{\frac{4\pi}{2J+1}} Y_{J,-M}(\beta,\alpha) \tag{A.0.0.21}$$

Finally, we obtain

$$\frac{d\sigma_I(\omega)}{dk d\omega} = 4\pi^2 \alpha\omega (-1)^{m_r} \sum_{LM} A_{LM} Y_{LM}(K) \tag{A.0.0.22}$$

where $A_{LM}(k, m_r, \Omega)$ is equal to

$$A_{LM} = \sum_{lm\gamma, l'm', \gamma'} (-1)^m \sqrt{\frac{(2l+1)(2l'+1)(2L+1)}{4\pi}} \begin{pmatrix} l' & l & L \\ m' & -m & M \end{pmatrix}$$

$$\begin{pmatrix} l' & l & L \\ 0 & 0 & 0 \end{pmatrix} D^{(-)}_{lm\gamma} D^{(-)*}_{l'm'\gamma'} (-1)^\gamma \sum_J (2J+1) \begin{pmatrix} 1 & 1 & J \\ \gamma' & -\gamma & \gamma - \gamma' \end{pmatrix}$$

$$\begin{pmatrix} 1 & 1 & J \\ m_r & -m_r & 0 \end{pmatrix} (-1)^{\gamma-\gamma'} \sqrt{\frac{4\pi}{2J+1}} Y_{J,\gamma'-\gamma}(\beta,\alpha) =$$

$$= \sum_{lm\gamma, l'm', \gamma'} (-1)^{m+\gamma'} \hat{l}\hat{l}'\hat{L}\hat{J} \begin{pmatrix} l' & l & L \\ m' & -m & M \end{pmatrix} \begin{pmatrix} l' & l & L \\ 0 & 0 & 0 \end{pmatrix} D^{(-)}_{lm\gamma} D^{(-)*}_{l'm'\gamma'}$$

$$\sum_J \begin{pmatrix} 1 & 1 & J \\ \gamma' & -\gamma & \gamma - \gamma' \end{pmatrix} \begin{pmatrix} 1 & 1 & J \\ m_r & -m_r & 0 \end{pmatrix} Y_{J,\gamma'-\gamma}(\beta,\alpha) \tag{A.0.0.23}$$

with $\hat{l} = \sqrt{2l+1}$).

At this point, it should be stressed out that the dynamical part of the cross section, i.e. the dependence on the photon energy, is only in the $D_{lm\gamma}$ term, in fact it depends on the initial and final states and on the Coulomb phase shift σ_l. All the other terms in the expressed equations are geometrical factors. The integral cross section is then obtained by integrating over all emission direction $\hat{k}$

$$\int Y_{LM}(\hat{k})d\hat{k} = \delta_{L0}\delta_{M0}\sqrt{4\pi} \tag{A.0.0.24a}$$

$$\sigma(\Omega) = \int \frac{d\sigma}{d\mathbf{k}}d\hat{k} = 4\pi^2\alpha\omega(-1)^{m_r}\sqrt{4\pi}A_{00} \tag{A.0.0.24b}$$

and the total cross section for randomly oriented molecules is obtained by averaging over Ω.

$$\frac{1}{8\pi^2}\int R^j_{m'm}(\Omega)d\Omega = \delta_{j0}\delta_{mm'} \tag{A.0.0.25a}$$

$$\frac{1}{8\pi^2}\int A_{00}(\Omega)d\Omega \to \delta_{j0}\delta_{\lambda\lambda'} \tag{A.0.0.25b}$$

$$\begin{pmatrix} l & l & 0 \\ m & -m & 0 \end{pmatrix}\begin{pmatrix} l & l & 0 \\ 0 & 0 & 0 \end{pmatrix}\sqrt{\frac{(2l+1)^2}{4\pi}} = (-1)^{l-m}(-1)^l\frac{1}{\sqrt{4\pi}} = \frac{(-1)^m}{\sqrt{4\pi}} \tag{A.0.0.25c}$$

$$\begin{pmatrix} 1 & 1 & 0 \\ \lambda & -\lambda & 0 \end{pmatrix}\begin{pmatrix} 1 & 1 & 0 \\ m_r & -m_r & 0 \end{pmatrix} = (-1)^{1-\lambda}(-1)^{1-m_r}\frac{1}{3} = \frac{(-1)^{1+m_r}}{3} \tag{A.0.0.25d}$$

Finally

$$\sigma = \frac{4}{3}\pi^2\alpha\omega\sum_{lm\gamma}|D^{(-)}_{lm\gamma}|^2 = \frac{4}{3}\pi^2\alpha\omega\sum_{lh\lambda\mu\gamma}|D^{(-)}_{lh\lambda\mu\gamma}|^2 \tag{A.0.0.26}$$

We can now calculate the differential cross section in the LF frame by re-expressing the $\hat{k}$ vector in the MF frame through the rotation matrices, and afterwards averaging over all the molecules orientations Ω.

$$Y_{LM'}(\hat{k}) = \sum_M Y_{LM}(\hat{k'})R^{L*}_{MM'}(\Omega) \tag{A.0.0.27a}$$

$$R^{L*}_{MM'}(\Omega)R^J_{\gamma-\gamma',0}(\Omega) = (-1)^{\gamma-\gamma'}\sum_{KQQ'}(2K+1)\begin{pmatrix} L & J & K \\ M' & \gamma'-\gamma & Q' \end{pmatrix}\begin{pmatrix} L & J & K \\ M & 0 & Q \end{pmatrix}D^K_{Q'Q}(\Omega) \tag{A.0.0.27b}$$

where $M'+\gamma'-\gamma+Q' ==$ and $Q = -M$. From equations (A.0.0.22) and (A.0.0.23) we can derive

$$(-1)^{m_r}\sum_{LM'}A_{LM'}(k,\Omega)Y_{LM'}(\hat{k})=(-1)^{m_r}\sum_{LM}\bar{A}_{LM}(k,\Omega)Y_{LM}(\hat{k'}) \tag{A.0.0.28}$$

$$\bar{A}_{LM}=\sum_{M'}A_{LM'}R^{L*}_{M'M}(\Omega)=\sum_{lm\gamma l'm'\gamma'}(-1)^{m+\gamma}\sum_{M'}\begin{pmatrix}l' & l & L\\ m' & -m & M'\end{pmatrix}\begin{pmatrix}l' & l & L\\ 0 & 0 & 0\end{pmatrix}$$
$$\sqrt{\frac{(2l+1)(2l'+1)(2L+1)}{4\pi}}D^{(-)}_{lm\gamma}D^{(-)*}_{l'm'\gamma'}\sum_{M'}(2J+1)\begin{pmatrix}1 & 1 & J\\ \gamma' & -\gamma & \gamma-\gamma'\end{pmatrix}$$
$$\begin{pmatrix}1 & 1 & J\\ m_r & -m_r & 0\end{pmatrix}(-1)^{\gamma-\gamma'}\sum_{K}(2K+1) \tag{A.0.0.29}$$
$$\begin{pmatrix}M' & J & K\\ M' & \gamma'-\gamma & Q'\end{pmatrix}\begin{pmatrix}M' & J & K\\ M & 0 & -M\end{pmatrix}D^{K}_{Q',-M}(\Omega)$$

in which $M'=m-m'$ and $Q'=\gamma-\gamma'-M'$. It follows that

$$\bar{A}_{LM}(k,\Omega)=\sum_{lm\gamma l'm'\gamma'}(-1)^{\gamma+1}\begin{pmatrix}l' & l & L\\ m' & -m & M\end{pmatrix}\begin{pmatrix}l' & l & L\\ 0 & 0 & 0\end{pmatrix}$$
$$\sqrt{\frac{(2l+1)(2l'+1)(2L+1)}{4\pi}}D^{(-)}_{lm\gamma}D^{(-)*}_{l'm'\gamma'}\sum_{JK}(2J+1)(2K+1)\begin{pmatrix}1 & 1 & J\\ \gamma' & -\gamma & \gamma-\gamma'\end{pmatrix}$$
$$\begin{pmatrix}1 & 1 & J\\ m_r & -m_r & 0\end{pmatrix}\begin{pmatrix}L & J & K\\ m-m' & \gamma'-\gamma & Q\end{pmatrix}\begin{pmatrix}L & J & K\\ M & 0 & -M\end{pmatrix}D^{K}_{Q',-M}(\Omega) \tag{A.0.0.30}$$

It is now possible to average over all the molecular orientations Ω.

$$\frac{1}{8\pi^2}\int\bar{A}_{LM}(k,\Omega)d\Omega=\bar{A}_{L0}(k)\equiv A_L(k)=$$
$$=\sum_{lm\gamma}(-1)^{m\gamma'}\begin{pmatrix}l & l' & L\\ -m & m' & M\end{pmatrix}$$
$$\begin{pmatrix}l & l' & L\\ 0 & 0 & 0\end{pmatrix}\sqrt{\frac{(2l+1)(2l'+1)(2L+1)}{4\pi}}D^{(-)}_{lm\gamma}D^{(-)*}_{l'm'\gamma'}(2L+1)$$
$$\begin{pmatrix}1 & 1 & L\\ -\gamma & \gamma' & \gamma-\gamma'\end{pmatrix}\begin{pmatrix}1 & 1 & L\\ -m_r & m_r & 0\end{pmatrix}\begin{pmatrix}L & L & 0\\ m-m' & \gamma'-\gamma & 0\end{pmatrix}\begin{pmatrix}L & L & 0\\ 0 & 0 & 0\end{pmatrix}=$$
$$=\sqrt{\frac{2L+1}{4\pi}}\sum_{lm\gamma l'm'\gamma'}(-1)^{m+\gamma}\begin{pmatrix}l' & l & L\\ -m & m' & M\end{pmatrix}$$
$$\begin{pmatrix}l & l' & L\\ 0 & 0 & 0\end{pmatrix}\sqrt{(2l+1)(2l'+1)(2L+1)}D^{(-)}_{lm\gamma}D^{(-)*}_{l'm'\gamma'}$$

$$\begin{pmatrix} 1 & 1 & L \\ -\gamma & \gamma' & \gamma-\gamma' \end{pmatrix} \begin{pmatrix} 1 & 1 & L \\ -m_r & m_r & 0 \end{pmatrix} \tag{A.0.0.31}$$

in which $m-m' = \gamma-\gamma'$. We then expand $A_L(k)$ in Legendre polynomials.

$$A_L(k)Y_{L0} = \sqrt{\frac{2L+1}{4\pi}} A_L(k) P_L(\cos\theta) \tag{A.0.0.32}$$

From which

$$\frac{d\sigma}{d\mathbf{k}} = \pi\alpha\omega(-1)^{m_r} \sum_L A_L P_L(\cos\theta') \tag{A.0.0.33}$$

(θ' is referred to the LF frame)

$$\begin{aligned} A_L(k) = (2L+1) \begin{pmatrix} l & l' & L \\ m_r & -m_r & 0 \end{pmatrix} \sum_{lm\gamma l'm'\gamma'} (-1)^{m+\gamma} \\ \sqrt{(2l+1)(2l'+1)} \begin{pmatrix} l & l' & L \\ 0 & 0 & 0 \end{pmatrix} \begin{pmatrix} l & l' & L \\ -m & m' & m-m' \end{pmatrix} \\ \begin{pmatrix} 1 & 1 & L \\ \gamma' & -\gamma & \gamma-\gamma' \end{pmatrix} \begin{pmatrix} 1 & 1 & L \\ -m_r & m_r & 0 \end{pmatrix} D^{(-)}_{lm\gamma} D^{(-)*}_{l'm'\gamma'} \end{aligned} \tag{A.0.0.34}$$

The term

$$\begin{pmatrix} 1 & 1 & L \\ -m_r & m_r & 0 \end{pmatrix}$$

implies that $0 \leq L \leq 2$, i.e. L can be only equal to $0, 1$ and 2. Moreover, in the case of LP light $m_r = 0$ and the term

$$\begin{pmatrix} 1 & 1 & L \\ 0 & 0 & 0 \end{pmatrix}$$

is non-zero only for even values of L. This implies that only the terms A_0 and A_2 are non-zero in eq.
eqrefeq:theo42. Integrating this equation for $P_0 = 1$

$$\begin{aligned} \sigma = \int \frac{d\sigma}{d\mathbf{k}} \sin\theta d\theta d\phi = \pi\alpha\omega(-1)^{m_r} A_0 \int 1 \sin\theta d\theta d\phi = \\ = 4\pi^2\alpha\omega(-1)^{m_r} A_0 \Rightarrow \frac{\sigma}{4\pi} = \pi^2\alpha\omega(-1)^{m_r} A_0 \end{aligned} \tag{A.0.0.35}$$

and

$$\frac{d\sigma}{d\mathbf{k}} = \pi\alpha\omega(-1)^{m_r} A_0 \left(1 + \frac{A_1}{A_0}\cos\theta + \frac{A_2}{A_0} P_2(\cos\theta)\right) \tag{A.0.0.36}$$

Here $P_2(\cos\theta) = \frac{1}{2}(3\cos^2\theta - 1)$ is the second-order Legendre Polynomial. If we define

$$b_1 = \frac{A_1(m_r = 1)}{A_0} \tag{A.0.0.37a}$$

$$b_2 = \frac{A_2(m_r = 0)}{A_0} \tag{A.0.0.37b}$$

We can obtain the differential photoionization cross section

$$\frac{d\sigma}{d\mathbf{k}} = \frac{\sigma}{4\pi}\left[1 + m_r b_1 \cos\theta + (-\frac{1}{2})^{m_r} b_2 P_2(\cos\theta)\right] \tag{A.0.0.38}$$

Appendix B

Data acquisition and data analysis

B.1 Epichlorohydrin

The vapor was admitted in the interaction region by an effusive source through a nonmagnetic hypodermic needle. The sample was kept at room temperature (23 °C) during the measurements, and the gas rating was adjusted to set a constant pressure of ∼1.0 x 10^{-6} mbar in the ionization chamber. For signal normalization purpose, the incident photon flux was recorded, along with the photoelectron signal, with two different methods, namely as current of a silicon photodiode (IRD-AXUV-100) set as beam stopper after the interaction region, and as current of the gold coated refocusing mirror mounted at the entrance of the ionization chamber. The measurements were performed in the 13 eV – 54 eV photon energy range and required various runs, and were carried out using both the Normal Incidence Monochromator (NIM) and the Spherical Grazing monochromator (SGM) of the beamline. The partial photoionization cross sections for the outer valence ionization channels of epichlorohydrin were measured as a function of the photon energy by recording photoelectron spectra at the magic angle and fixed photon energies. The spectra were corrected by the spectrometer transmission function, as appropriate, taking into account the change in electron detection efficiency due to the different value of the electron kinetic energy and the selected constant pass energy value. For this purpose, photoelectron spectra of two reference gases, He and Ar, were recorded at different kinetic energies and pass energies, 5 eV and 10 eV, to determine the spectrometer transmission functions. The experimental relative values of the epichlorohydrin valence cross sections were obtained in a large photon energy range by combining low energy and high energy measurements taken by the NIM and SGM, respectively. To properly merge the two sets of data together, epichlorohydrin PE spectra were recorded at 32.5 eV and 34.5 eV photon energies by both the NIM and SGM, using the same experimental conditions. Furthermore, the PE

spectrum of the first four PE bands of epichlorohydrin was systematically acquired at the photon energies 22.5 eV (NIM range) and 34.5 eV (SGM range) and at 0° detection angle, as reference spectra, to monitor possible small changes in the experimental conditions over time, and eventually correct the relative cross section values and estimate errors in measuring these observables. The asymmetry parameters were obtained from the peak areas of the considered band obtained at $\theta = 0°$ and $\theta = 54.7°$, respectively. The peak areas at the two different angles were referred to the same photon flux and molecular target density. The errors on the epichlorohydrin β values were estimated by measuring, with the same experimental procedure, well known asymmetry parameters of reference gases, namely Ar, He and O_2, in a wide photon energy range and exhibiting a large variety of β values[268, 269, 270]. The relative values of $\sigma(h\nu)$ and $\beta(h\nu)$ parameters were obtained by extracting from the spectrum the relative intensities of the single PE components in terms of peak areas obtained by the global multipeak fitting procedure described below [Global Multipeak Fitting Package implemented in the IGOR PRO data analysis program (WaveMatrix).]. The background contribution was systematically removed from all the spectra, by fitting the measured background spectrum (without sample) with an arctangent function plus a linear function (χ-square fitting mrthod), and subtracting the latter from the epichlorohydrin spectrum. The obtained net spectra where analysed by the global multipeak fitting method by dividing the spectra in two not overlapping regions. The first group of four bands, the 24a - 20a components in the 10.0 -13.0 eV IE range, could be analyzed separately from the other bands. These four bands exhibit a variety of shapes and intensities, as well as different extent of overlap. In order to describe their envelopes and ionization potentials precisely and consistently, a program was developed which efficiently curve fits the spectral data. Because all bands have an asymmetric shape, with longer tail on the high IE side (right side), an asymmetric Gaussian was adopted, namely a set of bi-Gaussian functions were used for the spectral deconvolution. Such an asymmetric function is made of two half Gaussian functions which share the summit of the peak. Four parameters fully define the function, the location of the summit (the vertical IE value E_0), the standard deviations σ_l and σ_r of the left and right half Gaussian functions, and the scale factor δ. This method [271, 272] has been fruitfully applied to analyze experimental PE spectra[273, 274]. The PE spectra recorded at all the photon energies, and at 0° and 54.7° detection angles, were included in the global fit, simultaneously. The four fit parameters defining the PE band positions, namely the vertical IEs, were considered differently. The IE of the first band (24a MO) was set as free parameter in each PE spectrum, whilst the positions of the other three bands were defined as relative IEs referred to the first HOMO PE peak and considered equal in all the spectra, since the relative positions of the PE bands are actually constant in all the spectra. The eight left and right standard deviation free parameters, which define

the peak shape of the four PE bands, were considered constant in all the spectra, namely each peak preserves its own shape (σ_l and σ_r values) on changing the photon energy and the angle of detection. The scale factors δ_i of the four bands were set as free fit parameters and specific for each PE spectrum. The global multipeak fit method thus allowed the photoelectron band relative intensities to be measured in terms of peak areas, and provided a systematic method to measure the $\sigma(h\nu)$ and $\beta(h\nu)$ parameters, for the valence photoionization processes of epichlorohydrin as a function of photon energy.
The six PE bands at higher energies, the 20a – 15a spectral components, were analyzed by a simpler procedure, since all these bands share, with good approximation, the same peak shape. The whole set of the PE experimental spectra, namely recorded at all the investigated photon energies and the 0° and 54.7° detection angles, were simultaneously involved in the global multipeak fit analysis. Similarly to the first group of bands, the six peak positions were referred to the vertical IE of the HOMO band and considered as six free fit parameters, whose values are preserved in all the spectra. Here, only two standard deviation free parameters, σ_l and σ_r, were sufficient to accurately describe the peak shape of the six bands. This peak shape was considered constant, being not significantly affected by the change in photon energy and angle of detection. The six scale factors, δ_i, were defined as free fit parameters and specific for each PE spectrum. The best fit scale factors δ_i and the standard deviations σ_l and σ_r, obtained by the global fit spectral analysis, allowed to measure the photoionization observables $\beta(h\nu)$ and $\sigma(h\nu)$ as a function of photon energy also for the high energy PE bands of epichlorohydrin. The high flexibility of the Global MultiPeak Fitting Package of IGOR PRO allowed us to provide the bi-Gaussian function as external (user-defined) model fit function to curve fit a large set of multicomponent experimental PE spectra, simultaneously, and to define the nature, constraints, and links to freely chosen experimental data subsets of the fit parameters, according to the description given above. The large change in relative intensity of the first four PE bands, observed in the investigated photon energy range, was fruitfully used, by means of the global multipeak fit analysis, to shed more light in this crowded PE spectral region.

B.2 Propylene oxide

The experiments on the double photoionization of propylene oxide were performed at the CiPo beamline of the Elettra Synchrotron by the use of the ARPES 3D ion imaging end station. The operating pressure of the ARPES end station was kept constant and set at the 10^{-7} mbar range. The high intensity energy tunable synchrotron light beam crosses at right angle an effusive molecular beam of propylene oxide molecules. Product ions and photoelectrons produced by each double photoionization event

are detected in coincidence. The monochromatic synchrotron radiation was scanned in the 18.0-37.0 eV range. The detection axis of the time-of-flight (TOF) mass spectrometer was set perpendicular to the the horizontal polarization plane of the linearly polarized radiation. The Normal Incidence Monochromator (NIM) of ther CiPo beamline allows to cover the entire investigated energy range with a resolution of about 2.0–1.5 meV. The use of the NIM geometry was adopted to reduce spurious effects, due to ionization by photons from higher orders of diffraction. The adoption of the NIM at the "CiPo" beamline, together with the emission spectrum of the electromagnetic wiggler allows to probe a lower photon energy range with respect to the linearly polarized light available at the "GasPhase" beamline.
During the experiment, the incident photon flux, the gas pressure, and the ion yields for each investigated channel were monitored and acquired. Each channel ion yield is normalized for the total ion yield in order to obtain the branching ratios as a function of the photon energy. The effusive molecular beam is produced by a 1.0 mm inner diameter stainless steel needle nozzle fed by a racemic mixture (99% nominal purity, Sigma Aldrich). A needle valve was placed between the glass cylinder containing the propylene oxide and the nozzle to optimize the molecular beam source pressure. The two-body fragmentation dynamics could be analyzed by using the momentum matching procedure, in which a filter to discriminate true coincidences related to each recorded fragmentation channels, produced by Coulomb explosion of the intermediate propylene oxide molecular dication, is applied. Such momentum matching filter allows the analysis of the ion coincidences by isolating only pulses due to true double coincidences. To do so the following analytic condition has been applied:

$$s \leq \frac{\sqrt{p_{x1,2}^2 + p_{y1,2}^2 + p_{z1,2}^2}}{|p_1| + |p_2|} \tag{B.2.0.1}$$

where $p_{x1,2}$, $p_{z1,2}$, and $p_{y1,2}$ are the sum of projections of p_1 and p_2 momentum vectors of the final ion pairs produced by the two-body fragmentation processes. In the present presented data analysis we used a value of $S \leq 0.1$, which is an empirical factor which is the result of a compromise between a good statistics of the recorded signal and the background subtraction. Following such a procedure we were able to extract the ion KER distributions, the angular distributions, and the relative cross sections for each of the measured two-body dissociation channel.

B.3 Osmium tetroxide

The experimental measurements were taken at the Gasphase Photoemission beamline of the Elettra synchrotron radiation source (Trieste,

Italy). The valence photoelectron (PE) spectra of the OsO_4 molecule were recorded at fixed photon energies spanning the 17-90 eV range and using the ARPES-TPES end station. The analyzer, equipped with the new developed 2D detector and deflecting electrode, was operated in constant pass energy mode, selecting 10 and 15 eV pass energies, respectively for PE spectra recorded at low and high photon energies, namely below and above 22 eV. The molecular vapor generated by the solid OsO_4 (Sigma-Aldrich, purity $\geq 99\%$), kept at constant room temperature (24°C), was admitted in the interaction region through a nonmagnetic hypodermic needle. The pressure in the ionization region could be kept below 1.0 x 10^{-6} mbar. The PE spectra were measured as a function of photon energy at two different detection angles with respect to the polarization plane of the linearly polarized radiation, namely at $\theta = 0°$ and $\theta = 54.7°$. The asymmetry parameter $\beta(h\nu)$ was derived according to the equation $\beta(h\nu)$ = R - 1, where R is the ratio between the peak areas of the selected PE band obtained at the two different angles, R = I(0°)/I(54.7°). The background spectrum was recorded as a function of photon energy at both detection angles and subtracted from the corresponding OsO_4 PE spectra, in order to remove its spurious contribution. The accuracy of the $\beta(h\nu)$ parameter measurements was checked by measuring well known asymmetry parameters of Ar and He, as reference data. The spectrometer resolution used at 10 eV pass energy was 45 meV (FWHM), as measured by recording atomic peaks of Ar. All PE spectra were energy calibrated against the known IE values of N_2 and Ar.

B.4 1-methoxy-2-propanol

The experiment on the 2-methoxy propanol was performed at the FELIX free electron laser facility at Radboud University (Nijmegen, The Netherlands). The far-IR and mid-IR spectra of the 1-methoxy-2-propanol diasteromeric dimers were measured using VUV-IRMPD spectroscopy in the 520 cm^{-1} - 1540 cm^{-1} spectral region. In an IRMPD experiment, the target molecules are confined in a small interaction region which is crossed by the tunable IR radiation. When the IR frequency υ_i coincides with the energy of a transition from the vibrational ground state to an excited vibrational level, resonant absorption of the IR pulse takes place. Between two or more IR excitation pulses Intramolecular Vibrational Redistribution (IVR) effect [275] takes place, redistributing the acquired internal energy over different vibrational modes. If the process is performed in absence of collisions, as in the case of supersonic jets, the acquired IR multi-photon internal energy leads to molecular dissociation as it exceeds the fragmentation energy threshold. The IVR process that takes place between two IR photons absorption can be more or less efficient, depending on the nature of the excited vibrational states. This implies that the multi-photon IR spectra can be not equivalent to the cor-

responding spectra recorded using single IR photon absorption; spectral lines can be broadened and shifted, and line intensities can differ from those predicted by the calculated IR spectrum. In the experimental setup the target species are prepared in their rovibronic ground states by means of supersonic-jet cooling and vibrationally excited by IR photons. The multiple absorption of IR-FEL photons leads to molecular fragmentation. The fragments are then probed with 10.49 eV VUV photons as a function of the IR wavelength, and the resulting ionized IRMPD products are analyzed by a TOF mass spectrometer, in order to obtain mass-selected IR spectra. The enantiomerically pure S-(+)-1-methoxy-2-propanol sample (purity $\geq$ 98.5%) and the racemic mixture (purity $\geq$ 99.5%) were obtained commercially from the Sigma Aldrich company. The heated sample compartment (T = 323 K) was positioned in front of a pulsed valve nozzle (0.5 mm orefice, Jordan TOF Products Inc.). A complete set of measurements was first performed for an enantiomerically pure sample and then for the racemic mixture. This procedure avoids any possible contamination of the enantiopure sample. The 1-methoxy-2-propanol vapours were then seeded in a supersoic-jet generated by a pulsed valve, using Ar (at 2 bar pressure) as a carrier gas, and admitted in the vaccum chamber region. The jet of electronically, vibrationally and rotationally cooled molecules was further collimated by a skimmer, and directed into the interaction region, where it was crossed by a pulsed IR FEL beam and a delayed VUV laser beam. The VUV laser photons were produced by focusing 355nm light (3^{rd} harmonic of Nd^{3+}:YAG laser) in a gas cell containing a 10:1 mixture of, respectively, Ar and Xe gases. The resulting 3^{rd} harmonic radiation, with wavelength of 118 nm (10.49 eV) and pulse duration of $\sim$ 2-3 ns, was refocused into the interaction region by a MgF_2 lens. When a molecular vibrational transition resonates with the scanned IR frequency, the molecule dissociate through the IRMPD mechanism. The resulting fragments and parent molecules are then ionized by the VUV laser radiation at the end of each FEL macropulse (6-8 μs), and the resulting ions are detected by a reflectron time-of-flight spectrometer, allowing recording the mass-selected IR-spectra. In order to measure reference mass spectra without the IR-FEL pulse at every VUV laser pulse, the VUV ionizing laser and the pulsed valve operated at 10 Hz, while the FELIX laser operated at 5 Hz. Different spectra in different spectral regions were recorded at different FELIX laser power attenuations, namely 0 dB, 3 dB, 5 dB and 8 dB.

The molecular structures optimization and the vibrational frequency calculations were performed using the Gaussian 16 package[276]. The geometry optimization of the (S)-1-methoxy-2-propanol and (R)-1-methoxy-2-propanol monomers were performed with the MOPAC program[277] using the PM6-D3H4 method. A conformational analysis of the dimers structures were performed by randomly changing all rotable torsions in the optimized (S)/(R)-1-methoxy-2-propanol monomers. The random dimer structures were initially optimized using the PM6 method, and only the

structures with an electronic energy below 300 KJ/mol were submitted to a further optimization at the DFT level using the ωB97x-D functional. The lowest energy conformer were submitted to another optimization cycle using the Tight optimization criterion (RMS force $< 10^{-5}$), and frequencies were calculated. The electronic energies, and accordingly the Boltzmann populations, of the optimized dimer conformers were calculated by the G4MP2 method[278]. Harmonic frequencies were calculated for the lowest energy conformers at the DFT level, using the B3LYP functional and the 6-311++G** basis set.

Acknowledgements

The list of people to acknowledge is infinitely long. First of all, I want to thank my supervisor, Prof. Stefano Stranges, that guided me and helped me during my Ph.D., and who taught me what it takes to be a good researcher. I want to thanks Michele Alagia, who worked with me every day and helped me so much. I want to thank Robert Richter for his advises, and for what I have learned from him during our countless beamtimes (and coffee breaks). My acknowledgments also go to all the people of the Gasphase, Cipo and LDM beamlines (Marcello, Monica, Cesare, Kevin, Carlo, Michelino, Oksana, Nicola, Stefano, Daniele and, of course, Fabio) for the help, the support and encouragement I received from them in these years. I thank Vitali Zhaunerchyk (and Vasyl) for the opportunity he gave me to spend a wonderful period in Gothenburg. I want to thank Stefano Falcinelli for the work that we did together, that helped me to grow as a researcher. I want to thank the Theoretical chemistry group of the University of Trieste (Prof. P. Decleva. Prof. M. Stener and Prof. D. Toffoli) for their important contribution to this work. Finally, I want to thank my friends, and please let me do it in my language, Italian.

Ringrazio gli amici, che mi hanno sempre sostenuto, con cui ho condiviso serate piene di risate e momenti amari. Ci sono gli amici di sempre (la coppia dell'ultimo banco, Danilo e Manuel), gli amici che ho incontrato da studente universitario (Andrea, Marco B. e Marco P., che hanno sempre saputo tirare fuori il peggio di me, Valeria e Veronica, che per me saranno sempre come sorelle, anche se le nostre strade si sono separate), e gli amici triestini (Alessandro, Alessandra, Valeria, Aurora, Sara, Stefano, Alessio, Gianmarco, Giannuz), anche se di triestino non hanno nulla. Poi c'è Giulia, che mi è sempre stata vicina, che ha sempre creduto in me, per cui poche righe non basteranno mai. Infine voglio ringraziare la mia famiglia, perché senza di lei non sarei qui a scrivere questa tesi.

Avrò sicuramente dimenticato qualcuno, e me ne scuso, ma per fortuna l'amicizia e l'affetto non si misurano con poche righe alla fine di una pagina, ma si dimostra giorno per giorno.

Bibliography

[1] Lord Kelvin. 1904. Baltimore lecture. London: Clay.

[2] G.E. Tranter, "Parity-violating energy differences of chiral minerals and the origin of biomolecular homochirality", *Nature.* **318**, 172 (1985), DOI: 10.1038/318172a0.

[3] J. L. Bada, "Origins of homochirality", *Nature* **374**, 594 (1995), DOI: 10.1038/374594a0.

[4] V. A. Pavlov, E. I. Klabunovskii, "Homochirality Origin in Nature: Possible Versions ", *Curr. Org. Chem.* **18**, 93 (2014), DOI: 10.2174/13852728113179990033.

[5] A. J. Hutt, S. C. Tan, "Drug Chirality and its Clinical Significance", *Drugs* **52**, 1 (1996), DOI: 10.2165/00003495-199600525-00003.

[6] C. Brown, "Chirality in drug design and synthesis",academic Press, London, 2013.

[7] Z. M. Wang, K. B. Sharpless, "A Solid-to-Solid Asymmetric Dihydroxylation Procedure for Kilogram-Scale Preparation of Enantiopure Hydrobenzoin", *J. Org. Chem.* **59**, 8302 (1994), DOI: 10.1021/jo00105a065.

[8] M. Bella, T. Gasperi, "Organocatalytic Formation of Quaternary Stereocenters", *Synthesis* **10**, 1583 (2009), DOI: 10.1055/s-0029-1216796.

[9] C. Train et al., "Strong magneto-chiral dichroism in enantiopure chiral ferromagnets", *Nat. Mat.* **7**, 729 (2008), DOI: 10.1038/nmat2256.

[10] F. Hache et al., "Nonlinear optical activity in chiral molecules: surface second harmonic generation and nonlinear circular dichroism", *C. R. Physique* **3**, 429 (2002), DOI: 10.1016/S1631-0705(02)01327-0.

[11] N. Berova, K. Nakanishi, R. W. Woody, "Circular dichroism. Principle and applications", Wiley, New York, 2000.

[12] L. D. Barron, " Molecular light scattering and optical activity", Cambridge University Press, Cambridge, 2004.

[13] C. Meinert et al., "N-(2-Aminoethyl)glycine and Amino Acids from Interstellar Ice Analogues", *ChemplusChem* **77**, 186 (2002), DOI: 10.1002/cplu.201100048.

[14] W. Soudijn, I. Van Wijngaarden, A. P. Ijzerman, "Enantioselectivity in Drug-Receptor Interactions". In: *Stereochemical Aspects of Drug Action and Disposition. Handbook of Experimental Pharmacology* **153**, Springer, Berlin, Heidelberg (2003), DOI: 10.1007/978-3-642-55842-9$_7$.

[15] T. Kitamura, T. Nishide, H. Shiromaru, Y. Achiba, N. Kobayashi, "Direct observation of dynamic chirality by Coulomb explosion imaging", *J. chem. Phys.* **115**, 5 (2001), DOI: 10.1063/1.1383793.

[16] M. Pitzer et al., "Direct determination of absolute molecular stereochemistry in gas phase by Coulomb explosion imaging", *Science* **341**, 1096 (2013), DOI: 10.1126/science.1240362.

[17] P. Herwig et al., "Imaging the Absolute Configuration of a Chiral Epoxide in the Gas Phase", *Science* **342**, 1048 (2013), DOI: 10.1126/science.1246549.

[18] S. Hüfner, "Photoelectron Spectroscopy: principles and applications", *Third Edition, Springer-Verlag Berlin Heidelberg* (2013), DOI: 10.1007/978-3-662-09280-4.

[19] S. Oswald, "X-ray photoelectron spectroscopy in analysis of surfaces", *John Wiley & Sons* (1887), DOI: 10.1002/9780470027318.a2517.pub2.

[20] G. Jenkin, C. G. Leckey, J. Liesegang, "The development of x-ray phoelectron spectroscopy 1900-1960", *J. Electron Spectros. Relat. Phenomena* **12**, 1-35 (1977), DOI: 10.1016/0368-2048(78)87006-6.

[21] J. C. Maxwell, "A dynamical theory of the electromagnetic field" *Phil. Trans. R. Soc. Lond.* **155**, 459-512 (1865).

[22] H. R. Hertz, "Über einen Einfluss des ultravioletten Lichtes auf die elektrische Entladung (On the influence of ultraviolet light on the electric discharge)", *Ann. Physik* **31**, 983 (1887), DOI: 10.1002/andp.18872670827.

[23] W. Hallwachs, "Über den Einfluß des Lichtes auf elektrostatisch geladene Körper (On the influence of light on electrostatically charged bodies)", *Ann. Phys.* **33**, 301-312 (1888), DOI: 10.1002/andp.18882690206.

[24] A. Righi, "Di alcuni nuovi fenomeni elettrici, provocati dalle radiazioni", *Nuovo Cim.* **23**, 61-64 (1888), DOI: 10.1007/BF02730228.

[25] W. C Röntgen, "Ueber eine neue Art von Strahlen (On a new kind of rays)", *Ann. Phys.* **300**, 12-17 (1898), DOI: 10.1002/andp.18983000103.

[26] J. J. Thomson, "Cathode Rays", *Phil. Mag.* **44**, 293-316 (1897), DOI: 10.1080/14786449708621070.

[27] P. von Lenard, "Ueber die lichtelektrische Wirkung (On the photoelectric effect)", *Ann. Phys.*, **313**, 149-198 (1902), DOI: 10.1002/andp.19023130510.

[28] M. Planck, "Zur Theorie des Gesetzes der Energieverteilung im Normalspectrum, In Verhandlungen der Deutchen Physikalischen Gesellschaft (On the law of distribution of energy in the normal spectrum)", *Verhandl. Dtsc. Phys. Ges.*, **2**, 202-237 (1902).

[29] A. Einstein, "Zur Elektrodynamik bewegter Körper (On the electrodynamics of moving bodies)", *Ann. Phys.*, **322**, 891-921 (1905), DOI: 10.1002/andp.19053221004.

[30] P. D. Innes, J. J. Thomson, "On the velocity of the cathode particles emitted by various metals under the influence of Röntgen rays, and its bearing on the theory of atomic disintegration", *Ann. Phys.*, **79**, 442-462 (1907), DOI: 10.1098/rspa.1907.0056.

[31] W. Friedrich, P. Knipping, M. Laue, "Interferenz-Erscheinungen bei Röntgenstrahlen (Interference phenomena with X-rays)", *Verl. der Kgl. Bayer. Akad. der Wiss*, **5**, 303-322 (1912).

[32] W. H. Bragg, "X-rays and Crystals", *Nature*, **90**, 219 (1912), DOI: 10.1038/090219a0.

[33] W. H. Bragg, "The Specular Reflection of X-rays", *Nature*, **90**, 410 (1912), DOI: 10.1038/090410b0.

[34] H. G. J Moseley, "The high-frequency spectra of the elements", *Phil. Mag.*, **26**, 1024-1034 (1913), DOI: 10.1080/14786441308635052.

[35] H. G. J Moseley, "The high-frequency spectra of the elements. Part II", *Phil. Mag.*, **27**, 703-713 (1914), DOI: 10.1080/14786440408635141.

[36] N. Bohr, "On the constitution of atoms and molecules", *Phil. Mag.*, **26**, 1-25(1913), DOI: 10.1080/14786441308634955.

[37] H. Robinson, E. Rutherford, "The secondary corpuscular rays produced by homogeneous X-rays", *Proc. Roy. Soc. Ser. A*, **26**, 455-479 (1923), DOI: 10.1098/rspa.1923.0121.

[38] R. Steinhardt, E. Serfass, "X-Ray Photoelectron Spectrometer for Chemical Analysis", *Anal. Chem.*, **23**, 1585-1590 (1951), DOI: 10.1021/ac60059a019.

[39] K. Siegbahn et al., "ESCA, atomic, molecular and solid state structure studied by means of electron spectroscopy", *Nov. Act. Uppsaliensis*, Ser. IV, Vol. 20 (1967).

[40] W. C. Price, "Chemical Spectroscopy and Photochemistry in the Vacuum-Ultraviolet", in *Proceedings of the Advanced Study Institute, held under the Auspices of NATO and the Royal Society of Canada, August 5–17, 1973, Valmorin, Quebec, Canada.*

[41] F. I. Vilesov, B. L. Kurbatov, A. N. Terenin, "Electron distribution over energies in the photoionization of aromatic amines in the gaseous phase", in *Dokl. Akad. Nauk SSSR*, **138**, 1329 (1961).

[42] F. I. Vilesov, "Photoionization of gases and vapours by vacuum ultraviolet radiation", in *Sov. Phys. Uspekhi*, **6**, 888-925 (1964).

[43] D. W. Turner, M. I. Al Jobory, "Determination of Ionization Potentials by Photoelectron Energy Measurement", *J. Chem. Phys.*, **37**, 3007-3008 (1962), DOI: 0.1063/1.1733134.

[44] D. W. Turner, "Molecular Photoelectron Spectroscopy", *Philos. Trans. Royal Soc. A* **268**, 7-31 (1970).

[45] C. R. Brundle, A. D. Baker (Editors), "Electron spectroscopy: Theory, techniques and applications, vol. 2", *Accademic Press* (1978)

[46] B. H. Bransden, C. .J Joachain, "Physics of Atoms and Molecules", *Prentice Hall* (2014)

[47] C. Cohen-Tannoudji, B. Diu, F. Laloe, "Quantum Mechanics, vol. 1 & 2", *John Wiley & Sons Inc* (1977)

[48] T. Koopman, "Uber die Zuordnung von Wellenfunktionen und Eigenwerten zu den Einzelnen Elektronen Eines Atoms", *Physica* **268**, 104-113 (1934), DOI: 10.1016/S0031-8914(34)90011-2.

[49] C. Laurence, J. Gal, "Lewis basicity and affinity scales: data and measurement", *Wiley* (2010)

[50] R. Shankar, K. Senthilkumar, P Kolandaivel, "Calculation of Ionization Potential and Chemical Hardness: A Comparative Study of Different Methods", *Int. J. Quantum Chem.* **109**, 764 (2009), DOI: 10.1002/qua.2188.

[51] J. C. Tully, R Stephen Barry, B. J. Dalton, "Angular distribution of molecular photoelectrons", *Phys. Rev.* **176**, 95 (1968), DOI: 10.1103/PhysRev.176.95.

[52] L. I. Schiff, "Quantum Mechanics, 3rd edition", *McGraw-Hill* (1968)

[53] V. K. Thankappan, "Quantum Mechanics, 2nd edition", *New age international* (1985)

[54] M. Ya. Amusia, "Atomic Photoeffect, in the Physicas of Atoms and Molecules Series", *Plenum Press* (1990)

[55] N. Chandra, "Photoelectron spectroscopic studies of polyatomic molecules: I. Theory", *J. Phys. B: At. Mol. Phys* **20**, 3405 (1986), DOI: 10.1063/1.1668742.

[56] J. R. Taylor, "Scattering Theory", *Dover Publications* (1983)

[57] J. W. Cooper, R. N. Zare, "Angular distribution of photoelectrons", *J. chem. Phys* **48**, 942 (1968), DOI: 10.1063/1.1668742.

[58] J. W. Cooper, "Photoionzation from outer subshells. A model study", *Phys. Rev.* **128**, 681 (1962), DOI: 10.1103/PhysRev.128.681.

[59] U. Fano, J. W. Cooper, "Spectral Distribution of Atomic Oscillator Strengths", *Rev. Mod. Phys.* **40**, 441 (1968), DOI: 10.1103/RevModPhys.40.441.

[60] T. A. Carlson et al., "Photoelectron dynamics of Cooper minimum in free molecules", *Z Phys D - Atoms, Molecules and Clusters* **2**, 309 (1986), DOI: 10.1007/BF01426235.

[61] T. N. Chang, "Quantitative assessment of the many-body interactions in the M-shell photoionization of Argon", *Phys. Rev. A* **18**, 1448 (1978), DOI: 10.1103/PhysRevA.18.1448.

[62] R. G. Houlgate, J. B. West, K. Codling, G. V. Marr, "The angular distribution of the 3p electrons and the partial cross section of the 3s electrons of argon from threshold to 70eV", *J. Electron Spectros. Relat. Phenomena* **9**, 205 (1976), DOI: 10.1016/0368-2048(76)81030-4.

[63] K. Codling, R. G. Houlgate, J. B. West, K. Codling, P. R. Woodruff, "Angular distribution and photoionization measurements on the 2p and 2s electrons in neon", *J. Phys. B: At. Mol. Phys.* **9**, L83 (1976), DOI: 10.1088/0022-3700/9/5/004.

[64] T. A. Carlson, M. O. Krause, "Angle resolved photoelectron spectroscopy of CS_2 and COS measured as a function of photon energy from 21 to 70 eV", *J. chem. Phys.* **77**, 1701 (1982), DOI: 10.1063/1.444067.

[65] T. A. Carlson, M. O. Krause, F. A. Grimm, P. Keller, J. W. Taylor, "Angle-resolved photoelectron spectroscopy of CCl_4: The Cooper minimum in molecules", *J. chem. Phys.* **77**, 5340 (1982), DOI: 10.1063/1.443782.

[66] A. W. Potts et al., "An experimental and theoretical study of the valence shell photoelectron spectrum of the chlorobenzene molecule", *Chem. Phys.* **254**, 385 (2000), DOI: 10.1016/S0301-0104(00)00023-9.

[67] A. B. Trofimov et al., "An experimental and theoretical study of the valence shell photoelectron spectra of thiophene, 2-chlorothiophene and 3-chlorothiophene", *Chem. Phys.* **263**, 167 (2001), DOI: 10.1016/S0301-0104(00)00334-7.

[68] M. H. Javani, H. S Chakraborty, S. T. Manson, "Valence photoionization of noble-gas atoms confined in the fullerene C_{60}", *Phys. rev. A* **89**, 053402 (2014), DOI: 10.1103/PhysRevA.89.053402.

[69] D. M. P. Holland et al., "A study of the valence shell electronic structure and photoionisation dynamics of ortho-dichlorobenzene, orthobromochlorobenzene and trichlorobenzene", *Chem. Phys.* **448**, 61 (2015), DOI: 10.1016/j.chemphys.2014.11.025.

[70] I. Powis et al., "Photoionization dynamics of cis-dichloroethene from investigation of vibrationally resolved photoelectron spectra and angular distribution", *J. Chem. Phys.* **149**, 074305 (2018), DOI: 10.1063/1.5042216.

[71] G. Rossi, I. Lindau, L. Braicovich, I. Abbati, "Cooper-minimum effects in the photoionization cross sections of 4d and 5d electrons in solid compounds", *Phys.Rev. B* **28**, 3031 (1983), DOI: 10.1103/PhysRevB.28.3031.

[72] R. J. Cole et al., "Solid-state effects on Ag in dilute alloys revealed by Cooper-minimum photoemission", *Phys. Rev. B* **46**, 3747 (1992), DOI: 10.1103/PhysRevB.46.3747.

[73] L. S. Molodtsov et al., "Cooper minima in the photoemission spectra of solids", *Phys. Rev. Lett.* **85**, 184 (2000), DOI: 10.1103/PhysRevLett.85.4184.

[74] K. L. Reid, "Photoelectron angular Distributions", *Annu. Rev. Phys. Chem.* **54**, 397 (2003), DOI: 10.1146/annurev.physchem.54.011002.103814.

[75] B. Ritchie, "Theory of the angular distribution of photoelectrons ejected from optically active molecules and molecular negative ions", *Phys. Rev. A* **13**, 1411 (1976), DOI: 10.1103/PhysRevA.13.1411.

[76] G. A. Garcia, H. Dossmann, L. Nahon, S. Daly, I. Powis, "Photoelectron circular dichroism andspectroscopy of trifluoromethyl- and methyl-oxirane: a comparative study", *Phys. Chem. Chem. Phys.* **16**, 16214 (2014), DOI: 10.1039/c4cp01941e.

[77] S. Turchini et al., "Valence photoionization dynamics in circulardichroism of chiral free molecules: Themethyl-oxirane", *J. Chem. Phys.* **122**, 244303 (2005), DOI: 10.1103/PhysRevA.70.014502.

[78] S. Stranges et al., "Circular dichroism in photoelectron spectroscopy of free chiral molecules: Experiment and theory on methyl-oxirane", *Phys. Rev. A* **70**, 014502 (2004), DOI: 10.1063/1.1940632122.

[79] D. Catone et al., "Photoelectron circular dichroism of isopropanolamine", *Chem. Phys.* **482**, 294 (2017), DOI: 10.1016/j.chemphys.2016.09.004.

[80] Visit, for example, the homepage of the ScientaOmicron company or the Thermo-Fisher company.

[81] N. Böwering, T. Lischke, B. Schmidtke, N. Müller, T. Khalil, U. Heinzmann, "Asymmetry in Photoelectron Emission from Chiral Molecules Induced by Circularly Polarized Light", *Phys. Rev. Lett.* **86**, 1187 (2001), DOI: 10.1103/PhysRevLett.86.1187.

[82] T. Lischke, N. Böwering, B. Schmidtke, N. Müller, T. Khalil, and U. Heinzmann, "Circular dichroism in valence photoelectron spectroscopy of free unoriented chiral molecules: Camphor and bromocamphor", *Phys. Rev. A* **70**, 022507 (2004), DOI: 10.1103/PhysRevA.70.022507.

[83] I. Powis, "Photoelectron Circular Dichroism in Chiral Molecules", *Adv. Chem. Phys.* **138**, 267 (2008), DOI: 10.1002/9780470259474.ch5.

[84] A. Giardini et al., "Angle-Resolved Photoelectron Spectroscopy of Randomly Oriented 3-Hydroxytetrahydrofuran Enantiomers", *Chem. Phys. Chem.* **6**, 1164 (2005), DOI: 10.1002/cphc.200400483.

[85] M. Stener, G. Fronzoni, D. Di Tommaso, P. Decleva, "Density functional study on the circular dichroism of photoelectron angular distribution from chiral derivatives of oxirane", *J. Chem. Phys.* **120**, 3284 (2004), DOI: 10.1063/1.1640617.

[86] G. A. Garcia, L. Nahon, C. J. Harding, I- Powis, "Chiral signatures in angle-resolved valence photoelectron spectroscopy of pure glycidol enantiomers", *Phys. Chem. Chem. Phys.* **10**, 1628 (2008), DOI: 10.1039/b714095a.

[87] I. Powis, C. J. Harding, G. A. Garcia, L. Nahon, "A Valence Photoelectron Imaging Investigation of Chiral Asymmetry in the Photoionization of Fenchone and Camphor", *Chem. Phys. Chem.* **9**, 475 (2008), DOI: 10.1002/cphc.200700748.

[88] I. Powis, "Photoelectron circular dichroism of the randomly oriented chiral molecules glyceraldehyde and lactic acid", *J. Chem. Phys.* **112**, 301 (2000), DOI: 10.1063/1.480581.

[89] M. Stener, D. Di Tommaso, G, Fronzoni, P. Decleva, "Theoretical study on the circular dichroism in core and valence photoelectron angular distributions of camphor enantiomers", *J. Chem. Phys.* **124**, 024326 (2006), DOI: 10.1063/1.2150438.

[90] A. T. J. B Eppink, D. H. Parker, "Velocity map imaging of ions and electrons using electrostatic lenses: Application in photoelectron and photofragment ion imaging of molecular oxygen", *Rev, Sci. Instrum.* **68**, 3477 (1997), DOI: 10.1063/1.1148310.

[91] S. D. Price, "Coincidence studies of the bond-forming reactivity and reaction dynamics of molecular dications", *Phys. Chem. Chem. Phys.* **5**, 1717 (2003), DOI: 10.1039/B301957H.

[92] D. K. Böhme, "Multiply-charged ions and interstellar chemistry", *Phys. Chem. Chem. Phys.* **13**, 18253 (2011), DOI: 10.1039/C1CP21814J.

[93] R. Thissen, O. Witasse, O. Dutuit, C. S. Wedlund, G. Gronoff, J. Lilensten, "Doubly-charged ions in the planetary ionospheres: a review", *Phys. Chem. Chem. Phys.* **13**, 18264 (2011), DOI: 10.1039/C1CP21957J.

[94] S. Falcinelli et al., "Kinetic Energy Release in molecular dications fragmentation after VUV and EUV ionization and escape from planetary atmospheres", *Planet. Space Sci.* **99**, 149 (2014), DOI: 10.1016/j.pss.2014.04.020.

[95] S. Falcinelli et al., "Molecular Dications in Planetary Atmospheric Escape", *Atmosphere* **7**, 112 (2016), DOI: 10.3390/atmos7090112.

[96] F. Falcinelli, F. Pirani, M. Alagia, L. Schio, R. Richter, S. Stranges, F. Vecchiocattivi, "The escape of O^+ ions from the atmosphere: An explanation of the observed ion density profiles on Mar", *Chem. Phys. Lett.* **666**, 1 (2016), DOI: 10.1016/j.cplett.2016.09.003.

[97] S. D. Price, "Investigating the gas-phase chemical reactions of molecular dications", *Int. J. Mass Spectrom.* **260**, 1 (2007), DOI: 10.1016/j.ijms.2006.06.018.

[98] A. Huetz, P. Selles, D. Waymel, J. Mazeau , "Wannier theory for double photoionization of noble gases", *J. Phys. B: At. Mol. Opt. Phys.* **24**, 1917 (1991), DOI: 10.1088/0953-4075/24/8/010.

[99] K. Hino, T. Ishihara, F. Shimizu, N. Toshima, J. H. McGuire, "Double photoionization of helium using many-body perturbation theory", *Phys. Rev. A* **48**, 1271 (1993), DOI: 10.1103/PhysRevA.48.1271.

[100] N. L. Manakov, S. I. Marmo, A. V. Meremianin, "A new technique in the theory of angular distributions in atomic processes: the angular distribution of photoelectrons in single and double photoionization", *J. Phys. B: At. Mol. Opt. Phys.* **29**, 2711 (1996), DOI: 10.1103/PhysRevA.48.1271.

[101] A. S. Kheifets, I. Bray, "Frozen-core model of the double photoionization of beryllium", *Phys. Rev. A* **65**, 012710 (2001), DOI: 10.1103/PhysRevA.65.012710.

[102] C. W. McCurdy, D. A. Horner, T. N. Rescigno, F. Martín, "Theoretical treatment of double photoionization of helium using a B-spline implementation of exterior complex scaling", *Phys. Rev. A* **69**, 032707 (2004), DOI: 10.1103/PhysRevA.69.032707.

[103] G. Turri et al., "Double photoionization of He at 80 eV excess energy in the equal-energy-sharing condition", *Phys. Rev. A* **65**, 034702 (2002), DOI: 10.1103/PhysRevA.65.034702.

[104] A. Knapp et al., "Mechanisms of Photo Double Ionization of Helium by 530 eV Photons", *Phys. Rev. Lett.* **89**, 033004 (2002), DOI: 10.1103/PhysRevLett.89.033004.

[105] J. Colgan, M. S. Pindzola, "Double photoionization of beryllium", *Phys. Rev. A* **65**, 022709 (2002), DOI: 10.1103/PhysRevA.65.022709.

[106] J. H. D. Eland, O. Vieuxmaire, T. Kinugawa, P. Lablanquie, R. I. Hall, F. Penent, "Complete Two-Electron Spectra in Double Photoionization: The Rare Gases Ar, Kr, and Xe", *Phys. Rev. Lett.* **90**, 053003 (2003), DOI: 10.1103/PhysRevLett.90.053003.

[107] P. Bolognesi, G. C. King, L. Avalsi, "Photo-double-ionization of atoms", *Rad. Phys. Chem.* **70**, 207 (2004), DOI: 10.1016/j.radphyschem.2003.12.013.

[108] T. Schneider, P. L. Chocian, J. Rost, "Separation and Identification of Dominant Mechanisms in Double Photoionization", *Phys. Rev. Lett.* **89**, 073002 (2002), DOI: 10.1103/PhysRevLett.89.073002.

[109] T. Schneider, J. Rost, "Double photoionization of two-electron atoms based on the explicit separationof dominant ionization mechanisms", *Phys. A* **67**, 062704 (2003), DOI: 10.1016/j.radphyschem.2003.12.013.

[110] G. Dujardin, S. Leach, O. Dutuit, P. M. Guyon, M. Richard-Viard, "Double photoionization of SO_2 and fragmentation spectroscopy of

SO_2^{++} studied by a photoion-photoion coincidence method", *Chem. Phys.* **88**, 339 (1984), DOI: 10.1016/0301-0104(84)87001-9.

[111] M. Ahmadl, P. Lablanquie, F. Penent, J. G. Lambourne, R. I. Hall, J. H. D. Eland, "Structure and fragmentation dynamics of N_2^{2+} ions in-double photoionization experiments", *J. Phys. B: At. Mol. Opt. Phys.* **39**, 3599 (2006), DOI: 10.1088/0953-4075/39/17/016.

[112] T. Hartman, R. Wehlit, "Double photoionization of tropone and cyclooctatetraene", *J. Chem. Phys.* **146**, 204306 (2017), DOI: 10.1063/1.4984074.

[113] R. E. Continetti, "Coincidence Spectroscopy", *Annu. Rev. Phys. Chem.* **52**, 165 (2001), DOI: 10.1063/1.1149751 .

[114] Y. P. Lee, "State-Resolved Dynamics of Photofragmentation", *Annu. Rev. Phys. Chem.* **44**, 54 (2003), DOI: 10.1146/annurev.physchem.54.011002.103803.

[115] K. Ueda, J. H. D. Eland, "Molecular photodissociation studied by VUV and softx-ray radiation", *J. Phys. B: At. Mol. Opt. Phy* **38**, S839 (2005), DOI: 10.1088/0953-4075/38/9/025.

[116] X. Yang, "Modern Trends in Chemical Reaction Dynamics", *Adv. Phys. Chem.* **14** (2004), DOI: 10.1142/5363 .

[117] M. N. R. Ashfold, D. Murdock, T. A. A. Oliver, "Molecular Photofragmentation Dynamics in the Gas and Condensed Phases", *Annu. Rev. Phys. Chem.* **68**, 63 (2017), DOI: 10.1146/annurev-physchem-052516-050756.

[118] J. H. D. Eland, F. S. Wort, R. N. Royds, "A photoelectron-ion-ion triple coincidence technique for the study of double photoionization and its consequences", *J. Electron Spectrosc. Relat. Phenom.* **41**, 297 (1986), DOI: 10.1016/0368-2048(86)85010-1.

[119] P. Salen et al., "Complete dissociation branching fractions and Coulomb explosion dynamics of SO_2 induced by excitation of O 1s pre-edge resonances", *J. Chem. Phys.* **143**, 134302 (2015), DOI: 10.1063/1.4931645.

[120] P. Salen, L. Schio, R. Richter, M. Alagia, S. Stranges, V. Zhaunerchyk, "Investigating core-excited states of nitrosyl chloride (ClNO) and their break-up dynamics following Auger decay", *J. Chem. Phys.* **149**, 164305 (2018), DOI: 10.1063/1.5047262.

[121] E. Itälä et al., "Fragmentation of imidazole, pyrimidine and purine induced by core ionization: Significance of small-scale chemical environment", *J. Photochem. Photobiol. A* **356**, 283 (2018), DOI: 10.1016/j.jphotochem.2018.01.003.

[122] M, A.Parkes, K. M.Douglas, S. D.Price, "Ionization of acetonitrile", *Int. J. Mass Spectrom.* **438**, 97 (2019), DOI: 10.1016/j.ijms.2018.12.012.

[123] R. D. Molloy, J. H. D. Eland, "Double photoionisation of toluene", *Chem. Phys. Lett.* **421**, 31 (2006), DOI: 10.1016/j.cplett.2006.01.051.

[124] J. H. D. Eland, R. Feifel, M. Hochlaf, "Double photoionization and dication fragmentation of CF_3I: Experiment and theory", *J. Chem. Phys.* **128**, 234303 (2008), DOI: 10.1063/1.2937901.

[125] S. Falcinelli et al., "Molecular Fragmentation of Acetylene by VUV Double Photoionization", *Proceedings* **1**, 81 (2017), DOI: 10.3390/ecas2017-04126.

[126] T D. Fridgen, L. MacAleese, T. B. McMahon, J. Lemaire, P. Maitre, "Gas phase infrared multiple-photon dissociation spectra of methanol, ethanol and propanol proton-bound dimers, protonated propanol and the propanol/water proton-bound dimer", *Phys. Chem. Chem. Phys.* **8**, 955 (2006), DOI: 10.1039/b516661f.

[127] N. C. Polfer, J. Oomens, "Vibrational spectroscopy of bare and solvated ionic complexes of biological relevance ", *Mass. Spectrom. Rev.* **28**, 468 (2009), DOI: 10.1002/mas.20215.

[128] F. X. Sunahori, G. Yang, E. N. Kitova, J. S. Klassen, Y. Xu, "Chirality recognition of the protonated serine dimer and octamer by infrared multiphoton dissociation spectroscopy", *Phys. Chem. Chem. Phys.* **15**, 1873 (2013), DOI: 10.1039/c2cp43296j.

[129] L. Jasikova, J. Roithova, "Infrared Multiphoton Dissociation Spectroscopy with Free-Electron Lasers: On the Road from Small Molecules to Biomolecules", *Chem. Eur. J.* **24**, 3374 (2018), DOI: 10.1002/chem.201705692.

[130] V. Yatsyna, D. J. Bakker, P. Salén, R. Feifel, A. M. Rijs, V. Zhaunerchyk, "Infrared Action Spectroscopy of Low-Temperature Neutral Gas-Phase Molecules of Arbitrary Structure", *Phys. Rev. Lett.* **117**, 118101 (2016), DOI: 10.1103/PhysRevLett.117.118101.

[131] V. Yatsyna et al., "Competition between folded and extended structures of alanylalanine (Ala-Ala) in a molecular beam", *Phys. Chem. Chem. Phys.* **21**, 14126 (2019), DOI: 10.1039/C9CP00140A.

[132] V. Yatsina et al., "Conformational Preferences of Isolated Glycylglycine (Gly-Gly) Investigated with IRMPD-VUV Action Spectroscopy and Advanced Computational Approaches.", *J. Phys. Chem. A* **123**, 862 (2019), DOI: 10.1021/acs.jpca.8b10881.

[133] B. H. Stuart, "Infrared Spectroscopy: Fundamentals and Applications",(Wiley Online Library, 2005).

[134] H. Hu et al., "Far-field nanoscale infrared spectroscopy of vibrational fingerprints of molecules with graphene plasmons", *Nat. Commun.* **12**, 12334 (2016), DOI: 10.1038/ncomms12334.

[135] J. Réhault et al., "Fourier transform spectroscopy in the vibrational fingerprint region with a birefringent interferometer", *Opt. Express* **55**, 4406 (2017), DOI: 10.1364/OE.25.004403.

[136] D. J. Nesbit, R. W. Field, "Vibrational Energy Flow in Highly Excited Molecules: Role of Intramolecular Vibrational Redistribution"", *J. Chem. Phys.* **100**, 12735 (1996), DOI: 10.1021/jp960698w.

[137] M. Yavor, "Chapter 6: Electrostatic Energy Analyzer", in *Rep. Prog. Phys.* **53**, 1621 (1990), DOI: 10.1016/S1076-5670(09)01606-1.

[138] D. Roy, D. Tremblay, "Design of electron spectrometers", *J. Electron Spectros. Relat. Phenom.* **125**, 221 (2002), DOI: 10.1088/0034-4885/53/12/003.

[139] T. J. M. Zouros, E. P. Benis, "The hemispherical deflector analyser revisited. I. Motion in the ideal 1/r potential, generalized entry conditions, Kepler orbits and spectrometer basic equation", *J. Electron Spectros. Relat. Phenom.* **125**, 221 (2002), DOI: 10.1016/S0368-2048(02)00137-8.

[140] O. Sise, M. Ullu, M. Dogan, G. Martinez, T. J. M. Zouros, "Fringing field optimization of hemispherical deflector analyzers using BEM and FDM", *J. Electron Spectros. Relat. Phenom.* **177**, 42 (2010), DOI: 10.1016/j.elspec.2010.01.00.

[141] O. Sise, "A study of the electron optical properties of hemispherical deflection analyzer aimed at optimizing their fringing field correction schemes", *U.P.B. Sci. Bull., Series A* **77**, 213 (2015).

[142] J. K. Ovrebo, J. L. Erskine, "Angle-resolving photoelectron energy analyzer designed for synchrotron radiation spectroscopy", *J. Electron Spectros. Relat. Phenom.* **24**, 189 (1981), DOI: 10.1016/0368-2048(81)80006-0

[143] G. C. King, "Chapter 5: Electron and ion optic", in *Experimental Methods in the Physical Sciences. Atomic, Molecular, and Optical Physics: Atoms and Molecules* **29A**, 189-207 (1995), Accademic Press Inc., DOI: 10.1016/S0076-695X(08)60656-0

[144] D. W. O. Heddle, " Electrostatic Lens Systems", 2nd edition (2000), IOP Press.

[145] E.P. Benis, T. J. M. Zouros, "The hemispherical deflector analyser revisited II. Electron-optical properties", *J. Electron Spectros. Relat. Phenom.* **163**, 28 (2008), DOI: 10.1016/j.elspec.2008.02.001

[146] C. D Child, "Discharge From Hot CaO", *Phys. Rev. (Series I)* **32**, 492 (1911), DOI: 10.1103/PhysRevSeriesI.32.4920

[147] I. Langmuir, "The Effect of Space Charge and Residual Gases on Thermionic Currents in High Vacuum", *Phys. Rev.* **2**, 450 (1913), DOI: 10.1103/PhysRev.2.450

[148] C. Tusche, Y. J. Chena, C. M. Schneider, J. Kirschner, "Imaging properties of hemispherical electrostatic energy analyzers for high resolution momentum microscopy", *Ultramicroscopy* **206**, 112815 (2019), DOI: 10.1016/j.ultramic.2019.112815

[149] R. Herzog, "Ablenkung von Kathoden- und Kanalstrahlen am Rande eines Kondensators, dessen Streufeld durch eine Blende begrenzt ist", *Z. Phys.* **96**, 596 (1935), DOI: 10.1007/BF01333901

[150] K. Jost, "Novel design of a 'spherical' electron spectrometer", *J. Phys. E: Sci. Instrum.* **12**, 1006 (1979), DOI: 10.1088/0022-3735/12/10/027

[151] N. Martensson et al., " A very high resolution electron spectrometer", *J. Electron Spectros. Relat. Phenom.* **70**, 117 (1994), DOI: 10.1016/0368-2048(94)02224-N

[152] P. Baltzer, B. Wannberg. M. C. Gothe, " Optimization and redesign of an electron spectrometer for high-resolution gas phase UV photoelectron, Auger electron, and ion fragment spectroscopy", *Rev. Sci. Instrum.* **62**, 643 (1991), DOI: 10.1063/1.1142518

[153] E. P. Benis, T. J. M. Zouros, "Improving the energy resolution of a hemispherical spectrograph using a paracentric entry at a non-zero potential", *Nucl. Instrum. Methods Phys. Res. A* **440**, 462 (2000), DOI: 10.1016/S0168-9002(99)00954-7

[154] T. J. M. Zouros, E. P. Benis, I.E. Schauer, "Charged particle trajectories in an ideal paracentric hemispherical deflection analyser", *AIP Conference Proceedings* **576**, 76 (2001), DOI: 10.1063/1.1395253

[155] O. Sise, T. J. M. Zouros, M. Ulu, M. Dogan, "Comparison of fringing field correction schemes for the 180° hemispherical deflector analyzer", *Phys. Procedia* **1**, 473 (2008), DOI: 10.1016/j.phpro.2008.07.129

[156] The field and particle trajectory simulator -Industry standard charged particle optics software SIMION, available at www.simion.com.

[157] G. Eschard, B.W. Manley, "Principle and characteristics of channel electron multipliers", *Acta Electron.* **14**, 19 (1971).

[158] J. L. Wiza, "Microchannel plate detectors", *Nucl. Instrum. Methods.* **162**, 587 (1979), DOI: 10.1016/0029-554X(79)90734-1.

[159] O. Jagutzki et al., "Multiple hit readout of a microchannel plate detector with a three-layer delay-line anode", *IEEE T. Nucl. Sci.* **49**, 2477 (2002), DOI: 10.1109/TNS.2002.803889.

[160] K. Smith, "Chapter 8: Position-sensitive particle detection with microchannel-plate electron multipliers", in *Experimental Methods in the Physical Sciences. Atomic, Molecular, and Optical Physics: Atoms and Molecules* **29A**, 253-271 (1995), Accademic Press Inc.

[161] M. Lampton, F, Paresce, "The Ranicon: A resistive anode image converter", *Rev. Sci. Instrum.* **45**, 1098 (1974), DOI: 10.1063/1.168681.

[162] F.R. Elder, A. M. Gurewitsch, R. V. Lamgmuir, H. C. Pollock, "Radiation from electrons in a Synchrotron", *Phys. Rev.* **71**, 829 (1947), DOI: 10.1103/PhysRev.71.829.5.

[163] G. Margaritondo, "A primer in Synchrotron Radiation: everything you wanted to ask about SEX (Synchrotron Emission of X-Rays) but were afraid to ask", *J. Synchrotron Rad.* **2**, 148 (1995), DOI: 10.1107/S0909049595001701.

[164] S. Mobilio, F. Boscherini, C. Meneghini, "Synchrotron Radiation: Basics, Methods and Applications", *Springer-Verlag Berlin Heidelberg* (2015), DOI: 10.1007/978-3-642-55315-8.

[165] For more info visit www.elettra.eu.

[166] K. C. Prince et al., "The gas-phase photoemission beamline at Elettra", *J. Synchrotron Rad.* **5**, 565 (1998), DOI: 10.1107/S090904959800065X.

[167] M. Alagia et al., "The gas-phase photoemission beamline at Elettra", *J. Synchrotron Rad.* **16**, 19 (2003), DOI: 10.1080/08940880308603010.

[168] D. Desiderio et al., "The ELETTRA circular polarization beamline and electromagnetic elliptical wiggler insertion device", *J. Synchrotron Rad.* **12**, 34 (1999), DOI: 10.1080/08940889908261012.

[169] G. Margaritondo, P. R. Ribic, "A simplified description of X-ray free-electron lasers", *J. Synchrotron Rad.* **18**, 101 (2011), DOI: 10.1107/S090904951004896X.

[170] For more information visit www.ru.nl/felix/.

[171] M. alagia et al., "Probing the potential energy surface by high-resolution x-ray absorption spectroscopy: The umbrella motion of the core-excited CH_3 free radical", *Phys. Rev. A* **76**, 022509 (2007), DOI: 10.1103/PhysRevA.76.022509.

[172] P. Salen et al., "Complete dissociation branching fractions and Coulomb explosion dynamics of SO_2 induced by excitation of O 1s pre-edge resonances", *J. Chem. Phys.* **143**, 134302 (2015), DOI: 10.1063/1.4931645.

[173] P. Salen, L. Schio, R. Richter, M. Alagia, S. Stranges, V. Zhaunerchyk, "Investigating core-excited states of nitrosyl chloride (ClNO) and their break-up dynamics following Auger decay", *J. Chem. Phys.* **149**, 164305 (2018), DOI: 10.1063/1.5047262.

[174] M. Lavollèe, "A new detector for measuring three-dimensional momenta of charged particles in coincidence", *Rev. Sci. Instrum.* **70**, 2968 (1999), DOI: 10.1063/1.1149855.

[175] M. Alagia et al., "Anisotropy of the angular distribution of fragment ions in dissociative double photoionization of N_2O molecules in the 30–50 eV energy range", *J. Chem. Phys.* **126**, 201101 (2007), DOI: 10.1063/1.2743616.

[176] M. Alagia et al., "Dissociative double photoionization of CO_2 molecules in the 36–49 eV energy range: Angular and energy distri-

bution of ion products", *Phys. Chem. Chem. Phys.* **12**, 5389 (2010), DOI: 10.1039/b926960f.

[177] W. E. Wiley, L. H. MacLAren, "Time-of-flight spectrometer with improved resolution", *Rev. Sci. Instrum.* **26**, 1150 (1955), DOI: 10.1063/1.1715212.

[178] J. H. D. Eland, "Dynamics of Fragmentation Reactions From Peak Shapes in Multiparticle Coincidence Experiments", *Laser Chem.* **11**, 259 (1991), DOI: 10.1155/lc.11.259.

[179] L. J. Frasinski, M. Stankiewicz, P. A. Hatherly, K. Codling, "Removal of false coincidences in triple coincidence experiments employing continuous excitation", *Meas. Sci. Technol.* **3**, 1188 (1992), DOI: 10.1088/0957-0233/3/12/012.

[180] A. E. Slattery, T. A. Fieldl, M. Ahmad, R. I. Hall, P. Lablanquie, F. Penent, "A method of false coincidence removal from measurements of quadruple coincidences between two photoelectrons and two photoions generated in molecular double photoionization", *Meas. Sci. Technol.* **13**, 2007 (2002), DOI: 10.1088/0957-0233/13/12/328.

[181] F. Jensen, "Introduction to computational chemistry: second edition", *John Wiley & Sons Ltd* (2007).

[182] C. Dykstra, G. Frenking, K. Kim, G. Scuseria, "Theory and Applications of Computational Chemistry: first edition", *Elsevier Science* (2005).

[183] P. G. Burke, "The low-energy scattering of electrons and positrons by Hydrogen atoms", *Rev. Mod. Phys.* **34**, 458 (1962), DOI: 10.1103/RevModPhys.34.458.

[184] J. Linderberg, Y. Ohrn, "Propagators in quantum chemistry", *Academic. London* **34** (1973).

[185] J. V. Ortiz, "Towards an exaxt one-electron picture of chemical bonding", *Adv. Quantum Chem.* **35**, 33 (1999), DOI: 10.1016/S0065-3276(08)60454-2.

[186] H. R. Hudok *et al.*, "Ab initio molecular dynamics and time-resolved photoelectron spectroscopy of electronically excited uracil and thymine", *J. Phys. Chem A* **111**, 8500 (2007), DOI: 10.1021/jp0723665.

[187] C. M. Oana, A. I. Krylov, "Dyson orbitals for ionization from the ground and electronically excited states within equation-of-motion coupled-cluster formalism: theory, implementation, and examples", *J. Chem Phys.* **127**, 234106 (2007), DOI: 10.1063/1.2805393.

[188] B. O. Roos, P. R. Taylor, P. E. M. Siegbahn, "A complete active space SCF method (CASSCF) using a density matrix formulated super-CI approach", *Chem Phys.* **48**, 157 (1980), DOI: 10.1016/0301-0104(80)80045-0.

[189] P. Hohenberg, W. Kohn, "Inhomogeneous Electron Gas", *Phys. rev.* **136**, B864 (1964), DOI: 10.1103/PhysRev.136.B864.

[190] W. Kohn, L. J. Sham, "Self-Consistent Equations Including Exchange and Correlation Effects", *Phys. rev.* **140**, A1133 (1965), DOI: 10.1103/PhysRev.140.A1133.

[191] R. O. Jones, O. Gunnarssonm, "The density functional formalism, its applications and prospects", *Rev. Mod. Phys.* **61**, 689 (1989), DOI: 10.1103/RevModPhys.61.689.

[192] A. D. Becke, "Density-functional exchange-energy approximation with correct asymptotic behavior", *Phys. rev. A* **38**, 3098 (1988), DOI: 10.1103/PhysRevA.38.3098.

[193] A. D. Becke, "A new mixing of Hartree–Fock and local density-functional theories", *J. Chem. Phys.* **98**, 1372 (1998), DOI: 10.1063/1.464304.

[194] Erich Runge, E. K. U. Gross, "Density-Functional Theory for Time-Dependent Systems", *Phys. Rev. Lett.* **52**, 997 (1984), DOI: 10.1103/PhysRevLett.52.997

[195] M. Petersilka, U. J. Gossmann, E. K. U. Gross, "Excitation Energies from Time-Dependent Density-Functional Theory", *Phys. Rev. Lett.* **76**, 1212 (1996), DOI: 10.1103/PhysRevLett.76.1212.

[196] I. J. Schoenberg, "Contributions to the problem of approximation of equidistant data by analytic functions. Part A. On the problem of smoothing or graduation. A first class of analytic approximation formulae", *Quart. Appl. Math.* **4**, 45 (1946), DOI: 10.1090/qam/15914.

[197] D. Toffoli, M. Stener, G. Fronzoni, P. Decleva, "Convergence of the multicenter B-spline DFT approach for the continuum", *Chem. Phys.* **276**, 25 (2002), DOI: 10.1016/S0301-0104(01)00549-3.

[198] G. te Velde et al., "Chemistry with ADF", *Angew. Chem. Int. Ed. Engl.* **22**, 931 (2001), DOI: 10.1002/jcc.1056.

[199] M. Brosio, P. Decleva, A. Lisini, "LCAO expansion in a spline basis for accurate variational determination of continuum wavefunctions. Applications to H_2^+ and HeH^{2+}", *Chem. Phys.* **181**, 85 (1994), DOI: 10.1016/0301-0104(94)85017-8.

[200] M. Venuti, M. Stener, P. Decleva, "Valence photoionization of C_6H_6 by the B-spline one-centre expansion density functional method", *Chem. Phys.* **181**, 85 (1994), DOI: 10.1016/0301-0104(94)85017-8.

[201] H. Q Pharm, M. J. Marks, "Epoxy Resins", *Ullmann's Encyclopedia of Industrial Chemistry*, Weinheim, Wiley-VCH (2005), DOI: 10.1002/14356007.a09$_5$47.*pub*2.

[202] C. Chang, M. He, J. Zhou, L. Zhang, "Swelling Behaviors of pH- and Salt-Responsive Cellulose-Based Hydrogels", *Macromelcules* **44**, 1642 (2011), DOI: 10.1021/ma102801f.

[203] E. J. McAlduff, K. N. Houk , "Photoelectron spectra of substituted oxiranes and thiiranes. Substituent effects on ionization potentials involving σ orbitals", *Can. J. Chem.* **55**, 318 (1977), DOI: 10.1139/v77-048.

[204] S. Daly, I. Powis, G. A. Garcia, H. Soldi-Lose, L. Nahon, "Photoionization of epichlorohydrin enantiomers and clusters studied with circularly polarized vacuum ultraviolet radiation", *J. Chem. Phys.* **134**, 064306 (2011), DOI: 10.1063/1.3536500.

[205] S. Stranges et al., "The valence electronic structure and conformational flexibility of epichlorohydrin", *Phys. Chem. Chem. Phys.* **13**, 12517 (2011), DOI: 10.1039/c0cp02730h.

[206] W. Von Niessen, G. Bieri, J. Schirmer, L. S. Caderbaum, "Hole-mixing effects in the ionization of some unsaturated oxo-compounds", *Chem. Phys.* **65**, 157 (1982), DOI: 10.1016/0301-0104(82)85065-9.

[207] 24. A. Ponzi, C. Angeli, R. Cimiraglia, S. Coriani, P. Decleva, , "Dynamical photoionization observables of the CS molecules: The role of the electron correlation", *J. Chem. Phys.* **140**, 204304 (2014), DOI: 10.1063/1.4876495.

[208] J. M. Dyke, S. D. Gamblin, A. Morris, T. G. Wright, A. E. Wright, J. B. West, "A photoelectron spectrometer for studying reactive intermediates using synchrotron radiation", *J. Electron Spectrosc. Relat. Phenom.* **97**, 5-14 (1998), DOI: 10.1016/S0368-2048(98)00253-9.

[209] A. Morris, J. M. Dyke, "Safe handling of corrosive chemicals in a vacuum environment: a case study – photoelectron spectroscopy of reactive intermediates", *Vacuum* **53**, 339-345 (1999), DOI: 10.1016/S0042-207X(98)00381-9.

[210] J. D, Barr et al., "Photoelectron spectroscopy of reactive intermediates using synchrotron radiation", *J. Electron Spectrosc. Relat. Phenom.* **108**, 47-61 (2000), DOI: 10.1016/S0368-2048(00)00145-6.

[211] J. M: Dyke, "Photoionization studies of reactive intermediates using synchrotron radiation", *Phys. Chem. Chem. Phys.* **21**, 9106 (2019), DOI: 10.1039/c9cp00623k.

[212] F. Innocenti et al., "Measurement of the partial photoionization cross sections and asymmetry parameters of S atoms in the photon energy range 10.0-30.0 eV using constant-ionic-state spectroscopy ", *J. Chem. Phys.* **126**, 154310 (2007), DOI: 10.1063/1.2720391.

[213] F. Innocenti et al., "Difluorocarbene Studied with Threshold Photoelectron Spectroscopy (TPES): Measurement of the First Adiabatic Ionization Energy (AIE) of CF_2", *Chem.: Eur. J.* **14**, 11452-11460 (2008), DOI: 10.1002/chem.200801699.

[214] L. Schio et al., "A Study of H_2O_2 with Threshold Photoelectron Spectroscopy (TPES)and Electronic Structure Calculations: Redetermination of the First Adiabatic Ionization Energy (AIE)", *J. Chem. Phys. A* **120**, 5220-5229 (2016), DOI: 10.1021/acs.jpca.6b01039.

[215] M. Lampton, O. Siegmund, R. Raffanti, "Delay line anodes for microchannel-plate spectrometers", *Rev. Sci. Instrum.* **58**, 2298-2305 (1987), DOI: 10.1063/1.1139341.

[216] M. Lampton and M. Marckwordt, "Stacked orthogonal serpentine delay lines with vias for two-dimensional microchannel plate readout", *Rev. Sci. Instrum.* **71**, 4611-4619 (2000), DOI: 10.1063/1.1326928.

[217] P. Torelli et al., "Experimental setup for high energy photoemission using synchrotron radiation", *Rev. Sci. Instrum.* **76**, 023909 (2005), DOI: 10.1063/1.1852323.

[218] G. Cautero et al., "A two-dimensional detector for pump-and-probe and time resolved experiments", *Nucl. Instr. and Meth. A* **595**, 447-459 (2008), DOI: 10.1016/j.nima.2008.06.046.

[219] B. F. G. Johnsons, "Transition Metal Clusters", John Wiley and sons, New York, (1980).

[220] O. Schalk, I. Josefsson, R. Richter, K. C. Prince, M. Odelius, M. Mucke, "Ionization and photofragmentation of $Ru_3(CO)_{12}$ and $Os_3(CO)_{12}$", *J. Chem. Phys.* **143**, 154305 (2015), DOI: 10.1063/1.4933060

[221] S. Paranthaman, J. Moon, J. Kim, D. E. Kim, T. K. Kim, "Performance of Density Functional Theory and Relativistic Effective Core Potential for Ru-Based Organometallic Complexes", *J. Phys. Chem. A* **120**, 2128 (2016), DOI: 10.1021/acs.jpca.6b00654.

[222] S. Manna, S. Mishra, "Correlation effects in the photoelectron spectrum and photoionization dynamics of OsO4", *Phys. Chem. Chem. Phys.* , 2020, Advance Article, DOI: 10.1039/C9CP05062K.

[223] Jennifer C.Green, N. Kaltsoyannis, K. H .Sze, M. A. MacDonald, "An investigation of the electronic structure of osmium tetroxide by photoelectron spectroscopy with variable photon energy", *Chem. Phys. Lett.* **175**, 359 (1990), DOI: 10.1016/0009-2614(90)80125-W.

[224] J. C. Green et al., "Variable photon energy photoelectron spectroscopy of osmium tetroxide and pseudopotential calculations of the valence ionization energies of OsO_4 and ruthenium tetroxide", *Inorg. Chem.* **31**, 1588 (1992), DOI: 10.1021/ic00035a013.

[225] E. Diemann, A Mûller, "The He(I) photoelectron spectra of OsO_4, and RuO_4", *Chem. Phys. Lett.* **19**, 538 (1973), DOI: 10.1016/0009-2614(73)85143-7.

[226] P. Burroughs, S. Evans, A. Hamnett, A. F. Orchard, N. V. Richardson, "He-I photoelectron spectra of some d^0 transition metal compounds", *J. Chem. Soc., Faraday Trans. 2* **70**, 1895 (1974), DOI: 10.1039/F29747001895.

[227] B. E. Bursten, J. C. Green, N. Kaltsoyannis, "Theoretical investigation of the effects of spin-orbit coupling on the valence photoelectron spectrum of OsO_4", *Inorg. Chem.* **33**, 2315 (1994), DOI: 10.1021/ic00089a002.

[228] Y. Akinaga, T. Nakajima, "Two-Component Relativistic Equation-of-Motion Coupled-Cluster Methods for Excitation Energies and Ionization Potentials of Atoms and Molecules", *J. Phys. chem. A* **121**, 827 (2017), DOI: 10.1021/acs.jpca.6b10921.

[229] T.Nakajima, K. Koga, K. Hirao, "Theoretical study of valence photoelectron spectrum of OsO_4: A spin-orbit RESC-CASPT2 study", *J. Chem. Phys.* **112**, 10142 (2000), DOI: 10.1063/1.481654.

[230] D. Coster, R. de L. Kronig, "New type of auger effect and its influence on the x-ray spectrum", *Physica* **2**, 13 (1935), DOI: 10.1016/S0031-8914(35)90060-X.

[231] C. Guillot et al., "Resonant Photoemission in Nickel Metal", *Phys. Rev. Lett.* **39**, 1632 (1977), DOI: 10.1103/PhysRevLett.39.1632.

[232] D. Briggs, "Handbook of X-ray and Ultraviolet Photoelectron Spectroscopy", Heyden, London, 1977.

[233] N. Adam et al., "Polyurethanes", *Ullmann's Encyclopedia of Industrial Chemistry*, Weinheim, Wiley-VCH (2005), DOI: 10.1002/14356007.a21$_6$65.*pub*2

[234] B. A. McGuire et al., "Discovery of the interstellar chiral molecule propylene oxide (CH_3CHCH_2O)", *Science* **352**, 6292 (2016), DOI: 10.1126/science.aae0328.

[235] D. C. Che, K. Kanda, F. Palazzetti, V. Aquilanti, T. Kasai, "Electrostatic hexapole state-selection of the asymmetric-top molecule propylene oxide: Rotational and orientational distributions", *Chem. Phys.* **399**, 180 (2012), DOI: 10.1016/j.chemphys.2011.11.020.

[236] J. Bailey, "Astronomical Sources of Circularly Polarized Light and the Origin of Homochirality", *J. Orig. Life Evol. Biosph.* **31**, 167 (2001), DOI: 10.1023/A:1006751425919.

[237] Data from NIST Chemical Webbook USA, webbook.nist.gov.

[238] F. Liu et al., "A Vacuum Ultraviolet Photoionization Mass Spectrometric Study of Propylene Oxide in the Photon Energy Region of 1040 eV", *J. Chem. Phys. A* **103**, 41 (1999), DOI: 10.1021/jp990635o.

[239] E. J. Gallegos, R. W. Kiser, "Electron Impact Spectroscopy of Ethylene Oxide and Propylene Oxide", *J. Am. Chem. Soc.* **83**, 773 (1961), DOI: 10.1021/ja01465a004.

[240] G. H. Wannier, "The Threshold Law for Single Ionization of Atoms or Ions by Electrons", *Phys. Rev.* **90**, 817 (1953), DOI: 10.1103/PhysRev.90.8174.

[241] G. H. Wannier, "Threshold Law for Multiple Ionization", *Phys. Rev.* **100**, 1180 (1955), DOI: 10.1103/PhysRev.100.1180

[242] J. Roithova, D. Schröder, J. Loos, H. Schwarz, H. C. Jankowiak, R. Berge, "Revision of the second ionization energy of toluene", *J. chem. Phys.* **122**, 094306 (2005), DOI: 10.1063/1.1856916

[243] J. Roithova,J. Zabka, D. Ascenzi, P. Franceschi, C. L. Ricketts, D. Schröder, "Energetics of fragmentations of indene dication from photoionization experiments", *Chem. Phys. Lett.* **423**, 254 (2006), DOI: 10.1016/j.cplett.2006.03.083

[244] P. Franceschini et. al, "Dissociative double photoionization of N_2 using synchrotron radiation: Appearance energy of the N^{2+} dication", *J. chem. Phys.* **126**, 134310 (2007), DOI: 10.1063/1.2714521

[245] M. Alagia et. al, "Dissociative double photoionization of singly deuterated benzene molecules in the 26-33 eV energy range", *J. chem. Phys.* **135**, 144304 (2011), DOI: 10.1063/1.3646516

[246] M. N. Piancastelli et. al, "Electronic structure of core-excited and core-ionized methyl oxirane", *J. Electron Spectrosc. Relat. Phenom.* **156-158**, 259 (2007), DOI: 10.1016/j.elspec.2006.12.068

[247] M. Cini, F. Maracci. R. Platania, "Auger electron spectra of gaseous halogen compounds", *J. Electron Spectrosc. Relat. Phenom.* **41**, 37 (1986), DOI: 10.1016/0368-2048(86)80030-5

[248] G. Alberti et. al, "Dichroism in core-excited andcore-ionized methyloxirane", *Phys. Scr.* **78**, 058120 (2008), DOI: 10.1088/0031-8949/78/05/058120

[249] R. D. Molloy, A. Danielsson, L. Karlsson, J.H.D.Eland, "Double photoionisation spectra of small molecules and a new empirical rule for double ionisation energies", *hem. Phys.* **335**, 49 (2007), DOI: 10.1016/j.chemphys.2007.03.016

[250] M. Alagia et. al., "Dissociative double photoionization of CO_2 molecules in the 36-49 eV energy range: angular and energy distribution of ion products", *Chem. Phys. Phys. Chem.* **12**, 5389 (2010), DOI: 10.1039/B926960F

[251] M. Alagia et. al., "Angular and energy distribution of fragmentions in dissociative double photoionization of acetylene molecules at 39 eV", *J. Chem. Phys.* **136**, 204302 (2012), DOI: 10.1063/1.4720350

[252] R. H. Nobes, W. J. Bouma, L. Radom, "Structure and stability of gas-phase $C_2H_3O^+$ ions: an Ab Initio molecular orbital study", *J. Am. Chem. Soc.* **105**, 309 (1983), DOI: 10.1021/ja00341a001

[253] P. C. Burgers, J. L. Holmes, J. E. Szulejko, A. A. Mommers, J. K. Terlouw, "The gas phase ion chemistry of the acetyl cation and isomeric $[C_2H_3O]^+$ ions. On the structure of the $[C_2H_3O]^+$ daughter ions generated from the enol of acetone radical cation ", *J. Mass Spectrom.* **18**, 254 (1983), DOI: 10.1002/oms.1210180607

[254] M. Dantus, R. M. Bowman, A. H. Zewail, "Femtosecond laser observations of molecular vibration and rotation", *Nature* **343**, 737 (1990), DOI: 10.1038/343737a0

[255] A. E. Slattery et al., "Spectroscopy and metastability of CO_2^{2+} molecular ions", *J. Chem. Phys.* **122**, 084317 (2005), DOI: 10.1063/1.1850895

[256] M. Alagia et. al., "Double photoionization of N_2O molecules in the 28-40 eV energy range", *Chem. Phys. Lett.* **432**, 398 (2006), DOI: 10.1016/j.cplett.2006.10.100

[257] M. Alagia et. al., "Double Photoionization of CO_2 Molecules in the 34-50 eV Energy Range", *J. Phys. Chem. A* **113**, 52 (2009), DOI: 10.1021/jp9048988

[258] T. A. Field, J. H. D. Eland, "Lifetimes of metastable molecular doubly charged ions", *Chem. Phys. Lett.* **211**, 436 (1993), DOI: 10.1016/0009-2614(93)87087-J

[259] D. Zimmerman, TH. Haber, H. Schaal, M. A. Suhm, "Hydrogen bonded rings, chains and lassos: the case of t-butyl alcohol clusters", *Mol. Phys.* **99**, 413 (2001), DOI: 10.1080/00268970010017009.

[260] K. Le Barbu-Debus *et al*, "Chiral recognition in jet-cooled complexes of (1R,2S)-(+)-cis-1-amino-2-indanol and methyl lactate: on the importance of the CH-π interaction", *Phys. Chem. CHem. Phys.* **11**, 7589 (2009), DOI: 10.1039/b906834a.

[261] M. Albrecht *et al*, "Chirality influence on the aggregation of methyl mandelate", *New J. Chem.* **34**, 1266 (2010), DOI: 10.1039/c0nj00142b.

[262] P. Asselin *et al*, "Competition between inter- and intra-molecular hydrogen bonding: An infrared spectroscopic study of jet-cooled amino-ethanol and its dimer", *J. Chem. Phys.* **145**, 224313 (2016), DOI: 10.1063/1.4972016.

[263] V. Yatsyna *et al*, "Far-infrared amide IV-VI spectroscopy of isolated 2- and 4-Methylacetanilide", *J. Chem. Phys.* **145**, 104309 (2016), DOI: 10.1063/1.4962360.

[264] F. X. Sunhaori *et al*, "Chirality recognition of the protonated serine dimer and octamer by infrared multiphoton dissociation spectroscopy", *Phys. Chem. Chem. Phys.* **15**, 1873 (2013), DOI: 10.1039/c2cp43296j.

[265] V. Yatsyna *et al*, "Infrared Action Spectroscopy of Low-Temperature Neutral Gas-Phase Molecules of Arbitrary Structure", *Phys. Rev. Lett.* **117**, 118101 (2016), DOI: 10.1103/PhysRevLett.117.118101.

[266] G. Herzberg, *Infra-Red and Raman Spectra of polyatomic molecules* (Van Nostrand, New York, 1945, pp. 201–226).

[267] J. P. Schermann, *Spectroscopy and Modeling of Biomolecular Building Blocks* (Elsevier, amsterdam, 2008, pp. 80-84).

[268] J. L. Dehmer, W. A. Chupka, J. Berkowitz, W. T. Jivery, "Wavelength dependence of the photoelectron angular distributions of the rare gases", *J. Electron Spectrosc. Relat. Phenom.* **12**, 1966 (1975), DOI: 10.1103/PhysRevA.12.1966.

[269] J. Kreile, A. Schweig, "Photoelectron asymmetry parameters of Ar, Kr, Xe, H_2, N_2, O_2, CO and CO_2: New measurements and a reconsideration of literature data", *J. Electron Spectrosc. Relat. Phenom.* **191**, 191 (1980), DOI: 10.1016/0368-2048(80)85016-X.

[270] D. M. P. Holand, J. L. Dehmer, J. B. West, "The angular distribution parameters of argon, krypton and xenon for use in calibration of electron spectrometers", *Nucl. Instrum. Meth.* **195**, 331 (1982), DOI: 10.1016/0029-554X(82)90793-5.

[271] T. S. Buys, K. De Clerk, "Bi-Gaussian fitting of skewed peaks", *Anal. Chem.* **44**, 1273 (1972), DOI: 10.1021/ac60315a005.

[272] T. Yu, H. Pengt, "Quantification and deconvolution of asymmetric LC-MS peaks using the bi-Gaussian mixture model and statistical model selection", *BMC Bioinformatics* **12**, 559 (2010), DOI: 10.1186/1471-2105-11-559.

[273] D. L. Lichtenberger, A. S. Copenhaver, "Ionization band profile analysis in valence photoelectron spectroscopy", *J. Electron Spectrosc. Relat. Phenom.* **50**, 335 (1990), DOI: 10.1016/0368-2048(90)87076-Z.

[274] A. Boccia et al., "Symmetry breaking effect in the ferrocene electronic structure by hydrocarbon-monosubstitution: An experimental and theoretical study", *J. Chem. Phys.* **128**, 154315 (2008), DOI: 10.1063/1.2898498.

[275] D. J. Nesbitt, "Vibrational Energy Flow in Highly Excited Molecules: Role of Intramolecular Vibrational Redistribution", *J. Phys Chem.* **100**, 12735 (1996), DOI: 10.1021/jp960698w.

[276] Gaussian 16, Revision B.01, M. J. Frisch, G. W. Trucks, H. B. Schlegel, G. E. Scuseria, M. A. Robb, J. R. Cheeseman, G. Scalmani, V. Barone, G. A. Petersson, H. Nakatsuji, X. Li, M. Caricato, A. V. Marenich, J. Bloino, B. G. Janesko, R. Gomperts, B. Mennucci, H. P. Hratchian, J. V. Ortiz, A. F. Izmaylov, J. L. Sonnenberg, D. Williams-Young, F. Ding, F. Lipparini, F. Egidi, J. Goings, B. Peng, A. Petrone, T. Henderson, D. Ranasinghe, V. G. Zakrzewski, J. Gao, N. Rega, G. Zheng, W. Liang, M. Hada, M. Ehara, K. Toyota, R. Fukuda, J. Hasegawa, M. Ishida, T. Nakajima, Y. Honda, O. Kitao, H. Nakai, T. Vreven, K. Throssell, J. A. Montgomery, Jr., J. E. Peralta, F. Ogliaro, M. J. Bearpark, J. J. Heyd, E. N. Brothers, K. N. Kudin, V. N. Staroverov, T. A. Keith, R. Kobayashi, J. Normand, K. Raghavachari, A. P. Rendell, J. C. Burant, S. S. Iyengar, J. Tomasi, M. Cossi, J. M. Millam, M. Klene, C. Adamo, R. Cammi, J. W. Ochterski, R. L. Martin, K. Morokuma, O. Farkas, J. B. Foresman, and D. J. Fox, Gaussian, Inc., Wallingford CT, 2016.

[277] MOPAC2016, James J. P. Stewart, Stewart Computational Chemistry, Colorado Springs, CO, USA.

[278] L. A, Curtiss *et al*, *J. Chem. Phys.* **127**, 214105 (2007), DOI: 10.1063/1.2770701.